

ISSN 1313 - 0927

Aerospace Research in Bulgaria

35

© **Aerospace Research in Bulgaria**
Space Research and Technology Institute
Bulgarian Academy of Sciences

bl.1, Acad. G. Bonchev St.,
1113 Sofia, Bulgaria
tel./fax: (+359 2) 988 35 03,
<http://www.space.bas.bg>

Bulgarian Academy of Sciences
Space Research and Technology Institute

2023

Aerospace Research in Bulgaria

35

Sofia, 2023

C o n t e n t s

1. *Peter Velinov, Simeon Asenovski, Lachezar Mateev*
COSMIC RAY SPECTRUM AND INTENSITY IN MIDDLE
ATMOSPHERE (CORSIMA) MODEL. USE AND APPLICATION
FOR SOLAR COSMIC RAYS.5
2. *Georgi Jelev*
USING REMOTE SENSING DATA AND GIS IN RESEARCH
OF MORPHOMETRIC CHARACTERISTICS OF THE COASTAL AREA
IN BULGARIA.16
3. *Maria Dimitrova, Plamen Trenchev*
SPACE DISTRIBUTION OF NO₂ POLLUTION OVER BULGARIA.28
4. *Plamen Trenchev, Maria Dimitrova, Deyan Gochev*
INCREASE OF CARBON DIOXIDE AND METHANE EMISSIONS
OVER BULGARIA ON THE BASE OF GOSAT SATELLITE DATA.34
5. *Adlin Dancheva, Temenuzhka Spasova*
USE OF OPEN, SPATIAL AND SATELLITE DATA FOR THE PURPOSE
OF RESEARCHING LANDFILLS FOR MUNICIPAL.41
6. *Antoaneta Frantzova*
DROUGHT MONITORING USING REMOTE SENSING DATA.52
7. *Hristo Nikolov, Mila Atanasova*
MONITORING COASTAL LANDSLIDES ALONG THE NORTHEAST
BLACK SEA OF BULGARIA USING SAR DATA.63
8. *Veselina Gospodinova, Todor Todorov*
THREE-DIMENSIONAL MODELLING OF A BRIDGE BY INTEGRATING
TERRESTRIAL AND AERIAL PHOTOGRAMMETRY APPLYING AN
ADAPTED CAPTURE METHOD.80
9. *Svetoslav Zabunov, Garo Mardirossian*
COMPOUND PRESELECTOR FOR MULTISTATIC PASSIVE
RADAR EMPLOYED IN REMOTE SENSING APPLICATIONS.96
10. *Ivan Ivanov*
USE OF LOW-POWER UNMANNED AERIAL VEHICLES FOR CONTROL
OF AN URBANIZED AREA.104

11. <i>Peter Getsov</i>	MODELING AND STUDY THE DISTRIBUTION OF OPERATOR ATTENTION IN CONTROLLING THE LATERAL MOVEMENT OF AN UNMANNED AERIAL VEHICLE.	114
12. <i>Konstantin Metodiev</i>	RETRACTABLE UNDERCARRIAGE DESIGN FOR A QUADCOPTER.	122
13. <i>Oleksandr Minai, Iryna Kuzmich</i>	CHOICE OF THE OPTIMUM DESIGN OF LATERAL PMD USING THE CFD METHOD.	128
14. <i>Nikolay Zagorski</i>	AVIATION SAFETY AND IMPACT ON THE RELIABILITY OF DATA FROM DIFFERENT SOURCES OF PHYSICAL SIZES.	145
15. <i>Anna Bouzekova-Penkova, Stanislav Klimov, Valery Grushin, Olga Lapshinova, Denis Novikov, Dimitar Teodosiev</i>	SPACE EXPERIMENT "OBSTANOVKA (1-STEP)", BLOCK DP - PM ON THE RUSSIAN SEGMENT OF THE INTERNATIONAL SPACE STATION.	156
16. <i>Boyko Tsyntsarski, Anna Bouzekova-Penkova, Urszula Szeluga, Georgi Georgiev, Petar Tzvetkov, Dimitar Teodosiev</i>	SEM AND EDX STUDY OF GLASSY CARBON COATINGS AFTER AN EXTENDE STAY ON THE INTERNATIONAL SPACE STATION (ISS). . .	165
17. <i>Nadia Marinova</i>	OPPORTUNITIES TO OPTIMIZE THE MANAGEMENT OF AEROSPACE PROJECTS.	174
 <u>Reviews</u>		
<i>Milen Chanev, Lachezar Filchev</i>	REVIEW OF THE APPLICATIONS OF SATELLITE REMOTE SENSING IN ORGANIC FARMING (PART I).	183
<i>Nataliya Stankova</i>	POST-FIRE RECOVERY MONITORING USING REMOTE SENSING: A REVIEW.	192
 <u>New books</u>		
<i>Peter Velinov</i>	REMOTE SENSING TECHNOLOGY IN ENGINEERING GEODESY.	201
 <u>In Memoriam</u>		
	IN MEMORY OF LEV DORMAN.	202

С Ъ Д Ъ Р Ж А Н И Е

1. **Петър Велинов, Симеон Асеновски, Лъчезар Матеев**
СПЕКТЪР И ИНТЕНЗИТЕТ НА КОСМИЧЕСКИТЕ ЛЪЧИ
ПО МОДЕЛА CORSIMA В СРЕДНАТА АТМОСФЕРА. ИЗПОЛЗВАНЕ
И ПРИЛОЖЕНИЕ ЗА СЛЪНЧЕВИТЕ КОСМИЧЕСКИ ЛЪЧИ. 5
2. **Георги Желев**
ИЗПОЛЗВАНЕ НА ДИСТАНЦИОННИ ДАННИ И ГИС
ПРИ ИЗСЛЕДВАНЕ НА МОРФОМЕТРИЧНИ ХАРАКТЕРИСТИКИ
НА КРАЙБРЕЖНАТА ЗОНА НА Р. БЪЛГАРИЯ.16
3. **Мария Димитрова, Пламен Тренчев**
ПРОСТРАНСТВЕНО РАЗПРЕДЕЛЕНИЕ НА ЗАМЪРСЯВАНЕТО С NO₂
НАД БЪЛГАРИЯ.28
4. **Пламен Тренчев, Мария Димитрова, Деян Гочев**
УВЕЛИЧЕНИЕ НА ЕМИСИИТЕ ОТ ВЪГЛЕРОДЕН ДИОКСИД И МЕТАН
НАД БЪЛГАРИЯ ПО СПЪТНИКОВИ ДАННИ ОТ GOSAT.34
5. **Адлин Данчева, Теменушка Спасова**
ИЗПОЛЗВАНЕ НА ОТВОРЕНИ ПРОСТРАНСТВЕНИ
И САТЕЛИТНИ ДАННИ ЗА ЦЕЛИТЕ НА ПРОУЧВАНЕ НА ДЕПА
ЗА БИТОВИ ОТПАДЪЦИ.41
6. **Антоанета Францова**
ИЗПОЛЗВАНЕ НА ДИСТАНЦИОННИ ДАННИ ЗА МОНИТОРИНГ
НА ПРОЦЕСИТЕ НА СУША И ЗАСУШАВАНЕ.52
7. **Христо Николов, Мила Атанасова**
МОНИТОРИНГ НА КРАЙБРЕЖНИТЕ СВЛАЧИЩА ПО
СЕВЕРОИЗТОЧНОТО ЧЕРНОМОРИЕ НА БЪЛГАРИЯ БАЗИРАНО
НА ДАННИ ОТ РАДАРИ СЪС СИНТЕЗИРАНА АПЕРТУРА.63
8. **Веселина Господинова, Тодор Тодоров**
ТРИИЗМЕРНО МОДЕЛИРАНЕ НА МОСТ ЧРЕЗ ИНТЕГРИРАНЕ
НА ЗЕМНА И ВЪЗДУШНА ФОТОГРАМЕТРИЯ, ПРИЛАГАЙКИ
АДАПТИРАН НАЧИН НА ЗАСНЕМАНЕ.80
9. **Светослав Забунов, Гаро Мардиросян**
СЪСТАВЕН ПРЕСЕЛЕКТОР ЗА МУЛТИСТАТИЧЕН ПАСИВЕН РАДАР
ЗА ДИСТАНЦИОННИ ИЗСЛЕДВАНИЯ.96
10. **Иван Иванов**
ИЗПОЛЗВАНЕ НА МАЛОМОЩНИ БЕЗПИЛОТНИ ЛЕТАТЕЛНИ
АПАРАТИ ЗА КОНТРОЛ НА УРБАНИЗИРАН РАЙОН.104
11. **Петър Гецов**
МОДЕЛИРАНЕ И ИЗСЛЕДВАНЕ НА РАЗПРЕДЕЛЕНИЕТО
НА ВНИМАНИЕТО НА ОПЕРАТОРА ПРИ УПРАВЛЕНИЕ
НА СТРАНИЧНОТО ДВИЖЕНИЕ НА БЕЗПИЛОТЕН
ЛЕТАТЕЛЕН АПАРАТ.114

12. Константин Методиев	
ПРОЕКТ НА ПРИБИРАЕМА СТОЙКА ЗА КВАДРОКОПТЕР.....	122
13. Олександр Минай, Ирина Кузмич	
ИЗБОР НА ОПТИМАЛЕН ДИЗАЙН НА СТРАНИЧЕН РМД С ИЗПОЛЗВАНЕ НА МЕТОДА CFD.....	128
14. Николай Загорски	
АВИАЦИОННАТА БЕЗОПАСНОСТ И ВЛИЯНИЕ НА ДОСТОВЕРНОСТТА НА ДАННИТЕ ОТ РАЗЛИЧНИ ИЗТОЧНИЦИ НА ФИЗИЧНИ ВЕЛИЧИНИ.....	145
15. Анна Бузекова-Пенкова, Станислав Климов, Валерий Грушин, Олга Лапишинова, Денис Новиков, Димитър Теодосиев	
КОСМИЧЕСКИ ЕКСПЕРИМЕНТ „ОБСТАНОВКА (1 - ЕТАП)", БЛОК ДП – ПМ НА РУСКИЯ СЕГМЕНТ НА МЕЖДУНАРОДНАТА КОСМИЧЕСКА СТАНЦИЯ.....	156
16. Бойко Цинцарски, Анна Бузекова-Пенкова, Урсула Шелуга, Георги Георгиев, Петър Цветков, Димитър Теодосиев	
SEM И EDX ИЗСЛЕДВАНЕ НА СЪГЛОВОУГЛЕРОДНИ ПОКРИТИЯ СЛЕД ПРОДЪЛЖИТЕЛЕН ПРЕСТОЙ НА МЕЖДУНАРОДНАТА КОСМИЧЕСКА СТАНЦИЯ (МКС).....	165
17. Надя Маринова	
ВЪЗМОЖНОСТИ ЗА ОПТИМИЗИРАНЕ УПРАВЛЕНИЕТО НА АЕРОКОСМИЧЕСКИ ПРОЕКТИ.....	174
<u>Обзори</u>	
Милен Чанев, Лъчезар Филчев	
ПРИЛОЖЕНИЕ НА СПЪТНИЦИ В БИОЛОГИЧНОТО ЗЕМЕДЕЛИЕ (ЧАСТ I).....	183
Наталия Станкова	
МОНИТОРИНГ НА ВЪЗСТАНОВИТЕЛНИТЕ ПРОЦЕСИ СЛЕД ПОЖАР С ИЗПОЛЗВАНЕ НА ДИСТАНЦИОННИ МЕТОДИ: ПРЕГЛЕД.....	192
<u>Нови книги</u>	
Петър Велинов	
ПРИЛОЖЕНИЕ НА ДИСТАНЦИОННИ ТЕХНОЛОГИИ В ИНЖЕНЕРНАТА ГЕОДЕЗИЯ.....	201
<u>In Memoriam</u>	
В ПАМЕТ НА ЛЕВ ДОРМАН.....	202

COSMIC RAY SPECTRUM AND INTENSITY IN MIDDLE ATMOSPHERE (CORSIMA) MODEL. USE AND APPLICATION FOR SOLAR COSMIC RAYS

Peter Velinov, Simeon Asenovski, Lachezar Mateev

Space Research and Technology Institute – Bulgarian Academy of Sciences

Keywords: *Solar cosmic rays spectra and intensities, Middle atmosphere, Lower ionosphere*

PACS Numbers: 94.10.-s, 94.20.-y, 96.40.-z

Abstract

The new model CORSIMA (COsmic Ray Spectrum and Intensity in Middle Atmosphere) is presented. The spectra and intensities of solar cosmic rays (SCR) from GLE (Ground Level Enhancement) 05 on 23 February 1956 and GLE 69 on 20 January 2005 at different altitudes are calculated. For this purpose, the operational CORSIMA model is applied. In the final version of the CORSIMA program, an approximation in 6 characteristic energy intervals of the Bohr-Bethe-Bloch function is used, including the charge decrease interval. Analytical expressions for the contributions of the energy intervals are provided. For the first time we present a quantitative and qualitative appreciation of the impact of Solar Cosmic Rays (SCRs) from the Solar Particle Events (SPEs) on the ionosphere and middle atmosphere (30 - 80 km). These altitudes are above the Regener-Pfotzer maximum. Unlike Galactic Cosmic Rays (GCR), the differential spectra of SCR essentially vary in time. The SCR fluxes also differ from each other during the different events. The spectrum and intensity behavior is explained considering the structure of the CORSIMA program. The calculation results are in agreement with the experimental data and show characteristic features of the propagation process for different altitudes and geomagnetic latitudes. The calculations are performed for geomagnetic latitudes 90° (cusp region). The development of this research is important for the processes and mechanisms of space weather.

Introduction

The relativistic particles of cosmic rays (protons and heavier nuclei of galactic and/or solar origin) [1, 2] induce complicated nuclear-electromagnetic-lepton cascades in the atmospheres of the Earth, planets and their moons [3–11], which eventually lead to ionization and excitation of the planetary environment. The ionization of the atmosphere caused by cosmic rays determines the effects of the precipitating particles on the physics and chemistry of the atmosphere [12–14].

Solar cosmic rays are an important factor in the ionization and energetic state of the ionosphere and atmosphere [1–4, 6, 14]. The new model CORSIMA (COsmic

Ray Spectrum and Intensity in Middle Atmosphere) is presented in this paper. CORSIMA is a submodel of CORIMIA (COsmic Ray Ionization Model for Ionosphere and Atmosphere) [15–19].

This paper presents the results of the CORSIMA program with application to GLE (Ground Level Enhancement) 05 on February 23, 1956 and GLE69 on January 20, 2005. Similar analyzes for GLEs 59, 69 and 70 are given in [20–23].

Spectra and electromagnetic interactions of SCRs

The corresponding differential spectra for GLE 69 were taken from the available GOES satellite data [22]. We investigate the SCR effects in the polar cusp region at geomagnetic latitudes of 90° during two of the strongest Solar Proton Events (SPEs) observed since the beginning of neutron monitor measurements of cosmic rays. In this way the extreme influence of solar activity on the ionization state of the ionosphere and middle atmosphere is calculated.

In contrast to the GCR cases, the SCR differential spectra essentially vary in time over the course of the event studied [24, 25]. It is difficult to generalize about the global impact of SCR on atmospheric chemistry and electrical conductivities for the entire time period. Therefore, it is useful to consider more than one-time point of the effects of SCR. In the case of GLE 69, we consider two characteristic time points – at 8:00UT and 23:00UT during SCR penetration. The corresponding differential spectrum in $\text{cm}^{-2} \cdot \text{s}^{-1} \cdot \text{MeV}^{-1}$ outside the atmosphere (according to GOES data) for the time at 8:00UT is:

$$(1) \quad D(E) = 1,55 \times 10^6 E^{-2,32},$$

and for the time point at 23:00UT is:

$$(2) \quad D(E) = 10^7 E^{-3,43}.$$

The differential spectrum for GLE 05 [3] is:

$$(3) \quad D(E) = 2,4 \times 10^{10} E^{-5}.$$

These spectra are determined in the following way. For each spectrum (1) and (2), two data points are taken from the GOES data. They belong to different energy intervals of the measurement as indicated in these data lists. Then a system of equations is solved for the two unknown parameters of the spectrum: the magnitude K and the exponent γ [5].

The CORSIMA program is applied for the first time to the SEP and the results show that it is suitable for calculating the propagation of solar particles. The model embedded in this program includes the full approximation of the Bohr-Bethe-

Bloch ionization losses function [15–19] using 6 characteristic energy intervals for cosmic ray (CR) nuclei groups:

$$(4) \quad -\frac{1}{\rho} \frac{dE}{dh} = \begin{cases} 2.57 \times 10^3 E^{0.5} & \text{if } kT \leq E \leq 0.15 \text{ MeV/n} & , \text{interval 1} \\ 1540 E^{0.23} & \text{if } 0.15 \leq E \leq E_a = 0.15 Z^2 \text{ MeV/n} & , \text{interval 2} \\ 231 \times Z^2 E^{-0.77} & \text{if } E_a \leq E \leq 200 \text{ MeV/n} & , \text{interval 3} \\ 68 \times Z^2 E^{-0.53} & \text{if } 200 \leq E \leq 850 \text{ MeV/n} & , \text{interval 4} \\ 1.91 \times Z^2 & \text{if } 850 \leq E \leq 5 \times 10^3 \text{ MeV/n} & , \text{interval 5} \\ 0.66 \times Z^2 E^{0.123} & \text{if } 5 \times 10^3 \leq E \leq 5 \times 10^6 \text{ MeV/n} & , \text{interval 6} \end{cases}$$

We investigate the case of solar protons penetration (charge $Z = 1$) into the Earth's atmosphere. That is, the interval 2 is not considered. On the other hand, we show that the last three high energy intervals (above 200 MeV) do not contribute to the ionization rate (GLE 69 at 23:00UT and GLE 05). The last two intervals (the energies above 2 GeV) for GLE 69 at 8:00UT are also without contribution (Fig. 1). Consequently, the dependence of the particle number on the characteristic energy intervals can be seen in Fig.1 (4). For comparison, we also show GCR spectra at solar minimum and maximum and anomalous CR (ACR) spectra for O^+ and He^+ with charge $Z = 1$, i.e. singly ionized. The ACR spectra are effective below 100 MeV and the GCR spectra - above 1 GeV (relativistic energies).

Model description

The operational model embedded in the CORIMIA program is developed in [15–19]. The mathematical expression for calculating the ionization rate in the atmosphere, including the full composition of CR, is as follows.

$$(5) \quad q(h) = \sum_i q_i(h) = \frac{1}{Q} \sum_i \int_{E_i}^{\infty} \int_{A=0}^{2\pi} \int_{\theta=0}^{\pi/2+\Delta\theta} D_i(E) \left(\frac{dE}{dh} \right)_i \sin \theta \, d\theta \, dA \, dE,$$

where A is the azimuth angle, θ is the angle towards the vertical, $\Delta\theta$ takes into account that at a given height the particles can penetrate from the space angle ($0^\circ, \theta_{\max}=90^\circ+\Delta\theta$), which is greater than the upper hemisphere angle ($0^\circ, 90^\circ$) for flat model. E_i are the energy cut-offs. The summation in the ionization integral (1) is made on the groups of nuclei: protons p, Helium (alpha particles), Light L ($3 \leq Z \leq 5$), Medium M ($6 \leq Z \leq 9$), Heavy H ($Z \geq 10$) and Very Heavy VH ($Z \geq 20$) nuclei in the composition of cosmic rays [1-4]. Z is the charge of the

nuclei, $Q=35\text{eV}$ is the energy which is necessary for formation of one electron-ion pair [6].

$D_i(E)$ is the corresponding SCR differential spectrum for protons which is given in (1) – (3).

Energy cut-offs E_i , which are lower boundary of integration in (5), are calculated on the base of geomagnetic E_R and atmospheric cut-offs E_A for given geomagnetic latitude λ_m and atmospheric altitude (traveling substance path \tilde{h}) with the following expression:

$$(6) \quad E_{\min} = \max\{E_R(\lambda_m), E_A(\tilde{h})\}$$

The geomagnetic cut-off [4] is evaluated in the equation (7):

$$(7) \quad E_R(\lambda_m) = \left(14.9 \left(\cos \left[\frac{\pi \lambda_m}{180} \right]^4 \right)^2 + 0.88 \right)^{1/2} - 0.938.$$

The atmospheric cut-offs take into account the traveling substance path and for the case of SCR protons (because of the characteristic energy interval ranges [18] take the forms E_{A1} and E_{A2} :

$$(8) \quad E_{A1}(h) = \left((kT)^{0.5} + 1285 \tilde{h} \right)^2,$$

$$(9) \quad E_{A2}(h) = \left[0.15^{1.77} - \frac{231 \times 1.77}{1285} \left(0.15^{0.5} - (kT)^{0.5} \right) + 231 \times 1.77 \tilde{h} \right]^{1/1.77}$$

From (5) we obtain the concrete expressions for the electron production rate caused by SCR protons penetration in the atmosphere. From Figure 1, it can be seen that the first three intervals are effective for the contributions to the ionization rate values. They are intervals 1, 3 and 4 in (4) for $Z = 1$. The energy decrease laws [8] without boundary crossing for these intervals are:

$$(10) \quad E_1(h) = \left[E_k^{0.5} - 1285 \tilde{h} \right]^2,$$

$$(11) \quad E_2(h) = \left[E_k^{1.77} - 231 \times 1.77 \tilde{h} \right]^{1/1.77}$$

$$(12) \quad E_3(h) = \left[E_k^{1.53} - 68 \times 1.53 \tilde{h} \right]^{1/1.53}$$

The energy decrease laws with boundary crossing have the form:

$$(13) \quad E_{21}(h) = \left[0.15^{0.5} - 1285\tilde{h} + \frac{1285}{231 \times 1.77} \times (E_k^{1.77} - 0.15^{1.77}) \right]^2$$

Expression (13) is valid if particles with initial energy in interval 2 cross the boundary due to ionization losses and cause ionization with energy in interval 1 at altitude h . Similar expression is derived when particles transfer the boundary between interval 3 and 2:

$$(14) \quad E_{32}(h) = \left[200^{1.77} + \frac{231 \times 1.77}{68 \times 1.53} (E_k^{1.53} - 200^{1.53}) - 231 \times 1.77\tilde{h} \right]^{1/1.77}.$$

We also include two coupling intervals for upper boundaries of interval 1 and 3 ($E_{0.15}(h), E_{200}(h)$) which have the form:

$$(15) \quad E_{0.15}(h) = \left[0.15^{1.77} + 231 \times 1.77\tilde{h} \right]^{1/1.77},$$

$$(16) \quad E_{200}(h) = \left[200^{1.53} + 1.53 \times 68\tilde{h} \right]^{1/1.53}.$$

The sub model for SCR protons penetration in the atmosphere is derived in equation (17):

$$(17) \quad q(h) = \frac{\rho(h)}{Q} \left\{ 2.57 \times 10^3 \int_{E_{\min}}^{0.15} D(E) [E_1(h)]^{0.5} dE + \right. \\ \left. 2.57 \times 10^3 \int_{0.15}^{E_{0.15}(h)} D(E) [E_{21}(h)]^{1/2} dE + \right. \\ \left. + 231 \int_{E_{0.15}(h)}^{200} D(E) [E_2(h)]^{-0.77} dE + 231 \int_{200}^{E_{200}(h)} D(E) [E_{32}(h)]^{-0.77} dE + \right. \\ \left. + 68 \int_{E_{200}(h)}^{850} D(E) [E_3(h)]^{-0.53} dE \right.$$

This expression is characteristic of SCR differential spectra, because it is restricted to the lower energy intervals of the ionization losses function.

Results and conclusions

The CORSIMA submodel for calculating of SCR penetration in the atmosphere considering the first three characteristic energy intervals (17) is applied to the GLE05 and GLE 69 events. These are the most powerful and well-known

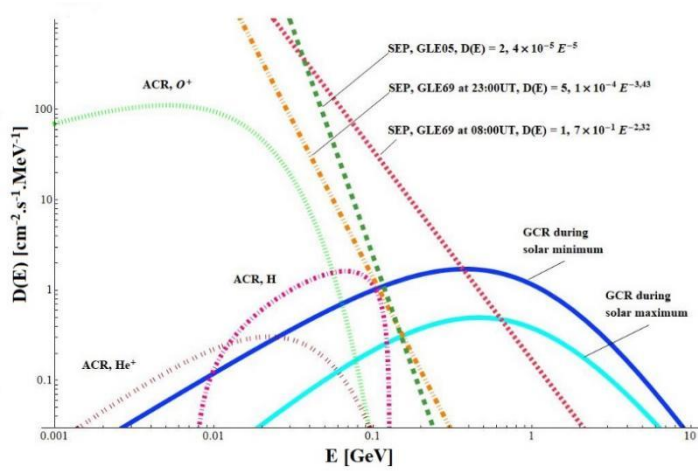


Fig. 1. Differential spectra of solar cosmic rays (SCRs) during GLE 05 and GLE 69 (8:00UT and 23:00UT). Here for comparison are presented also galactic cosmic ray (GCR) spectra during solar maximum (light blue) and solar minimum (dark blue) and anomalous cosmic ray (ACR) spectra for O^+ , He^+ and H^+ .

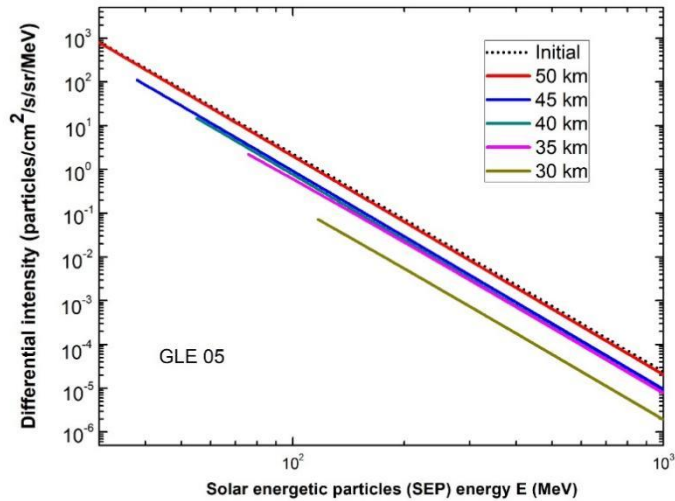


Fig. 2. Solar energetic particles (SCRs) spectrum from SPE event on 23 February 1956 at altitudes 30, 35, 40, 45, 50 km with initial spectrum outside of the atmosphere (dotted curve), this is the most powerful solar proton event in the history of space era

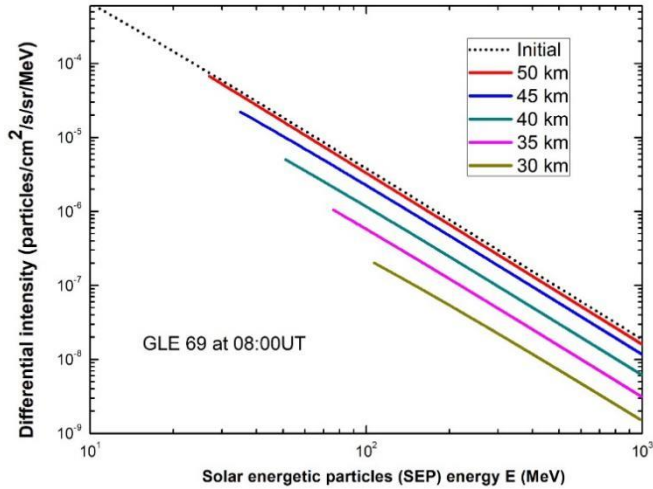


Fig. 3. Solar energetic particles (SCRs) spectrum from SPE event on 20 January 2005 at 8:00 UT for altitudes 30, 35, 40, 45, 50 km with initial spectrum outside of the atmosphere (dotted curve). This is the second powerful solar proton event in the space era.

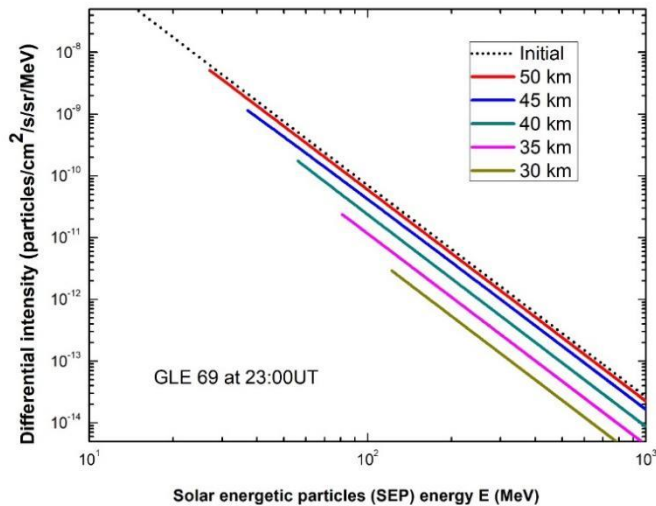


Fig. 4. Solar energetic particles (SCRs) spectrum from SPE event on 20 January 2005 at 23:00 UT for altitudes 30, 35, 40, 45, 50 km with initial spectrum outside of the atmosphere (dotted curve). This is the second powerful solar proton event in the space era.

events in the history of space exploration. Figures 2, 3 and 4 show the main results of the spectra calculated with the CORSIMA program.

The intensity of the spectrum of SCR depends on the trajectory of the substance (dependence on altitude, atmospheric cut-offs and ionization losses), geomagnetic cut-offs, neutral density (dependence on altitude), strength of the spectrum and exponent (number of charged particles).

Fig. 1 shows the GCR spectra for solar minimum and solar maximum with their characteristic maxima at 600 MeV. The SCR spectra for GLE05 and GLE69 at 8:00UT and 23:00UT are also shown. The ACR (Anomalous Cosmic Ray) spectra for O⁺ and He⁺ have lower energy values as shown in Fig. 1. On Fig. 1 are presented the main ionization sources in the upper atmosphere.

Fig. 2 shows the results of the spectra calculation of GLE 05, the strongest event observed in the history of solar cosmic ray research. This is the strongest solar proton event observed in the history of solar cosmic ray investigations. The characteristic behavior of the spectra for all altitudes is due to the wandering substance path and the corresponding atmospheric cut-offs for each altitude value. This is correct because we calculate the intensities for the polar cusp where the geomagnetic cut – off rigidity is nearly zero.

Figures 3 and 4 present the spectra of SCR during GLE 69 with spectra measured on 20.01.2005 at 8:00UT and 23:00UT. These curves reflect spectra in the polar cusp region for $\lambda_m \approx 90^\circ$ where the corresponding geomagnetic cut-offs are ≈ 0 GV. The altitude region covers the heights interval (30–80) km. As can be seen in Figures 2 and 3, the spectra increase with altitude.

The SCR spectra at latitude 90° cross due to the different energy power and magnitudes of the differential spectra for 8:00 and 23:00 UT (see Fig. 1). For lower altitudes (larger cut-off values) the spectrum with lower power dominates. For higher altitudes, the decreasing neutral density already dominates.

The differential spectrum with the smaller exponent (8:00 UT) causes larger values for lower altitudes. The reason is the strong atmospheric cut-off at these altitudes. At higher altitudes, the influence of the larger spectrum (23:00UT) dominates.

The CORSIMA and CORIMIA programs (which are based on the Mathematica program system) are able to calculate the SCR spectra and intensity stably and accurately for the effects of any solar CR impact on the lower ionosphere and middle atmosphere. The structure of the program is user–friendly, with detailed descriptions of input and output data in corresponding windows. In the future, we will further develop and improve the CORSIMA program as a directly applicable routine for the study of space weather and climate [26–29].

References

1. Ginzburg, V. L., S. I. Sirovatsky. The Origin of Cosmic Rays, Moscow, Publishing House of the USSR Academy of Sciences, 1963, 385 p.
2. Dorman, L. I. Cosmic rays in the Earth's atmosphere and underground, Dordrecht, Kluwer Academic Publishers, 2004, 606 p.
3. Usoskin, I., L. Desorgher et al., Ionization of the Earth's atmosphere by solar and galactic cosmic rays, 2009, *Acta Geophys.*, 57, 1, 88–101.
4. Gronoff, G., C Mertens, J. Lilensten, L. Desorgher, E. Fluckiger et al. Ionization processes in the atmosphere of Titan-III. Ionization by high-Z nuclei cosmic rays, 2011, *Astron. Astrophys.*, 529, A143.
5. Tsagouri, I., A. Belehaki, N. Bergeot, C. Cid, V. Delouille et al. Progress in Space Weather Modeling in an Operational Environment, 2013, *J. Space Weath. Space Clim.*, 3, A17, 1–72.
6. Velinov, P. I. Y. On ionization of the ionospheric D-region by galactic and solar cosmic rays, 1968, *J. Atmos. Terr. Phys.*, 30, 11, 1891–1905.
7. Velinov, P. I. Y., L. Mateev. Improved Cosmic Ray Ionization Model for the System Ionosphere - Atmosphere. Calculation of Electron Production Rate Profiles, 2008, *J. Atmos. Solar-Terr. Phys.*, 70, 2–4, 574–582.
8. Velinov, P. I. Y., A. Mishev, L. Mateev. Model for Induced Ionization by Galactic Cosmic Rays in the Earth Atmosphere and Ionosphere, 2009, *Adv. Space Res.*, 44, 1002–1007.
9. Mishev, A., P. I. Y. Velinov. The Effect of Model Assumptions on Computations of Cosmic Ray Induced Ionization in the Atmosphere, 2010, *J. Atmos. Solar-Terr. Phys.*, 72, 476–481.
10. Velinov, P. I. Y., M. Buchvarova, L. Mateev, H. Ruder. Determination of Electron Production Rates Caused by Cosmic Ray Particles in Ionospheres of Terrestrial Planets, 2001, *Adv. Space Res.*, 27, 11, 2001, 1901–1908.
11. Velinov, P. I. Y., H. Ruder, L. Mateev, M. Buchvarova, V. Kostov. Method for Calculation of Ionization Profiles Caused by Cosmic Rays in Giant Planet Ionospheres from Jovian Group, 2004, *Adv. Space Res.*, 33, 2, 232–239.
12. Velinov, P. I. Y., L. Mateev, N. Kilifarska. 3D Model for Cosmic Ray Planetary Ionization in the Middle Atmosphere, 2005, *Annales Geophysicae*, 23, 9, 3043–3046.
13. Mishev, A., P. I. Y. Velinov. Atmosphere Ionization Due to Cosmic Ray Protons Estimated with CORSIKA Code Simulations, 2007, *C. R. Acad. Bulg. Sci.*, 60, 3, 225–230.
14. Mishev, A., P. I. Y. Velinov. Time evolution of ionization effect due to cosmic rays in terrestrial atmosphere during GLE 70, 2015, *J. Atmos. Solar-Terr. Phys.*, 129, 78–86.
15. Velinov, P. I. Y., S. Asenovski, L. Mateev. Simulation of cosmic ray ionization profiles in the middle atmosphere and lower ionosphere on account of characteristic energy intervals, 2011, *C. R. Acad. Bulg. Sci.*, 64, 9, pp. 1303–1310.
16. Velinov, P. I. Y., S. Asenovski, L. Mateev. Improved Cosmic Ray Ionization Model for the Ionosphere and Atmosphere (CORIMIA) with account of 6 characteristic intervals, 2012, *C. R. Acad. Bulg. Sci.*, 65, 8, 1137–1144.

17. Velinov, P. I. Y., S. Asenovski, L. Mateev. Ionization of Anomalous Cosmic Rays in Ionosphere and Middle Atmosphere Simulated by CORIMIA Code, 2012, C. R. Acad. Bulg. Sci., 65, 9, 1261–1268.
18. Velinov, P. I. Y., S. Asenovski, L. Mateev. Ionization of Solar Cosmic Rays in Ionosphere and Middle Atmosphere Simulated by CORIMIA Programme, 2013, C. R. Acad. Bulg. Sci., 66, 2, 235–242.
19. Asenovski, S., P. I. Y. Velinov, L. Mateev. Determination of the spectra and ionization of anomalous cosmic rays in polar atmosphere, 2013, C. R. Acad. Bulg. Sci., 66, 6, 865–870.
20. Mishev, A., P. I. Y. Velinov. Ionization Effect Due to Cosmic Rays during Bastille Day Event – GLE 59 on Short and Mid Time Scales, 2016, C. R. Acad. Bulg. Sci. 69, 11, 1479–1484.
21. Mishev, A., P. I. Y. Velinov. Ionization rate profiles due to solar and galactic cosmic rays during GLE 59 Bastille day 14 July, 2000, 2015, C. R. Acad. Bulg. Sci., 68, 3, 359–366.
22. Mishev, A., P. I. Y. Velinov, L. Mateev. Atmospheric Ionization Due to Solar Cosmic Rays from 20 January 2005 Calculated with Monte Carlo Simulations, 2010, C. R. Acad. Bulg. Sci., 63, 11, 1635–1642.
23. Mishev, A., P. I. Y. Velinov. Determination of Medium Time Scale Ionization Effects at Various Altitudes in the Stratosphere and Troposphere During Ground Level Enhancement due to Solar Cosmic Rays on 13.12.2006 (GLE 70), 2015, C. R. Acad. Bulg. Sci., 68, 11, 1425–1430.
24. Velinov, P. I. Y., A. Mishev. Cosmic Ray Induced Ionization in the Atmosphere Estimated with CORSIKA Code Simulations, 2007, C. R. Acad. Bulg. Sci., 60, 5, 493–500.
25. Mishev, A., P. I. Y. Velinov. Influence of Low Energy Hadron Interaction Models on Atmospheric Ionization Due to Cosmic Ray Heavy Nuclei, 2014, C. R. Acad. Bulg. Sci., 67, 6, 2014, 843–854.
26. Abunina, M., A. Abunin, A. Belov, A. Gaidash, Y. Tassev et al. Properties of magnetic fields in coronal holes and geoeffective disturbances in solar cycle 24, 2014, C. R. Acad. Bulg. Sci., 67, 5, 699–704.
27. Mukhtarov, P., R. Bojilova. Influence of solar and geomagnetic activity on the ionosphere over Bulgaria. C. R. Acad. Bulg. Sci., 2017, 70, 9, 1289–1296.
28. Kilifarska, N., R. Bojilova. Geomagnetic focusing of cosmic rays in the lower atmosphere—evidence and mechanism, 2019, C. R. Acad. Bulg. Sci., 72, 3, 365–374.
29. Bojilova, R., P. Mukhtarov. Relationship between the critical frequencies of the ionosphere over Bulgaria and geomagnetic activity, 2020, C. R. Acad. Bulg. Sci., 73, 8, 1113–1122.

СПЕКТЪР И ИНТЕНЗИТЕТ НА КОСМИЧЕСКИТЕ ЛЪЧИ ПО МОДЕЛА CORSIMA В СРЕДНАТА АТМОСФЕРА. ИЗПОЛЗВАНЕ И ПРИЛОЖЕНИЕ ЗА СЛЪНЧЕВИТЕ КОСМИЧЕСКИ ЛЪЧИ

П. Велинов, С. Асеновски, Л. Матеев

Резюме

Представен е новият модел CORSIMA (COsmic Ray Spectrum and Intensity in Middle Atmosphere). Изчислени са спектрите и интензитетите на слънчевите космически лъчи (SCR) от GLE (Ground Level Enhancement) 05 на 23 февруари 1956 г. и GLE 69 на 20 януари 2005 г. на различни височини. За целта се прилага операционният модел CORSIMA. В окончателната версия на програмата CORSIMA е използвана апроксимация в 6 характерни енергийни интервала на функцията на Бор-Бете-Блох, включително интервала за намаляване на заряда. Дадени са аналитични изрази за приносите на енергийните интервали. За първи път представяме количествена и качествена оценка на въздействието на слънчевите космически лъчи (SCR) от събитията със слънчеви частици (SPE) върху йоносферата и средната атмосфера (30–80 km). Тези височини са над максимума на Регенер-Пфотцер. За разлика от галактическите космически лъчи (GCR), диференциалните спектри на SCR значително варират във времето. SCR потоците също се различават един от друг по време на различните събития. Поведението на спектъра и интензитета е обяснено като се има предвид структурата на програмата CORSIMA. Резултатите от изчисленията са в съответствие с експерименталните данни и показват характерни особености на процеса на разпространение за различни височини и геомагнитни ширини. Изчисленията са извършени за геомагнитни ширини 90° (касп-област). Развитието на това изследване е важно за процесите и механизмите на космическото време.

USING REMOTE SENSING DATA AND GIS IN RESEARCH OF MORPHOMETRIC CHARACTERISTICS OF THE COASTAL AREA IN BULGARIA

Georgi Jelev

*Space Research and Technology Institute – Bulgarian Academy of Sciences
e-mail: g_jelev@abv.bg*

Keywords: *Remote sensing, GIS, DEM processing, Coastal area, Black sea*

Abstract

Remote sensing methods provide information on both the natural objects on the earth's surface, water bodies, water-land boundaries, and relief and relief forms. Satellite images were used to determine the characteristics of the coastline and Black Sea area (about 50 km distance) of the Republic of Bulgaria. Its fractal dimension and curvature are determined. A number of thematic maps have been generated through the digital elevation model to assist in the interpretation and geomorphologic characteristics of the study area. A database was created as part of the project MARINEGEOHAZARD – “Set-up and implementation of key core components of a regional early-warning system for marine geohazards of risk to the Romanian-Bulgarian Black Sea coastal area” from CBC Romania-Bulgaria Programme.

Introduction

Since 2005, the international scientific community has started implementing the 10-year Global Earth Observing Systems (GEOSS) program. It is part of the Earth Observatory Group (GEO). In December 2017, the European Commission completed a large-scale study analyzing the economic, social and environmental benefits of the Copernicus program, focusing only on Europe for the period 2017–2035. The timely and cost-effective provision of information depends to a large extent on the successful implementation of the INSPIRE Directive, which provides for the creation and exchange of data and metadata, on the implementation of EU policies, and in particular in the field of environmental protection [8].

Remote sensing methods provide information on both the natural objects on the earth's surface, water bodies, water-land boundaries, and relief and relief forms. Increasingly large archives of freely available space images and products (of different spatial resolution and of different satellites) make it possible to observe and study different processes and phenomena occurring on the Earth's surface, oceans

and atmosphere. Filling in the archives with new data on the current state of the Earth allows tracking of processes and phenomena over time.

Study area

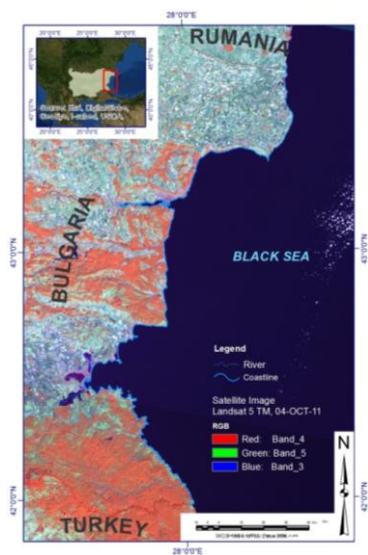


Fig. 1. Study area

The study area in this article is the coastline and Black Sea area (about 50 km distance) of the Republic of Bulgaria (Fig. 1).

The purpose is to collect a coastal strip survey data, using remote sensing methods, in a GIS environment as part of the project: MARINEGEOHAZARD – “Set-up and implementation of key core components of a regional early-warning system for marine geohazards of risk to the Romanian-Bulgarian Black Sea coastal area”.

Materials and Methods

Satellite data and DEM

The data used is collected entirely from free-access sources. From Land Processes Distributed Active Archive Center, the data for a digital elevation model (ASTER GDEM, v.3) cell size $\sim 30 \times 30$ m were downloaded. Eight granules representing 3601×3601 pixel size raster images in *.tiff format and 16 Bit pixel depths were downloaded.

Freely available vector databases and satellite images were used to determine the characteristics of the coastline from which the water-land boundary given in Table 1 was derived. Vector data is in *.shp format and images are downloaded from Earth Observation Data Hub and Copernicus Open Access Hub as scenes in *.tiff format.

The capabilities of remote sensing methods, image processing methods, geographical information systems, statistical and cartographic methods for analyzing the collected data were used. All data are in the WGS 1984 coordinate system, UTM projection, zone 35N.

Results and Discussions

Satellite data processing

The satellite images most clearly show the terrestrial surface and the relief with its shapes and structures. The relief along with the geological structure (Fig. 2 and Fig. 3) define the complete geological-geomorphological space. The lithologic

diversity of the rock base along the Black Sea coast implies a different degree of resistance to endogenous processes occurring at the land-water boundary.

Satellite images are one of the current sources for accurately determining the ground-water boundary through the ability to use different combinations of spectral channels. The geo-bases make it possible to obtain data on the Black Sea border of Bulgaria on different scales. The measured coastline length depends on the spatial resolution (PDS) in satellite images and on the scale of the information sources (Table 1).

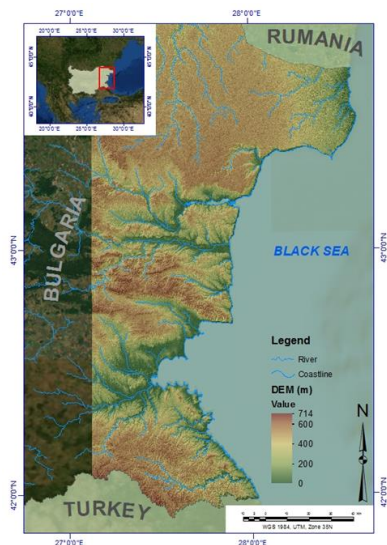


Fig. 2. Map of DEM

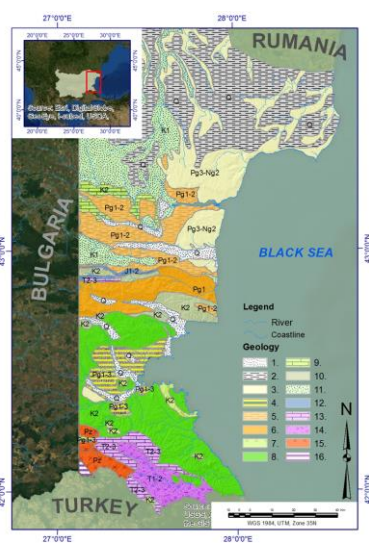


Fig. 3. Geological map¹

Due to its character, the coastal strip is a natural fractal, characterized by self-similarity on different scales – fractal dimension [7]. Regardless of the difference in length, the fractal dimension and the curvature of the coastline are the same (Table 1) and are calculated by the formulas:

$$1) \quad D = \frac{\log(n)}{\log(n) + \log(\frac{d}{L})},$$

$$2) \quad S = L/d,$$

where: D is the fractal dimension, n is the number of segments, d is the distance between the start and end points along the arc of the terrestrial spheroid and L is the length of the coastline (the sum of the length of the segments), S is the curvature.

¹The legend is from Geological maps for Bulgaria (M 1:500 000)

The close to one (1.10) fractal dimension indicates the more complex nature of the shoreline relative to a simple linear structure and at the same time a relatively slightly indented line (Table 1).

Table 1. Sources, fractal dimension and curvature of the Bulgarian coastline

Source	n	d (m)	L (m)	D	S
Landsat-5 MSS/TM	59102	200203	536216,90	1,10	2,68
Landsat-7 ETM	5145	200203	409174,00	1,09	2,04
Sentinel2	8651	200203	481602,15	1,11	2,41
Jika GIS database	12248	200203	415464,13	1,08	2,07
NaturalEarth, M 1:10,000,000	174	200203	337003	1,11	1,68
NaturalEarth, M 1:110,000,000	5	200203	224646	1,08	1,12

DEM processing

From the digital elevation model (Fig. 2.) were made thematic maps of some basic morphometric characteristics. The morphometric parameters were calculated using mathematical formulas from the altitude output variables and the planned coordinates [5]. Using the Spatial Analyst Tools tool and the Surface function in ArcGIS environment, a number of thematic layers were formed in thematic maps.

Map of relief types (Fig. 4); Based on the digital elevation model (Fig. 2), a thematic map of relief types is drawn up. The map shows that the altitude of the Bulgarian Black Sea coast is low – from 0 to about 700 m (maximum 714 m). Nearly 55 % of the territory, the relief is lowland with an altitude of up to 200 m, including the eastern parts of Dobrudzha, the estuaries of the Provadiyska (Varna-Beloslavski) rivers, Batova, Kamchia, Burgas lowlands, parts of the Strandzha part of the coast. Between 200 m and 500 m altitude is 45 % of the territory (hilly terrain), and these are the Dobrudzha, Frangensko, Momino (Avrensko) plateaus, the hills surrounding the Burgas lowland, the Kamchiiska, Eminska and Aytoska mountains, the Bosnia ridge. Only 0.4% is low mountainous terrain (over 500 m) and includes the highest ridges of the Balkan Range and Strandzha [9].

Map of relief forms (Fig. 5); The “incline slope” morphometric indicator (Table 2, Fig. 6) shows the actual inclines of the slope and serves as a basis for the classification of the relief forms. Nearly 19 % of the area is dominated by accumulation processes. These are the plain parts, river terraces, ridge and technogenic levels. The area with active gravitational and gravitational-aqual processes is 3.5 % and is attached to the river breaches in the Strandzha and the Stara Planina Strip, as well as at a number of places along the coastline. Among the relief forms in the strip on the Bulgarian Black Sea coast are the remains of past relief

forming activity. Residual relief forms have two stages of leveling (two denudation surfaces). The Pontic (Old Pliocene) denudation surface occupies the upper flattened parts of the Dobrudzha, Frangen and Momino Plateau, the ridge of the Emina Mountain and the highest parts of the Strandzha Coast at about 450 m above sea level. The younger Levantian (Young Pliocene) denudation surface is represented as a slope of the plateau in the North Coast and the Eminska Mountains, as well as along the ridge levels of the Kamchiyska and Aytoska Mountains [4].



Fig. 4. Map of Types of Terrain

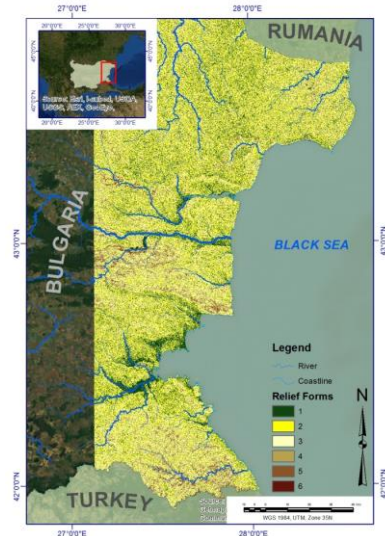


Fig. 5. Map of Relief Forms described in Table 2

Map of actual inclines of the slopes (Fig. 6); For each cell, the incline is calculated as the maximum rate of change in the altitude value of the cell of its neighbors. In principle, the maximum change in the level and distance between the cell with the adjacent eight identifies the steepest descents from the cell and represents the actual incline of the slope. They in turn serve as a basis for the classification of relief forms (Table 2, Fig. 5);

Map of the slope exposition (Fig. 7); The exposure reflects the maximum value of the orientation change in the maximum slope of each cell relative to its neighbors. It is measured clockwise in degrees from 0° (north) to 360° (again north), in a complete circle. Flat areas (-1) are areas where the slope is close to 0°. Both physical and biological factors in the study area are related to the nature of the exhibition.

Table 2. Area distribution of the types of processes and forms of relief in relation to the incline of the slope

No	Incline of slope (°)	Forms of relief	Types of processes	Area	
				(km ²)	%
1	0–3	Plain, river terraces, grasslands and technogenic levels	No erosion processes, accumulation processes; (plain, river terraces, grassland and technogenic)	2987.87	18.87
2	3–7	The beginning of the foot	Lower boundary of the foot, furrow (stream) erosion	6170.84	38.97
3	7–15	The foot	Upper limit of the foot, (trenches)	5222.98	32.98
4	15–20	Slope	Gravity-aqual processes (fluvial (constantly flowing water) and slope processes)	897.27	5.67
5	20-30			485.35	3.06
6	> 30			72.06	0.46
Σ Area:				15836.37	100.00

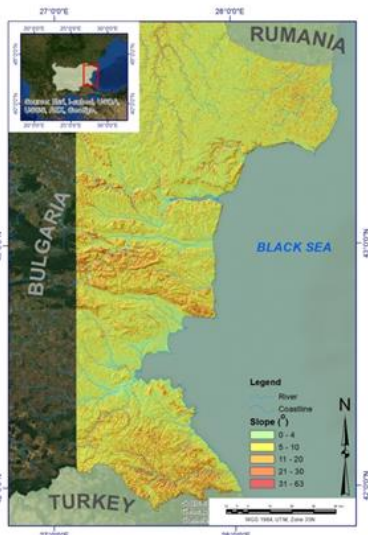


Fig. 6. Map of Slope

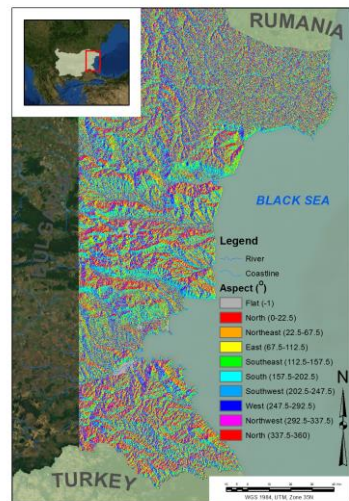


Fig. 7. Map of Aspect

Map of the vertical partition of the relief (Fig. 8); The vertical partition of the relief enables the determination of the type and nature of the relief, outlines territories with different vertical elevation rates, global or regional block structures. Spatially outlines the various relief forms (valleys, depressions, plateaus, ridges,

etc.). The field of vertical division represents the plasticity of the relief as a function of the differences in the type and sign of the vertical deformations of the individual earthquake blocks that make up the study area, as well as of the lithology of the rocks that make up the catchments.

Map of the horizontal partition of the relief (Fig. 9); The study of the intensity of the erosion breakdown of the relief based on morphometric methods is important for predictive assessments of the possible manifestation of modern morphogenetic processes and is an objective morphometric factor allowing the separation of areas subject to different types of geo-hazards. The map is a graphic expression of the relief plastic as a function of sculptural (exogenous) processes. It also reflects the density of the river and / or hostile network.

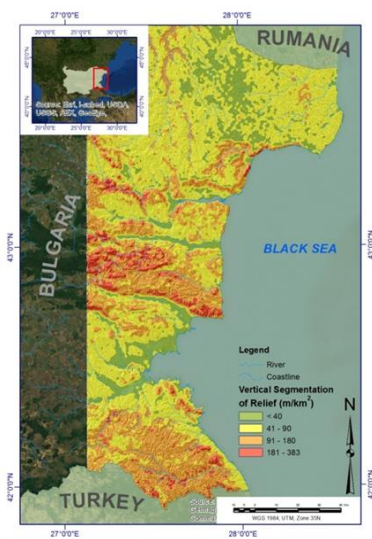


Fig. 8. Map of Vertical Segmentation of Relief

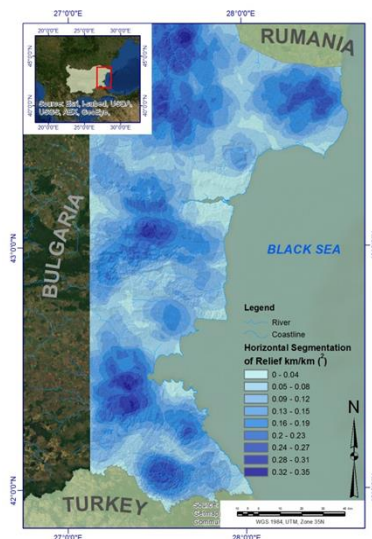


Fig. 9. Map of Horizontal Segmentation of Relief

Map of slope curvature (Fig. 10); The slope curvature is calculated as a derivative of the value from the surface, or the incline of the slope for each cell relative to its adjacent. Three types of curvature are calculated – general, profile curvature (vertical) (Fig. 11), which is in the direction of maximum slope and curvature in plan (horizontal) (Fig. 12) – perpendicular to the direction of maximum slope. From an application point of view, slope curvature can be used to describe the physical characteristics of the catchment area in an effort to understand erosion and bogging processes. The slope reflects the degree of movement on the slope. An aspect determines the direction of movement of a stream. The profile curvature reflects the acceleration and deceleration of flow, therefore affecting erosion and

accumulation (deposition). Plan curvature affects the convergence and divergence of the flow.

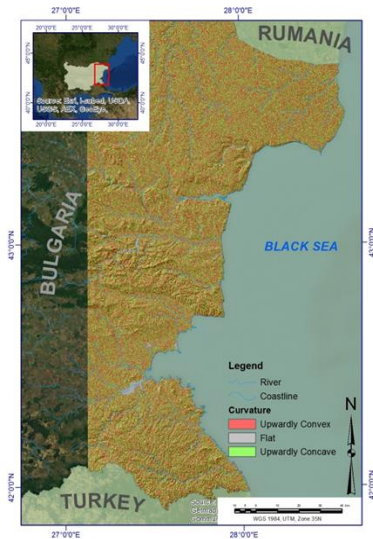


Fig. 10. Map of Curvature



Fig. 11. Map of Profile Curvature

A positive overall curvature indicates that the surface is convex in this cell. A negative curvature indicates that the surface is concave in this cell. A value of 0 indicates that the surface is flat.

For the profile curvature, a positive value indicates that the surface is vertically convex in this cell (convex slopes), a negative value indicates that the surface is concave in this cell (concave slopes). A value of 0 indicates the surface is flat.

For the curvature in plan, a positive value indicates that the surface is convex horizontally in this cell (divergent slopes). A negative value indicates that the surface is concave horizontally in this cell (convergent slopes). A value of 0 indicates the surface is flat.

Negative values of curvatures and profile and plan outline areas of accumulation of eroded material, surface species, pollutants and more. Areas with positive values of the two types of curvature are export areas (denudation) of eroded material, surface species, pollutants, etc. In the other seven combinations between the values of the curvatures by profile and by plan, zones of transit of eroded material, surface species, pollutants, etc. are outlined [5].



Fig. 12. Map of Plan Curvature

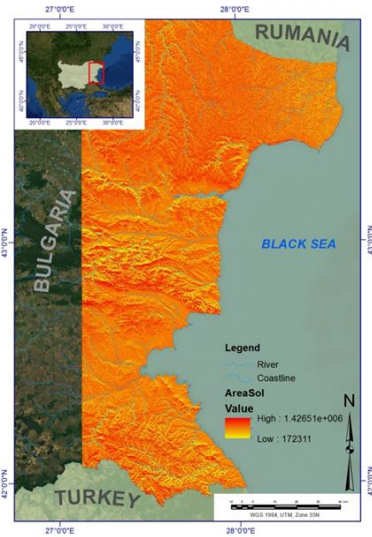


Fig. 13. Map of Solar Radiation

Map of global solar radiation (solar radiation) (Fig. 13); Solar radiation is the solar radiation of a given region and is calculated on the basis of the hemispherical visibility method and algorithm (hemispherical view shed algorithm) developed by P. Rich, 1989 [3] and further developed in 1999–2000.

The map of global solar radiation spatially outlines and makes it possible to analyze the impact of sunlight on a given geographical area for specific periods of time.

The total amount of radiation calculated for a given place or area is given as global radiation. The calculation of direct, diffuse and global solar radiation is made for each characteristic location or for any location on the topographic surface and is a map of global solar radiation for the entire geographical area.

Global solar radiation is calculated as the sum of direct and diffuse solar radiation over the entire surface by celestial sectors. The total amount of incoming solar radiation (sunshine) is the driving force for the planet's physical and biological systems. Knowledge of the magnitude of radiation at a particular geographical location is useful in various fields such as agriculture, resource management, meteorology, civil engineering and environmental studies.

Conclusion

Based on the collected and generated layers and thematic maps, it can be seen that in the strip of the Bulgarian Black Sea coast there are characteristic coastal (abrasion) processes and landforms formed under the influence of sea water such as cliffs, surfboards, abrasion terraces. In general, the coastline, as already indicated, is

slightly cut (its fractal dimension is 1.10). Mostly the mechanical type of abrasion is developed as a result of the wave-surf activity. Abrasion is weak - about half of Cliff's coast is poorly susceptible to destruction. The highest rate of abrasion processes occurs in landslide sites. Landslides are characteristic of the northern part of the Black Sea coast (Balchik, Varna) and less widespread in the south. The strongest abrasion processes are in the presence of storm northeast winds and the formation of large sea waves. The coastline north of Cape Shabla is the most severely destroyed due to the presence of loess (Fig. 3). The abrasion terraces are not very well preserved due to the susceptibility of the rocks to collapse. The Lower and Middle Pleistocene terraces constitute a single complex, with their formation occurring under the conditions of the predominance of abrasion processes.

The Upper Pleistocene terraces form a separate complex, widespread throughout the coast. They occupy the capes along the Burgas-Strandzha and Stara Planina coasts. Along the Dobrudzha and Varna coasts, the terraces are cut in old landslides.

The Holocene terraces form a narrow strip along the beaches, with the base of the slopes adjacent to them, as well as the firth and lagoon lowlands. The beaches occupy 1/3 of the length of the Bulgarian coast. The largest beaches are located north of Varna and between Bourgas and Cape Emine. As a result of the accumulative wind activity southwest of Nessebar, dunes reaching 8–10 m were formed. height. As a result of the sinking of the coast, the estuaries of the Batova and Kamchia rivers formed at the end of the Quaternary. Estuaries represent wide alluvial lowlands. The sandy forms accumulated from the coastal streams have blocked the river mouths and turned them into estuary lakes. Such are the Durankulak, Burgas lakes and others. During the upper Miocene and during the Pliocene, two planning stages and two ascents occur, leading to the formation of denudation levels of Sarmatian-Pontic and Levantine ages. The first level is observed in the highest parts of the Dobrudzha, Frangen, Avren plateau, Emina mountain and Strandzha ridges. The Levantian denudation level has the character of a slope step located at a height of 120–140 m [9].

The main conclusions can be drawn

Modern remote sensing methods provide information and monitoring of active processes occurring along our Black Sea coast (abrasion, landslides, collapses, storage, etc.).

To perform this research, it is necessary that a number of data be processed in vector and / or raster format as layers in a single geographical information system. Creating and organizing the available data as thematic layers in the GIS database enables the sharing of heterogeneous and large-scale information about the studied objects and processes by applying spatial analyzes.

All geomorphological forms have a clear expression in the relief and are emphasized by the calculated various morphometric indicators. All these geomorphological forms are observed on cosmic images and their evolution over time can be traced. They have a clear expression in the relief and are emphasized by the calculated different morphometric parameters.

Acknowledgements

This research was supported by project MARINEGEOHAZARD – “Set-up and implementation of key core components of a regional early-warning system for marine geohazards of risk to the Romanian-Bulgarian Black Sea coastal area” from CBC Romania-Bulgaria Programme.

References

1. Fu, P. and P. M. Rich. 2000. A geometric solar radiation model and its applications in agriculture and forestry. Proceedings of the Second International Conference on Geospatial Information in Agriculture and Forestry. 1357-36
2. Fu, P. and Rich, P. (1999) Design and Implementation of the Solar Analyst: An Arc View Extension for Modeling Solar Radiation at Landscape Scales. Proceedings of the Nineteenth Annual ESRI User Conference, San Diego. http://professorpaul.com/publications/fu_rich_1999_esri.pdf
3. Rich, P. M. 1989. A manual for analysis of hemispherical canopy photography. Los Alamos National Laboratory Report LA-11733-M
4. Stoyanov, K., & E. Gachev, 2011. Recent Landform Evolution in Bulgaria. Recent Landform Evolution, 377–412. doi:10.1007/978-94-007-2448-8_14
5. Попов, А., 2012, Географски информационни системи, Изд. Анубис, София, 471 с.
6. Geological map of Bulgaria M 1: 500 000 (2 sheets) and explanatory note. - in: Year. Dir. geol. and min. Dep. A, 4, C., Geogr. institute.
7. Georgiev, Tsv., 2011. Introduction to fractal analysis of natural structures, Ecology 2011, NBU, pp. 9–18.
8. Official Journal of the European Union, 2007. Directive 2007/2 / EC of the European Parliament and of the Council of 14 March 2007 establishing an Infrastructure for Spatial Information in the European Community (INSPIRE), L 108, 50, p. 108, ISSN 1830-3617.
9. География на България, 2002, Физическа и социално-икономическа география, 2002., част 1, част 3, Физическа география, под ред. И. Копралев, М. Йорданова, Ч. Младенов, изд. ФорКом, 2002, 760 с.

Internet sources

<https://earthexplorer.usgs.gov/> - EarthExplorer – Home page, - U.S. Geological Survey
<https://landsat.gsfc.nasa.gov/> - Landsat Science
<https://scihub.copernicus.eu/dhus/#/home> - Copernicus Open Access Hub, ESA

<https://sentinel.esa.int/web/sentinel/user-guides/sentinel-2-msi/overview> - ESA Sentinel on line
<http://marine.copernicus.eu/services-portfolio/access-to-products/>- COPERNICUS Marine Environment Monitoring Service
<https://www.naturalearthdata.com/downloads/> - Natural Earth,
https://lpdaac.usgs.gov/product_search/ - Land Processes Distributed Active Archive Center
<https://asterweb.jpl.nasa.gov/gdem.asp> - ASTER Global Digital Elevation Map Announcement
<http://www.esri.com/> - ESRI homepage
<http://help.arcgis.com/en/arcgisdesktop/10.0/help/> - ArcGIS Help Library
http://help.arcgis.com/en/arcgisdesktop/10.0/help/index.html#/How_solar_radiation_is_calculated/009z000000tm000000/ - ArcGIS Resource Center

ИЗПОЛЗВАНЕ НА ДИСТАНЦИОННИ ДАННИ И ГИС ПРИ ИЗСЛЕДВАНЕ НА МОРФОМЕТРИЧНИ ХАРАКТЕРИСТИКИ НА КРАЙБРЕЖНАТА ЗОНА НА Р. БЪЛГАРИЯ

Г. Желев

Резюме

Чрез дистанционните методи се получава информация както за природните обекти на земната повърхност, водни обекти, границите вода–суша, така и за релефа и релефните форми. Използвани са спътниковите изображения за определяне на характеристиките на бреговата ивица и Черноморска зона (около 50 km отстояние) на Р. България. Определена е нейната фрактална размерност и кривина. Чрез дигиталния модел на релефа са генерирани редица тематични карти, които помагат при интерпретацията и геоморфоложката характеристика на изследвания район. Създадена е база данни, като част от работата по проект MARINEGEOHAZARD – “Set-up and implementation of key core components of a regional early-warning system for marine geohazards of risk to the Romanian-Bulgarian Black Sea coastal area” from CBC Romania-Bulgaria Programme.

SPACE DISTRIBUTION OF NO₂ POLLUTION OVER BULGARIA

Maria Dimitrova, Plamen Trenchev

*Space Research and Technology Institute – Bulgarian Academy of Sciences
e-mail: maria@space.bas.bg*

Keywords: *Ecology, Remote sensing, TROPOMI, Greenhouse gases*

Abstract

In this work, we aim to track the behaviour of nitrogen dioxide over Bulgaria for the period 30th April 2018 to the end of July 2022 based on data from the Sentinel 5P data. We conclude that the biggest pollutant still remains the industrial regione near Stara Zagora. The second and third sources are respectively big cities and highways.

Introduction

Atmospheric pollution is one of the most important environmental issues of the industrialized developed and developing countries around the world. Both the energy production based on fossil fuels [1] and road traffic [2] are key factors creating serious public health problems, from local to regional and national levels [3, 4]. Nitrogen dioxide (NO₂) is one of the main air quality pollutants of concern in many urban and industrial areas worldwide, and particularly in the European region, where in 2017 almost 20 countries exceeded the NO₂ annual limit values imposed by the European Commission Directive 2008/50/EC [5, 6]. NO₂ pollution monitoring and regulation is a necessary task to help decision makers to search for a sustainable solution for environmental quality and population health status improvement.

The recording of atmospheric pollutants is carried out in two main ways, by direct and by remote measurements.

Direct measurements are carried out at a single point (local), while remote methods provide data on volumetric content. Measurements from satellites contain the content for a given pollutant in the whole column of the atmosphere over a given area corresponding to the spatial resolution of the instrument. To obtain a complete picture of the phenomenon, it is best to use both sources of information in conjunction.

In this work, we aim to track the behaviour of nitrogen dioxide over Bulgaria for the period 30th April 2018 to the end of July 2022 based on the data from the Sentinel 5P data [7, 8]

Satellite data

TROPOMI [9, 10], launched in October 2017 aboard of the European Space Agency's (ESA's) S5P spacecraft, provides measurements in four channels (UV, visible, NIR and SWIR) of various trace gas columns, as well as cloud and aerosol properties, from an ascending Sun-synchronous polar orbit, with an Equator crossing at about 13:30 local time (LT). NO₂ retrieval is performed from the visible band (400–496 nm), which has spectral resolution and sampling of 0.54 and 0.20 nm, with a signal-to-noise ratio of around 1500.

Individual ground pixels are 7.2 km (5.6 km as of 6 August 2019) in the along-track and 3.6 km in the across-track directions in the middle of the swath. The full swath width is about 2600 km, with which TROPOMI achieves global coverage each day, except for narrow strips between orbits of about 0.5° wide at the Equator. The swath is across-track divided into 450 ground pixels (rows) and their size remains more or less constant towards the edges of the swath (the largest pixels are ~14 km wide).

In this work we use daily NO₂ data from Sentinel-5P Pre-Operations Data Hub [8] as well as visualization from EO browser [7]. For each one of the days for the period of April 30, 2018, till July 31, 2022, we download and process data for NO₂ and point the places with NO₂ increase over Bulgarian region. For the NO₂ increase we've considered to use all values above 7.5 E-5 mol/m².

We must mention that in many cases we see values above 1 E-4 mol/m².

Results and Discussions

As a result of this research, we observe several regions over Bulgaria with repetitive NO₂ increases. Most often, more than once at every 3 days, we have observed increase over the region of open mining near Stara Zagora. Below we named this region only “Stara Zagora”, but it is not the region over the city.

The second place is Sofia as the biggest Bulgarian city, then Plovdiv. Unexpectedly after Plovdiv comes Kyustendil region. Then comes Varna, Ruse, Burgas, Pazardjic, Pernic and others.

On the Fig. 1 we show comparison between days with NO₂ increase over the first 5 of the above-mentioned places.

On the Fig. 2 we show one typical case of NO₂ pollution distribution over Bulgaria with increases over several places.

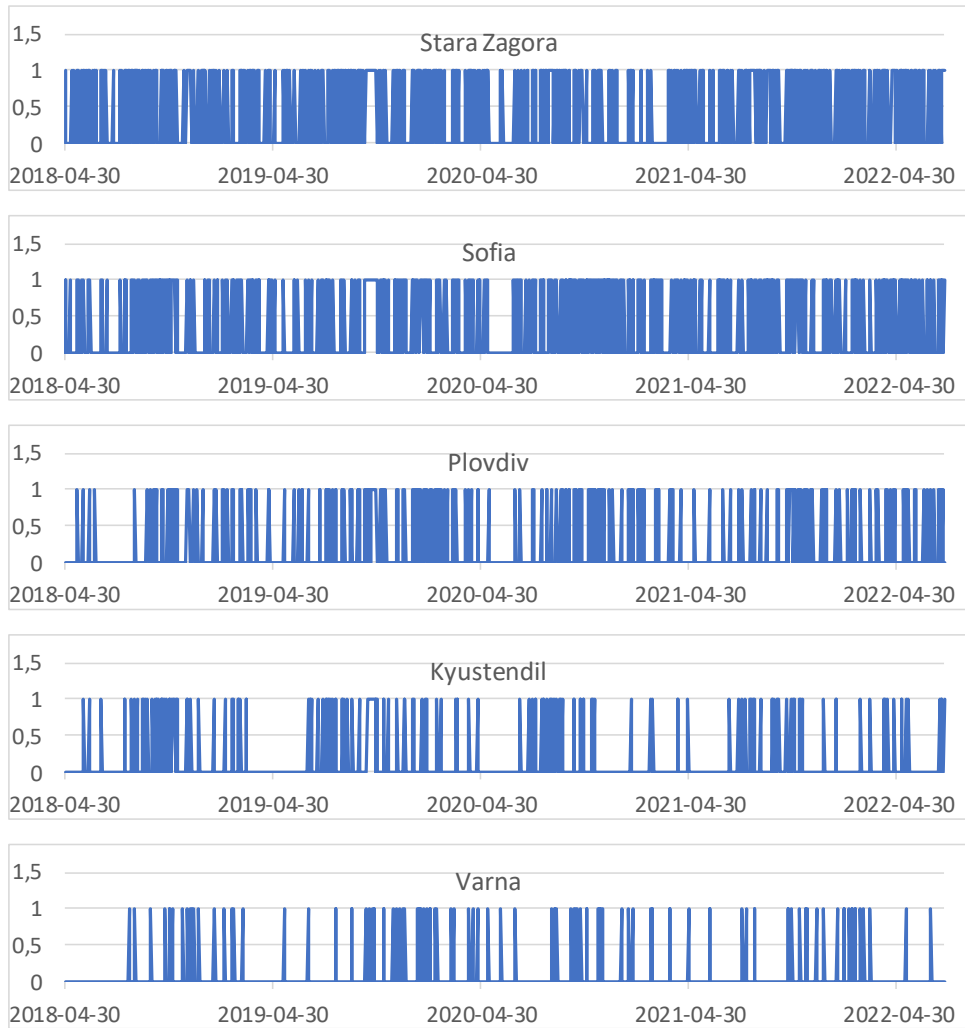


Fig. 1. Days with NO₂ increase over different places over Bulgaria

The increase of NO₂ over the region of open mining near Stara Zagora covers a very big area (as we see on Fig. 2), while big cities pollute mainly the nearest of their area region.

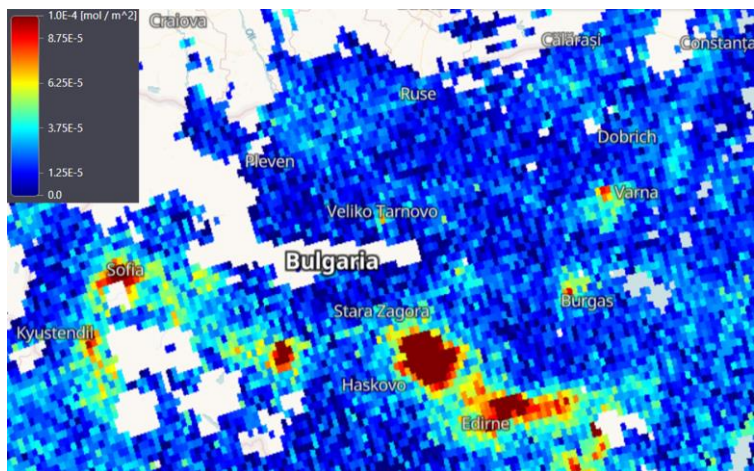


Fig. 2. An example of NO₂ pollution distribution over Bulgaria

On Figures 3 and 4 we show respectively seasonal and temporal distribution of days with NO₂ increase over the above-mentioned places.

As we see on Fig. 3, NO₂ increases are more often during the autumn months.

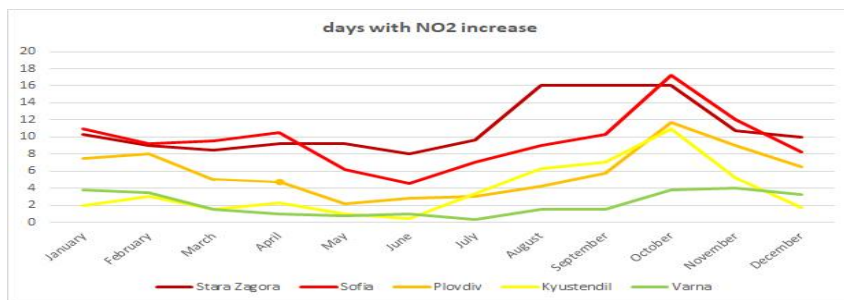


Fig. 3. Seasonal distribution of days with NO₂ increase over different Bulgarian regions

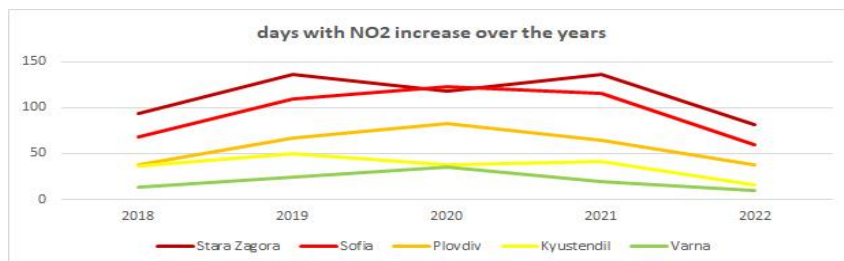


Fig. 4. Distribution of days with NO₂ increase over different Bulgarian regions over the years

On the Fig. 4 we see that there was some decrease in NO₂ pollution during 2020 over open mining region and Kyustendil. Decrease in 2020 is caused by a smaller period (only 7 months).

Other repetitive picture is the increase of NO₂ over big regions above the two highways – Struma and Trakia. An example for this we show on Fig. 5.

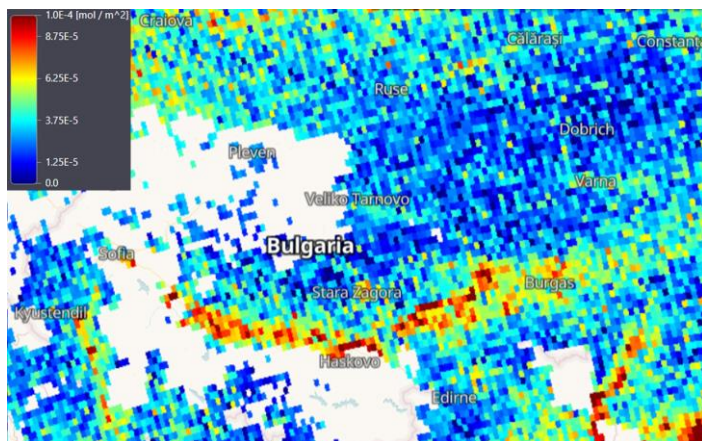


Fig. 5. An example of NO₂ pollution above highways in Bulgaria

Conclusion

With the help of the Sentinel 5P data, we can register and investigate the space distribution of air pollution over Bulgaria. We can also study NO₂ ground sources.

The biggest air pollution source is still the industrial region, east-south of Stara Zagora. For the NO₂ pollution in Bulgaria big cities are the usual sources, as well the highways.

References

1. Meetham, A. R.; Bottom, D.; Cayton, S. Atmospheric Pollution: Its History, Origins and Prevention; Elsevier: Amsterdam, The Netherlands, 2016. [Google Scholar]
2. Olmo, N.R.S.; Saldiva, P.; Braga, A.L.F.; Lin, C.A.; Santos, U.D.P.; Pereira, L.A. A review of low-level air pollution and adverse effects on human health: Implications for epidemiological studies and public policy. Clinics 2011, 66, pp. 681–690. [Google Scholar] [CrossRef] [PubMed][Green Version]
3. Sokhi, R.; Kitwiroon, N. Air pollution in urban areas. In World Atlas of Atmospheric Pollution; Anthem Press: London, UK, 2011; pp. 19–34. [Google Scholar]

4. Lavaine, E. An Econometric Analysis of Atmospheric Pollution, Environmental Disparities and Mortality Rates. Environ. Resour. Econ. 2014, 60, pp. 215–242. [Google Scholar] [CrossRef]
5. EEA. Air Quality in Europe; European Environment Agency, Publications Office of the European Union: Luxembourg, 2019; 99 p.
6. Marina Virghileanu, Ionuț Săvulescu, Bogdan-Andrei Mihai, Constantin Nistor, Robert Dobre, Nitrogen Dioxide (NO₂) Pollution Monitoring with Sentinel-5P Satellite Imagery over Europe during the Coronavirus Pandemic Outbreak, *Remote Sens.* 2020, 12(21), 3575; <https://doi.org/10.3390/rs12213575>
7. <https://www.sentinel-hub.com/>
8. <https://s5phub.copernicus.eu/dhus/#/home>
9. Veeffkind, J. P., Aben, I., McMullan, K., Förster, H., de Vries, J., Otter, G., Claas, J., Eskes, H. J., de Haan, J.F., Kleipool, Q., van Weele, M., Hasekamp, O., Hoogeveen, R., Landgraf, J., Snel, R., Tol, P., Ingmann, P., Voors, R., Kruizinga, B., Vink, R., Visser, H. and Levelt, P. F.: TROPOMI on the ESA Sentinel-5 Precursor: A GMES mission for global observations of the atmospheric composition for climate, air quality and ozone layer applications, *Remote Sens. Environ.*, 120, 70–83, <https://doi.org/10.1016/j.rse.2011.09.027>, 2012
10. Jos van Geffen, Henk Eskes, Steven Compernelle, Gaia Pinardi, Tjil Verhoelst, Jean-Christopher Lambert, Maarten Sneep, Mark ter Linden, Antje Ludewig, K. Folkert Boersma, J. Pepijn Veeffkind, Sentinel-5P TROPOMI NO₂ retrieval: impact of version v2.2 improvements and comparisons with OMI and ground-based data, *Atmos. Meas. Tech.*, 15, 2037–2060, 2022, <https://doi.org/10.5194/amt-15-2037-2022>

ПРОСТРАНСТВЕНО РАЗПРЕДЕЛЕНИЕ НА ЗАМЪРСЯВАНЕТО С NO₂ НАД БЪЛГАРИЯ

М. Димитрова, Пл. Тренчев

Резюме

В тази работа се стремим да проследим поведението на азотния диоксид над България за периода 30 април 2018 г. до края на юли 2022 г. въз основа на данни от Sentinel 5P. Заклучаваме, че най-големият замърсител все още остава индустриалният район край Стара Загора. Вторият и третият източник са съответно големите градове и магистралите.

INCREASE OF CARBON DIOXIDE AND METHANE EMISSIONS OVER BULGARIA ON THE BASE OF GOSAT SATELLITE DATA

*Plamen Trenchev, Maria Dimitrova, **Deyan Gochev***

*Space Research and Technology Institute – Bulgarian Academy of Sciences
e-mail: ptrenchev@space.bas.bg*

Key words: *Ecology, Remote sensing, Greenhouse gases*

Abstract

The paper presents an assessment of the change in carbon dioxide and methane concentrations in the atmosphere over Bulgaria over the last 13 years. GOSAT data for the period April 2009 to the end of 2021 are used for this purpose. The data are presented as monthly averages with a spatial resolution of 2.5×2.5 degrees. The seasonal and spatial behaviour of carbon dioxide and methane emissions in the respective regions of interest has also been investigated.

Introduction

Air pollution is a local, pan-European and intercontinental problem and is now one of the major environmental concerns worldwide. Air pollutants emitted in one country can be transported into the atmosphere and degrade air quality elsewhere [1]. More than 80 % of Europe's urban population is exposed to pollutants at concentrations significantly above the limit values for the pollutant type concerned.

Atmospheric pollution is a volumetric phenomenon. They are most often triggered by a specific source and then spread relatively rapidly (within hours) both in altitude and in different directions in the atmosphere. Each individual type of pollutant has a different lifetime (residence time in the atmosphere). In some cases, pollution is local and mainly affects the region around its source (mainly industrial sites and transport). In others, however, there is long-range atmospheric transport and areas thousands of kilometres away can be affected. Depending on the specificity of the phenomenon under investigation, the choice of methods and data for its recording also becomes important.

The recording of atmospheric pollutants is carried out in two main ways, by direct and by remote measurements.

Direct measurements are carried out at a single point (local), while remote methods provide data on volumetric content. Measurements from satellites obtain

the content for a given pollutant in the whole column of the atmosphere over a given area corresponding to the spatial resolution of the instrument. To obtain a complete picture of the phenomenon, it is best to use both sources of information in conjunction.

Particularly important from an ecological and climatic point of view are so-called greenhouse gases. The generic term 'greenhouse gases' refers to all gases that warm the Earth's surface and the lower atmosphere. Carbon dioxide allows the sun's rays to reach the Earth's surface but prevents the heat from radiating back. Other gases that act in the same way are methane, nitrogen oxides and chlorofluorocarbons (Freons), which are used in aerosol preparations, in old refrigerators and in many air conditioners.

The relative share of major greenhouse gases is:

- About 80 % CO₂
- About 10 % methane
- About 5 % NO₂
- About 2 % hydrofluorocarbons
- About 3 % other.

CO₂ is the most widespread greenhouse gas, which is why it is the biggest problem. But CO₂ emissions have been stable in recent years and concentrations are rising at a predictable rate, as shown by many large-scale studies, including satellite observations. Methane emissions are lower as a percentage of CO₂, but it has a much higher global warming potential and is better at trapping heat than carbon dioxide.

Unfortunately, satellite measurements of these pollutants, especially methane, are still very poor.

In this work, we aim to track the behaviour of carbon dioxide and methane over Bulgaria for the period April 2009 to the end of 2021 based on data from the GOSAT satellites [2–6].

Satellite data and data processing

In this work, we have used averaged monthly CO₂ and CH₄ data from GOSAT [5, 6]. The spatial resolution is equal to 2.5×2.5 degrees. Fig. 1 shows some of the study areas over Bulgaria with their corresponding numbers.

For each of the study areas, we processed and obtained monthly averages for CO₂ and CH₄ for each month from April 2009 to the end of 2021 inclusive. Based on these values, we have plotted the seasonal distribution of the averaged value, the temporal distribution with the calculated percent change for the entire study period, and the variance of the values for each area. This process was conducted in parallel for both CH₄ and CO₂.

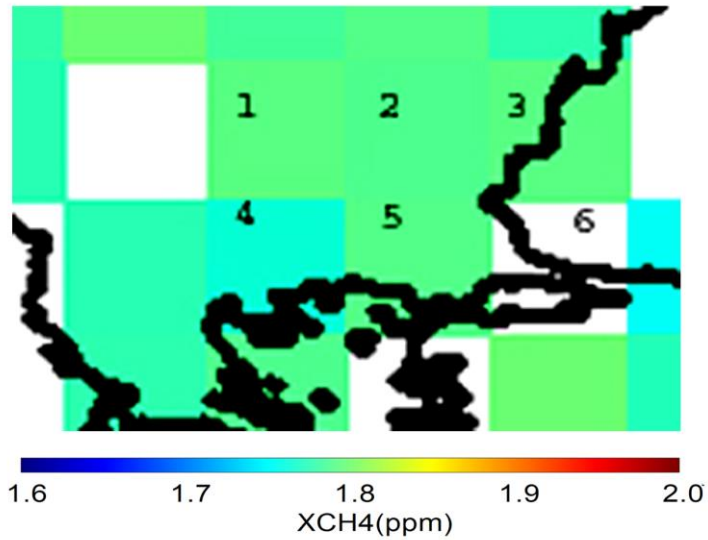


Fig. 1. Areas and an example of monthly average CH₄ value

Results and Discussions

Figures 2–4 show the averaged seasonal distribution of CH₄ over Bulgaria (for the 6 regions in Fig. 1), the temporal variation of CH₄ for each of the 6 regions and the averaged temporal variation of CH₄ over Bulgaria.

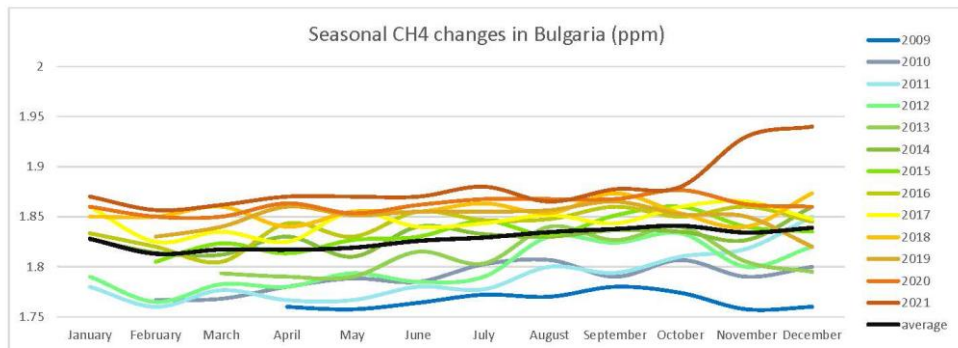


Fig. 2. Seasonal behavior of CH₄ over Bulgaria

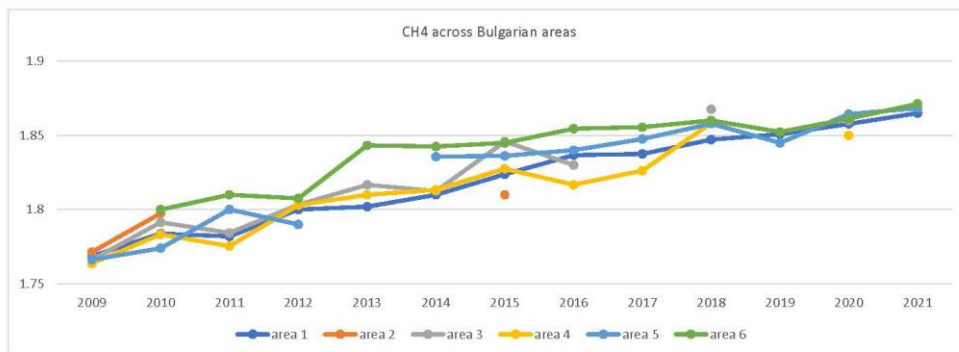


Fig. 3. Temporal behavior of CH₄ over different Bulgarian regions

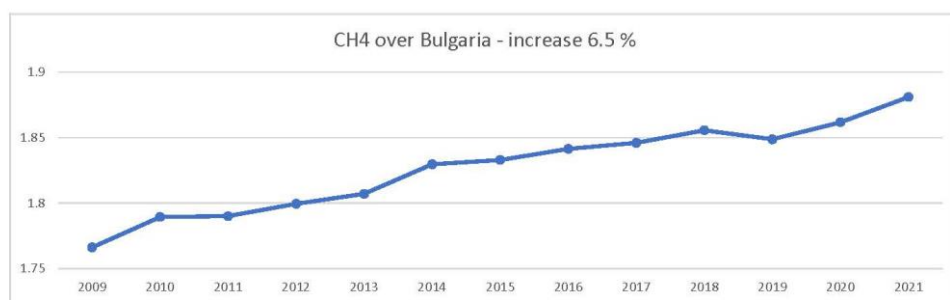


Fig. 4. CH₄ increase over Bulgaria

As can be seen in Fig. 4, CH₄ emissions over Bulgaria have been increasing by nearly 6% for about 12 years. This result is in line with the observed trend for Europe and globally.

Figures 5–7 show the CO₂ values for the respective studies.

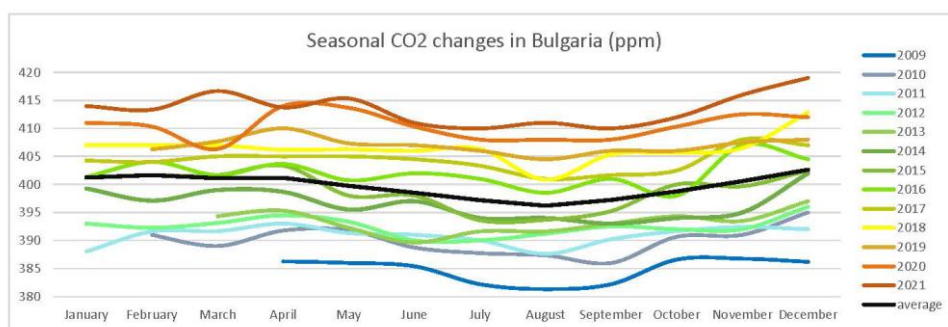


Fig. 5. Seasonal behavior of CO₂ over Bulgaria

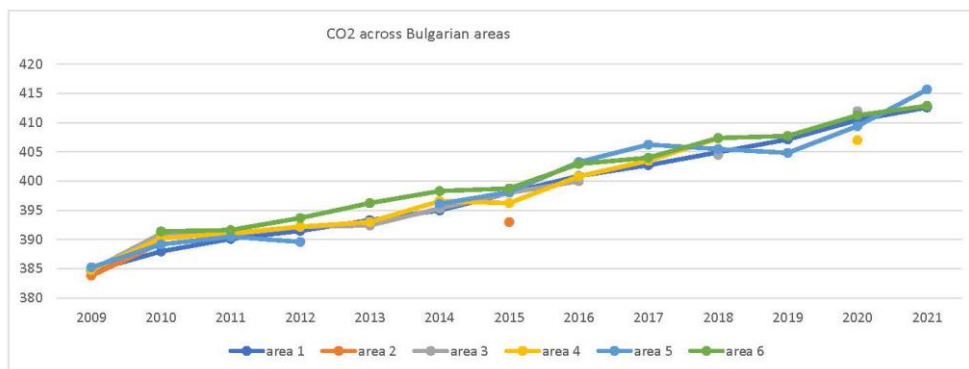


Fig. 6. Temporal behavior of CO₂ over different Bulgarian regions

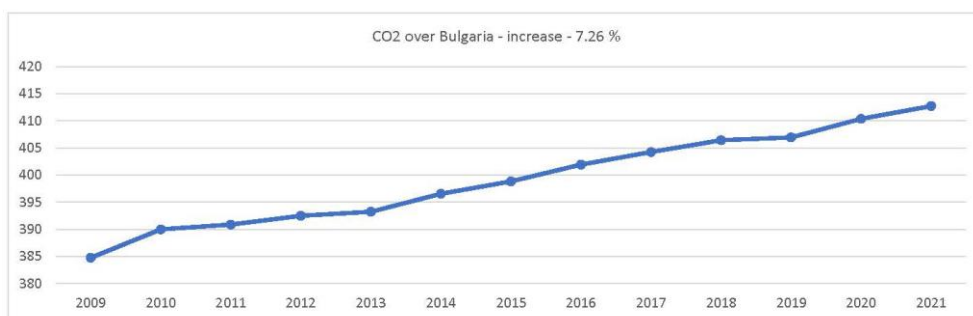


Fig. 7. CO₂ increase over Bulgaria

As can be seen from Fig. 7, CO₂ emissions in Bulgaria have been increasing by more than 7 % for about 12 years.

Another result of our study is that both pollutants show an increase in winter values. But while CH₄ has a maximum in October, for CO₂ the maximum is in February.

Moreover, the increase of CO₂ is almost the same in all 6 regions, while CH₄ shows higher values in the 6th region. The interesting thing about the 6th region is that it covers the southeastern part of Bulgaria (around Burgas) up to the Black Sea where there are no major industrial sources of methane, except the Neftohim-Burgas oil refinery. Therefore, we can conclude that this is also one of the main sources of CH₄ in Bulgaria. More research in this regard is needed to determine the magnitude, intensity of these emissions as well as the level of transport from adjacent areas that affect the pollutant totals for the regions studied.

It should be borne in mind that the results shown here are very global. For a more detailed picture of the spatial distribution of the pollutants considered, satellite data with higher spatial resolution are needed. Such data can be obtained from the Tropomi instrument on the Sentinel-5P satellite, which have a pixel

resolution of 3.5×7 km and a daily acquisition. Several comparisons have been made between the results from GOSAT data and the results obtained from Tropomi data processing [7–9]. These comparisons show good agreement of the results from these two independent sources about CH₄ emissions. Tropomi instrument does not measure CO₂.

Conclusion

Based on the GOSAT data we can say that there has been a significant increase in CH₄ and CO₂ over the last 12 years or so. This increase is about 6.5 % for CH₄ and about 7.3 % for CO₂. CO₂ pollution over Bulgaria is almost evenly distributed. CH₄ shows slightly higher values in the south-eastern region.

References

1. Manisalidis, I., E. Staropoulou, A. Stavropoulos, E. Bezirtzoglou, Environmental and Health Impacts of Air Pollution: A Review, *Front. Public Health*, 20 February 2020 <https://doi.org/10.3389/fpubh.2020.00014>
2. Butz, A., S. Guerlet, O. Hasekamp, D. Schepers, A. Galli, I. Aben, C. Frankenberg, J.-M. Hartmann, H. Tran, A. Kuze, G. Keppel-Aleks, G. Toon, D. Wunch, P. Wennberg, N. Deutscher, D. Griffith, R. Macatangay, J. Messerschmidt, J. Notholt, and T. Warneke, Toward accurate CO₂ and CH₄ observations from GOSAT, *GEOPHYSICAL RESEARCH LETTERS*, 2011, VOL. 38, L14812, doi:10.1029/2011GL047888, <https://agupubs.onlinelibrary.wiley.com/doi/pdfdirect/10.1029/2011GL047888>
3. Morino, I., O. Uchino, M. Inoue, Y. Yoshida, T. Yokota, P. O. Wennberg, G. C. Toon, D. Wunch, C. M. Roehl, J. Notholt, T. Warneke, J. Messerschmidt, D. W. T. Griffith, N. M. Deutscher, V. Sherlock, B. Connor, J. Robinson, R. Sussmann, and M. Rettinger, Preliminary validation of column-averaged volume mixing ratios of carbon dioxide and methane retrieved from GOSAT short-wavelength infrared spectra, *Atmos. Meas. Tech.*, 2011., 4, 1061–1076, doi:10.5194/amt-4-1061-2011, www.atmos-meas-tech.net/4/1061/2011
4. Turner, A. J., D. J. Jacob, K. J. Wecht, J. D. Maasackers, E. Lundgren, A. E. Andrews, S. C. Biraud, H. Boesch, K. W. Bowman, N. M. Deutscher, M. K. Dubey, D. W. T. Griffith, F. Hase, A. Kuze, J. Notholt, H. Ohyama, R. Parker, V. H. Payne, R. Sussmann, C. Sweeney, V. A. Velasco, T. Warneke, P. O. Wennberg, and D. Wunch, Estimating global and North American methane emissions with high spatial resolution using GOSAT satellite data, *Atmos. Chem. Phys.*, 2015, 15, 7049–7069, doi:10.5194/acp-15-7049-2015, www.atmos-chem-phys.net/15/7049/2015/
5. GOSAT project - <http://www.gosat.nies.go.jp/en/>
6. GOSAT instrument and data - <https://earth.esa.int/eogateway/missions/gosat>

7. Haili Hu, Jochen Landgraf, Rob Detmers, Tobias Borsdorff, Joost Aan de Brugh, Ilse Aben, André Butz, and Otto Hasekamp, Toward Global Mapping of Methane With TROPOMI: First Results and Intersatellite Comparison to GOSAT, Geophysical Research Letters 10.1002/2018GL077259, <https://agupubs.onlinelibrary.wiley.com/doi/pdfdirect/10.1002/2018GL077259>
8. Wecht, K. J., D. J. Jacob, M. P. Sulprizio, G. W. Santoni, S. C. Wofsy, R. Parker, H. Bösch, and J. Worden, Spatially resolving methane emissions in California: constraints from the CalNex aircraft campaign and from present (GOSAT, TES) and future (TROPOMI, geostationary) satellite observations, Atmos. Chem. Phys., 2014., 14, 8173–8184, doi:10.5194/acp-14-8173-2014, www.atmos-chem-phys.net/14/8173/2014
9. H. Lindqvist^{1,2}, C. W. O'Dell¹, S. Basu^{3,4}, H. Boesch⁵, F. Chevallier⁶, N. Deutscher^{7,8}, L. Feng⁹, B. Fisher¹⁰, F. Hase¹¹, M. Inoue^{12,13}, R. Kivi¹⁴, I. Morino¹², P. I. Palmer⁹, R. Parker⁵, M. Schneider¹¹, R. Sussmann¹⁵, and Y. Yoshida, Does GOSAT capture the true seasonal cycle of carbon dioxide?, Atmos. Chem. Phys., 2015., 15, 13023–13040, doi:10.5194/acp-15-13023-2015, www.atmos-chem-phys.net/15/13023/2015

УВЕЛИЧЕНИЕ НА ЕМИСИИТЕ ОТ ВЪГЛЕРОДЕН ДИОКСИД И МЕТАН НАД БЪЛГАРИЯ ПО СПЪТНИКОВИ ДАННИ ОТ GOSAT

Пл. Тренчев, М. Димитрова, Д. Гочев

Резюме

В статията е представена оценка на изменението на концентрациите на въглероден диоксид и метан в атмосферата над България през последните 13 години. За тази цел са използвани данни от GOSAT за периода от април 2009 г. до края на 2021 г. Данните са представени като средномесечни стойности с пространствена разделителна способност 2,5×2,5 градуса. Изследвано е също така сезонното и пространственото поведение на емисиите на въглероден диоксид и метан в съответните области на интерес.

USE OF OPEN, SPATIAL AND SATELLITE DATA FOR THE PURPOSE OF RESEARCHING LANDFILLS FOR MUNICIPAL

Adlin Dancheva, Temenuzhka Spasova

*Space Research and Technology Institute – Bulgarian Academy of Sciences
e-mail: adlin.dancheva@space.bas.bg; tspasova@space.bas.bg*

Keywords: *Climate change, Landfill, Landsat 9, Open data, SAR*

Abstract

The present work traces the development of an illegal landfill near the town of Svoge in Bulgaria. After 2016, a waste management plan is prepared on the territory of the municipality and a decision is made to dispose of it by depositing it in a regional landfill for municipal waste in the town of Kostinbrod. The aim of the study is to trace the development of biochemical processes that took place on the territory of the former landfill and whether their impact continues to this day. Data from the Open Data Portal (<https://data.egov.bg/>), the National Spatial Data Portal INSPIRE (<https://inspire.egov.bg/bg>), satellite data and GIS, several spectral profiles and indices such as Normalized difference vegetation index (NDVI), Tasseled Cap Transformation (TCT) were used.

Composite images from the multispectral instrument (MSI) of the Sentinel 2 platform and radar (SAR) from the Sentinel 1 platform of the Copernicus program of the European Space Agency were used. The surface temperature of the landfill was calculated using the heat channels from the Landsat 5–7 (ETM) and Landsat 8 and Landsat 9 (OLI / TIRS) sensors. A combination of radar and optical data was made. Data from different seasons and years were used to monitor the dynamics of thermal pollution in the study area. Quantitative and qualitative assessment of the territory on which the landfill is located has been made. Last but not least, the role of high-value open data in environmental monitoring has been demonstrated, which will reduce the administrative burden of making responsible decisions for each smaller municipality and will be successfully implemented in future methodologies for improving Digital twins through technical work in Destination Earth (DestinE) and information about any point, area or globally significant territories.

Introduction

More and more open and spatial data have been used in making adequate and fast decisions not only in business and decentralized administrations, but also in large numbers in municipalities and settlements, as there is a huge shortage of highly qualified experts, especially in the Northwest region of Bulgaria.

Low budgets in small settlements and capacity shortages are the reason for the introduction of this type of research, which can be carried out by much less but qualified staff.

When there is such an abundance of high-value data in the administration, Open and Spatial data, the Copernicus and Landsat program, data from daily and year-round measurements of the Ministry of Environment and Water, it must be used and achieve great economic benefits and added value.

Many administrations, NGOs, citizens, and business organizations in Bulgaria are involved in environmental monitoring and climate change, but they often miss the opportunity to minimize the administrative burden and the re-use of data and the use of data from research projects.

There are many unregulated landfills in the country, but control measures and sanctions are often neglected. Many of these landfills are visible to citizens on a daily basis. The situation is similar at this landfill, which is near the Iskar River. There are many settlements along the river and unfortunately in most of them the biological and physico-chemical indicators are not good, moderate or are unknown, the presence of Cu, Mn, Al, Fe is observed.

Nowadays, with the ability to generate as much information as possible from a point, profile or area, a different method or approach makes it possible to successfully generate Digital Twins on Earth and obtain information not only about landfills or pollution, but about all spheres of life in real or near real time.

In times of economic crisis, war, shortage of drinking water in many parts of the world cannot be allowed to pollute such a strategic river that flows into the Danube and not to use the great amount of different types of Open Data.

Study area

The researched site is located in close proximity to one of the natural landmarks of the Republic of Bulgaria – the Iskar Gorge. From there passes the longest river, which flows entirely within the state – the Iskar River, which is a right tributary of the Danube. The landfill is located on the western slope, which has a steep slope between the town of Svoge and the village of Tserovo. The site has existed for at least 20 years and can be on the list of illegal dumps to this day. In January 2021, the landfill posed a great danger of environmental catastrophe, as much of the garbage fell into the Iskar River, leading to congestion and difficult cleaning of the riverbed.

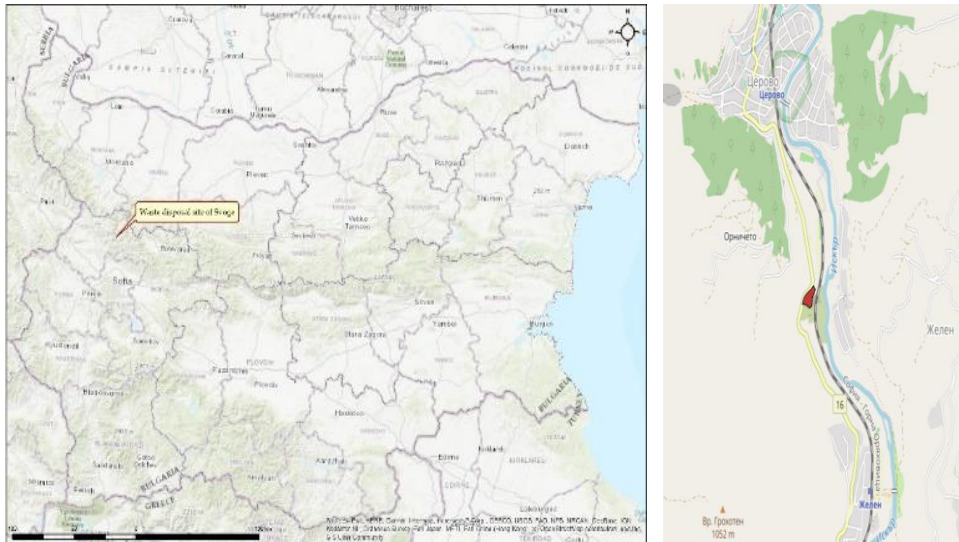


Fig. 1. Map of areas of interest

Materials and Methods

This survey methodology is based on the use of satellite data that examines bands on the thematic infrared sensors (TIRS). From this data, information is extracted about the actual heat emission of waste disposal sites, which is related to the land surface temperature of the surveyed sites. The landfill temperature is calculated using the Digital Number (DN) contained in the TIRS. In this case, data from the Landsat 5 TM sensors is most appropriate, using a band 6 with a wavelength of 10.40–12.50 μm for Landsat 8 OLI / TIR band 10 wavelength 10.6–11.19 μm [1, 2] for calculation of the endemic heat radiation from the landfill. The selected images are from different years and different seasons. The multispectral instrument (MSI) Sentinel-2 sensor data is used for the spectral characteristics. The same data was also used for Tasseled Cap Transformation (TCT), and this is the most used landfills recognition method. This approach was chosen because it is possible to interpret, classify and analyze phenomena and processes related to the dynamics and change of the basic components of the earth's surface – moisture, soil, and vegetation [3, 4]. For better visualization of the landfills, a combination of radar and optical images from Sentinel 1 SAR and Sentinel 2 MSI were used (Table 1) [5].

Data from the Open Data Portal, Copernicus and Landsat data and test spatial and spectral profiles were used [6, 7].

Table 1. Satellite data

DATE	SATELLITE
18.07.2010	Landsat 5 ETM
08.05.2022	Landsat 9 OLI
28.08.2015	Sentinel 2 MSI
13.04.2022	Sentinel 2 MSI
15.08.2015	Sentinel 1 SAR

We can write a general formula for Landsat 4–8: [3, 5–8]

$$1) \quad T_{[K]} = a * \ln^{-1} \left(\frac{b}{c * Q + d} + 1 \right)$$

Where a, b, c, d are the constants for the different types of Landsat images, T is the pixel temperature (K), Q is the spectral brightness coefficient of the surface in the thermal channel Landsat (4–8) satellite images are downloaded from web page <https://earthexplorer.usgs.gov/>. After the georeferencing procedure of the thermal images the cutting out of the rectangular sections in each image covering the vicinity of the geographic coordinates is carried out. The time series $\{Q_1, Q_2, \dots, Q_n\}$ of the images in the thermal channel of each WDS are extracted. The data from the image is converted into the surface temperature $\{T_1, T_2, \dots, T_n\}$ using transformation:

$$2) \quad T_{[C^{\circ}]} = a * \ln \left(\frac{b}{c * Q + d} + 1 \right) - 273.15,$$

Where:

a is the K_2 = Thermal conversion constant for the band

(K2_CONSTANT_BAND_n from the metadata);

b is K_1 = Thermal conversion constant for the band

(K1_CONSTANT_BAND_n from the metadata);

c is M_l = Radiance multiplicative scaling factor for the band

(RADIANCE_MULT_BAND_n from the metadata);

d is L_{λ} = Spectral radiance ($W/(m^2 * sr * \mu m)$);

Q = L1 pixel value in DN;

T = TOA (Top of Atmosphere) Brightness Temperature

The time series for WDS are formed together with the mask for clouds and “blankness” and are entered into the database. The time series of images for temperature for each landfill or WDS is systematized [9].

Results and Discussions

This article traces the development of the illegal landfill over a period of 12 years. Different methods were used for identification and visualization of the studied object. An established methodology for recognizing and calculating the temperature of the earth's surface was used to study the development and what happens after most of the waste has been moved to a recultivated landfill in the town of Kostinbrod.



*Fig. 2. Composite image from Sentinel 2 from 28.08.2015 Bands: 4-3-2;
Fig. 3. Composite image from Sentinel 2 from 13.04.2022 Bands: 4-3-2; Average of all
images used in the analysis for Landsat 7 (left) and Landsat 8 (right)*

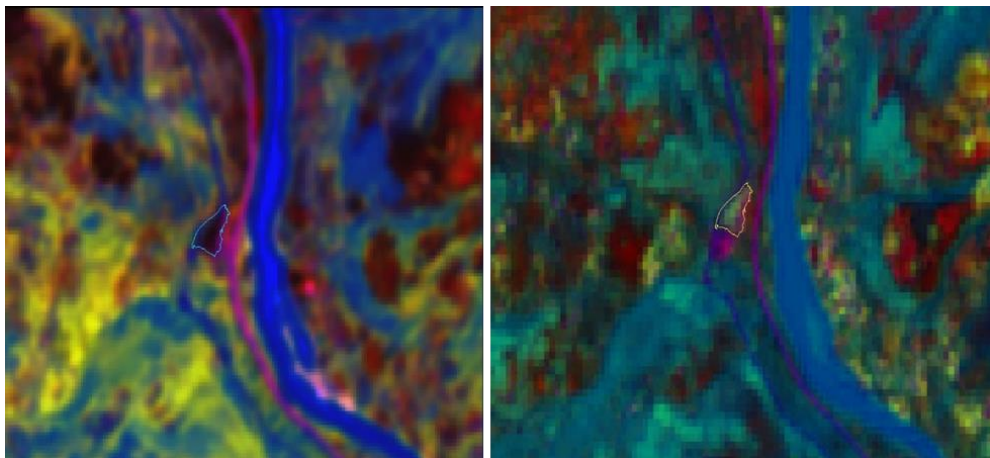
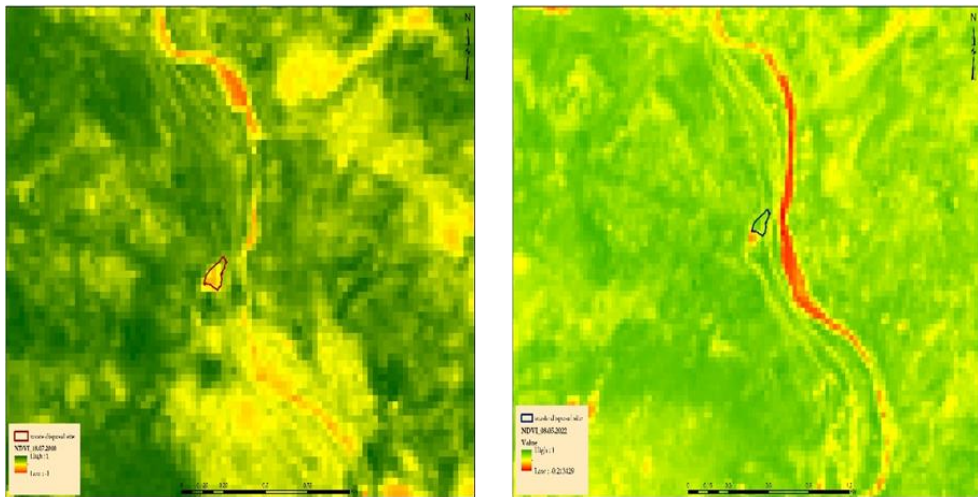


Fig. 4. TCT from 28.08.2015

Fig. 5. TCT from 13.04.2022

The composite optical images (Fig. 2 and Fig. 3) are from the multispectral instrument Sentinel 2 MSI in the visible range and bands 4, 3, 2. The image from 28.08.2015 clearly shows the boundaries of the landfill, as it was made on a clear day and without atmospheric disturbances. TCT transformation (Fig. 4 and Fig. 5) remains the safest way to identify landfills. The outlines are clearly visible, but in 2022 (Fig. 3 and Fig. 5) there is a relocation of the landfill south of the borders and its volume is significantly reduced, but it is still there and obviously not everything is transported to Kostinbrod, as is mentioned in a 2017 report of the municipality of Svoje and again remains a serious problem.

The second-class road II-16 passes through it, and just below it is an important railway artery that connects Northern and Southern Bulgaria.



*Fig. 6. NDVI from 18.07.2010; Fig. 7 NDVI from 08.05.2022
LST averaged over threetime intervals: 2000–2005, 2006–2010,
and 2011–2015 (left to right)*

The NDVI (Fig. 6 and Fig. 7) again showed the same trend as in the figures above. In the image from 18.07.2010 (Fig. 6) the landfill is completely within its boundaries, but in Fig. 7 from 08.05.2022 it has been slightly shifted to the south, and a new landfill has been formed. No change and damage to the vegetation is observed, except in the places where the landfill is.

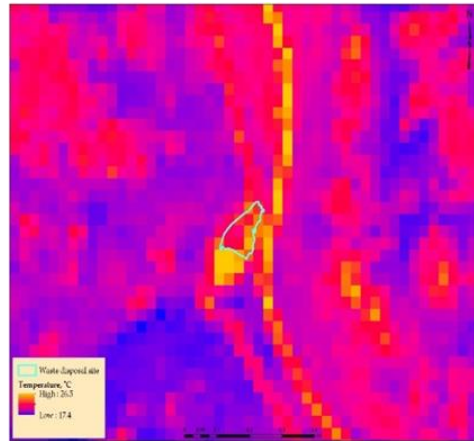
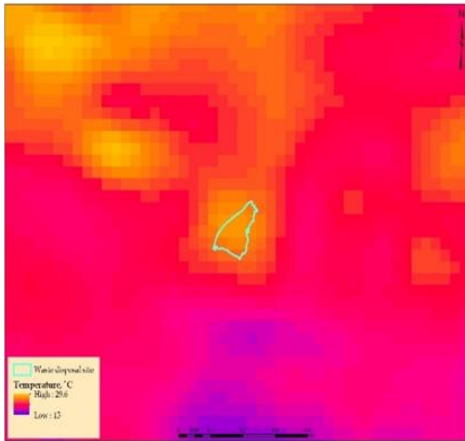


Fig. 8. Land Surface Temperature (LST) from 08.07.2010; Fig.9 Land Surface Temperature (LST) from 13.04.2022

Landsat 5 ETM was used to represent the surface temperature from 08.07.2010 (Fig. 8). There is a clear increase in temperature at the landfill, reaching +29.6 °C in the center of the site, which is typical for all studied landfills. The trend continues with the next image (Fig. 9) from 13.04.2022. Here the trend is similar to that of the TCT, NDVI of 2022 based on data from Copernicus. The landfill has been moved directly to the south of its borders, with the highest temperature in the newly formed landfill +26.5 °C and continues to radiate heat in its old border.



Fig. 10 and Fig. 11. Field images, author: Adlin Dancheva, Temenuzhka Spasova

The images from the field research (Figures 10 and 11) were taken in May 2022. The rubbish and part of the rock structures and vegetation on which spectral profiles are made are clearly visible (Fig. 12). From the spectral profiles one can clearly see the spectral curve at five different points and the fifth point is from the waters of the Iskar River. The high values of reflectance are noticed, which is also observed from the SAR image from 15.08.2015. Spectral reflectance levels are high in the area of the landfill, which contrasts sharply with data from the vegetation in the area. Both types of polarization vv vertical and vh vertical-horizontal were used for verification, as there is a strongly truncated relief.

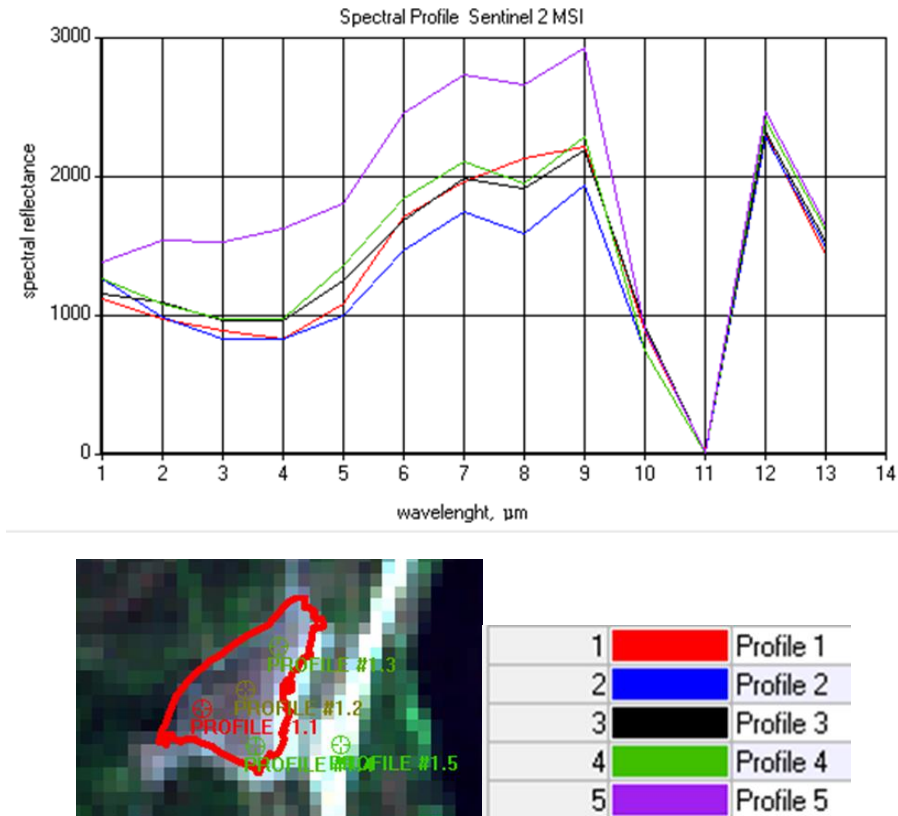


Fig. 12. Spectral profile Sentinel 2 MSI (28.08.2015)

Conclusion

Urgent measures must be taken to remove the waste and clean up the region once the administration has been notified, as this is a precondition for a serious environmental disaster. Climate change signals are not a myth in the area, but a clear

sign that has been proven even by local temperature changes based on Remote sensing.

The data from the Open Data Portal have been used successfully as a source for verification of information and show that the physicochemical parameters are moderate or unknown, the specific pollutants along the Iskar River are copper, manganese, aluminum and iron, biological indicators range from moderate to poor, and unknown data are available for some of the sites.

The analysis of data from Copernicus and Landsat shows an increase in temperature around the landfill, as well as an expansion of its borders to the south.

Of the spectral profiles made, the TCT and NDVI optical indices used, composite optical images in good and clear weather are a reliable source of information, and radar images further verify the information as they are not affected by weather and weather conditions.

From the developed methodology and the use of so many different sources of Open and Spatial Data, correct and informed decisions can be made in environmental monitoring, as well as management decisions at the local or regional level.

Last but not least, this type of information could be used to supplement the information about the specific territory in the construction of the Digital Twins of the Earth, which are in connection with the initiative of The European Commission's Destination Earth1 initiative (DestinE). Information from all sources in a single point or territory that is interoperable will result in high-value environmental data and information and reduce the administrative burden in the country.

References

1. Dancheva, A. and Asenovski, S. "Study of waste disposal thermal radiation using satellite data and considering solar influence," *Aerospace Research in Bulgaria*. 30.
2. Richter, A., M. Kazaryan, M. Shakhramanyan, R. Nedkov, D. Borisova, N. Stankova, I. Ivanova, and M. Zaharinova. "Quality enhancement of satellite images and its application for identification of surroundings of waste disposal sites," *Proc. SPIE 10444*, 104441N-1-7 (2017).
3. Nedkov, R., "Orthogonal transformation of segmented images from the satellite Sentinel-2," *Comptes rendus de l'Académie bulgare des sciences*, 70(5), pp. 687–692 (2017).
4. Stankova, N., Nedkov, R., Ivanova, I., Avetisyan, D.. "Modeling of forest ecosystems recovery after fire based on orthogonalization of multispectral satellite data". *Proc. SPIE 10790, Earth Resources and Environmental Remote Sensing/GIS Applications IX*, 10790, SPIE, 2018, DOI:10.1117/12.2325643
5. Dancheva, A. "Differential estimation of temperature changes in landfills through the use of satellite data", *Proc. SPIE 11534, Earth Resources and Environmental Remote Sensing/GIS Applications XI*, 115340J (20 September 2020); <https://doi.org/10.1117/12.2574057>

6. <https://data.egov.bg/organisation/7816be10-bdaa-4d00-8e0b-936a40348965/datasets?&page=1>
7. <https://earthexplorer.usgs.gov/>
8. Richter A., Kazaryan M., Shakhramanyan M., Nedkov R., Borisova D., Stankova N., Ivanova I., Zaharinova M., Estimation of thermal characteristics of Waste disposal sites using Landsat satellite Images, *Comptes rendus de l'Académie bulgare des Sciences*, 2017, 70, 2, 2017.
9. Kuenzer, C. et al. Spaceborne thermal infrared observation – an overview of most frequently used sensors for applied research, in: Kuenzer, C. and S., Dech, (eds) *Thermal Infrared Remote Sensing SE-7*. Springer Netherlands (Remote Sensing and Digital Image Processing), 131–148. DOI: 10.1007/978-94-007-6639-6_7.
10. C. J. Tucker & P. J. Sellers (1986) Satellite remote sensing of primary production, *International Journal of Remote Sensing*, 7:11, 1395–1416, DOI: 10.1080/01431168608948944
11. <https://scihub.copernicus.eu/dhus/#/home>
12. <https://sentinel.esa.int/web/sentinel/user-guides/sentinel-2-msi>
13. <https://data.egov.bg/organisation/7816be10-bdaa-4d00-8e0b-936a40348965/datasets?&page=1>
14. European Environment Agency, Resource efficiency and waste, URL: <https://www.eea.europa.eu/bg/signals/signali-2014-g/statii/otpadatsite-problem-ili-resurs>.
15. USGS, Landsat 8 Data Users Handbook, 2016, vol.2 URL: <https://landsat.usgs.gov/sites/default/files/documents/Landsat8DataUsersHandbook.pdf>

ИЗПОЛЗВАНЕ НА ОТВОРЕНИ ПРОСТРАНСТВЕНИ И САТЕЛИТНИ ДАННИ ЗА ЦЕЛИТЕ НА ПРОУЧВАНЕ НА ДЕПА ЗА БИТОВИ ОТПАДЪЦИ

А. Данчева, Т. Спасова

Резюме

Настоящата работа проследява развитието на незаконно сметище край град Своге в България. След 2016 г. се изготвя План за управление на отпадъците на територията на общината и се взема решение за депониране в Регионално депо за битови отпадъци в гр. Костинброд. Целта на изследването е да се проследи развитието на биохимичните процеси, протекли на територията на сметището и дали тяхното въздействие продължава и до днес. Използвани са данни от Портала за отворени данни (<https://data.egov.bg/>), Националния портал за пространствени данни INSPIRE (<https://inspire.egov.bg/bg>), сателитни данни и ГИС, няколко спектрални профила,

вегетационен индекс (NDVI). Направена е ортогонална трансформация на изображенията (ТСТ).

Използвани са композитни изображения от мултиспектралния инструмент (MSI) на платформата Sentinel 2 и радар (SAR) от платформата Sentinel 1 на програмата Copernicus на Европейската космическа агенция. Повърхностната температура на депото е изчислена с помощта на топлинните канали от сензорите Landsat 5–7 (ETM) и Landsat 8 и Landsat 9 (OLI / TIRS). Направена е комбинация от радарни и оптични данни. Използвани са данни от различни сезони и години, за да се проследи динамиката на топлинното замърсяване в изследваната територия.

Направена е количествена и качествена оценка на територията, на която е разположено депото.

Не на последно място, демонстрирана е ролята на отворените данни с висока стойност в мониторинга на околната среда, което ще намали административната тежест за вземане на отговорни решения за всяка по-малка община и ще бъде успешно внедрено в бъдещи методологии за подобряване на дигитални близнаци (Digital twins) чрез техническа работа в Дестинация Земя (DestinE) и информация за всяка точка, област или глобално значими територии.

DROUGHT MONITORING USING REMOTE SENSING DATA

Antoaneta Frantzova

*Geological Institute – Bulgarian Academy of Sciences
e-mail: afrantzova@gmail.com*

Keywords: *Vegetation indexes, Remote sensing, Comparative analysis, Drought*

Abstract

The paper deals with the application of the remote sensing for drought monitoring. A way of their application in practice are shown through example for monitoring of drought that is done for three different area in Bulgaria with different pattern, for the same time (July) and for eleven randomly selected years from 1994 to 2009. For the purpose, NDVI, LAI and FPAR vegetation indexes are used. According to Intergovernmental Panel on Climate Change (IPCC) drought and floods are the most severity events threatening the country, so attention is paid on drought monitoring.

Introduction

Theoretical Description of Vegetation Indices

The theoretical basis for ‘empirical-based’ vegetation indices is derived from examination of typical spectral reflectance signatures of leaves. The reflected energy in the visible is very low because of high absorption by photosynthetically active pigments with maximum sensitivity in the blue (470 nm) and red (670 nm) wavelengths. Nearly all the near-infrared radiation is scattered (reflected and transmitted) with very little absorption, in a manner dependent upon the structural properties of a canopy (LAI, leaf angle distribution, leaf morphology). As a result, the contrast between red and near-infrared responses is a sensitive measure of vegetation amount, with maximum red-NIR differences occurring over a full canopy and minimal contrast over targets with little or no vegetation. For low and medium amounts of vegetation, the contrast is a result of both red and NIR changes, while at higher amounts of vegetation, only the NIR contributes to increasing contrasts as the red band becomes saturated due to chlorophyll absorption.

The spectral reflectance of vegetation is detectable in three major Electromagnetic spectrum regions [1, 2]:

1. Visible region (400–700 nm) – Low reflectance, high absorption, and minimum transmittance. The fundamental control of energy-matter interactions with vegetation in this part of the spectrum is plant pigmentation.

2. NIR (700–1350 nm) – High reflectance and transmittance, very low absorption. The physical control is internal leaf structures.

3. MIR (1350–2500 nm) – As wavelength increases, both reflectance and transmittance generally decrease from medium to low, while absorption increases from low to high.

Method

Drought monitoring using NDVI NOAA AVHRR data

NOAA AVHRR and MODIS (Terra/Aqua satellites) data are used for drought monitoring. They can be summarized in: MOD13 A1 (250 m 16 days NDVI, 250 m 16 days EVI); MOD13 A2 (1 km 16 days NDVI, 1 km 16 days EVI) MOD15A1 (Fpar 1 km, Lai 1 km); MOD17 (Npp 1km); MOD44A (Land Cover Change Metrics Past 3 Months)

Land cover monitoring using NOAA NDVI is done by calculations of NDVI for three different regions with various land patterns for following years: 1994, 1997, 2000, 2002, 2005, 2007, 2009, 2010 2005, 2007 and 2009: region 1 – Central North Bulgaria (Fig. 5); region 2 – Central Bulgaria, around Chirpan city (Fig. 6); and region 3 – part of Rhodope mountain, Eastern Rhodope (Fig. 2). Selected regions are shown on the image below.

Normalized Difference Vegetation Index (NDVI) provides information of vegetation health and a means of monitoring changes in vegetation over time. NDVI is calculated from the visible and near-infrared light reflected by vegetation. Healthy vegetation absorbs most of the visible light that hits it and reflects a large portion of the near-infrared light. Unhealthy or sparse vegetation reflects more visible light and less near-infrared light. Calculations of NDVI for a given pixel always result in a number that ranges from minus one (–1) to plus one (+1); however, no green leaves give a value close to zero. A zero means no vegetation and close to +1 (0.8–0.9) indicates the highest possible density of green leaves.



Fig. 1. Vegetation anomaly in 2007(earthobservatory.nasa.gov) and selected areas

NOAA AVHRR NDVI database used for land cover monitoring contains monthly and weekly reference images for the period from April to October (weekly

image is composed by 21 images – 3 images per one day). Database is made with the data published in DLR EOWEB and the data received in former Space Monitoring Center at the Ministry of Interior (Bulgaria). Because of the large volume of data for the selected regions, in the report are presented only the result for Rhodope mountain region (Region 3). The pixel values are presented in DN from 0 to 255. Each DN value corresponds to NDVI value. Calculations of NOAA NDVI for a given pixel always result in a number that ranges from minus one to 0,7.

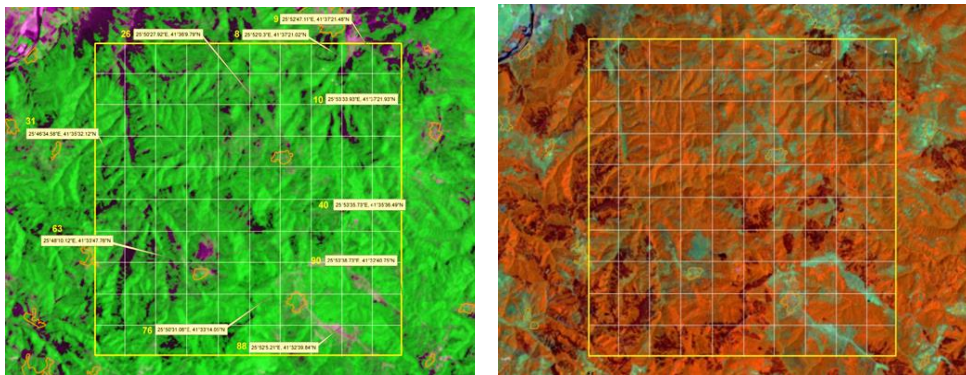


Fig. 2. DMC satellite images. Region 3, July 2008 and 2011. Each selected area is divided on the grid with dimension of 10x10 km.; each one pixel has resolution of 1000 m.
 41°37'26.28", 25°46'13.81"; 41°37'30.57", 25°53'14.81"
 41°32'10.23", 25°46'19.80"; 41°32'14.50", 25°53'20.23"

Table 1. DN and NDVI value

NDVI	0–255	NDVI	0–255	NDVI	0–255
0.1 – 0.2	94	0.3 – 0.4	127 – 158	0.5 – 0.6	191 - 218
0.2 – 0.3	95 – 126	0.4 – 0.5	159 – 190	0.6 – 0.7	219 – 254

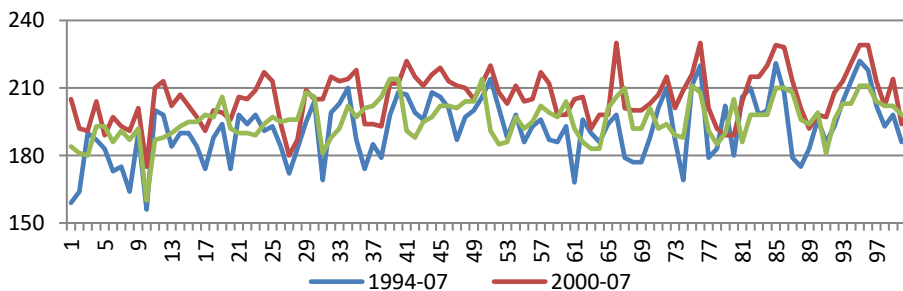


Fig. 3. Years with minimal values of NOAA NDVI

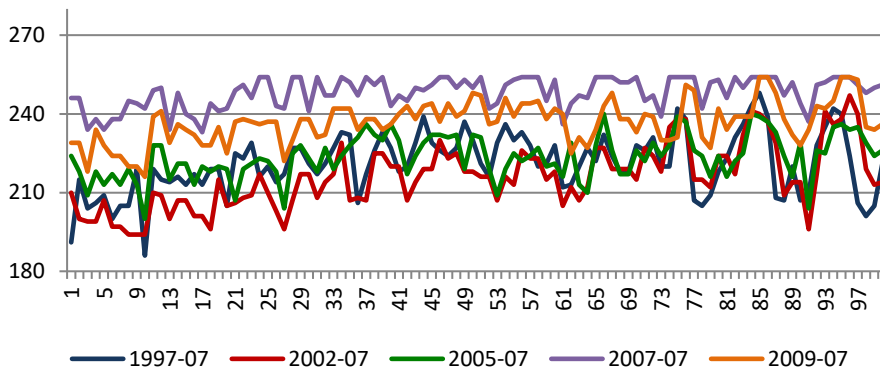


Fig. 4. Years with maximal values of NOAA NDVI

The average annual temperatures are progressively increased in the recent decades. They are highest in 1994, by 1–2 °C higher than average. The maximum temperature in July 2000 was a record - 40–45 °C, with 2–4 °C above the climatic norms. Minimum temperatures are consistently abnormal, with excesses to 22 °C. 2002 remains the third warmest year in recent years, following by 2000.

According to the results, we can conclude that the data from 1994, 2000 and 2007 can be used as lower threshold for monitoring and risk assessment of drought. For the Eastern Rhodope (Region 3) years with minimal values for July are 1994, 2000, 2002 and 2010 (Fig. 3), and the years for maximal values are 1997, 2002, 2005, 2007 and 2009 (Fig. 4).

Table 2. Amounts of rainfall for summertime from 2000 to 2010 (<http://eea.government.bg>)

	Precipitation- mm	Precipitation- mm	Precipitation- mm	Precipitation- mm	Precipitation- mm
Month/Year	2000	2001	2002	2003	2004
June	82.35	93.2	98.6	118	204
July	11.82	118.41	348	78	106
August	8.47	58.712	129	66	128
September	35.07	46.887	165	73	72

	Precipitation	Precipitation	Precipitation	Precipitation	Precipitation	Precipitation
Month/Year	2005	2006	2007	2008	2009	2010
June	56	219	15	154	85	210
July	178	86	2.8	12.6	55.0	117
August	1	9	96.1	19.5	18.5	7
September	39	57	125.3	29.4	119.6	54

MODIS NDVI, LAI and FPAR comparative analysis and correlation

The aim of the study is to show the relationship between vegetation indices derived from satellite data, and the way in which they are change for different types of surfaces. There is a strong relationship between NDVI-LAI, FPAR-NDVI and LAI-FPAR as is shown on the figures below.

The MOD 15 Leaf Area Index (LAI) and Fraction of Photosynthetically Active Radiation absorbed by vegetation (FPAR) are 1 km at-launch products provided on a daily and 8-day basis. LAI defines an important structural property of a plant canopy, namely the one-sided leaf area per unit ground area. FPAR measures the proportion of available radiation in the photosynthetically active wavelengths (400 to 700 nm) that a canopy absorbs. The LAI product will be a LAI value between 0 and 8 of the global gridded database. The FPAR product will be an FPAR value between 0.0 and 1.0 assigned to each 1 km cell of the global gridded database. Leaf Area Index (LAI) is defined as the one-sided green leaf area per unit ground area in broadleaf canopies, or as the projected needleleaf area per unit ground area in needle canopies. The Fraction of Absorbed Photosynthetically Active Radiation (FAPAR, sometimes also noted fAPAR or fPAR) is the fraction of the incoming solar radiation in the Photosynthetically Active Radiation spectral region that is absorbed by a photosynthetic organism, typically describing the light absorption across an integrated plant canopy. This biophysical variable is directly related to the primary productivity of photosynthesis and some models use it to estimate the assimilation of carbon dioxide in vegetation [5].

The LAI and FPAR data are generated by MOD15A2 algorithm, which is a Level 4 product and is generated automatically every 8 days with a spatial resolution of 1 km in Sinusoidal projection.

Once generated, the values obtained are stored digitally with a scale-factor and offset applied to transform the values to their biophysical correspondence. The equation used to decode the digital values to their analysis form is the following [6, 7]:

$$\text{Analyticalpixel} = \text{scale factor} \cdot (\text{digitalpixel value} - \text{offset})$$

Research and Applications: LAI and FPAR are biophysical variables that describe canopy structure and are related to functional process rates of energy and mass exchange. Both LAI and FPAR have been used extensively as satellite derived parameters for calculation of surface photosynthesis, evapotranspiration, and NPP. These products are essential in calculating terrestrial energy, carbon, water-cycle processes, and biogeochemistry of vegetation. The LAI product is an input to Biome BGC (Biogeochemical) models to produce conversion-efficiency coefficients, which are combined with the FPAR product to produce daily terrestrial PSN (photosynthesis) and annual NPP [3, 4].

MOD15A2 provides global LAI and FPAR data derived from the atmospherically corrected BRDF (MOD 09) using up to 7 spectral ranges (0.47 μm , 0.555 μm , 0.688 μm , 0.588 μm , 1.24 μm , 2,130 μm).

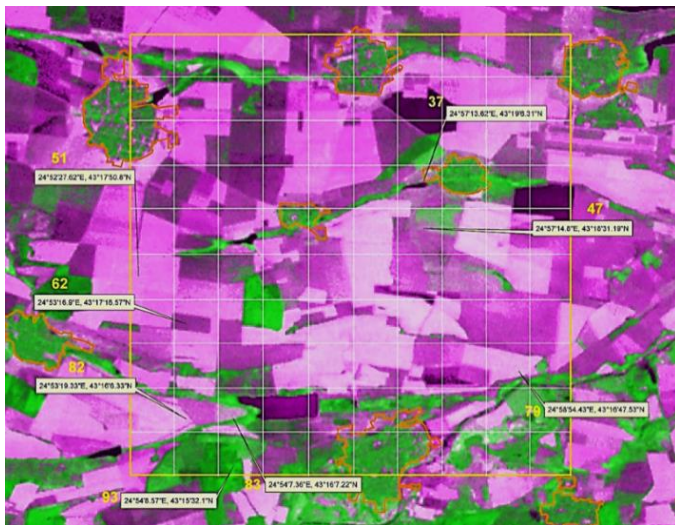


*Fig. 5. Region 2 – Chirpan city area, Central Bulgaria
 $42^{\circ}12'49,86''\text{N}$, $25^{\circ}21'9,08''\text{E}$; $42^{\circ}12'55,74''\text{N}$, $25^{\circ}28'13,90''\text{E}$
 $42^{\circ}7'33,89''\text{N}$, $25^{\circ}21'17,27''\text{E}$; $42^{\circ}7'39,76''\text{N}$, $25^{\circ}28'21,51''\text{E}$*

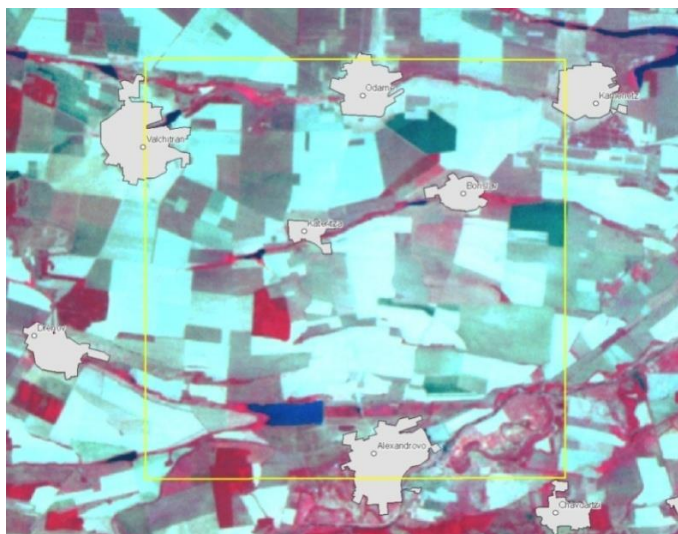


*Fig. 6. Region 1 – Central North Bulgaria, DMC image, 32 m
 $43^{\circ}20'49,67''\text{N}$, $24^{\circ}52'4,91''\text{E}$; $43^{\circ}20'57,51''\text{N}$, $24^{\circ}59'17,44''\text{E}$
 $43^{\circ}15'33,86''\text{N}$, $24^{\circ}52'15,94''\text{E}$; $43^{\circ}15'41,67''\text{N}$, $24^{\circ}59'27,85''\text{E}$*

The following charts (Figures 7, 8 and 9) show the relationship between the NDVI, LAI and FPAR. Theoretically, the relationship between NDVI/FPAR is linear, as FPAR is inherently derived from NDVI – electromagnetic radiation used to determine of NDVI, is used to determine of FPAR (photoactive radiation).

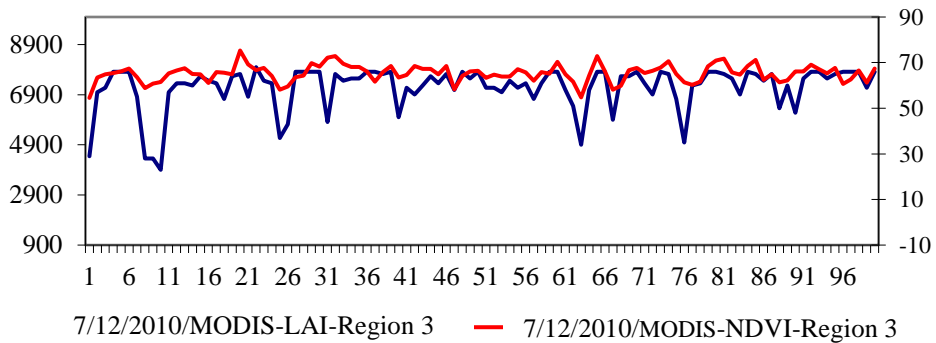


Fig. 7. Relationship between pixel values for NDVI and LAI for Region 3, July 2010. (Actual pixel values for NDVI: The values depicted on y-axis must be divided by 10,000)

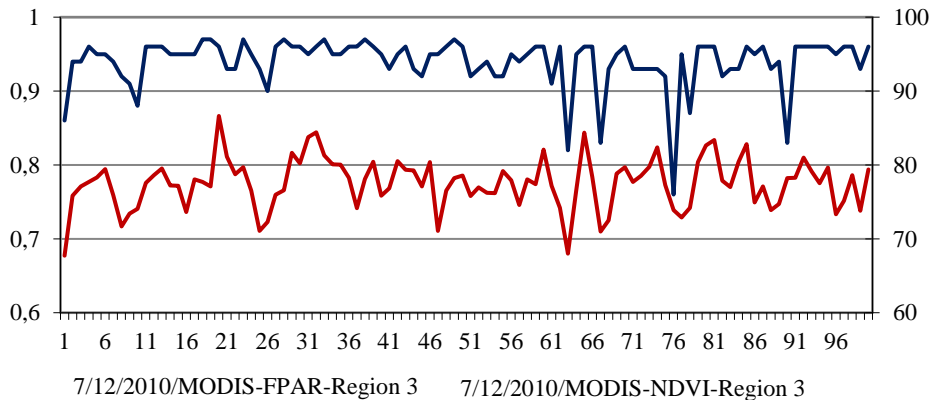


Fig. 8. Relationship between pixels values for NDVI and FPAR. Region 3, July 2010

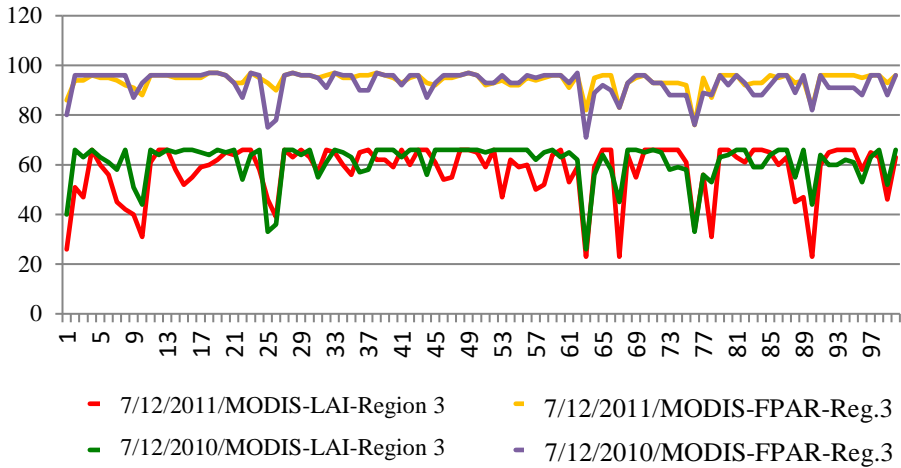


Fig. 9. Relationship between pixels values for LAI and FPAR. Region 3, July 2010 and 2011

It should be noted, in the areas lacking vegetation cover, NDVI and FPAR have very similar values. In areas with dense vegetation cover with maximum LAI values, FPAR also reach maximum values. It is obvious that the denser and "green" vegetation, result in the higher values of the vegetation indices. In our case, logically, the highest values for all indices are observed for the Rhodope mountain region.

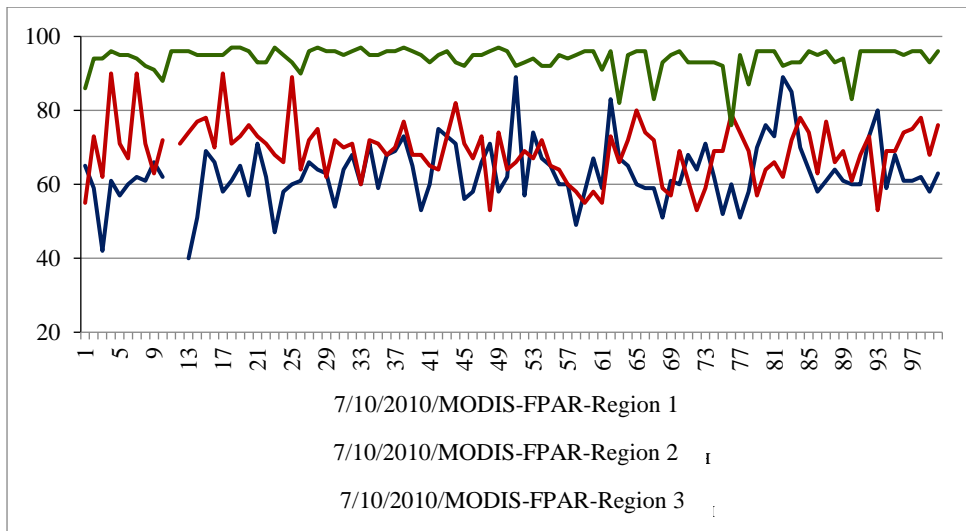


Fig. 10. Relationship between pixels values for FPAR indexes, July 2010

Applicability of remote sensing data in the risk management process of drought

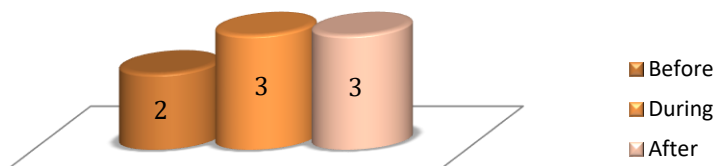


Fig. 10. Applicability of remote sensing data in the risk management process of drought; 1 – low; 2 – medium; 3 – high

Table 3. Applicability of remote sensing data in the risk management process of drought – land cover: “before” means – early warning, preparedness, risk and vulnerability assessment, (including modeling); “during” – monitoring and fast response; “after” – damage assessment, (including modeling); 1 – low; 2 – medium; 3 – high

Satellite	Instrument	Before	During	After	Resolution
High resolution	Camera system	1	1	1	2–10 m
Middle resolution	Camera system Radiometer	3	3	3	10–60 m
AQUA, TERRA	MODIS	3	3	3	250–1100 m
NOAA/POES	AVHRR/3	1	1	1	1100 m

Table 4. Applicability of remote sensing data in the risk management process of drought – water resources

Satellite	Instrument	Before	During	After	Resolution
High resolution	Camera system	1	2	2	2–10 m
Middle resolution	Camera system Radiometer	3	3	3	10–60 m
AQUA, TERRA	MODIS	1	2	2	250–1000 m
NOAA/POES	AVHRR/3	1	1	1	1100 m

Criteria selection for classification are divided in two broad groups. The first group covers the physical parameters related to particular natural hazards and risk process in the context of their study and investigation. On the other hand - the second group is connected with technical characteristics and operating parameter of the space platforms and technical equipment on the board.

Conclusion

The impact and negative effects of a drought depend on its duration, the severity and territorial distribution of the deficit, but also to a large extent on the environment and the socio-economic vulnerability of the affected areas. Desertification is largely caused by inadequate and unsustainable use of land in adverse climatic conditions, usually resulting from poverty and lack of livelihoods and livelihoods.

Land degradation and desertification resulting from prolonged droughts combined with the socio-economic impact and vulnerability of society are particularly evident in arid (dry) areas/areas. The global significance of the problem is underlined by the fact that dry regions cover about 41 % of the Earth's surface and that they are home to about 1/3 of the world's population.

Future climate change scenarios indicate that today's light/medium-sized drought and drought-related processes are likely to shift to future severe and prolonged droughts in less than 30 years.

The methodology for land cover monitoring and drought related processes related to the drought are discussed. It is based on the vegetation indices derived from satellite data and mathematical algorithms/"products" from satellite data. The main vegetation indices are considered, and the results of the calculations and comparative analyzes for several different cases are presented, including different vegetation indices showing the condition of the vegetation roof and having a direct relation to its condition and the processes of drought and drought.

References

1. Lusch, D.P. (1999). Introduction to environmental remote sensing. Center for remote sensing and GIS, Michigan State University, BRSI, 247 p.
2. Govender, M., Chetty K., Bulcock (2007). A review of hyperspectral remote sensing and its application in vegetation and water resource studies, Water Research Commission, AJOL, Vol. 33 No. 2, DOI: 10.4314/wsa.v33i2.49049
3. Global pattern of NPP to GPP ratio derived from MODIS data: effects of ecosystem type, geographical location and climate
4. Jiang. H. (1999). Modelling the spatial pattern of net primary productivity in Chinese forests, Ecological Modelling, Volume 122, Issue 3, 20 Oct. 1999, pp. 275–288. [https://doi.org/10.1016/S0304-3800\(99\)00142-8](https://doi.org/10.1016/S0304-3800(99)00142-8)
5. Christensen, O.B., Goodess, C.M., Harris, I., Watkiss, P. (2011). European and Global Climate Change Projections. Discussion of Climate Change Model Outputs, Scenarios and Uncertainty in the EC RTD ClimateCost Project. Summary of Results from the ClimateCost. Project, funded by the European Community's Seventh Framework Programme. Copyright: ClimateCost, 2011, First published September 2011

6. Tucker, C.J., (1979). Red and photographic infrared linear combination for monitoring vegetation, *Remote Sens. Environ.*, 8, pp. 127–150.
7. Руменина Е. (2008). Научен отчет по договор ДВ 08/001.12.06.2008 г. Разработване на методология и създаване на национална база данни за NDVI, NPP и LAI на основата на спътникови данни от NOAA и MODIS. ИКИ–БАН.

ИЗПОЛЗВАНЕ НА ДИСТАНЦИННИ ДАННИ ЗА МОНИТОРИНГ НА ПРОЦЕСИТЕ НА СУША И ЗАСУШАВАНЕ

А. Францова

Резюме

В настоящата статия се разглежда приложението на дистанционните изследвания за наблюдение на процесите, свързани със суша и засушаване. Начинът на тяхното приложение в практиката е показан чрез пример за мониторинг, извършен за три различни района в България, с различни географски характеристики и за един и същи времеви период – м. юли (за период от единайсет произволно избрани години от 1994 до 2009 г.). Използват се вегетационни индекси NDVI, LAI и FPAR. Според Междуправителствения панел по изменение на климата (IPCC) сушата и наводненията са най-тежките събития, застрашаващи територията на страната, поради което настоящето изследване обръща внимание на мониторинга на сушата.

MONITORING COASTAL LANDSLIDES ALONG THE NORTHEAST BLACK SEA OF BULGARIA USING SAR DATA

Hristo Nikolov¹, Mila Atanasova²

¹*Space Research and Technology Institute – Bulgarian Academy of Sciences*

²*National Institute of Geophysics, Geodesy and Geography – Bulgarian Academy
of Sciences*

e-mail: hristo@stil.bas.bg

Keywords: *Landslides monitoring, Coastal zone, DInSAR processing, Local geodetic networks*

Abstract

The geological conditions along the Northeast Black Sea coast of Bulgaria are favourable for landslides emergence and development. Those processes have been rigorously documented in the last fifty years by Earth science researchers. Their efforts contributed in a broader context to the landscape conservation and to mitigate the risks for the population caused by the mentioned surface disruptions. In this paper the obtained results record the temporal behaviour of several landslides located in stated region during the last five years. The main data source to monitor the mentioned landslides is data from synthetic aperture radar (SAR) instrument processed by the differential interferometric SAR (DInSAR) method. The produced results were validated by means of global navigation satellite system (GNSS) measurements carried out at purposely created geodetic networks, satellite images with high spatial resolution and digital images obtained by unmanned aerial systems (UASs). The results presented in this paper unambiguously confirm the usability of the produced information for the local authorities and other stakeholders thus contributing to the improvement of landslide risk management practices and to the better planning of the territory where the researched landslides are located.

1. Introduction

The geophysical hazards, such as earthquakes, floods, landslides, severe storms, droughts to name a few, indisputably have negative impact on the landscape and on the ecosystems. To this end the protection from them is crucial in saving human lives, keeping the animals' habitats, and decreasing the economic losses not only at national, but at continental level, since it is often the case that single event is affecting more than one country [1]. At present the data delivered by large number of sources e.g. remote sensing Earth observation from satellites or UAS, in-situ observations and measurements largely increases the accuracy of the data that support the development of new geophysical models for alleviation of the effects from the said negative events. On the other hand, the modern geographic information systems (GIS) taking advantage of the increased processing and communicational

capabilities of supercomputers, workstations, and mobile devices allow handling of large data volumes needed by the models. All said eventually results in better understanding of the georisk processes and their management by the authorities at local and national level. In order to facilitate the understanding of the mentioned landslide processes we decided to investigate several areas located along the coastal zone of Northeast Bulgaria known to have suffered by such events [2]. To this end we proposed and implemented an approach that took advantage of large number of data sources (available or emerging) that will lead to more complete identification and registration of the future landslides activation in the researched region.

In this context it was necessary to find more sources of regularly updated and reliable information with regard to the ground surface motions in the investigated area, which was one of the tasks we had to cope with initially and is still ongoing. In this paper we realized an integrative approach based on variety of sources the SAR and GNSS being the main ones, but supported by other such as modern geological maps, maps of land cover/land use, high accuracy digital elevation models (DEMs), data from local UAS campaigns and excerpts from national orthophoto coverage, reports from regional authorities [3]. Such an approach, according to the best of our knowledge, has not been implemented before in investigation of landslide processes registered at the coastal zone of Northeast Bulgaria or in other area of the country.

For the whole Black Sea coastal zone of Bulgaria, it was estimated that the landslide areas occupy about 13% of its length. In addition, it should be highlight that the said unfavorable processes also decrease the biodiversity as well as the quantity and quality of the ecosystem services provided by the technogenically overwhelmed areas of the landscape consisting of industrial, residential and touristic buildings [4].

In this paper the authors have narrowed their research only on the area along the seashore zone between the town of Varna and the Kaliakra cape. According to [3] in the said strip found are 124 stabilized, semi-stabilized and active landslides. The overall conclusion is that for the development of landslide processes in the studied region those processes haven't activated abruptly, and no large impact was observed for the investigated period January 2015 to September 2021¹. On the other hand, for the majority of the researched zones the surface movements are still ongoing.

The all above stated (landslides occurrence, technogenic load, landscape preservation) prompted the authors to set the main focus of this paper on underlining the possibilities for regular monitoring of the landslide processes occurring on coastal zone in NE Bulgaria provided by processing satellite data from SAR instrument onboard the ESAs' Sentinel-1 (S-1) mission. The main advantages offered by the mentioned data source are - large area for observation; data provision at fixed intervals; open data policy, accessible and validated software for processing.

¹This period is defined by the terrain observations and measurements made by the authors.

The aim of the research is to summarize the achievements of the authors by showing the results from their research concerning the integral and complementary use of multisource data to deliver up-to-date, reliable, and frequently updated information to the competent authorities and to the public with regard to the ongoing surface deformations caused by recent surface movements at the monitored landslide areas. In this research the authors took advantage of the joint use of data from GNSS and SAR.

2. Region of study and geological setting

2.1. Geography and climate

The researched region is located in northeast part of the Balkan Peninsula known with numerous landslides found at the cliffs along sea shore. The main factors that cause their activation are as follows – the sea erosion the rainfalls and snow melt (leading to fluctuations in groundwater levels); the seismic events; anthropogenic impact. According to the Global Earthquake Model [5] the seismic hazard measured in PGA for the area is relatively high 0.08 to 0.20 (g), but in the last years no large landslide event could be directly related with seismicity. The impact of the rest factors on the landslides' activation will be discussed later-on in the section 5.

The northern part of Bulgarian Black Sea coast includes the coastal zone north of the city of Varna ending at Bulgarian-Romanian border. This zone includes ancient and modern landslides having different degrees of activity. The factors mentioned in the previous paragraph trigger landslide activity in this region causing slow horizontal and vertical movements of the Earth's surface. Depending on the degree of the impact, the geological structure and lithological composition of the rocks along with their engineering geological properties, two large landslide zones can be separated – Varna and Balchik areas. During the 60s of the last century two types of landslides were differentiated along the Varna and Balchik coasts – of circus type for the Varna coast, and linear-stepped, package type for landslides for the Balchik coast [2]. The geology engineers connected the separate types of landslides with the features of coarse-sandy facies in the Varna area (Dalgiya Yar) and with clay-marl - in the Balchik area (“Fish-Fish” and “Thracian Cliffs”) [2].

3. Materials and methods

3.1 Interferometric processing of SAR data

Radar systems are active remote sensing instruments operating in the microwave part of the electromagnetic spectrum (EMS) used on aircrafts and satellites. The side looking antenna sends pulses at precise wavelengths (currently used are L, C and X bands of EMS see [6] for details) to surface targets and registers the backscattered signal, which is composed of amplitude and phase. The magnitude of the amplitude reflects the physicochemical properties of the target surface such as roughness, while the phase corresponds to the distance to it. The modern radar systems are imaging radars with synthetic aperture, which simulates large antenna

in order to increase the spatial resolution of the produced image. This concept is illustrated on Fig. 1. The smallest imaged surface area (called “ground element”) registered by the SAR instrument is product of the range and azimuth in sensor geometry and only after appropriate processing ending with transformation to specific datum is converted to an image pixel that corresponds to an area of the Earth’s surface. The mentioned imaging geometry has some drawbacks known as geometric distortions, because during the data registration the platform is off-nadir [7]. Besides them during SAR data processing additional parameters such as type of the orbit, position of the satellite during the acquisition, internal parameters of the instrument, etc. are different for each acquisition and must be accounted too. To this end this information available in a form of metadata in the SAR data product and must be used during the processing in order to obtain correct results for the behaviour of the studied surface areas [8].

The information concerning the ground deformations that took place in the studied region was obtained by using the repeat-pass interferometry approach [9]. This method uses two SAR images obtained at different dates to form an interferometer the data from which after differential interferometric processing form an image based on the phase component of the backscattered radar signal. Besides the interferogram as separate image band produced are the values for coherence, which is used to estimate the quality of the interferometric band. After removing the contribution of the underlying topography from the interferometric image we infer conclusions on the occurred surface motions [10]. For the last procedure DEM with spatial resolution comparable with or better than single ground element is needed and is a prerequisite for the processing. To improve the interferometric results additional processing steps were performed such as spatial filtering and multilooking. To transform the phase values from the range $[-\pi; +\pi]$ to a metric unit a phase unwrapping must be carried out (see [6]). Concerning the unwrapping process, we followed the recommendation made in [11] to process smaller portions of interferometric image in order to avoid low coherent areas. From the unwrapped phase the displacement values in LOS (the line denoted with R in Fig. 1) were produced. Finally, a transformation to a desired geodetic datum was performed enabling the displacement images to be analyzed in GIS or other software as well. All mentioned processing steps were realized in the Sentinel-1 toolbox of SNAP software developed by ESA.

Serious advantage of the SAR data compared to the optical imagery in landslides monitoring is the ability to create inventory maps shortly after a landslide event despite of the weather conditions and in absence of illumination from external source. This fact is confirmed by the growing number of new satellite missions that will deliver SAR data at different wavelengths (X, C and L bands) with single or dual polarization, with improved spatial resolution (less than 1 m) and short revisiting time (daily or less in case of SAR constellation).

3.2 DInSAR and photogrammetry for landslides movements

In the last decades satellite SAR data processed by differential interferometry was used in landslides inventories. The InSAR method attracted the professionals from different fields delivering monitoring of wide areas, much higher point density, and most important low dependency on geography of the investigated areas and on weather conditions in comparison with the optical remote sensing, GNSS and terrain investigations. Further development of the mentioned approach is Multi Temporal Interferometry (MTInSAR or MTI) methods (e.g. Persistent Scatterers Interferometry (PSInSAR); Small Baseline Subset (SBAS)).

In the recent years the photogrammetry benefitted from latest achievements in UAS technology which made possible their integral use with PSInSAR. This approach was also used by the authors to research the latest surface movements in the RA “Fish-fish” (see sub-section 4.3 below) by comparing the results by both methods.

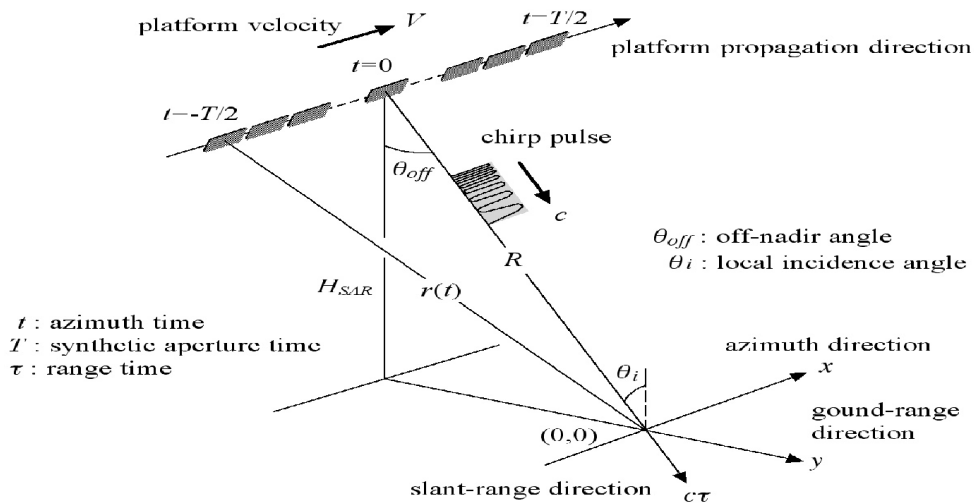


Fig. 1. Imaging geometry of a SAR sensor. (as in [6])

4. Results

The main focus of this study is on the successful application of SAR data to research the landslide movements at several areas in the region of Northeast Bulgaria. They were investigated as pilot sites in order to be able to provide reliable information on the ongoing geodynamical process in the said zone. Since the main consequence from landslides activations is movement of earth masses in horizontal and vertical directions the main data source must be a SAR data product that contains the phase component of the backscattered signal. Such data products from S-1 are those stored in Single Look Complex (SLC) format with double polarization (VV and VH) processed to Level-1 as described in. In order to facilitate the data sets

selection for present and future studies in the study area the authors created and continuously update is a local archive with SLC SAR imagery starting from year 2015. This archive allowed selection of optimal interferometric SAR pairs in terms of orbit direction and suitable perpendicular baseline [12] and at present contains more than 700 data products.

Initially to produce the interferograms data from ascending and descending S-1 orbits were used, but after obtaining the first results it became evident that better results have been produced using the descending orbit only. This decision was based on the fact that larger number of areas with high values for the coherence band were obtained from that orbit. Also, for most of the investigated sites the topography caused geometrical distortions (mostly shadows), noticeable on results obtained from ascending orbit data sets, since the inclination of the slopes at the whole coastal zone is high. Other challenge, known as temporal decorrelation, that was faced is the presence of large areas covered by vegetation in the investigated zones, which decreased the quality of the produced interferograms. To this end selected for processing were only those data sets that were registered out of the growing season for the vegetation i.e. from mid-autumn to mid-spring.

One more restriction we had to consider was the size of the area that had to be processed in order to avoid large areas with low coherence since those areas have negative influence during the unwrapping transformation [11]. For this reason, to obtain correct final results after producing the interferogram only part of it is further processed based on datum coordinates of the area subject to a specific study. Besides the vegetation the studied region is specific with having maritime areas that exhibit same decorrelation effect due to sea water evaporation and this is why the water areas had to be avoided (if possible) or removed during processing as well. For this reason, in the most of the interferograms reflecting the occurred surface motions at the studied sites presented in this section the pixels that had corresponding coherence below 0.3 were removed from the final displacement images (see Figures 2, 3 and 5). One more consideration that became apparent from our research was that the VV polarization of the radar signal S-1 delivers better results compared to the VH one.

4.1. Dalgiya Yar

4.1.1. Description of the AOI

This site is quite specific since this is an ancient landslide strip almost 10 km long, which is currently broken into smaller ones. It was established that the sliding surface of all landslides starts from a plateau located about 1 km from the seashore suggesting that the prime driving factor for their activations should be the varying level of the underground waters the marine erosion almost has no impact on them. [3] It should be noted that in this area a distinctive phenomenon is observed – a smaller landslide develops inside a larger one.

For the last half century, the oldest registered activation there dates back to 1971. Due to displacement of earth masses reaching 17 m width a landslide with shaft 4 m high reaching the sea and notch up to 15 m was formed. Its perimeter was established to be 250 m in length and 800 m width thus covering an area of 2 km². In the next 15 years due to increased technogenic intervention (building of houses and other infrastructure) there were several other activations took place destroying some 30 houses. In this it was confirmed that geological and hydrogeological conditions are at fragile steadiness state that could be easily disrupted by construction activities. This finding was affirmed by activation of a large landslide, which resulted in collapse of tens of thousands of cubic meters earth masses along a line about 2 km long. This event completely demolished a lighthouse and buildings in a fisherman village putting in danger the seaside road Varna-Balchik. It is supposed that the main cause for this activation was the increase of the underground water levels caused of rain and snow melting, sewage water, etc.

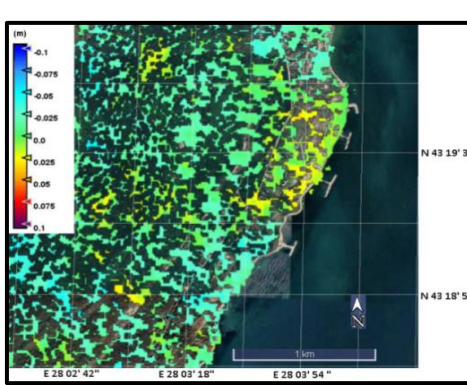
4.1.2. GNSS networks

To study the deformations due to the landslide processes in this area usage of GNSS technology has been adopted. It is based on data from two types of GNSS networks - points located on geologically stable terrain and points located in the landslide body. Data for the stable points located in non-deformable zones in the region are provided by the stations from the continuously operating reference stations (CORS) from the National GNSS Network. It needs to be highlighted that the velocities of the points from the said network in the northern Black Sea region are relatively small, less than 1 mm/year, while in other regions of Bulgaria they can reach 3–4 mm/year. To obtain the movements of the points from the purposely created local geodynamic networks their GNSS measurements were processed together with the GNSS measurements from the points of National GNSS network.

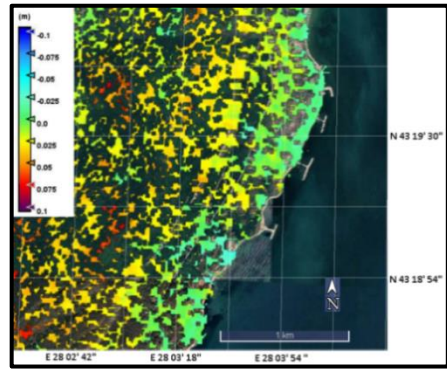
In the area of Dalgiya Yar a local geodetic network consisting of 30 points well stabilized in the ground with steel pipes or bolts was created. The GNSS measurements on this network were performed in three cycles since 2019 in the period June-July.

4.1.3. SAR results

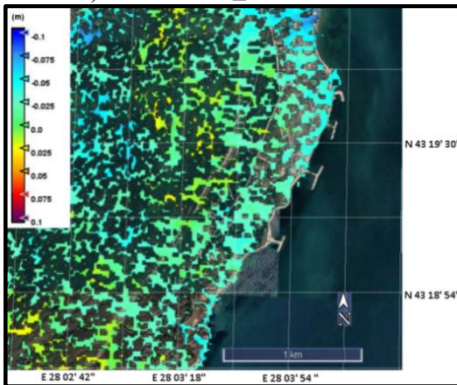
For researching this study area produced was a set of interferograms from descending orbit of S-1 only. Since the outcome of the processing is focused on surface deformations during the processing a constraint concerning the length of the perpendicular baseline for single pair was set to be less than 35 m.



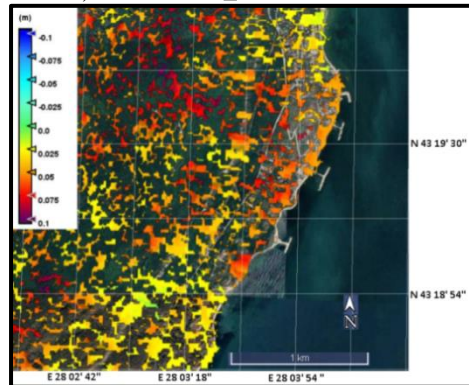
a) 20Nov2015_11Mar2016



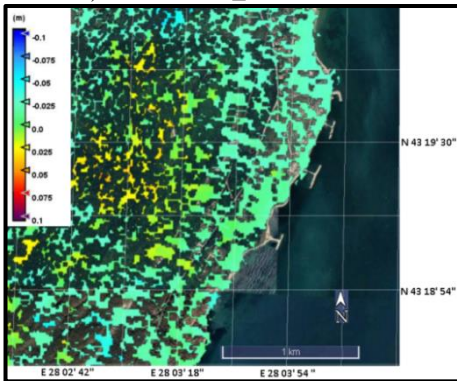
b) 26Nov2016_20Mar2017



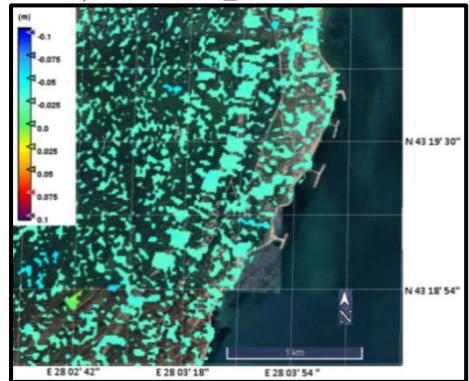
c) 15Nov2017_27Mar2018



d) 20Nov2018_22Mar2019



e) 29Nov2019_28Mar2020



f) 23Nov2020_23Mar2021

Fig. 2. Maps of SAR-derived displacements for the winter periods from 2015 to 2021

In order to correctly compare and analyze the displacements results SAR data pairs from winter season with 4 months span that satisfy the said constraint were used. On Fig. 2 excerpts from larger interferograms over a raster layer, on which only pixels having high coherence values (above 0.3) were coloured accordingly, while the rest were left transparent (a-f).

4.2. Residential area(RA)“Fish-fish”

4.2.1 Description of the AOI

In the zone of this RA located are three landslides – one potential, one active and one stabilized. The active landslide processes at this site were first registered in year 2000 (according to local inhabitants) and as probable cause for their activation a water mains accident was pointed out. In year 2010 it developed further increasing the affected area up to 5600 m². After that it is difficult to provide the exact size of the landslide area due to presence of high and dense vegetation, and gradual earth masses collapses along the steep coast, but an estimate by experts affirm that currently its area is about 57000 m² i.e. 10 times increase since the first registration. According to the competent local authorities this landslide activated twice in the last 6 years destroying houses and other infrastructural objects.

All said underline the importance of satellite-borne SAR data to produce reliable information for the regular monitoring of the ground deformations and possible earth masses subsidence accidents at this site.

For this site again the main reason for landslide activations is the rise of the underground water level caused by different sources – torrential rains, fast snow melting, human activities. In the RA “Fish-Fish” the landslide, which developed on streets “3rd” and “4th”, is registered using their names. It is located within an ancient landslide strip that starts from Albena resort and reaches the town of Balchik with a typical for this region landslide geomorphology. Currently its width is about 600–700 m and is formed on the slopes of the Dobrudzha plateau to the sea. The landslide toe has elevations of about 40–50 m ASL and forms a steep slope towards the sea [3].

The landslide on streets “3rd” and “4th” has developed above the edge of a 65–75 m high, steep 50°–60° slope towards the sea. Above the landslide scarp to the west, in the RA begins a relatively flat terrain, part of a slope with an inclination of about 5°–8° in south-southeast direction. In April 2010 its upper limit was at heights of 8.50–9.00 m on the vertical landslide slope above the sea front. The landslide is frontally extended with a length in the direction of movement of about 40–50 m, a width of 120–150 m and an area of about 5600 m². During the months September–October 2010 the slope reached and passed to the northeast on “2nd” street.

4.2.2. SAR results

It should be noted that an event that took place in August 2018 is well detected by SAR data, but it was once again confirmed that the presence of high slopes in the zone hampers the registrations from ascending orbit. The results obtained, despite the short period that was studied, are consistent (showing same movement in the area of the collapse) and reliable (have high coherence values). As shown on the figure below the detected deformations for smaller and larger periods confirm the expected displacements to be in the range of 0.02–0.06 m and exhibit seasonal variations. The latter evidenced by the different number of points with coherence values above 0.3.

Besides using SAR data, the RA “Fish-fish” was researched within two UAS campaigns (first on June 22nd 2019 and the second on Nov 25th 2020). Both campaigns were carried out with the aim to establish the displacements in the area for the mentioned period. But it needs to be emphasized that for regular and long-term monitoring of this site the UASs has the disadvantage that they depend heavily on the weather conditions such as strong gusts and need external illumination having an optical payload. Nevertheless, they could provide data with high spatial resolution for zones inaccessible for terrain measurements – for this specific object the area between the affected zone and the seashore has parts where the inclination reaches 60° at some locations. This why under certain assumptions it could be appropriate to substitute the GNSS measurements in local geodetic networks with UAS acquisitions.

In order to compare and analyse the results obtained by UAS and satellite SAR acquisitions with regard to the ground motions occurred in the landslide zone for time interval of 1 year and 5 months (between both UAS acquisitions) a number of interferometric images were produced at different intervals in order to compare the values obtained by both methods.

To estimate the degree (respectively the influence) of the temporal decorrelation caused by the large time intervals to the DInSAR results the authors experimented by creating a set of interferograms at different monthly intervals (see Fig. 4). On Fig. 4 b) presented are the displacements obtained from SAR data for the whole period of 1 year and 5 months where it can be seen that the decorrelation effect is visible since the obtained values are in the interval [- 0.04; 0.02] m which is comparable with those for much shorter periods (two months e.g. Fig. 4 h) and for this reason it should not be considered as reliable. For this site the results seen on images e) and j) on Fig. 3 confirm the contribution of high decorrelation in the results in case the time period between the SAR registrations is too large e.g. one year or 8 months. The remaining excerpts (Fig. 3 d, e, g, h, i, and k) are considered as correct representation of the ground motions occurred in the mentioned periods.

4.4. "Thracian Cliffs"

4.4.1. Description of the AOI

The activations in this landslide site could be attributed to large degree to the human activities in a narrow (less than 5 km) coastal area between the villages of Topola and Bozhurets. The landslide Thracian Cliffs has developed on the coastal slope located before the entrance of the golf club having the same name (see Fig. 4a).

The landslide Thracian Cliffs was first registered in 2014 and has manifested in front of an ancient stabilized landslide, known as "Kalkan Tepe". The researched landslide has a width of 1500 m and a length (in the direction of its movement) of about 500 m. The landslide scarp has a height of about 50–80 m, the landslide toe is manifested in the sea and is probably blurred. The coastal cliffs in the area are 20–30 m high, almost vertical, and not forested. The main reasons for the activation of landslide processes are over wetting of the earth masses by waters of unknown origin (possibly underground, fed by domestic ones), leaks from the compromised sewerage system built on the way to the golf complex, sea erosion and possibly others [3].

4.4.2 GNSS and SAR results

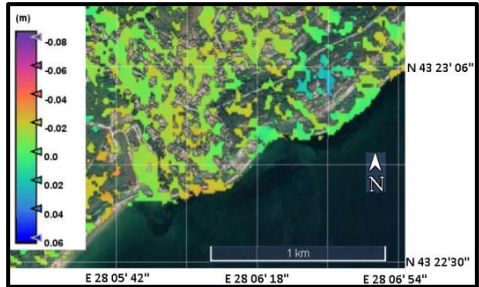
During the last 5 years this site was researched by using data from several sources - UAS acquisition (a point cloud seen on Fig. 4 a) and local DEM Fig. 4 b) local GNSS network (see Fig. 5 a). In order to establish the ground displacements with high precision a local GNSS network was created and the data from it were processed using data from the national CORSs. It included 10 stabilized points used to monitor deformations on the road leading to the golf club (points 601–604 on Fig. 5 a) and points located in the rocks and the path connecting the sea shore with the resort "Topola Skies" (points 503, 504, 605 on Fig. 5 a). Up to date three cycles of GNSS measurements on the local geodetic network were made in years 2019, 2020 and 2021 and all acquired data were processed and the results for the displacements registered by this method are shown in Table 1. Unfortunately, the point numbered 504 was not found (probably destroyed) after the last GNSS measurement and this is the reason in the same table to have absent values.

In 2020, a survey with a UAS was made in order to generate local DEM that could be used to improve the quality in the SAR data processing as well as to generate 3D representation of the objects in the area.

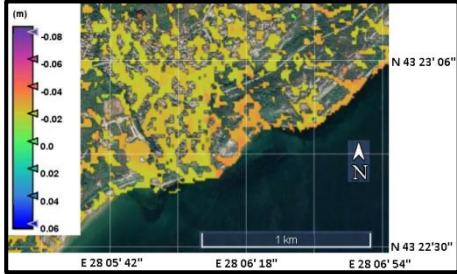
From the local SAR data archive mentioned in section 3 for this area large number of interferograms (see Fig. 5) were created covering several winter periods in consecutive years. The areas having large displacements are shown in dark blue and purple, the less vulnerable in yellow and in green are those where the displacements are smaller. From same figure derived were ground displacements in



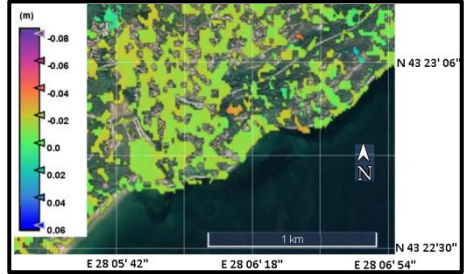
a) The surveyed area as in Google Earth



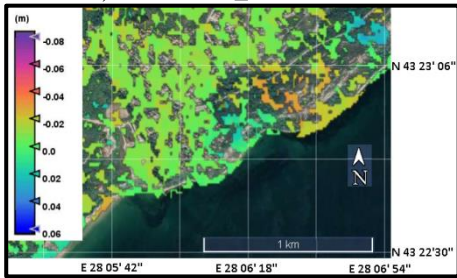
b) 20Jun2019_23Nov2020



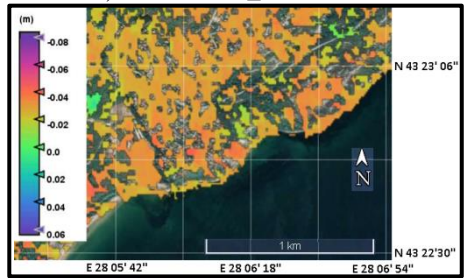
c) 20Jun2019_23Nov2019



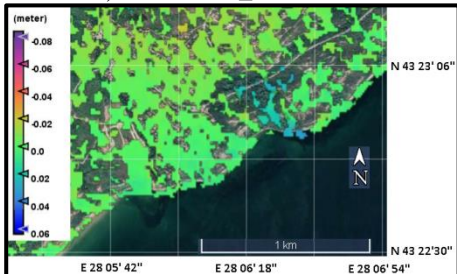
d) 23Nov2019_14Jun2020



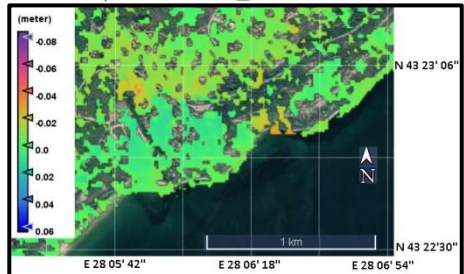
e) 20Jun2019_14Jun2020



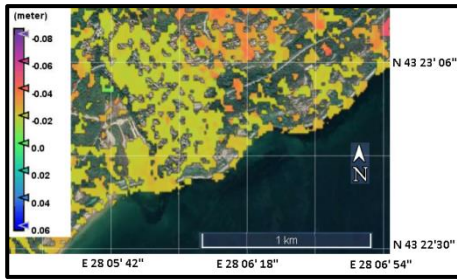
f) 14Jun2020_23Nov2020



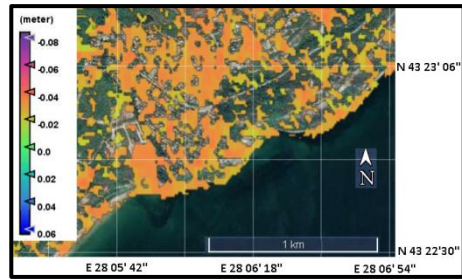
g) 23Nov2019_22Jan2020



h) 22Jan2020_27Apr2020



i) 23Nov2019_27Apr2020



j) 27Apr2020_23Dec2020

Fig. 3. Raster image of RA “Fish-fish” (a) and maps of SAR-derived displacements (b-j)

LOS the lowest value being - 8 cm. On the images b) to f) of the same figure visible is the influence of the coherence change on the final results even within same seasons, but for consecutive years. In this case even the dates for the SAR pairs are almost identical the displacements are different in different years.

5. Discussion

As mentioned in 4.1, Dagiya Yar is large site consisting of several landslide areas (some even overlapping) that was researched during the winter periods from 2015 to 2021 and the overall inference from the SAR results presented on Fig. 2 is that landslides movements vary from one period to the next. In our investigations we narrowed our focus on a small strip being 0.5 km wide that starts from the sea toward mainland and where the local geodetic network was established and measured. For this strip the obtained results for each of the winter periods the dominant movement is uplift with observed maximum the period for 2018–2019 amounting to 0.075 m.

In the area of RA “Fish-fish” it was of interest to register the development of an active landslide as well as possible activation of a potential one. For this site we made an experiment to correlate results from SAR and UAS. This experiment confirmed the need for more frequent UAS yearly campaigns (e.g. every 6 months – one in mid-autumn and one in late spring) in order to provide more data for the period into which landslide activations are more likely to occur and the time interval is not too large the temporal decorrelation to decrease the quality of the SAR-derived information.

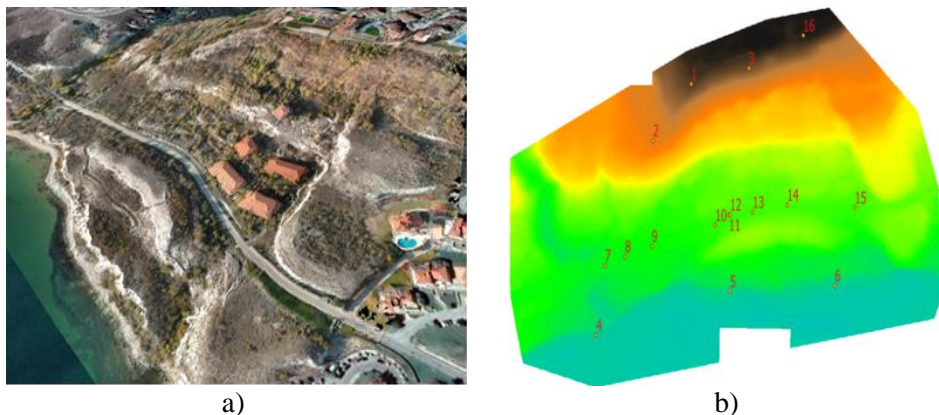


Fig. 4. 3D representation of the site from point cloud data a) and a local DEM overlaid by the GNSS RTK points used in UAS survey b)

The landslide Thracian Cliffs was researched via GNSS starting in 2019. From the results provided in Table 1 it is evident that the vertical movements are not constant and even for the periods 2020–2019 and 2021–2020 are showing different behaviour changing from subsidence to uplift.

Table 1. Displacements obtained by processing data from three GNSS measurement cycles

point	2020-2019			2021-2020			2021-2019		
	ΔX [m]	ΔY [m]	ΔH [m]	ΔX [m]	ΔY [m]	ΔH [m]	ΔX [m]	ΔY [m]	ΔH [m]
501	-0.032	0.002	-0.054	0.042	-0.03	0.087	0.01	-0.028	-0.067
502	0.007	-0.004	-0.019	0.008	-0.03	0.005	0.015	-0.034	-0.014
504	0.007	0.016	0.01	–	–	–	–	–	–
601	-0.025	0	-0.032	0.011	-0.033	0.064	-0.014	-0.033	0.032
602	-0.022	-0.018	-0.024	0.01	-0.028	0.066	-0.012	-0.046	0.042
603	0.005	-0.013	-0.017	-0.004	-0.034	0.058	0.001	-0.047	0.041
604	0.007	-0.006	-0.032	-0.003	-0.038	0.08	0.004	-0.044	0.048
605	-0.011	0.004	-0.032	0.008	-0.04	0.06	-0.003	-0.036	0.028

Acknowledgements This study was supported by Bulgarian National Science Fund under contract KP-06-OPR 06/1.14.12.2018.

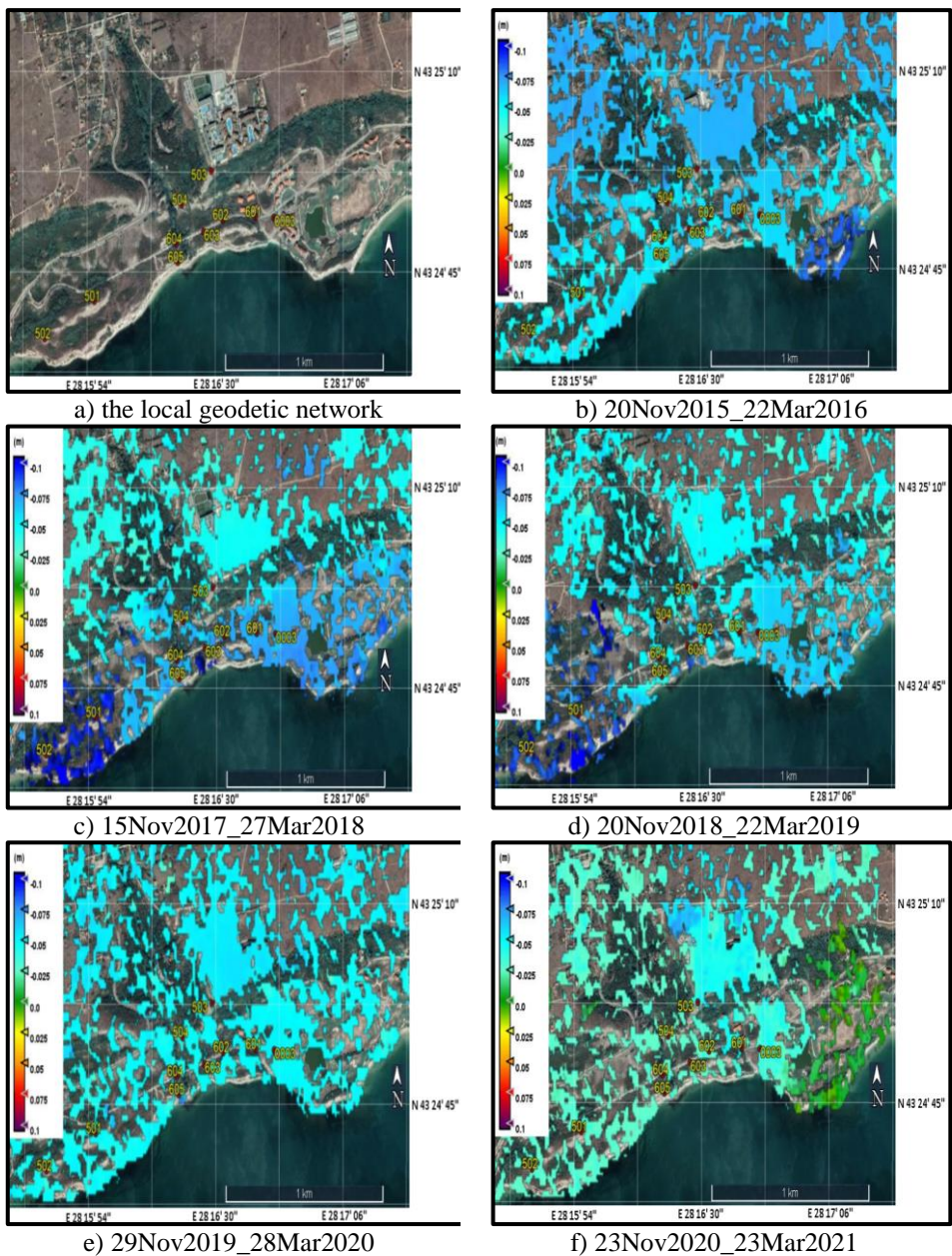


Fig. 5. Displacements registered at the landslide Thracian Cliffs for the period 2015–2020

References

1. Overview of natural and man-made disaster risks the European Union may face, Commission staff working document 2020, European Union, 2021.
2. Nankin, R.; Ivanov, P. Current state of the landslides affecting the Northern Bulgarian Black Sea Coast. *Rev. Bulg. Geol. Soc.* 2019, Volume 80, 3, pp. 176–178 (in Bulgarian with English abstract).
3. Yearly report of Geozastita Ltd., 2020, Available online: https://www.mrrb.bg/static/media/ups/articles/attachments/GO_%2020208f96c6989872d7c224855352c05185f4.pdf, (accessed on 06.12.2021 – in Bulgarian).
4. Stancheva, M., Marinski, J., Peychev, V., Palazov, A., Stanchev, H. . Long-term coastal changes of Varna bay caused by anthropogenic influence. *GeoEcoMarina*, 17, 2011.
5. Pagani, M., et al. Global Earthquake Model (GEM) Seismic Hazard Map (version 2018.1 - December 2018), 2018, DOI: 10.13117/GEM-GLOBAL-SEISMIC-HAZARD-MAP-2018.1 Popov, V., Mishev, K. *Geomorphology of the Bulgarian Black Sea Coast and Shelf*, Ed. of the Bulgarian Academy of Sciences, Sofia, 1974
6. Ouchi, K. Recent Trend and Advance of Synthetic Aperture Radar with Selected Topics. *Remote Sens.* 2013, 5, 716–807. <https://doi.org/10.3390/rs5020716>
7. Colesanti, C., Wasowski, J. Investigating landslides with space-borne Synthetic Aperture Radar (SAR) interferometry. *Engineering Geology*, 2006, vol. 88, no. 3-4, pp. 173–19, 10.1016/j.enggeo.2006.09.013
8. SAR Formats, <https://sentinels.copernicus.eu/web/sentinel/user-guides/sentinel-1-sar/data-formats/sar-formats>, (accessed on 25.03.2022)
9. Graham, L., Synthetic interferometer radar for topographic mapping. in *Proceedings of the IEEE*, vol. 62, no. 6, pp. 763-768, June 1974, doi: 10.1109/PROC.1974.9516.
10. Massonnet, D.; Feigl, K.; Rossi, M.; Adragna, F. Radar interferometric mapping of deformation in the year after the Landers earthquake. *Nature* 1994, 369,
11. Hanssen, R. F., *Radar interferometry: data interpretation and error analysis*. Dordrecht, Netherlands: Kluwer Academic Publishers; 2001.
12. Vassileva, M. et al. Satellite SAR interferometric techniques in support to emergency mapping, *European Journal of Remote Sensing*, 2017, 50:1, 464–477, DOI: 10.1080/22797254.2017.1360155

МОНИТОРИНГ НА КРАЙБРЕЖНИТЕ СВЛАЧИЩА ПО СЕВЕРОИЗТОЧНОТО ЧЕРНОМОРИЕ НА БЪЛГАРИЯ БАЗИРАНО НА ДАННИ ОТ РАДАРИ СЪС СИНТЕЗИРАНА АПЕРТУРА

Хр. Николов, М. Атанасова

Резюме

Геоложките условия по Североизточното Черноморие на България са благоприятни за възникване и развитие на свлачища. Тези процеси са документирани през последните петдесет години в рамките на научни и научно-практически разработки на учени в различни области от направление

„Науки за Земята“. В по-широк контекст техните усилия допринесоха за опазването на ландшафта и намаляване на рисковете за населението, причинени от споменатите явления. В тази статия получените резултати показват времевото поведение през последните пет години на няколко свлачища, разположени в посочения регион. Основният източник на данни за наблюдение на споменатите свлачища са данни от радар със синтезирана апертура (РСА), обработени по метода на диференциалната интерферометрия на РСА данни (DInSAR). Въпреки средната пространствена разделителна способност на използваните данни те позволяват да бъдат създадени дълги времеви редове и да се правят изводи по отношение на преместванията на земната повърхност. Получените резултати са валидирани с помощта на измервания чрез глобалната навигационна спътникова система (ГНСС), които бяха проведени в специално създадени локални геодезични мрежи, сателитни изображения с висока пространствена разделителна способност в оптичната част на електромагнитния спектър, както и цифрови изображения, получени от безпилотни летателни системи (БЛС). Резултатите представени в тази статия, недвусмислено потвърждават, че получената информация е от важно значение за местните власти и други заинтересовани страни, като по този начин допринасят за подобряване на действията, които се предприемат при управление на риска от свлачища, както и за по-добро планиране на териториите, където са разположени изследваните свлачищни обекти.

THREE-DIMENSIONAL MODELLING OF A BRIDGE BY INTEGRATING TERRESTRIAL AND AERIAL PHOTOGRAMMETRY APPLYING AN ADAPTED CAPTURE METHOD

Veselina Gospodinova¹, Todor Todorov²

¹University of Mining and Geology “St. Ivan Rilski”- Sofia

*²University of Mining and Geology “St. Ivan Rilski”- Sofia
e-mail: veselina.gospodinova@mgu.bg*

Keywords: *Low-cost approach, UAV, Close-range photogrammetry, Structure from Motion (SfM), Masonry bridge*

Abstract

Three-dimensional (3D) photogrammetric modelling is a contemporary remote sensing method for generating digital models with their specific appearance and texture, which are used in various areas of life. The modelling of complex geometry objects, such as masonry bridges, is not an easy task, because of their specific features (the presence of arches and various niches). This determines the choice of an adapted capture method according to the individual characteristics of the object. The paper presents research aimed at generating a highly accurate three-dimensional model of a bridge, by combining terrestrial and aerial photogrammetry. A low-cost unmanned aerial system (UAS) was used for capturing the upper side of the bridge. This significantly optimised capture time. But its capabilities do not allow to capture the bridge arches from the bottom upwards, nor to obtain an accurate model of the bridge railing. Because of this, a terrestrial survey was made with a digital camera, thus complementing the information required to generate a comprehensive model of the bridge. The integration of aerial and terrestrial capturing using low-cost cameras and systems, along with the application of modern algorithms for processing, allow to create precise, accurate, and detailed digital models. It is all very important for future conservation, restoration, adaptation, and socialisation of such type of objects which are monuments of culture.

Introduction

Cultural monuments and in general cultural wealth are of indisputable importance for the cultural identity of any society. The development of commonly accepted ways of managing cultural heritage and a cultural tourism strategy are major tasks faced by any country.

According to a number of recommendations and resolutions of the European Council, Europe needs to prepare commonly accepted ways of heritage management and, in view of sustainable development of cultural heritage, a strategy for cultural tourism. The sustainable progress of the cultural and natural heritage will be

guaranteed by reaching the full capacity of the following three basic principles: economic and social development, and environmental protection. The cultural and natural heritage will be preserved and used as a factor of development at the local and regional level, when its physical integrity is preserved and when the message it carries is successfully relayed and assimilated by contemporary society [1].

Due to its strategic location and history, Bulgaria is rich in cultural monuments, some of which are still in use today – for example, masonry bridges. According to unofficial data, they amount to about 150 and their preservation, restoration, and use is of utmost significance. The potential presence of erosion, abrasion, landslide activities, and the anthropogenic factor are all prerequisites for the need for periodic activities related to the monitoring and restoration of such sites. Remote sensing, as a non-destructive method which in some cases requires the acquisition of images from low altitudes (in particular photogrammetry), provides promptness and necessary accuracy, ensuring the safety of the work process. The ability to establish methods for capturing, along with the creation and storage of high-precision models of these types of objects, would provide experts from different fields with exclusive opportunities to have data on the exact location of every detail of those sites and objects.

There is a range of studies related to the creation of 3D models of masonry bridges. Some of these are based on the application of entirely terrestrial photogrammetry. For example, in a study implemented in 2006, a virtual photogrammetric model of the Kapuagasi bridge was created. The bridge is located in Istanbul and has a length of 74.4 m. More than 30 stereo images were taken with a *Samsung Digimax 430* digital camera. 40 reference points were used. Photogrammetric processing was performed in the *Pictran-D* software environment and the generated bridge model was input in 3D Studio Max for texturing [2].

A test and subsequently a field study related to photogrammetric modeling of a bridge are presented. The captured images were used by the *PhotoModeler* custom software to measure bridge characteristics. A field surveying was also performed. Based on the comparison between photogrammetric and manual measurements, it can be said that photogrammetry provides sufficient accuracy and is a non-contact, inexpensive and practical method for creating three-dimensional geometric textured models [3].

A 2017 study presents the Meram Bridge in Turkey captured. The bridge is 29.5 m long and 4.5 m wide and has five arches along its length. The capture was performed with a *Canon PowerShot A2200* and a *Canon EOS 100D* digital cameras. 70 control points were used and subsequent photogrammetric mapping was performed in *Photomodeler*. Another type of software was also employed, namely *Photoscan*, and 6 reference points were used for georeferencing. According to the result of this research, both photogrammetric approaches are validated as a low-cost method for 3D modelling of a masonry arch bridge [4].

Terrestrial photogrammetry has been established to this day as low-cost, accurate, and fast methodology for 3D modelling of architectural objects and for extracting metric data about them. In some cases, terrestrial photogrammetric capture is more difficult due to factors, such as situational features of the object and its surroundings. Unmanned aerial systems (UAS) are an alternative to this.

In a study, carried out in Italy, a bridge of special architectural and historical value was investigated. It was captured by a quadcopter equipped with a Sony camera with a 21MP (5344×4016) CMOS sensor. Twelve control points were used for georeferencing. The photogrammetric processing was performed in the Agisoft Metashape software. The Rhinoceros software and several additional developments were also used to construct the geometry of individual bridge elements. The obtained results prove the potential of the method in projects related to three-dimensional modelling of masonry bridges to be used for their maintenance and restoration [5].

A test study was implemented in 2020 related to the investigation of cracking of concrete samples in laboratory conditions using UAV. Several digital three-dimensional texture models of these samples were created and after that edge detectors were used to detect cracks. The presented results of the laboratory tests show that very accurate results are obtained with an error of less than 1 mm [6].

Another research presents the creation of digital photogrammetric models of two bridges for their visual inspection. The *DJI Mavic 2 Pro* unmanned aerial system with a 20Mp camera was used for the experiment. The data were processed in *Agisoft Metashape*. Both bridge models were validated by laser scanner surveying. After that, the obtained point clouds were compared. The validity of both photogrammetric models was verified. The obtained dense point clouds can be used as a basis in solving subsequent tasks and in analyses related to detecting bridge status and their periodic monitoring [7].

In some cases, the use of low-cost UAS poses a problem with digital cameras, mounted on their platforms. These cameras cannot capture the bridge's arches from bottom to top. This disadvantage can be solved by using images, obtained from terrestrial and aerial photogrammetry.

Until recently, simultaneous processing of terrestrial and aerial images was impossible. With the development of new software solutions and the *Structure from Motion* method, this obstacle has already been removed. This has generated the idea of collaboration between terrestrial and aerial photogrammetry, which allows the efficient construction of precise, detailed, textured three-dimensional models of various objects, including bridges. More flexibility, convenience, promptness, and completeness in their capture is thus provided.

To the best of our knowledge, a bridge of this size has not been captured in Bulgaria. But it can be borrowed from other captures abroad which actually prove that such a combination can be successfully used in photogrammetric surveying and modelling of this type of object.

A 2017 study proved the applicability of the collaboration between aerial and terrestrial photogrammetric surveying in the generation of a digital three-dimensional model of a bridge in Taiwan. It is consisted of three sections with an overall length of 60 meters, each 20 m wide and 8 m high. It consisted of three sections with an overall length of 60 m, each 20 m wide and 8 meters high. About 10 000 images were taken by a UAS equipped with a *SONY α7R2* digital camera. Some of the images were acquired by terrestrial photogrammetric surveying using a pole with a length of 2–8 m. All images were processed by Agisoft PhotoscanPro. The resulting root mean square error was less than 3 cm. The three-dimensional geometric model was subsequently used to identify cracks on the surface of the bridge [8].

Identical research related to the capture of the San Cono Roman bridge, located in the southern part of Italy, was carried out in 2019. A *Canon EOS 100D* digital camera with an 18 mm lens and a *Xiaomi Mi* unmanned aerial system with a 12.4 Mpx camera were used for this purpose. The photogrammetric processing was performed in the programming environment of the Russian *Agisoft PhotoScan* software. The resulting root mean square error of the model was 0.011m. The generated 3D model of the masonry bridge was successfully used for performing a structural analysis by specialised software and proves the capability of this methodology for generating 3D models of bridges [9].

In 2020, another research confirmed that the combination of aerial and terrestrial photogrammetry could be employed to create digital models necessary for the monitoring of concrete bridges and viaducts in Italy. In 2020, another research confirmed that the combination of aerial and terrestrial photogrammetry could be employed to create digital models for the monitoring of concrete bridges and viaducts in Italy. A visual inspection of a standard concrete overpass in L'Aquila was done. The resulting orthophotomosaic was used to perform an object-based analysis to identify and classify disturbed areas and shapes. The results have shown satisfactory identification of deteriorated areas. This allows to carry out easy and quick periodic inspections in order to evaluate the development of processes related to bridge faults and to plan activities to preserve the facility [10].

All these studies prove that remote sensing in particular photogrammetry is a method well-established in practice as a fast, inexpensive, and safe way to generate three-dimensional digital models with high accuracy and detail.

Method and data

The main purpose of the presented study is to establish sustainable methods for capturing and modelling types of objects like masonry bridges, using low-cost cameras and systems, as well as commercial data processing software, applying the "structure from motion" method. This method allows free placement of the capturing stations (projection centres), thus facilitating the performance of the task. This would

contribute to an easier and cost-effective modelling of these objects across the territory of Bulgaria. It is important to note that these models can be used not only to preserve the cultural and historical heritage of the country, but also for the monitoring of such transport facilities.

Photogrammetric processing is related to the creation of a digital model of an object/surface or parts of it, which is applied in various spheres of life. This processing includes several stages. After the images are loaded in the software (the camera is assumed to be calibrated), correlation procedures are performed to detect the so-called connection points in the corresponding images. Based on stereophotogrammetric principles, 3D points in space are calculated and generated. The camera positions for the scheme are also calculated. Initially, a texture-free model is built, which is called a skeleton model (the object is represented as an irregular triangular network – a combination of vertices and edges). Subsequently, a texture of the object is also generated. Its quality depends on the characteristics of the camera (for example, the high spatial resolution of the camera provides a better-textured model). A photorealistic virtual 3D model of the object is obtained from these images [11].

Analytical processing methods are used in the fore-described procedures related to the creation of photorealistic three-dimensional models. They are essential for the calculation of the internal and external image orientation parameters. Thereafter, the relationship between image and object is established and the necessary information (coordinates and geometric elements) about the captured object is subsequently obtained.

Usually, the stages of orientation are as follows:

- Providing information about the object (control points, distances, geometric elements);
- Measuring of image points for orientation (image coordinates);
- Calculation of the internal and external orientation parameters;
- Object reconstruction from the oriented images (new points, geometric elements).

Depending on the method used and the application of the photogrammetric data, these steps are performed sequentially, concurrently, or iteratively [11].

The modern *Structure from Motion (SfM)* method allows simultaneous processing of images acquired at different distances from objects, at different capture angles, and at different focal lengths. This is a significant advantage over traditional photogrammetric methods, making it possible to simultaneously process aerial and terrestrial photogrammetric images taken with different cameras. It is most suited to processing images with a high degree of overlap that capture the full three-

dimensional structure of the scene. The method differs fundamentally from conventional photogrammetry, in that the geometry of the scene along with the camera positions and orientation are solved simultaneously, using an iterative bundle adjustment procedure, based on a database of features automatically retrieved from a set of multiple overlapping images.

The *Structure from Motion* (SfM) method follows a certain sequence of processing activities. The first stage, after the images to be processed have been loaded comprises detecting identical points in all the overlapping images, applying the Scale Invariant Feature Transform (SIFT) algorithm. This algorithm allows linking individual images or their characteristic points. The images do not need to be in the same scale, i.e. they may be of different resolution. Then, the so-called bundle adjustment is carried out. This algorithm is based on multiple iterative procedures. At this stage, the parameters of inner and outer orientation, automatically retrieved from the overlapping images, are calculated. In addition, a sparse point cloud is created (the three-dimensional coordinates of the object are obtained in a random coordinate system based on the homologous points, detected in the photographic images). Having obtained the geometry of the object, the creation of a dense point cloud commences. This includes calculating the respective 3D point for almost every pixel of the image. Afterwards, this may result in generating digital elevation models, digital terrain models, three-dimensional textural surfaces and ortho-rectified images (orthophoto mosaics) etc. [12]. This is precisely the reason why all stages of photogrammetric image processing can be performed fully automatically in modern software products, such as *Agisoft Metashape*, *Pix4D*, *Meshroom*, *Autodesk ReCap* and others, making them suitable for use by non-specialist users.

The object of interest is the "Humpback" Bridge, which is located in the town of Harmanli in the central southern part of Bulgaria (Fig. 1). This transport construction was built in 1585 to facilitate the crossing of the Olu Dere River for the *caravans* (the convoys of the day). Its length spans 109 m, and it is 6 m wide. It is known as the "Humpback" Bridge because of the tapering shape (resembling a kind of humpback) in the middle of its central arch. The bridge is with a large 22 m arch symmetrically flanked by two smaller ones in its main and longest part, and by another 6.3 m arch after the bend in the northern part.

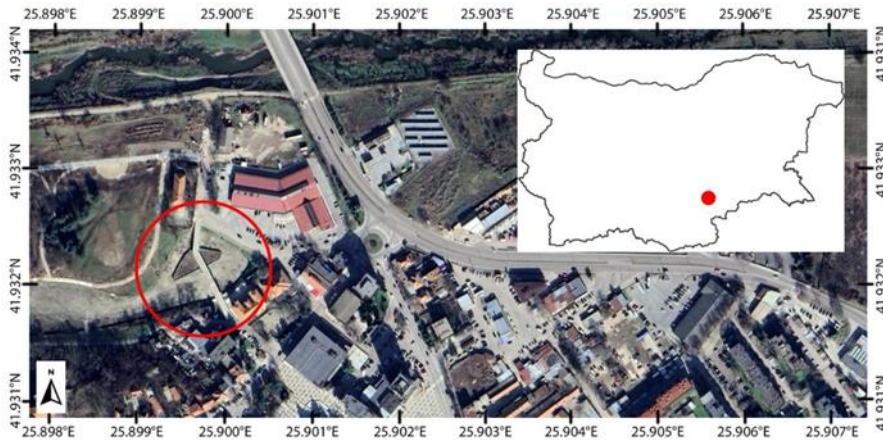


Fig. 1. Location of the studied object

The facility is more than 400 years old and as an architectural work is a representative of the school of one of the most famous Ottoman architects - Mimar Sinan. He designed over 300 buildings throughout the empire, and the most famous ones in Bulgaria are the Banya Bashi Mosque in Sofia and the Kodja Dervish Mehmed Pasha Mosque (the present-day Church of the Holy Septuagints in Sofia).

This unusual, yet functional and aesthetic solution of urban planning demonstrates the high level of construction skills of its creators. The spanned distance of over 22 m is remarkable for the technical capabilities of the day.

Results

Photogrammetric capturing of the bridge

The location of the bridge is near the city marketplace and considering it might be busy and overpopulated at specific time zones, those were avoided when working on the project. In order to ensure monochromatic lighting and minimal shading of the areas of interest, the hours selected for work were early in the morning and late in the evening, i.e. when the Sun is low above the easterly or westerly horizon.

The aerial shots for the project are taken with a *DJI Mini 2* UAS. With its mere 249 grams, it is lightweight and powerful, and thanks to its intuitive and advanced functions, it offers complete freedom of flight. It has a 31-minutes battery life and five levels of wind resistance. It rises to 4000 meters above sea level. It supports up to 10km of HD video transmission to the controller. With a 12MP sensor along with 4K/30fps video and 3-axis motor stabilisation, it provides high quality footage [13].

The *DJI Mini 2* is controlled by an RC controller, which requires connecting a mobile device with the appropriate control software installed.

Map Pilot Pro software installed on an iPhone 13 Pro mobile device was used to create a plan mission. The application serves to plan and execute a flight along an optimal trajectory in order to create maps or three-dimensional models.

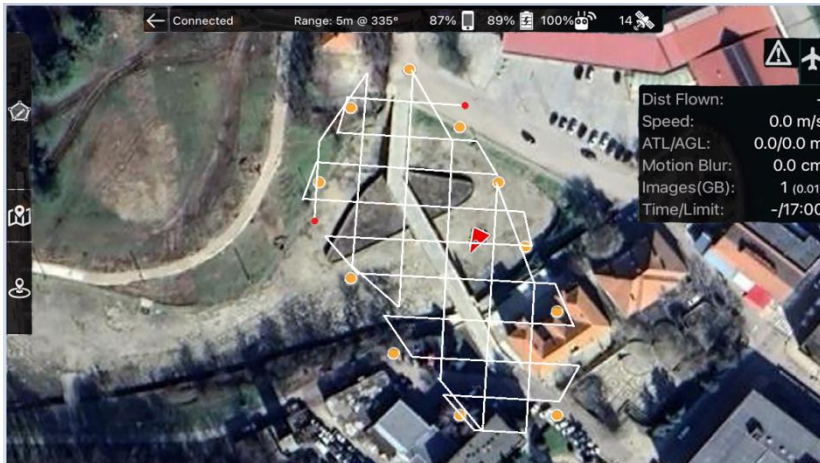


Fig. 2. Mission plan for the "Humpback" Bridge in Harmanli, prepared through the Map Pilot Pro software

Two flights at an altitude of 30 m have been executed with a 3D mode flight mission trajectory.

- Flight 1 produced 128 nadir images;
- Flight 2 produced 111 photos with a shooting axis tilted at 45°.

The images were saved in .jpeg format. The total flight time was 44 minutes. Considering the technical specifications of the camera and the selected flying height, the resulting pixel size on the real object was Ground Simple Distance (GSD) = 2.4 cm.

Because of the complex structure of the object, its shooting with a UAV cannot be termed sufficient. As it is impossible to lift the optical axis above the horizon when shooting with a *DJI Mini 2* drone, the low coverage of arches from their underside is very insufficient. After the aerial survey, an approach was taken to shoot the façades and the underside part of the arches with a digital camera. Additional photos of the railings and the walkway part of the bridge were also taken for better detailed description and in order to increase the quality of the model.

The shooting was performed with a *Nikon D90 SLR* camera with a *NIKKOR* lens. Its 12.3-megapixel *DX*-format *CMOS* sensor and *EXPEED* image processing system offer exceptional image quality with a wide ISO sensitivity range.

The eastern and western façades were captured with a perpendicular and tilted optical axis at a distance of about 15 m.

An individual approach was taken when shooting the arches and niches of the bridge. The images were taken with a perpendicular optical axis from one side to the other side of the main arch foundation across its width. Additionally, fan-shaped exposures were taken in a semi-circle, starting from one foundation, and reaching the other foundation of the arch.

The niches, symmetrically flanking the large arch on both sides, were photographed with opposite forward moves and at each station, exposures were made with the perpendicular camera axis inclined upwards.

The experiments have established that photographing the railings across the width with exposures only from one side of the bridge to the other did not give satisfactory results. Therefore, additional exposures were made in a circle, providing shots of part of the paving stones in order to produce a precise model of the bridge railings. This ensured that no information was missing from the model (no holes in the model). Fig. 3 is a schematic illustration of the shooting method.

The established capture approach can successfully be applied to the modelling of other masonry bridges with similar geometry.



Fig. 3. Visualisation of the exposure moments in terrestrial shooting

A total of 1012 images were obtained: 237 of the eastern façade, 161 of the western façade, 110 images of the underside of the arches, 471 of the pedestrian pavement and railings, and 33 photographs of the rhomboids symmetrically located around the main arch of the western façade of the bridge. The capturing of the façades was performed at a distance of 15 m, with a focal length of 18 mm, and a pixel size on the actual object $GSD = 0.45$ cm was obtained on the bridge façades.

Photogrammetric processing. Generating of a digital 3D model

Data processing was performed on an *Acer Swift 3 Ultrabook* with the following parameters: RAM - 8GB, Intel core i5 processor with a working frequency of 1.60GHz, NVIDIA GeForce MX 250 video card with 2GB of own memory and 4 GB of shared memory. The computer operating system was Windows 10 Professional, 64-bit.

The *Agisoft Metashape Version 1.8.4* software was used to process the terrestrial and aerial images.

A very important part is the selection of images to be used in the processing, as their quality determines the final results. Therefore, before starting the photogrammetric processing, it is necessary to review those carefully and select the most suitable ones. To create a three-dimensional model of the "Humpback" Bridge, a total of 1,251 terrestrial and aerial photographs were loaded and processed simultaneously into one Chunk.

Following the image assessment, a sparse cloud of points was created. The result of this processing step was a point cloud containing triangular positions of key points corresponding to the images. In many cases, UAVs are equipped with GPS/GNSS systems to measure external orientation parameters during the flight. In the presented case, the function for rough referencing of the model by camera coordinates was not selected. This was due to the technical parameters of the drone, specifically the lack of an RTK module and low positioning accuracy. The sparse point cloud was created at the high accuracy setting. This step took 3 hours and 4 minutes to process. The sparse cloud contains 2,304,529 points and can be seen in the figure below.



Fig. 4. Sparse point cloud

During the aerial survey of the bridge, 7 reference points were used for georeferencing the model. They were marked with square-shaped marks consisting

of contrasting squares. Four of the marks were placed on the paving stones in the pedestrian part of the bridge, and three in the bed of the man-made pool underneath. Their coordinates were measured in the BGS 2005 coordinate system using a *CHCNAV i50* GPS receiver. Afterwards, through the *BGS Trans* programme, they were transformed into the WGS 84 zone 35 system in order to be employed in the project. Geodetic altitudes were used for georeferencing the model.

The next standard stage in photogrammetric processing is recognising these seven reference points in the images.

Agisoft Metashape Professional software uses markers to indicate the locations of points in the images. The position of markers is determined by their coordinates in the images. To determine the spatial coordinates of the reference points, it is necessary to measure their image (planar) coordinates on at least 2 images. Metashape supports two approaches to marker placement: manual and guided marker placement. Manual approach implies that the marker projections should be indicated manually on each image. It should be noted that incorrect projection markers affect accuracy of the model. Manual marker placement does not require 3D model and can be performed even before image alignment. In the guided approach marker projection is specified for a single image only. Metashape automatically projects the corresponding ray onto the model surface and calculates marker projections on the rest of the photos where marker is visible. Marker projections defined automatically on individual photos can be further refined manually. Guided marker placement usually speeds up the procedure of marker placement significantly and also reduces the chance of incorrect marker placement. It is recommended in most cases unless there are any specific reasons preventing this operation [14].

Guided marker placement was implemented in the presented study. After the reference points were recognised, the adjustment equation parameters were set, and optimisation was performed. The root mean square error (the absolute accuracy of the model) was 0.004 m.

A dense point cloud is created after the adjustment completed. Metashape software tends to produce extra dense point clouds which are of almost the same density, if not denser, as LIDAR point clouds. A dense point cloud can be edited and classified within Metashape environment and used as a basis for such processing stages as build Mesh, build DEM, build /generate orthomosaic. The software also allows to export/ exporting of point clouds in formats compatible with other software [14].

The "Humpback" Bridge dense point cloud, containing 141,068,817 points, was created at the high precision setting and can be seen in the Fig. 5 below. The processing of this step was performed within 13 hours and 33 minutes.



Fig. 5. Visualisation of the dense point cloud for the whole object

The next standard stage of the photogrammetric processing is creating a polygonal model (Mesh). If the model is already georeferenced, it is not necessary to place a limit on the area in which to create a Mesh model. The software automatically generates this with the necessary detail and in the correct geometry [14].

For the object of study, the Mesh model was created from the dense point cloud by selecting a high value for accuracy. The processing of this step was performed within 9 hours and 13 minutes. The resulting model contains 20,074,615 triangles and can be seen in the Fig. 6 below.

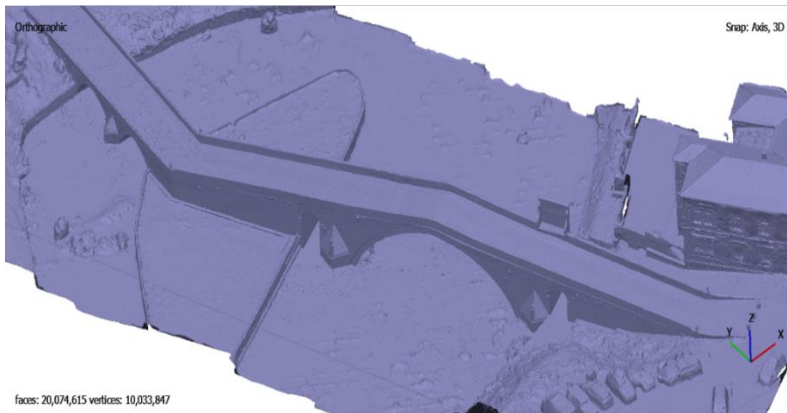


Fig. 6. Visualisation of the polygonal model (Mesh) of the bridge

The software offers a function for creating a three-dimensional textured model, which displays the geometric body in the full range of colours and textures.

Thereby, the object is actually recreated. The images are selected as output data, which allows building a colour texture map (diffuse map). The renderings below show the textured model of the bridge, as well as fragments of it.



A



B



C



D

Fig. 7. Visualisation of the created three-dimensional textured digital model of the "Humpback" Bridge and its fragments: (A) West façade; (B) Rhomboid on the left side of the large vault; (C) Lower side of the great arch; (D) North entrance

Conclusions

The generation of highly accurate 3D models, as an execution of already existing cultural monuments and other facilities is in itself a project for the conservation, restoration, adaptation, and socialisation of similar facilities.

The models of 3D digital visualisation can facilitate the communication, interpretation, and protection of traditional buildings and places which have gained significance for public heritage. Henceforth, cultural heritage can be interpreted in collaboration among residents, professionals, associated communities, and other stakeholders. 3D digital modelling can also provide new approaches for cultural heritage management. Digital modelling is not only used for data processing and

visualisation of buildings which are cultural monuments, but also helps giving meaning and direction of cultural heritage management [15].

The technological development of the devices and systems used for collecting information and the commercialisation of modern software products are prerequisites for the application of photogrammetric methods in various areas of life, such as agriculture and forestry, ecology, archaeology, architecture, mining, and other engineering application areas. The various modern commercial software solutions for photogrammetric processing make it easy to choose a program for image processing, and simplified work environments make handling them easier and easier. The possibility of combined processing of terrestrial and aerial images using the *Structure from Motion* (SfM) algorithm as the basis of a range of modern software products, such as *Agisoft*, *Pix4D*, *PhotoModeler* and others, allows easier work with images obtained from different distance from the object, at different angles of capture, and at different focal length. This is a significant advantage over traditional photogrammetric methods.

The application of unmanned aerial systems for civil purposes has opened new horizons for photogrammetry. The possibility of obtaining images from positions that are inaccessible or hard to be accessed by an operator, as well as the speed of operation, increase the interest in this type of technique.

With such advantages as low-cost equipment, high accuracy, and detail close-range photogrammetry remains a desirable and preferred photogrammetric capture method.

The collaboration between terrestrial and aerial photogrammetry opens up unlimited possibilities specialist from different areas to survey, map, and make 3D models of facilities with complex geometry.

The "Humpback" Bridge is in its essence such an object, whereupon the use of different types of images obtained from terrestrial and aerial photogrammetry, as well as the proven shooting methodology, allow the creation of a three-dimensional model of the facility. This accurate and detailed model gives a comprehensive idea of the object and its physical properties like dimensions, heights, colours, texture. All of the above are very important when planning future activities related to the restoration and adaptation of the bridge.

The model has been handed over to the Municipality of Harmanli as a conceptual project for the conservation of the "Humpback" Bridge.

References

1. Ivanova, R. How can we preserve our cultural and historical heritage to show it to the world and pass on to future generations?
2. Şeker, D., E. Avşar, U. Aydar, Modeling of Historical Bridges Using Photogrammetry and Virtual Reality. In: XXIII FIG Congress and XXIX General Assembly - Shaping the Change, October 8-13, 2006, Munich, Germany, 12 p.

3. Jáuregui, D., Y. Tian, R. Jiang, Photogrammetry applications in routine bridge inspection and historic bridge documentation. *Transportation Research Record: Journal of the Transportation Research Board*, 2006, 1958, 1, 24–32, doi:10.1177/0361198106195800103.
4. Altuntas, C., M. Pehlivanl, S. Kurban. Low-Cost 3D Imaging and Measurement Techniques for Documentation of Meram Masonry Arch Bridge in Turkey. *International Journal of Sensors and Sensor Networks*, 2017, 5, 5, 63–69.
5. Pepe, M., D. Costantino, UAV Photogrammetry and 3D Modelling of Complex Architecture for Maintenance Purposes: the Case Study of the Masonry Bridge on the Sele River, Italy. *Periodica Polytechnica Civil Engineering*, 2021, 65, 1, 191–203. doi:10.3311/PPci.16398.
6. Habeenzu, H., P. McGetrick, D. Hester, Towards automated UAV assisted bridge inspections using photogrammetry and image processing techniques. 2020, CERI 2020, Cork, Ireland. <http://www.cerai.net/page/7/home/index.htm>
7. Pinto L., F. Bianchini, V. Nova, D. Passoni, Low-cost uas photogrammetry for road infrastructures' inspection, *Int. Arch. Photogramm. Remote Sens. Spatial Inf. Sci.*, 2020, XLIII-B2-2020, 1145–1150, <https://doi.org/10.5194/isprs-archives-XLIII-B2-2020-1145-2020>.
8. Rau J., K. Hsiao, J. Jhan et al., Bridge crack detection using multi-rotary Uav and object-base image analysis, *Int. Arch. Photogramm. Remote Sens. Spatial Inf. Sci.*, 2017, XLII-2/W6, 311–318, <https://doi.org/10.5194/isprs-archives-XLII-2-W6-311-2017>.
9. Pepe, M., D. Costantino, N. Crocetto, A. Restuccia Garofalo, 3D modeling of roman bridge by the integration of terrestrial and uav photogrammetric survey for structural analysis purpose. *Int. Arch. Photogramm. Remote Sens. Spatial Inf. Sci.*, 2019, XLII-2/W17, 249–255, <https://doi.org/10.5194/isprs-archives-XLII-2-W17-249-2019>.
10. Zollini S., M. Alicandro, D. Dominici, R. Quaresima, M. Giallonardo, UAV Photogrammetry for Concrete Bridge Inspection Using Object-Based Image Analysis (OBIA). *Remote Sens.*, 2020, 12, 3180, doi:10.3390/rs12193180
11. Gospodinova, V., Application of Terrestrial and Aerial Photogrammetry and Laser Scanning in Mining. Sofia, “St.Ivan Rilski” Publishing house, 2020, 127, ISBN 978-954-353-416-6.
12. Gospodinova, V., R. Neycheva. Capturing of the *National Sports Academy* Stadium with an Unmanned Aerial System and Subsequent Comparison between Two of the Most Common Software Products, “Geodesy, Cartography, Land Development”, 2021, 5–6, 12–17.
13. <https://store.dji.bg/bg/dron-dji-mini-2.html>
14. Agisoft Metashape User Manual: Professional Edition, Version 1.8.4.
15. Hanan, H., D. Suwardhi, T. Nurhasanah, E. Santa Bukit, Batak Toba Cultural Heritage and Close-range Photogrammetry. *Procedia - Social and Behavioral Sciences*, 2015, 184, 187–195, doi: 10.1016/j.sbspro.2015.05.079

ТРИИЗМЕРНО МОДЕЛИРАНЕ НА МОСТ ЧРЕЗ ИНТЕГРИРАНЕ НА ЗЕМНА И ВЪЗДУШНА ФОТОГРАМЕТРИЯ, ПРИЛАГАЙКИ АДАПТИРАН НАЧИН НА ЗАСНЕМАНЕ

В. Господинова, Т. Тодоров

Резюме

Триизмерното фотограметрично моделиране е един съвременен дистанционен метод за изграждане на числени (цифрови) модели с присъщия им облик и текстура, които намират приложение в различни области от живота. Моделирането на обекти със сложна геометрия, такива като зидани мостове, е нелека задача поради специфичните им особености (в повечето случаи наличието на сводове и различни ниши), което предопределя и избора на адаптиран начин на заснемане спрямо индивидуалните характеристики на обекта. Статията представя изследване, целящо изграждането на високо точен триизмерен модел на мост, комбинирайки въздушно и земно заснемане. За заснемането на горната част на моста е използвана нискобюджетна безпилотна летателна система (БЛС), която значително оптимизира времето за заснемане. Но нейните възможности не позволяват заснемане на арките на моста отдолу нагоре, както и получаване на прецизен модел на перилата на моста. Поради това е извършено и наземно заснемане с цифров фотоапарат, което допълва необходимата информация за генерирането на цялостен модел на моста. Интегрирането на въздушно и земно заснемане, използвайки нискобюджетни апарати и системи, както и прилагането на съвременни алгоритми за обработка, позволяват създаването на автентични, точни и детайлни цифрови модели, което е от изключително значение при бъдеща консервация, реставрация, адаптация и социализация на такъв тип обекти - паметници на културата.

COMPOUND PRESECTOR FOR MULTISTATIC PASSIVE RADAR EMPLOYED IN REMOTE SENSING APPLICATIONS

Svetoslav Zabunov, Garo Mardirossian

Space Research and Technology Institute — Bulgarian Academy of Sciences

Keywords: *Multistatic Passive Radar, Passive Radar Front-end Preselector, Remote Sensing of Earth Ionosphere*

Abstract

Passive radars and multistatic passive radars in particular are gaining increasing attention. It is due to their effectiveness in detecting, tracking and identifying targets.

Multistatic passive radars are used in remote sensing observations of the Earth's ionosphere, meteors, space junk, etc. Another application is the detection and tracking of manmade objects and vehicles in the atmosphere or on the surface of the Earth.

The current paper discusses a hardware design approach applicable to the front-end of a multistatic passive radar receiver, namely a compound preselector. The preselector is a very important part of the radio receiver in cases where there are strong neighbouring signals in the radio band of operation. Such strong signals may overload the receiver or the low noise preamplifier and render the whole system dysfunctional. This article elaborates on a two-component preselector having very high rejection ratio to nearby emitters, still keeping the receiver simple and reliable.

The authors have registered several utility models on innovations in multistatic passive radars at Patent Office of Republic of Bulgaria.

Introduction

The multistatic passive radar is a type of a passive radar that employs more than one receiving antennas and/or more than one non-cooperative transmitters. The broader term “passive radar” on the other hand is a radar that relies on so called non-cooperating radio transmitters and does not have transmitters as part of its system [1]. The non-cooperative transmitters are transmitters that are maintained by other parties unknowingly of their use in the passive radar system. Such transmitters are also called transmitters of opportunity. Examples of non-cooperative radio transmitters are the FM/digital commercial broadcasting transmitters, communication networks base stations, etc.

Multistatic passive radars are implemented at tasks similar to other types of radars (Fig. 1). Nevertheless, their installation and maintenance costs are much lower [2]. Examples of passive radar applications are detection, ranging, identification and tracking of objects having radio frequency reflection properties. Such objects may

be of anthropogenic origin, such as airplanes, Earth surface vehicles, spacecraft, space junk or they may be naturally occurring objects such as meteors, aurora, the Earth's ionosphere, etc.

Lately, an elevated interest in the scientific community has been established towards passive radars as means of remote sensing instruments. Exploring near Earth space and its phenomena is possible using passive radars. Interest has been shown in observing meteors, space junk and the ionosphere of our planet.

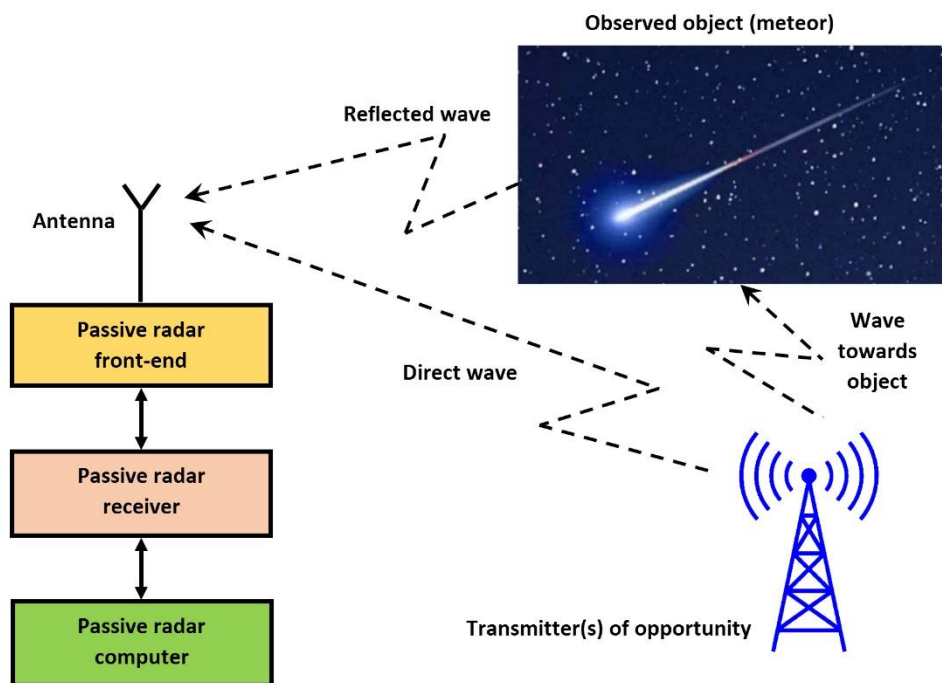


Fig. 1. Multistatic passive radar employing a compound preselector

There are plenty of transmitters of opportunity available for these purposes [3]. Some examples include the FM radio commercial broadcasting network [4, 5]. Other variant is the Digital Video Broadcast, either the terrestrial one (DVB-T) or the satellite based one (DVB-S) [6]. Another option is employing the cellular phone base stations. Still another possibility is to utilize the GPS signals and their reflections.

In Bulgaria, where the development of the proposed radar takes place, there are still functioning FM broadcasting transmitter not only located in the state's territory but also in neighbouring countries. Due to their low frequency of transmission FM broadcasting transmitters tend to be preferable transmitters

of opportunity for such targets as the ionosphere [7–9], where higher frequencies would render the observed object radio wave transparent.

Compound preselector design

A passive radar system, as already mentioned, does not involve the installation and maintenance of its own radio transmitters. The only apparatus such a system encompasses is a radio receiver or a multitude thereof. The receiver may employ only one antenna (single channel) or several channels. After receiving and digitizing the signal the receiver feeds it to a computer where computation takes place [10]. Passive radar needs to compare the direct signal coming from the transmitter of opportunity and the reflected signal coming as a reflection from the observed object [11].

The simplest possible receiver would employ a single antenna/channel and will be using this single channel for receiving both signals. Such a design is rather inefficient because it would need a very high dynamic range receiver and the computation needed for separation of the two signals will be very complex and with unsatisfactory results and quality. To avoid these drawbacks a general rule with passive radar designs is to implement at least two antennas. One of the channels is involved in reception of the direct signal and the other one – for listening to the reflected signal(s). By positioning the two antennas separated in space from each other and by employing directional antennas the system will obtain good separation between the two signals. Most multistatic passive radar systems employ three or more channels to benefit from optimal positioning of the antennas in respect to different transmitters of opportunity or possible directions of the incoming reflected signals.

Every radio receiver is prone to overloading on its input. When a very strong signal is present incident to the antenna a high voltage is induced in the antenna feed and enters the receiver. This situation may have two aspects:

1. The unwanted strong signal is out-of-band, i.e. its frequency is not very close to the receiving frequency and is essentially out of the band of reception. In this case the parasitic signal needs to be very strong to penetrate the input filter of the receiver. When this happens the receiver input shall be overloaded rendering the receiver non-functional.
2. The parasitic signal's frequency is close to the frequency of reception. This is called an in-band interference. The input filter of the receiver would admit the unwanted signal entering the receiver's input non-attenuated. Thus, the parasitic signal may either overload the input of the receiver easily, or lead to distortion and leaking into the received signal and degrade the reception.

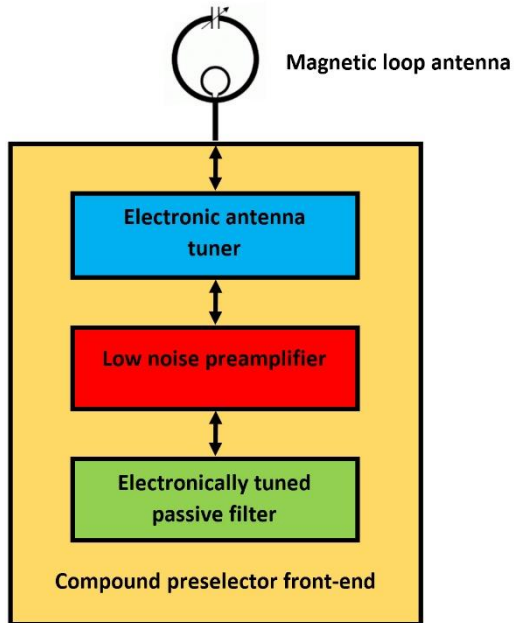


Fig. 2. Multistatic passive radar front-end consisting of a magnetic loop antenna, a two-stage preselector and a low noise preamplifier

In both cases a preselector should be used to attenuate the unwanted signal or signals to levels harmless for the normal operation of the receiver (Fig. 2). In the case of multistatic passive radars the operation is often taking place in bands where the transmitters of opportunity have strong signals. These signals are inherently in-band signals. They are capable of easily interfering with the reception. For this purpose, a sophisticated preselector is required [12, 13]. Such a preselector must also be simple to manufacture and operate and must have high efficiency and low noise. A way to achieve such a goal is to use a compound preselector consisting of two stages, the first stage of which is the antenna itself. Employing a high-Q factor antenna that is dynamically tuned will provide adequate efficiency and high selectivity. The tuning of the antenna must be electronic to achieve fast retuning and reliability. The filtered signal is then fed to a low noise preamplifier. Further, the signal enters the second stage of the preselector – an electronically tuned band-pass filter – where it is filtered again. The band-pass filter may consist of several components. The minimum filter order should be 4. The higher the order, the better the filtering, at the cost of increased complexity and cost. Such a receiver front-end guarantees very high dynamic range, extremely good rejection of unwanted signals that are in very close proximity by frequency to the received signal, low noise, low cost for manufacturing and maintenance, and high reliability.

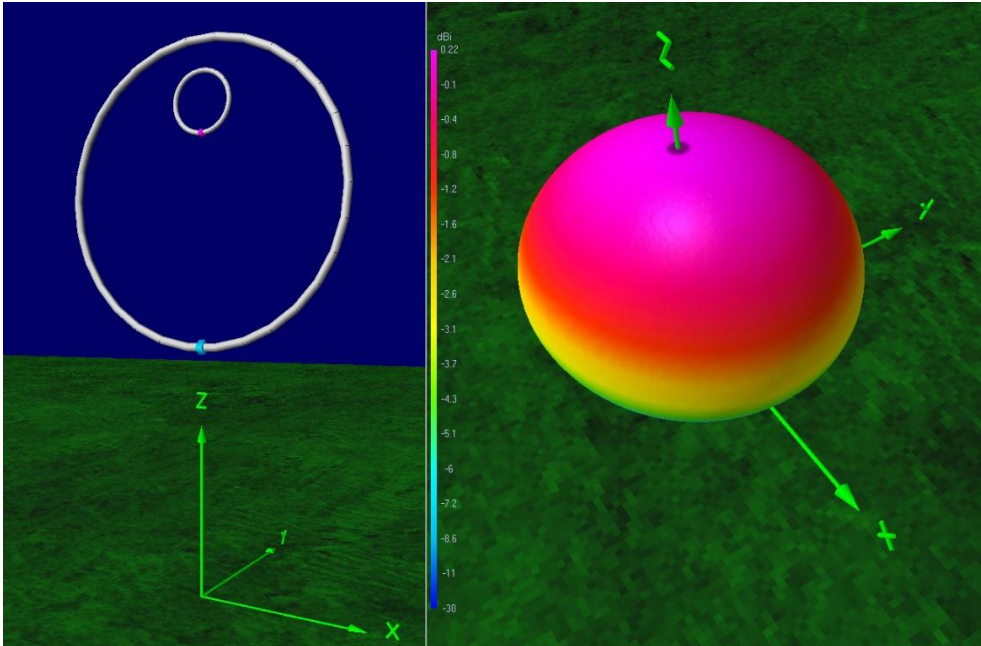


Fig. 3. Magnetic loop antenna represents the first stage of the compound preselector

Employing a magnetic loop antenna as a high-Q antenna that is easy to tune electronically is a good idea [14, 15]. This antenna has a number of benefits for the purpose of the multistatic passive radar such as deep nulls in its gain pattern, small size, preselector properties, easy to articulate using servos, small wind resistance, hard to spot by visual inspection, etc. The antenna was simulated using 4NEC2 free software for numerical antenna simulations. Some of the results in visual form are presented in Fig. 3 – the geometric electrical construction along with the antenna reception pattern is shown in the figure.

The principle electric schematic with only the essential components disclosed is presented in Fig. 4. The signal travels from left to right. The first component is the antenna shown as an inductor L-ANT. This inductor is tuned in resonance using electronic tuning component – varicap D1. Then the signal is amplified through a low noise preamplifier. After the preamplifier it is fed to a band-pass filter. This filter is also electronically tuned through the means of varicaps. Different orders for the filter are applicable. For clarity, Fig. 4 shows a 4th order band-pass filter consisting of two inductors L1 and L2 and two varicaps D2 and D3. Blocking capacitors are utilized to separate different stages of the circuit in regard to lower frequencies and the zero-frequency component. The varicaps are controlled by means of isolation resistors that have low capacity and high resistance.

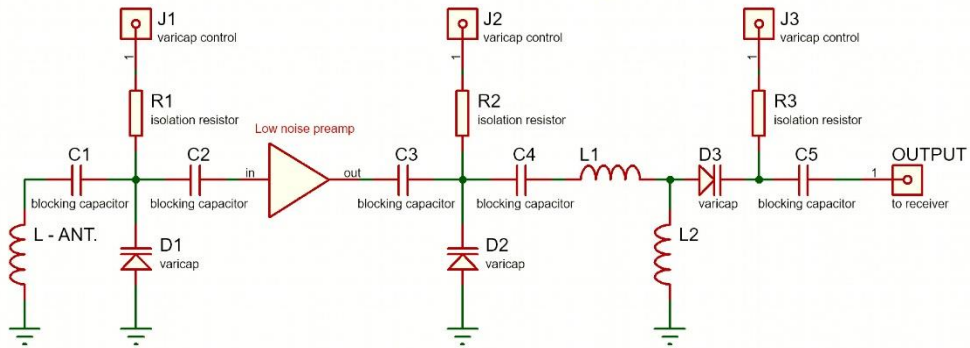


Fig. 4. Compound preselector principle electronic schematic

Conclusions

Multistatic passive radars are a fast-growing field of technological innovation and scientific research. Being appropriate for scientific observations in remote sensing applications, our team at the Space Research and Technology Institute – Bulgarian Academy of Sciences, has been profoundly involved in during the recent years. The Institute already has several registered utility models on different innovation aspects of multistatic passive radars [16–19].

Our future invention horizon aims at improvements in the hardware, novel approaches, and algorithms in the software, testing of modern supercomputing hardware for the purpose of computations, developing self-contained field-deployed base stations, improving the communications between base stations and data collecting servers, development, and design of antenna systems, etc.

Another field of work concerning multistatic passive radars in our Institute is their application in remote sensing observations of the Earth's ionosphere, especially from the location of our country Bulgaria, due to the fact the in our territory to our disposal we can utilize a large number of Bulgarian and foreign transmitters of opportunity. This fact follows from our country being relatively small with many neighbouring countries that haven't yet abandoned the FM radio broadcasting band.

References

1. Howland, P. E. "A Passive Metric Radar Using the Transmitters of Opportunity," *Int. Conf.on Radar*, Paris, France, May 1994, 251–256.
2. Carson, S., Kilfoyle D., Potter M. and Vance J. "A passive, multi-static radar system," *2007 IET International Conference on Radar Systems*, Edinburgh, UK, 2007, pp. 1–4, doi: 10.1049/cp:20070497.
3. RADIO SPECTRUM DISTRIBUTION PLAN, Communications Regulation Commission, Republic of Bulgaria, 2019, https://crc.bg/files/_bg/647.pdf

4. Malanowski, M., Kulpa K. S., Kulpa J., Samczynski P., Misiurewicz J. "Analysis of the detection range of FM-based passive radar," *IET Radar, Sonar & Navigation*, Volume 8, Issue 2, February 2014, p. 153–159, DOI: 10.1049/iet-rsn.2013.0185.
5. Howland, P. E., Maksimiuk D., Reitsma G. "FM radio based bistatic radar," *Radar, Sonar and Navigation*, IEE Proceedings, Vol. 152, Issue 3, 3 June 2005, pp. 107–115.
6. Brisken, S., Moscadelli M., Seidel V. and Schwark C., "Passive radar imaging using DVB-S2," *2017 IEEE Radar Conference (RadarConf)*, Seattle, WA, 2017, pp. 0552-0556, doi: 10.1109/RADAR.2017.7944264.
7. Lind, F. D., Erickson P. J., Coster A. J., Foster J. C., Marchese J. R., Berkowitz Z., Sahr J. D. "Intercepted signals for ionospheric science," *Radio Science*, vol. 48, pp. 248–264.
8. Chernogor, L. F., Garmash K. P., Guo Q., Rozumenko V. T., Zheng Y. "Passive Radar for Oblique-Incidence Ionospheric Sounding: Observations of Ionospheric Storms," *2020 IEEE Ukrainian Microwave Week (UkrMW)*, Kharkiv, Ukraine, 2020, pp. 253–258.
9. Sahr, J. D., Gidner D. M., Chucui Zhou, Lind F. D. "Passive VHF radar for ionospheric physics," *Journal of Atmospheric and Solar-Terrestrial Physics*, vol. 63, issues 2–3, 2001, pp. 117–122.
10. Pölönen, K. "Signal Processing Methods for Multicarrier Passive Radar and Communication Systems," *Doctoral dissertation 69/2016*, Alto University publication series, 13.May.2016.
11. Meyer, M. G., Sahr J. D. "Passive coherent scatter radar interferometer implementation, observations, and analysis," *Radio Science*, vol. 39, RS3008, pp. 1–10.
12. Garry, J. L., Baker C. J. and Smith G. E. "Evaluation of Direct Signal Suppression for Passive Radar," *IEEE Transactions on Geoscience and Remote Sensing*, vol. 55, no. 7, pp. 3786–3799, July 2017, doi: 10.1109/TGRS.2017.2680321.
13. Cutsogeorge, G. "*Managing Interstation Interference with Coaxial Stubs and Filters (2nd ed.)*," Aptos, CA: International Radio Corporation. P. 75.
14. Kraus, J. "*Antennas 2nd Ed.*," MacGraw Hill, 1988.
15. Carr, J. J. "*Practical Antenna Handbook, fourth ed.*," McGraw-Hill, p. 625.
16. Zabunov, S., Mardirossian G., Nedkov R. "Recent Innovations in Circularly Polarized Antennas for Drone Radio Communication," *Comptes rendus de l'Academie bulgare des Sciences*, 2020, vol. 73, no. 9, pp. 1286–1290.
17. Zabunov, S., Mardirossian G., Nedkov R. "MULTISTATIC PASSIVE RADAR," *Patent Office of Republic of Bulgaria*, 2020, <https://portal.bpo.bg>, utility model #3928/29.10.2020
18. Zabunov, S., Mardirossian G., Getsov P., JeleV G. "INTERNET-OF-THINGS STATIONS SYSTEM FOR PASSIVE RADAR," *Patent Office of Republic of Bulgaria*, <https://portal.bpo.bg>, 2022, utility model #4279/08.07.2022
19. Zabunov, S., Mardirossian G., Getsov P., JeleV G, Vasev V. "MULTISTATIC PASSIVE RADAR WITH MAGNETIC LOOP ANTENNA," *Patent Office of Republic of Bulgaria*, 2022, <https://portal.bpo.bg>, utility model #4337/25.10.2022

СЪСТАВЕН ПРЕСЕЛЕКТОР ЗА МУЛТИСТАТИЧЕН ПАСИВЕН РАДАР ЗА ДИСТАНЦИОННИ ИЗСЛЕДВАНИЯ

С. Забунов, Г. Мардиросян

Резюме

Мултистатичните пасивни радары се използват за дистанционни изследвания на земната йоносфера, следене на метеори, космически боклук и др. Друго приложение е при откриване и следене на антропогенни обекти и средства, които летят в атмосферата, Космоса или се намират на повърхността на Земята.

Настоящата статия дискутира подход при хардуерната конструкция на входното звено на мултистатичен пасивен радар, а именно преселекторът. Той се явява много важна част от радиоприемника в случаите, когато са налични силни сигнали с близка до приеманата честота в радиообхвата, в който се извършват наблюденията. Такива силни и близки по честота сигнали могат да пренатоварят (наситят) приемника и/или ниско шумовия предусилвател. Такова пренасящане би довело до неработоспособност на приемника, а оттам и на цялата радарна система. Публикацията обсъжда идеята за преселектор, състоящ се от две звена, който има много високо отношение на желание към нежелания радиосигнал. Нежеланият сигнал се намира в честотно измерение много близо до желаните. Предложеното решение запазва ниска степен на сложност на хардуерната конструкция на приемника и така гарантира висока надеждност на работа и ниска цена за изработка и настройка.

USE OF LOW-POWER UNMANNED AERIAL VEHICLES FOR CONTROL OF AN URBANIZED AREA

Ivan Ivanov

*“Georgi Benkovski” Bulgarian Air Force Academy
e-mail: IKIvanov@af-acad.bg*

Keywords: UAV, UAS, Urbanized area, Crisis events

Abstract

The article presents an analysis of the current classification of unmanned aerial systems according to the European Aviation Safety Agency related to the use of unmanned aerial vehicles for urban area monitoring. The possible tasks solved by unmanned aerial vehicles in an urbanized area were investigated. An analysis of the crisis events – floods, fires, and landslides in the Pleven region of the Republic of Bulgaria for the period from 2010 to 2020 was made and a model for the use of unmanned aircraft was proposed.

Introduction

Under the control of an urbanized area using unmanned aerial vehicles (UAVs) in this article should be understood the processes of monitoring and management of objects and parameters in specific conditions of the situation in this area. Control can be permanent, periodic, and episodic.

Ground-based measuring stations and/or long-duration fixed-wing unmanned aerial vehicles are sufficient for continuous monitoring. Periodic and episodic control of an urbanized area is carried out in a certain period of time, in a critical situation, with fixed-wing and rotary-wing unmanned aerial vehicles. Low-power UAVs of the “multicopter” type are suitable for periodic and episodic monitoring of an urbanized area.

The tasks of UAVs for aerial surveillance in an urbanized area require knowledge of the specifics of the objects, the environmental conditions, the capabilities of the UAVs and the requirements for the extracted information.

Problem status and area of research

The crisis situations in the Pleven region of the Republic of Bulgaria are investigated, using data from the National Statistical Institute. The classification of

unmanned aerial systems (UAS) regulated by the European Aviation Safety Agency and scientific articles have been used to define the tasks of UAVs in urbanized areas.

There are various classifications of UAVs and UASs in the scientific press. With the adoption of regulation [1], the requirements for the design of UAVs with a maximum take-off mass of up to 25 kg are fulfilled by using a marking with the designation “CE”, which applies to products sold in the European Union. All UAS that are placed on the market also have a number between 0 and 6, which defines the class of the UAS (C0, C1, C2, C3, C4, C5 and C6). The UAS classes presented in Table 1 [1] are regulated for the European Union.

Table 1. UAS classes

	Unlimited category						
	C0 	C1 	C2 	C3 	C4 	C5 	C6 
Max. Take Off Mass	<250 g	< 900 g or max.kinetic energy<80J	<4 kg	< 25 kg	< 25kg	< 25 kg	< 25 kg
Max. speed at flight	19 m/s	19 m/s	not applicable	not applicable			< 50 m/s
Max. height of flight	120 m	120 m	120 m	120 m		not applicable	not applicable
Loss of connection	not applicable	A reliable procedure to restore the connection	A reliable procedure to restore the connection	A reliable procedure to restore the connection			
Power supply	electrical	electrical	electrical	electrical			electrical or other
Distance from pilot in mode “follow me”	50 m	50 m if equipped	not applicable	not applicable			
Identification	not applicable	Unique serial number and remote identification	Unique serial number and remote identification (unless tied down)	Unique serial number and remote identification (unless tied down)			
Geo-restriction	not applicable	Mandatory	Mandatory	Mandatory		if equipped	if equipped

From the presented requirements for the classification of UAS, it is established that they can be used for periodic and episodic control in an unlimited category of use, and the low-power ones will be in classes C0, C1, C2 and C3.

The advantages of low-power UAVs are safety, flexibility, and a variety of sensors on board. Safety is concerned with the preservation of human life in flights to perform dangerous missions for the pilot on board. Their flexibility in performing certain tasks is increased. UAVs can better maneuver in small spaces and can even fly into buildings. They are able to take off at any time and deliver the necessary information in a short time. Different sensors such as digital, high-quality video cameras combined with infrared sensors provide their day and night monitoring capabilities. Sensors for various gases facilitate the study of the environment.

Possible uses of UAS for civilian application can be in six areas: disaster response and management; national security; critical infrastructure protection; communications missions; environmental protection; scientific-research activity [2].

In these application areas, low-power UAVs can perform tasks in urbanized areas presented in Fig. 1.

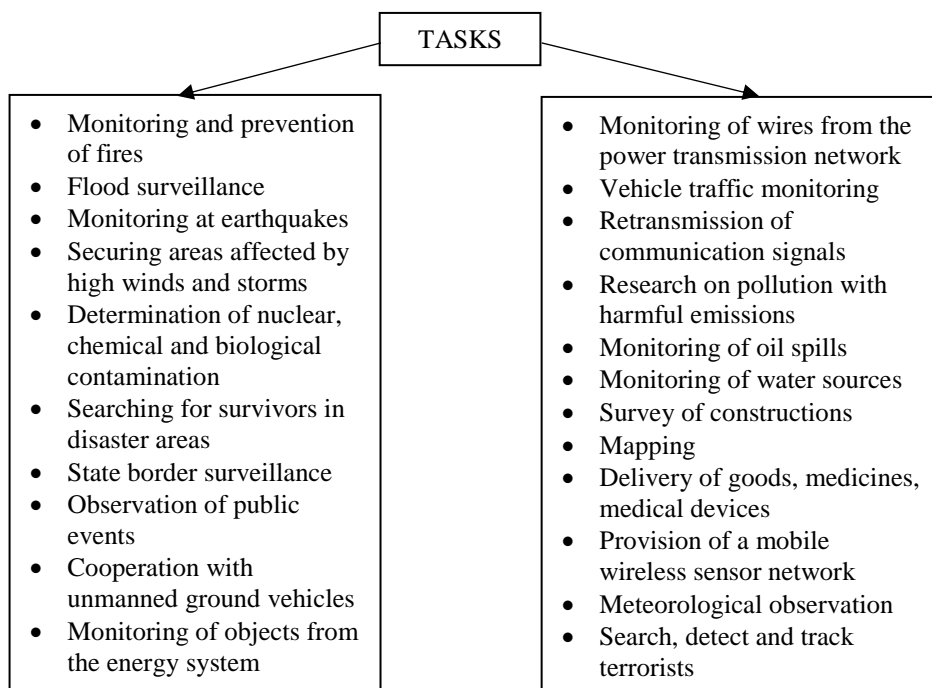


Fig. 1. Possible tasks to be performed by low-power UAVs in an urbanized area

The urbanized territory of Pleven region is 254.58 km² and constitutes 5.47 % of its total territory [3]. In Fig. 2 are presented data from [4] about floods in the Pleven region for the period from 2010 to 2020.

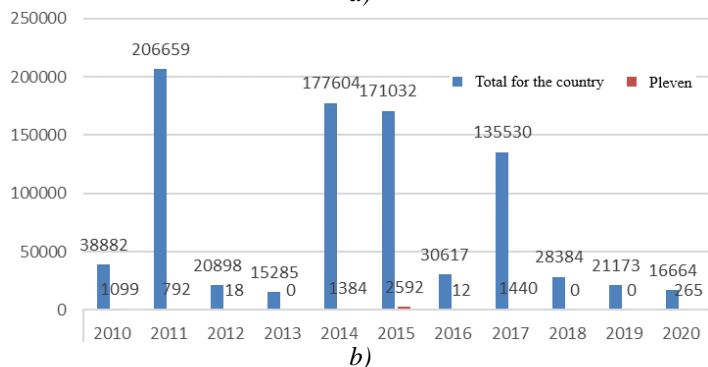
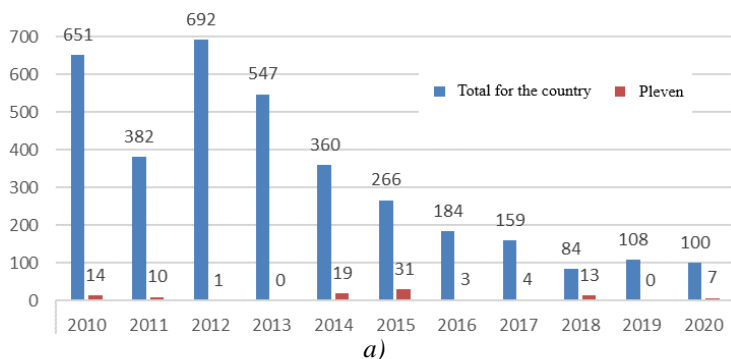
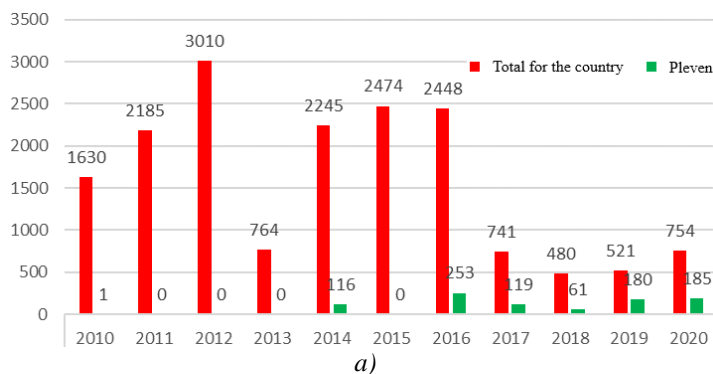


Fig. 2. Floods in Plevna region 2010 – 2020: a) Number; b) Established damages – thousands of BGN

The number of floods in the Plevna district compared to that of the country is relatively small. Their average annual number for the considered period is 11. The established damages were maximum in 2015 – BGN 2,592,000, while the annual average for the period was BGN 950,000.



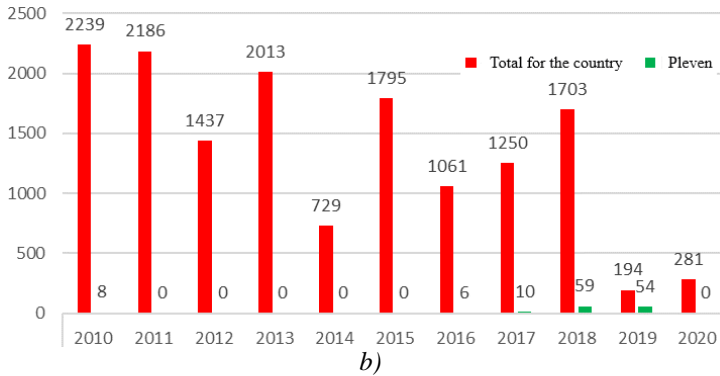


Fig. 3. Fires in Plevan region 2010–2020: a) Number; b) Established damages—thousands of BGN

In Fig. 3 are shown the number and established damages of the fires in Plevan region [4].

In the last four years of the considered period, the fires in the Plevan district have a relatively large share of those in the country. The established damages from fires were the largest in 2018 and 2019 and reached BGN 59,000.

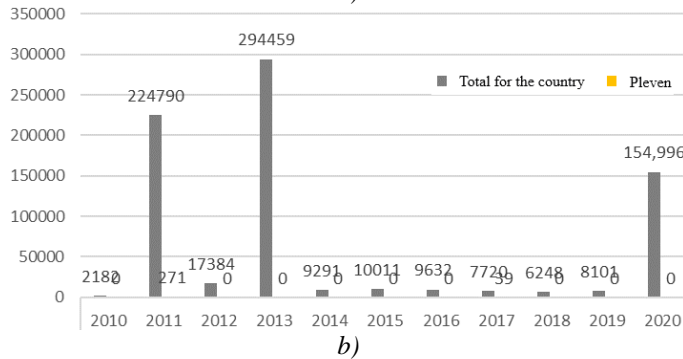
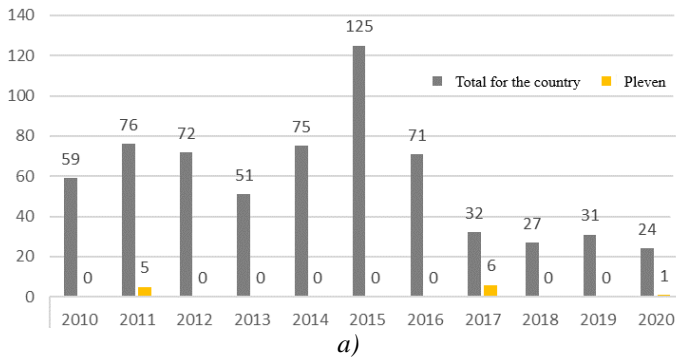


Fig. 4. Landslides in Plevan region 2010–2020: a) Number; b) Established damages – thousands of BGN

The data on landslides in Pleven region for the period 2010–2020 are presented in Fig. 4 [4].

A total of 12 landslides were registered for the Pleven region for the period under review, with the established damages amounting to BGN 310,000.

To control an urbanized area, a system can be built with a structure presented in Fig. 5.

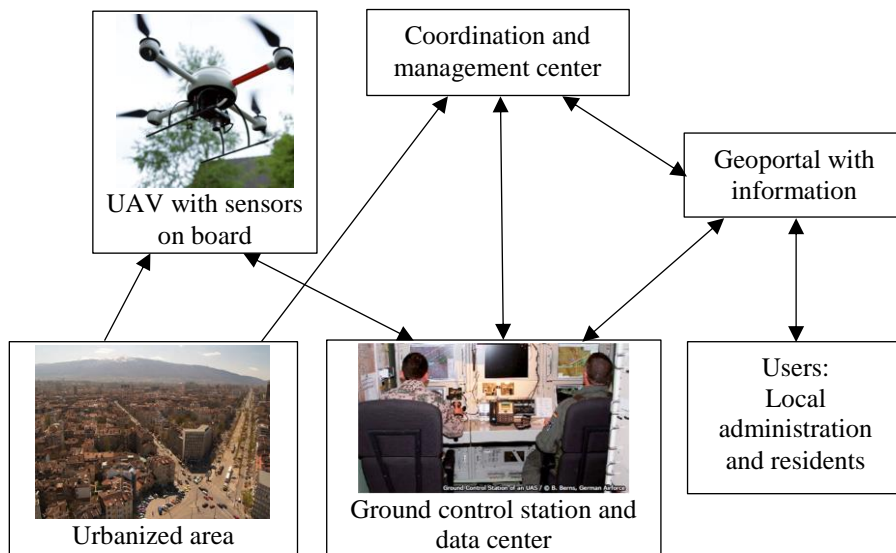


Fig. 5. Structure model of an urbanized area control system

Unmanned aerial vehicles must be sufficient in number so that with their characteristics they can perform their tasks in an urbanized area of a certain size [2, 5–8]. The sensors on board the UAV need to be suitable for the task at hand. The control station and data center need to have the capability to maintain the UAV, process the data and transmit it for visualization to the users. The coordination and management center is permanently based and coordinates the activity of the mobile groups equipped with UAVs.

According to [9], an electric powered multicopter has characteristics presented in Table 2.

Table 2. Technical characteristics of a multicopter

	Electric powered multicopter	
	hover mass	hang time/battery mass
Payload mass 5 kg	25 kg	1 h/7,5 kg 0,5 h/3,75 kg
Payload mass 1 kg	5 kg	1 h/1,5 kg 0,5 h/0,75 kg

For unmanned platforms, UAV multicopter type with electric power supply classes C0, C1, C2, C3 with a maximum take-off mass of up to 25 kg are suitable.

For monitoring objects and researching environmental parameters, it is appropriate to use: UAV multicopter type with a payload of at least 1 kg, wind resistance up to at least 10 m/s, with a built-in camera and image stabilization system and sensors registering the monitored parameters of the environment. To reduce costs and increase the number of UAVs, it is possible to use C0, C1 and/or C2 class multicopters with a maximum take-off mass of up to 4 kg. Examples of such quadcopters are: for C1 - MD4-200 [10], for C2 - DJI Phantom 4 Pro [11] and for C3 - MD4-1000 [12] (Fig. 6).



Fig. 6. Types of quadcopter models

The coordination and management center for the Pleven region should be based in the area of the “Georgi Benkovski” Bulgarian Air Force Academy in the city of Dolna Mitropolia. The mobile groups, consisting of a motor vehicle, 3 drones and a ground control station can be located in the outsourced aviation education complex of the Bulgarian Air Force Academy in the city of Pleven.

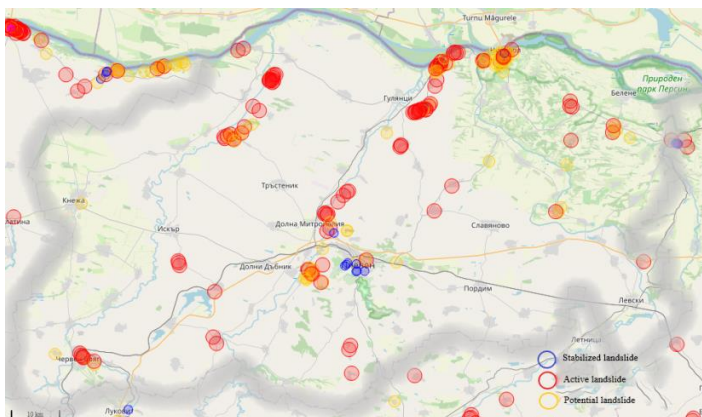


Fig. 7. Map of landslides in Plevan region

In Fig. 7 are shown the landslides in Plevna region [13]. A possible urbanized area for UAV survey is an active landslide and dam near the village of Gorni Dabnik.

The observation route of the designated area is presented in Fig. 8.



Fig. 8. Survey route

The route is 22311 m long. The UAV is a multicopter flying at a speed of 10 m/s at 50 m above the terrain of the area. The farthest point on the planned route is at a distance of 3050 m from the take-off position, which is within the range for telemetry control and data transmission for this area. The estimated time to complete the mission is 51 minutes and 38 s including take-off, en-route flight, and landing. Provided that the task is performed with low-power UAVs with electric power, their flight time is usually 30 min. The above-mentioned circumstances give reason to state that two multicopters flying on different parts of the route will successfully fulfill the task of monitoring an area with a possible manifestation of a crisis situation. In case of loss or major damage of the UAV, it is necessary for the mobile team to have at least one spare UAV.

Conclusion

The variety of tasks that low-power UAVs of the “multicopter” type can perform to save and improve people's lives requires the construction in a given area of a system of UAVs with the possibility of a wide range of sensors on board. The information provided by the UAV, after processing, analysis, and summarization, will be used to make informed decisions by the local authority and for good awareness of the residents of a certain urbanized area. A good practice would be the exchange of information between such systems built in other urbanized areas.

Acknowledgments

The research in this article was carried out in fulfillment of Task 3.1.9. “Construction of a network of autonomous low-powered aerial devices (quadcopters) for control of an urbanized area” by the National Scientific Program “Security and Defense”, adopted by RMS No. 731 of 21.10.2021. and according to Agreement No. D01-74/19.05.2022.

References

1. Commission Delegated Regulation (EU) 2019/945 of 12 March 2019 on unmanned aircraft systems and on third-country operators of unmanned aircraft systems. <https://eur-lex.europa.eu/legal-content/BG/TXT/?uri=CELEX%3A02019R0945-20200809&qid=1622455917814> (11 January 2023).
2. Skrzypietz Therese. Unmanned Aircraft Systems for Civilian Missions. BIGS Policy Paper No.1, February 2012. <https://www.bigspotsdam.org/en/research/completed-projects/the-use-of-uas-for-civilian-missions> (11 January 2023).
3. National Statistical Institute (NSI) BG. Balans na teritoriyata na Republika Bŭlgariya kum 31.12.2021 godina. www.nsi.bg (11 January 2023) (in Bulgarian).
4. <https://www.nsi.bg> (11 January 2023).
5. Noor, Norzailawati, A. Abdullah, M. Hashim. Remote sensing UAV/drones and its applications for urban areas: a review. IOP Conference Series: Earth and Environmental Science, 2018, 169, 012003. DOI: 10.1088/1755-1315/169/1/012003.
6. Hildmann, H., Ernő Kovacs. Review: Using Unmanned Aerial Vehicles (UAVs) as Mobile Sensing Platforms (MSPs) for Disaster Response, Civil Security and Public Safety, Drones, 2019, 3, 59. doi: 10.3390/drones3030059.
7. Single European Sky ATM Research 3 Joint Undertaking. European drones outlook study: unlocking the value for Europe. Publications Office, 2017. <https://data.europa.eu/doi/10.2829/085259> (11 January 2023).
8. Penev, P. Osnovi i prilagane na vazdushnata mosht. VA, 2012, 155–157 (in Bulgarian).
9. Getsov, P., W. Bo, D. Zafirov et. al. An unmanned aerial surveillance system in urban environments. Aerospace Research in Bulgaria, 2017, 29, 94–110.
10. Mika, Pat. Emergency Service Use of UAS. 2009/2010 UAS Yearbook - UAS: The Global Perspective - 7th Edition - June 2009, 138–224.
11. Phantom 4 pro v2.0, DJI Technology Co. Ltd., <https://www.dji.com/phantom-4-pro-v2> (11 January 2023).
12. <https://www.homelandsecurity-technology.com/projects/microdrones-md4-1000-uav/> (11 January 2023).
13. <http://gz-pleven.mrrb.government.bg> (11 January 2023).
14. Peleshko, D., T. Rak, J. R. Noennig, V. Lytvyn, V. Vysotska. Drone Monitoring System DROMOS of Urban Environmental Dynamics. IPTM, 2020, 178–193.

ИЗПОЛЗВАНЕ НА МАЛОМОЩНИ БЕЗПИЛОТНИ ЛЕТАТЕЛНИ АПАРАТИ ЗА КОНТРОЛ НА УРБАНИЗИРАН РАЙОН

И. Иванов

Резюме

Статията представя анализ на съвременната класификация на безпилотни авиационни системи според Европейската агенция за авиационна безопасност, свързан с използването на безпилотни летателни апарати за мониторинг на урбанизиран район. Изследвани са възможните задачи, решавани с безпилотни летателни апарати в урбанизиран район. Направен е анализ на кризисните събития – наводнения, пожари и свлачища в област Плевен на Република България за периода от 2010 г. до 2020 г. и е предложен модел за използване на безпилотни летателни апарати за тази цел.

MODELING AND STUDY THE DISTRIBUTION OF OPERATOR ATTENTION IN CONTROLLING THE LATERAL MOVEMENT OF AN UNMANNED AERIAL VEHICLE

Peter Getsov

*Space Research and Technology Institute – Bulgarian Academy of Sciences
e-mail: getsovp@mail.space.bas.bg*

Keywords: “Operator-UAV” system, Distribution of visual attention, Transverse movement of the UAV, Stabilization of the course, heel and distans

Abstract

The report examines the transients in the system "Operator-Unmanned Aerial vehicle" in case of external disturbing influences. A model of the system in the system "MATLAB Simulink" has been developed, taking into account the distribution of the visual attention of the Operator. The parameter area of the transmission functions of the Operator is defined depending on the switching of attention.

Introduction

In recent years, Unmanned Aerial Vehicles (UAVs) have been increasingly used both in warfare and for civilian tasks in various areas of economic activities, which requires systematic analysis and synthesis in their construction and operation.

The study of the "Operator-UAV" system can be carried out by modeling and analytical study of the control loop of the UAV Operator, consisting of three units (blocks) [1] and using the transmission functions of the UAV derived from the linearized system equations describing the aerodynamics of the UAV (Fig. 1).

According to a Diamantidis transmission function [2,3]

$$(1) \quad W_{on}(p) = W_1(p) \cdot W_2(p) \cdot W_3(p) = k_{on} e^{-n\tau p} \frac{T_1 p + 1}{(T_2 + 1)(T_3 + 1)},$$

where:

$$W_1(p) = e^{-n\tau p}; \quad W_2(p) = k_{op} \frac{T_1 p + 1}{(T_2 + 1)}; \quad W_3(p) = \frac{1}{(T_3 + 1)},$$

n – parameters, controlled by the operator;

τ – delay in receiving information on one parameter only;

k_{op} – amplification factor (transmission factor) of operator.

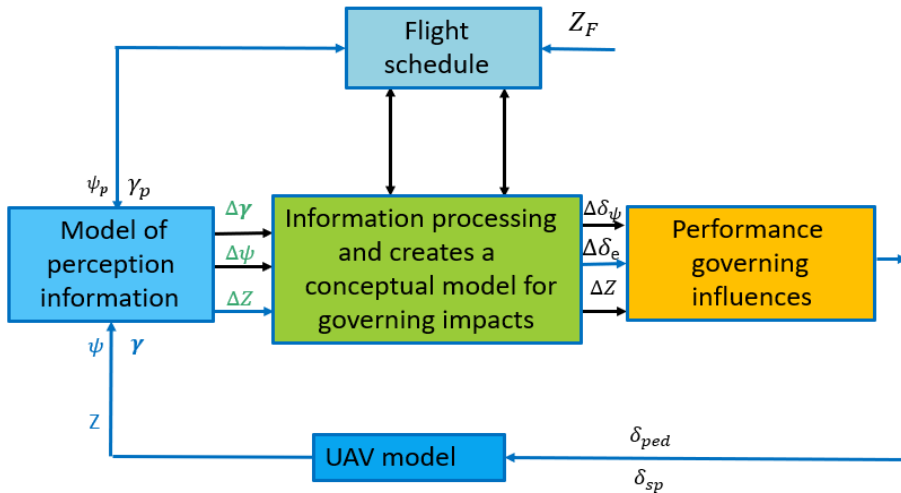


Fig. 1. Conceptual model for the study of the Operator

The delay block $W_1(p) = e^{-n\tau p}$ is characterized by time τ (s) for excitation of receptors, passage of the excitation signal to the nervous system, interpretation of the received information.

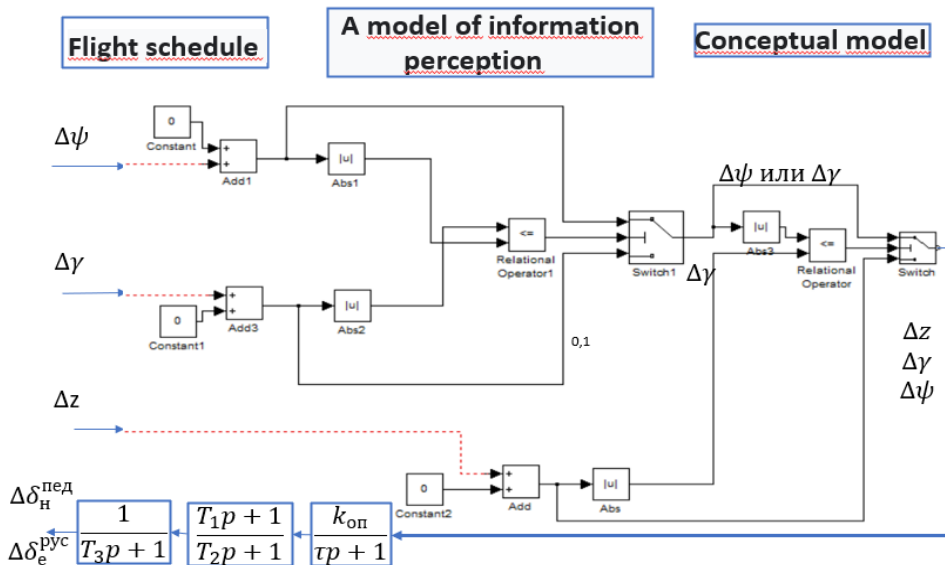


Fig. 2. Model of the distribution of the visual attention of the Operator

The second block $W_2(p) = k_{op} \frac{T_1 p + 1}{(T_2 + 1)}$ is corrective and it reflects the ability of a person to self-tune and adjust to the dynamic characteristics of the other units of the loop and to the spectral characteristics of the input signal. The adjustment is done by the variation of k_{op} , T_1 and T_2 .

The third block (neuro-muscular) $W_3(p) = \frac{1}{(T_3 + 1)}$ reflects the delay between the entry of the command into the neuromuscular system and the muscular impact on the control lever.

The modelling of switching the attention of the Operator can be accomplished by comparing the relative values of the course, heel and lateral bias by the choice of the dominant value of the specified parameters with the help of the UAV model in a “MATLAB Simulink” system (Fig. 2) [5, 6].

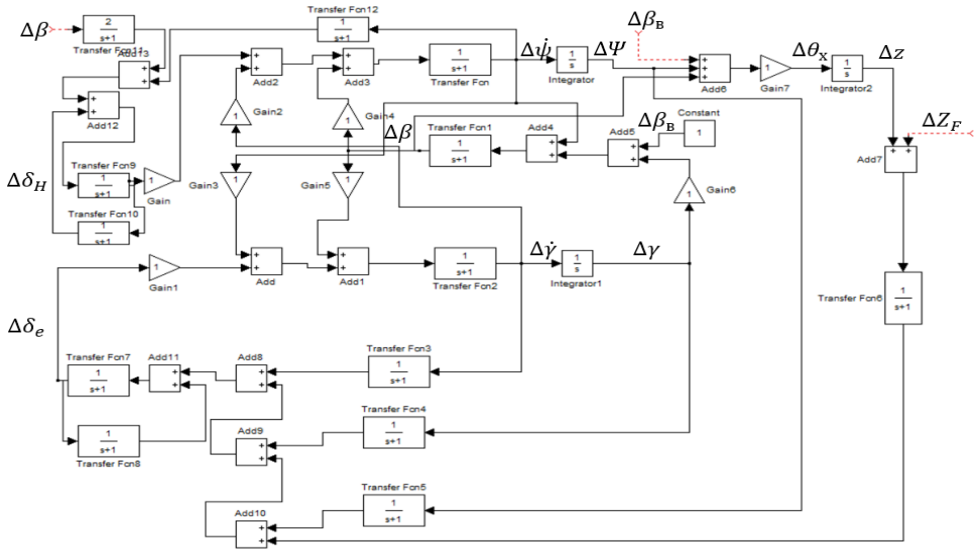


Fig. 3. BLA continuous motion model in MATLAB Simulink environment

The equations for the transverse motion of the UAV are obtained by a Laplace transform of the Eulerian equations [4]:

$$(2) \quad \begin{cases} (p + a_z^\beta) \Delta\beta(p) - p\Delta\psi(p) + a_z^\gamma \Delta\gamma(p) = 0; \\ a_{m_y}^\beta \Delta\beta(p) + (p^2 + a_{m_y}^{\omega_y} p) \Delta\psi(p) + a_{m_y}^{\omega_x} p \Delta\gamma(p) = a_{m_y}^{\delta_H} \Delta\delta_H(p); \\ a_{m_x}^\beta \Delta\beta(p) + (p^2 + a_{m_x}^{\omega_x} p) \Delta\gamma(p) + a_{m_x}^{\omega_y} p \Delta\psi(p) = a_{m_x}^{\delta_e} \Delta\delta_e(p), \end{cases}$$

The proposed model allows the study of transients in external interference effects (single stepping signal; random stepping signal with white noise distribution and periodic stage) (Fig. 6).

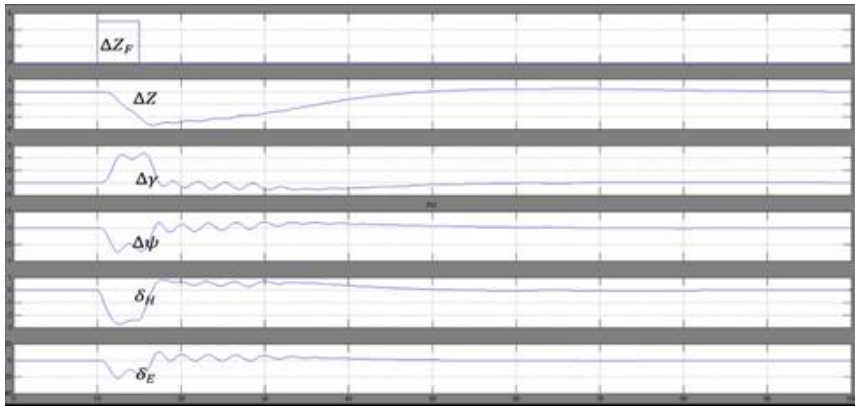


Fig. 6. Transient processes of UAV under external disturbance

From experiments they found that there is a possibility to determine the zones of the distribution of attention between the aviohorizont (γ), the compass (P_{Si}), distans (z) (Fig. 7).

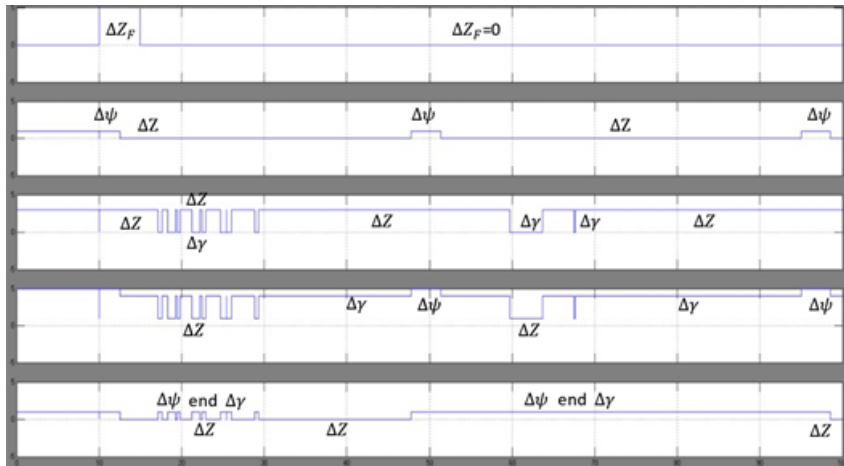


Fig. 7. Areas of distribution of visual attention

In Table 1, Table 2 and Fig. 8 the dependence of the number of switches on the parameters of the transmission function of the Operator shown distribution of $N_{(1,2)_{so}} = f_{(1,2)}(k_{op}, \tau, T_1, T_2, T_3)$ attention, where 1, 2 are Rudder Channel and Aileron Channel respectively.

Table 1. Switching visual attention in the direction rudder channel $n_1 = f_1(X_{1so})$

N \ f(x)	0.1	0.2	0.3	0.4	0.5	0.6	0.7	0.8	0.9	1
$N_{\delta_H} = (K_{on})$	33	32	31	24	22	19	17	12	10	9
$N_{\delta_H} = f(\tau)$	22	19	18	16	14	13	13	13	13	13
$N_{\delta_H} = f(T_1)$	14	13	13	13	14	14	16	18	18	19
$N_{\delta_H} = f(T_2)$	65	58	58	53	40	39	33	27	25	23
$N_{\delta_H} = f(T_3)$	25	19	19	25	16	16	14	14	13	13

Table 2. Switching visual attention in the aileron channel $n_2 = f_2(X_{2so})$

N \ f(x)	0.1	0.2	0.3	0.4	0.5	0.6	0.7	0.8	0.9	1
$N_{\delta_e} = (K_{on})$	20	20	22	19	19	17	18	16	14	11
$N_{\delta_e} = f(\tau)$	19	18	19	21	19	19	18	18	19	21
$N_{\delta_e} = f(T_1)$	21	21	21	21	21	21	21	21	21	19
$N_{\delta_e} = f(T_2)$	19	19	19	19	19	19	21	18	20	18
$N_{\delta_e} = f(T_3)$	21	18	19	21	19	19	18	18	17	21

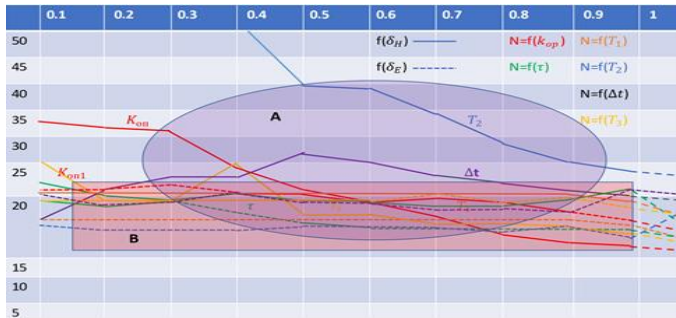


Fig. 8. Distribution of visual attention depending on the condition of the Operator

Areas (A) and (B) show plots of the distribution of visual attention as a function of variation in the parameters of the Operator's transfer functions for the rudder channel and ailerons, respectively.

Conclusions

1. The developed linear model of the longitudinal channel of the “Operator-UAV” system in a MATLAB-Simulink environment makes it possible to study the transients under external disturbing and controlling influences.

2. On the basis of the developed model, the optimal parameters of the distribution of visual attention between the aircraft horizon and the altimeter in horizontal flight are determined, depending on the preparedness and individual qualities of the Operator.

3. The proposed conceptual model to determine the disagreement of managed parameters, information processing and the implementation of managing impacts can be used as an element of artificial intelligence in the automatic management of UAVs.

Acknowledgments: This article was prepared within the framework of project t.1.1.6 of the National Science Program “Security and Defense” (adopted with PMS No 731 of 21.10.2021) and according to Agreement No. D01-74/19.05.2022 between the Ministry of Education and Science and Defense Institute “Professor Tsvetan Lazarov”.

References

1. Kashkovskiy, V. V., I. I. Tihiy, Y. Shishkin, Identification of dynamic models of pilot parameters from data of on-board recording device, Journal of Tomsk State University, 2004 (in Russian).
2. Yordanov, D. V., P. S. Getsov, S. P. Getsov, Modelling and research of pilot-aircraft systems, Autoprint-Plovdiv, 2019 (in Bulgarian).
3. Dobrolenskiy, Y. P., N. D. Zavyalova, V. A. Ponomarenko, V. A. Tuvaev, Methods of engineering-psychological research in aviation, ed. “Mechanical Engineering”, Moscow, 1975 (in Russian).
4. Kashkovskiy, V. V., Field Control Systems of Manned Aircraft, VVIA Publication “N. E. Zhukovsky”, 1971 (in Russian).
5. Getsov, P., Wang Bo, Sv. Zabunov, G. Mardirossian, Innovations in the area of unmanned aerial vehicles, Aerospace Res. in Bulgaria, 29, 2017, pp. 111–119.
6. Getsov, P., Modelling and study of the distribution of the operator's attention when controlling the longitudinal movement of an unmanned aerial vehicle, Eighteen International Conference “Space Ecology Safety - SES 2022”, Proceedings, pp. 89–93 (in Bulgarian).

МОДЕЛИРАНЕ И ИЗСЛЕДВАНЕ НА РАЗПРЕДЕЛЕНИЕТО НА ВНИМАНИЕТО НА ОПЕРАТОРА ПРИ УПРАВЛЕНИЕ НА СТРАНИЧНОТО ДВИЖЕНИЕ НА БЕЗПИЛОТЕН ЛЕТАТЕЛЕН АПАРАТ

П. Гецов

Резюме

В доклада са изследвани преходните процеси в системата „Оператор-Безпилотни летателни апарати“ при външни смущаващи въздействия. Разработен е модел на системата в среда „MATLAB Simulink“ с отчитане на разпределението на зрителното внимание на Оператора. Определена е зоната на параметрите на предавателните функции на Оператора в зависимост от превключването на вниманието.

RETRACTABLE UNDERCARRIAGE DESIGN FOR A QUADCOPTER

Konstantin Metodiev

*Space Research and Technology Institute – Bulgarian Academy of Sciences
e-mail: komet@space.bas.bg*

Keywords: *Undercarriage, Quadcopter, Autodesk inventor, Four bar linkage*

Abstract

In the current paper, design of a foldable undercarriage for quadcopter is suggested and investigated. The deploying/retracting mechanism comprises a four-bar linkage. The mechanism lowermost configuration forms a kinematic lock. A solution to complex variable equations has been worked out to put together the mechanism geometry. In addition, a 3D CAD model has been developed to visualize the design better.

Introduction

Retractable landing gear design is primarily employed to reduce drag of the aircraft. It is somewhat unfortunate that the retractable landing gear may alter longitudinal balance of the aircraft. In addition, the actuating mechanism adds extra weight. Despite a few shortcomings, the retractable landing gear is indispensable part of a high-speed airplane.

In case of a quadcopter, the undercarriage design is specific. It must meet following expectations:

- not to obstruct the payload (camera) field of view
- not to collapse whenever the servo motor is switched off, i.e. a kinematic lock is required
- to protect the payload (gimbal camera)
- to meet stress and strain requirements: yield, fatigue, deformation, etc.
- to be lightweight

The project goal is to devise a two-dimensional mechanism for undercarriage deploying/retracting that meets the aforementioned design requirements. Source code has been developed in C and build by TDM-GCC [1] to work out a solution to kinematic design equations with regard to a complex variable. In addition, it was rather necessary to develop a 3D CAD model to fulfil the project objectives better. In the current research, a trial version of Autodesk Inventor [2] has been used to investigate the construction thoroughly.

Method

Design milestones are described below. The design comprises two stages: developing a source code in C to fulfil kinematic analysis (see Appendix section) and a CAD model to test the solution.

Analysis

Given prescribed rotations, it is desirable for the four-bar linkage to obey the Grashof's law:

$$(1) \quad s + l \leq a + b$$

where variables stand for following: s – the shortest link, l – the longest link, a , b – remaining links. If the shortest link is adjacent to the fixed link, the mechanism is called “a crank rocker four-bar linkage.” However, in the current project, the shortest link is unable to perform a full revolution. It is not necessary either.

The four-bar linkage analysis follows algorithm described in textbook [3]. Standard dyad form of the governing equations has been employed according to following expression and Fig. 1:

$$(2) \quad \mathbf{W}(e^{i\varphi_j} - 1) + \mathbf{Z}(e^{i\gamma_j} - 1) = \delta_j = \mathbf{r}_j - \mathbf{r}_{j-1} = \mathbf{X}(e^{i\psi_j} - 1), \quad j = 1, 2, 3$$

In eq. (2) angles φ_j , γ_j , $j = 1, 2, 3$ are prescribed in advance. Values are assigned to displacement vector δ_j by trial and error. Vectors \mathbf{W} , \mathbf{Z} , and \mathbf{X} are complex.

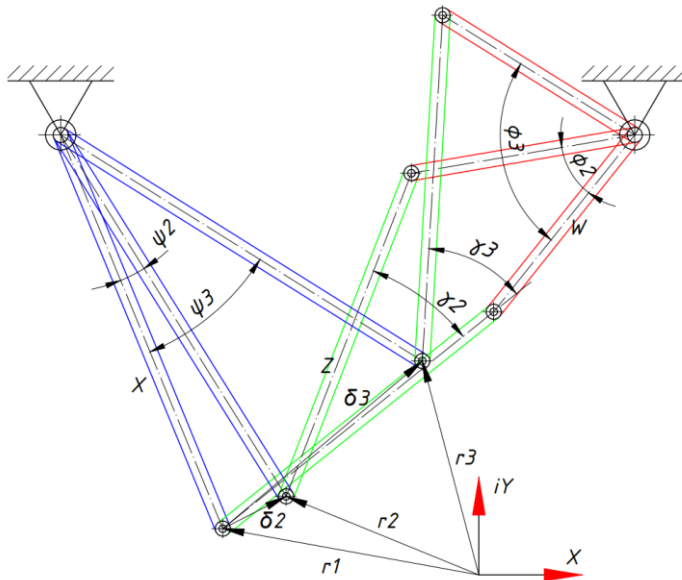


Fig. 1. Three initial configurations of the four-bar linkage

Considering eq. (2), it is straightforward to work out vector $\exp(i\theta)$ modulus by means of Euler's identity ($i = \sqrt{-1}$, θ is an arbitrary angle):

$$(3) \quad |e^{i\theta}| = |\cos(\theta) + i \sin(\theta)| = \sqrt{\cos^2(\theta) + \sin^2(\theta)} = 1$$

Therefore, having been multiplied by $\exp(i\theta)$, a vector rotates through angle θ .

Eq. (2) could be written down taking into account each initial position.

$$(4) \quad \begin{aligned} \mathbf{W}(e^{i\varphi_2} - 1) + \mathbf{Z}(e^{i\gamma_2} - 1) &= \delta_2 \\ \mathbf{W}(e^{i\varphi_3} - 1) + \mathbf{Z}(e^{i\gamma_3} - 1) &= \delta_3 \end{aligned}$$

This is a system of equations linear in the complex unknown vectors \mathbf{W} and \mathbf{Z} . It might be solved by Cramer's rule. A source code is available in Appendix section.

$$(5) \quad \mathbf{W} = \frac{\begin{vmatrix} \delta_2 & e^{i\gamma_2} - 1 \\ \delta_3 & e^{i\gamma_3} - 1 \end{vmatrix}}{\begin{vmatrix} e^{i\varphi_2} - 1 & e^{i\gamma_2} - 1 \\ e^{i\varphi_3} - 1 & e^{i\gamma_3} - 1 \end{vmatrix}}; \quad \mathbf{Z} = \frac{\begin{vmatrix} e^{i\varphi_2} - 1 & \delta_2 \\ e^{i\varphi_3} - 1 & \delta_3 \end{vmatrix}}{\begin{vmatrix} e^{i\varphi_2} - 1 & e^{i\gamma_2} - 1 \\ e^{i\varphi_3} - 1 & e^{i\gamma_3} - 1 \end{vmatrix}}$$

Assembly

The mechanism outline is shown in Fig. 2. A four-bar linkage is clearly visible. It is made up of two cranks (dark blue and dark red), a rocker (green), and a support (yellow) at which the entire mechanism is suspended. Input link is the dark red one which is actuated by a servo motor. It is important to note that both input crank and rocker are collinear on purpose at the linkage dead center. This is a configuration at which the transmission ratio is minimum. The kinematic lock imposes a constraint on the entire mechanism in deployed configuration. It is formed by a zero-force member (a fork) right beneath the middle axis, Fig. 2 - left.

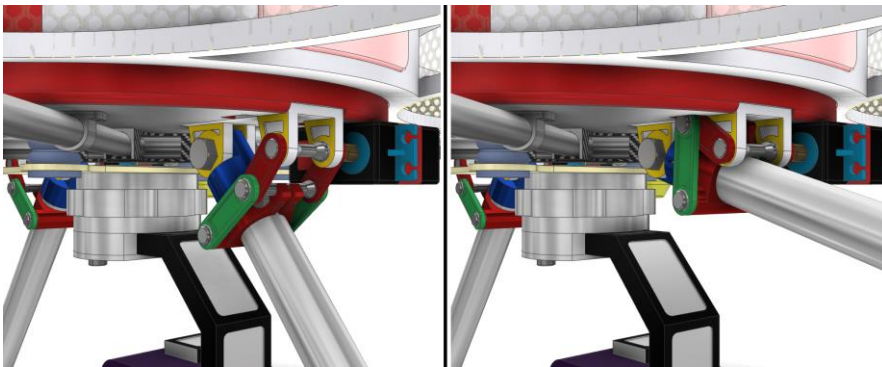


Fig. 2. The undercarriage fulcrum: deployed (left) and retracted leg

Results

In Fig. 3, both deployed and retracted mechanism configurations are depicted. Although the retracted rods are not quite horizontal, it is evident that the gimbal motion is not restricted, neither is the camera field of view.

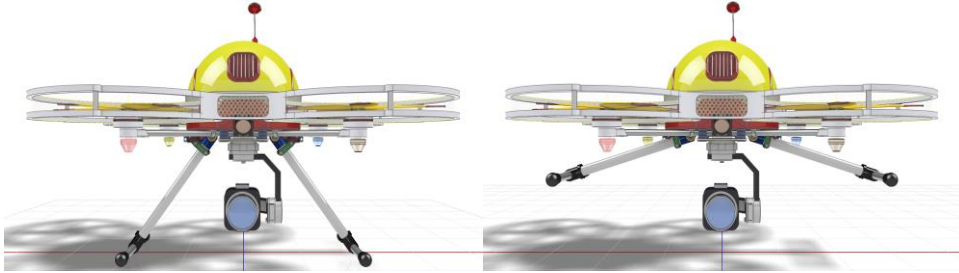


Fig. 3. Deployed (left) and retracted configuration of the undercarriage

Initial values, according to notation adopted in Fig. 1, follow. Rotation counterclockwise is positive.

$$\mathbf{r}_1 = -16.949 + \mathbf{i} * 3.068; \mathbf{r}_2 = -12.753 + \mathbf{i} * 5.215; \delta_2 = -\mathbf{r}_1 + \mathbf{r}_2$$

$$\mathbf{r}_3 = -3.739 + \mathbf{i} * 14.196; \delta_3 = -\mathbf{r}_1 + \mathbf{r}_3$$

$$\varphi_2 = -41.75 \text{ deg}; \varphi_3 = -83.5 \text{ deg}; \psi_2 = 30.101 \text{ deg}; \psi_3 = 47.893 \text{ deg}$$

After building and executing the source in Appendix section, following values were obtained (console output):

$$W = -9.34 - 11.74i$$

$$Z = -17.93 - 14.40i$$

$$|W| = 15.00 \quad |Z| = 23.00$$

Process returned 0 (0x0) execution time: 0.018 s

Press any key to continue.

Length of both input crank W and rocker Z are exact. There is a full agreement between analytical results and blueprint.

Conclusion

Deployed linkage configuration is considered stable enough. A kinematic lock (a.k.a. downlock) prevents the deployed mechanism from collapsing. Hence, the actuating servo motor might be switched off safely.

Further project development, according to Fig. 4, is to carry out stress and strain analyses.



Fig. 4. Perspective projection of the quadcopter [4]

References

1. <https://jmeubank.github.io/tdm-gcc/articles/2021-05/10.3.0-release>
last visit on 29th of June, 2022
2. <https://www.autodesk.com/products/inventor/overview>
last visit on 29th of June, 2022
3. Erdman, A. G., G. N. Sandor, S. Kota, Mechanism Design, Analysis and Synthesis, Vol. 1, p. 573, Fourth Edition, Prentice Hall, ISBN 0-13-040872-7
4. <https://grabcad.com/library/quadcopter-234>
last visit on 29th of June, 2022

ПРОЕКТ НА ПРИБИРАЕМА СТОЙКА ЗА КВАДРОКОПТЕР

К. Методиев

Резюме

В настоящата статия е предложен и изследван проект на прибираема стойка за квадрокоптер. Механизмът се състои от шарнирен четиризвенник. Крайната конфигурация на механизма образува кинематична ключалка. Механизмът бе синтезиран посредством решаване на уравнения с комплексна променлива. В допълнение бе разработен 3D CAD модел за по-добра визуализация на механизма.

Appendix. Source code in C for working out a solution to eq. (5), Fig. 1

```
#include <stdio.h>
#include <complex.h>
#include <stdlib.h>
#define PI 3.1415926535897932384626433832795

typedef double complex cplx;

cplx* Cramer(double *a, cplx d2, cplx d3); // forward declaration

int main() {

    cplx r1 = -16.949 + 3.068*I;
    cplx r2 = -12.753 + 5.215*I;
    cplx d2 = -r1 + r2;

    cplx r3 = -3.739 + 14.196*I;
    cplx d3 = -r1 + r3;

    double a[4] = {-41.75, -83.5, 30.101, 47.893}; // phi, psi
    double *pa = &a[0];

    cplx *ans = Cramer(pa, d2, d3);

    printf("W = %.2f%+.2fi\n", creal(ans[0]), cimag(ans[0]));
    printf("Z = %.2f%+.2fi\n", creal(ans[1]), cimag(ans[1]));
    printf("|W| = %.2f\t|Z| = %.2f\n", cabs(ans[0]), cabs(ans[1]));

    free(ans);

    return 0;
} // main

cplx* Cramer(double *a, cplx d2, cplx d3) {

    for (int i = 0; i < 4; i++) a[i] *= PI / 180.;

    cplx W = (d2 * (cexp(a[3]*I) - 1.) - d3 * (cexp(a[2]*I) - 1.)) /
    ((cexp(a[0]*I) - 1.) * (cexp(a[3]*I) - 1.) -
    (cexp(a[2]*I) - 1.) * (cexp(a[1]*I) - 1.));

    cplx Z = ((cexp(a[0]*I) - 1.) * d3 - (cexp(a[1]*I) - 1.) * d2) /
    ((cexp(a[0]*I) - 1.) * (cexp(a[3]*I) - 1.) -
    (cexp(a[1]*I) - 1.) * (cexp(a[2]*I) - 1.));

    cplx* foo = (cplx*)calloc(2, sizeof(cplx));
    foo[0] = W;
    foo[1] = Z;

    return foo;
} // Cramer
```

CHOICE OF THE OPTIMUM DESIGN OF LATERAL PMD USING THE CFD METHOD

Oleksandr Minai, Iryna Kuzmich

*Yuzhnoye State Design Office, Dnepr, Ukraine
e-mail: minayan1976@gmail.com, kuzmichiyu82@gmail.com,*

Keywords: *Residues Propellant; Propulsion System; Propellant Tank; Propellant Components; PMD; Numerical Simulation; CFD Method*

Abstract

Residues of propellant components in the power system of the propulsion system, at the end of the operation of the launch vehicle, to a large extent affect its energy characteristics. Propellant management devices (PMD), which are equipped with tanks of modern launch vehicles, provide a continuous supply of liquid propellant components from the tank to the propulsion system without disturbing the continuity of the flow and minimize of the residues of the propellant components. In the tank of a launch vehicle, the presence of a tunnel pipeline complicates, and in certain cases excludes the possibility of taking from the pole of the tank. In this case, the use of a lateral PMD allows solving the problem of propellant intake. The authors carried out a search and justification for the optimal design of the PMD using the example of the fuel tank of the first stage of the "Cyclone-4" launch vehicle, which is equipped with an PMD in the form of a profiled plate. The designs of the siphon and annular PMD are considered. An analytical calculation using empirical dependences, a physical experiment and numerical simulation of their main parameters was carried out. The result of the experimental and computational-analytical work was the determination of the most optimal variant of the PMD, which, according to several parameters, turned out to be a siphon PMD. The introduction of a more advanced siphon PMD into the design of the fuel tank of the "Cyclone-4" launch vehicle will improve the energy characteristics of the launch vehicle by increasing the weight of the output payload by 5.4 kg.

Introduction

The energy characteristics of modern launch vehicles are largely influenced by the residues of propellant components in tanks and highways at the end of the rocket stage. Residues propellant components are the amount of propellant in the power system of the propulsion system that cannot be produced due to violations of the requirements for continuity, pressure, propellant temperature at the inlet to the propulsion system, as well as due to the design features of the tank and the pipeline.

The PMD is an important element of the propellant tank, which provides a continuous supply of propellant components from the tank to the propulsion system

without disturbing the continuity of the flow (without gas inclusions), that is, their maximum production.

In the process of designing propellant tanks and systems for supplying propellant components to propulsion systems, both for the lower stages [1, 2] and for space stages of launch vehicles [3, 4], choosing the most optimal type of PMD is important. This will further determine: the timing of the design of PMD; volume and duration of experimental development (physical and numerical) [5, 6]; the material and technical part necessary for experimental testing; the energy characteristics of the launch vehicle (due to the residues of propellant components) and, as a result, the total time and material and technical costs for the development of PMD and the launch vehicle as a whole [7, 8].

The main parameter that determines the efficiency of the PMD is the critical height of the dip in the level of the propellant component (H_{cr}) in static conditions. It represents the height of the liquid level in the tank, at which a breakthrough of the gas phase in the PMD occurs. The mass of unusable residues of propellant components directly depends on this value.

1. Statement of the problem

The presence of a tunnel pipeline in the fuel tanks of some launch vehicles, a small distance between the engine inlet and the bottom of the tank, the need for separate power supply of several engines from one tank to supply the propulsion system with propellant components complicate the possibility of taking propellant from the propellant tank.

The purpose of the research work given in this article is to search and select the optimal design of the PMD in the tank with the presence of a tunnel pipeline, which provides an increase in the energy characteristics of the launch vehicle.

One of the common solutions for taking propellant from the tank in this case is the use of lateral PMD.

Lateral PMDs are characterized by an angle of location relative to the pole of the tank β (for central PMD, the angle $\beta = 0$). The presence of the angle β leads to an uneven level of gas breakthrough to the inlet to the pipeline and, as a result, a significant increase in the residuals propellant components, which adversely affects the energy characteristics of the launch vehicle [9, 10].

In a previous article by the authors [11], using the example of the fuel tank of the first stage of the "Cyclone-4" launch vehicle, equipped with lateral PMD in the form of a profiled plate (dish) to eliminate the disadvantages inherent in the lateral PMD, the authors considered the use instead of the lateral plate (dish) – siphon and annular PMD. For this, design work was carried out to determine their main geometric parameters (development of design schemes), and the calculation of H_{cr} was made, according to the method [12], which is based on empirical and semi-

empirical dependencies, whose coefficients were obtained from the results of experimental testing of models, the design of which is most similar to the designed PMD.

After that, a comparative analysis of the change in the energy characteristics of the launch vehicle was carried out, depending on the chosen PMD design.

Structural schemes of the existing PMD launch vehicle "Cyclone-4" in the form of a fuel lateral plate (dish) and designed siphon and annular PMD are shown in Fig. 1, respectively. In more detail, the general parameters of the siphon and annular PMD, together with the basic principles of their design, were considered in the article [11].

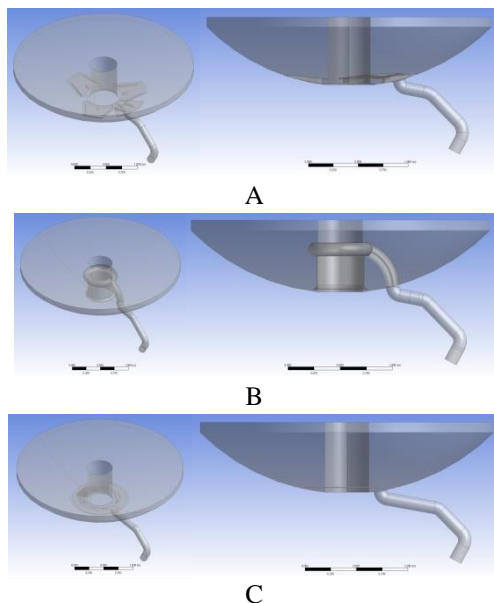


Fig. 1. Structural schemes of the PMDs, in the fuel tank of the first stage of the "Cyclone-4" launch vehicle: (A) – lateral PMD in the fuel tank of the first stage of the "Cyclone-4"; (B) – siphon PMD; (C) – annular PMD

Based on the results of computational and analytical work, a comparative analysis of the operating parameters of the PMD under consideration was carried out.

The values of the critical height of the dip in the level of the propellant component and the residues of propellant components in the fuel tank with the presence of a tunnel pipeline during the implementation of various PMD schemes are given in Table 1 [11].

Table 1. The values of the critical height of the dip in the level of the propellant component and the corresponding value of the residues of the fuel component in the fuel tank

№	Parameter	H_{cr} , mm	M_{RC}^{stat} , kg	M_{RC}^{struc} , kg	M_{RC}^{total} , kg
1	Existing design of lateral plate (dish) PMD	147	94,8	–	94,8
2	Siphon PMD	40	8,69	22,91	31,6
3	Annular PMD	104	47,4	–	47,4

Table 1 uses the following designations:

H_{cr} – is the critical height of the dip in the level of the propellant component relative to the theoretical pole of the tank;

M_{RC}^{stat} – is the mass of the static hydraulic residues of the propellant component;

M_{RC}^{struc} – is the mass of the structural residues of the propellant component;

M_{RC}^{total} – is the total mass of the residues of the propellant component.

In the development of the design work given in the article [11], with the aim of a more perfect calculation of the operating parameters of PMD, the authors carried out:

- physical experiment to determine the residues of the propellant component for lateral PMD, on prototype construction;
- numerical simulation of hydrodynamic processes during the tank emptying and determination of the residues of the propellant component for lateral PMD using ANSYS Fluent;
- verification of numerical simulation based on the results of a physical experiment;
- numerical simulation of hydrodynamic processes during the tank emptying and determination of the residues of the propellant component for siphon and annular PMD;
- comparative analysis and determination of the optimal design of the PMD by the factor of influence of the obtained values of the residues of the propellant component on changes in the energy characteristics of the launch vehicle, based on the results of numerical simulation.

1.1. Physical experiment to determine the residues of the propellant component for the lateral PMD

A physical experiment to determine the static hydraulic residue component for the lateral PMD was carried out on the fuel tank prototype of the lateral PMD of scales M_1 1:1 and M_2 1:4 under gravity. As model fluids: M_1 1:1 – distilled water; M_2 1:4 – kerosene, were used.

The similarity of the hydrodynamic processes, occurring during the emptying of the propellant tank prototype in terrestrial conditions, to the processes occurring during the emptying of full-scale propellant tanks under space flight conditions, was ensured by the equality of the dimensionless complexes (numbers): Froude (Fr), Reynolds (Re), Struhal (St), and geometric similarity [13].

The prototype construction M_1 1:1 was the lower part of a regular fuel tank, together with a lateral PMD and a pipeline, at the end of which a photometric continuity sensor was installed. Before starting the experiment, the prototype construction was filled with a model liquid (water). The required value of the liquid flow rate during the experiment was provided due to the preliminary adjustment of the throttle mechanism of the cut-off valve. During the experiment, after detecting the presence of gas inclusions in the liquid flow with a continuity sensor, the residues of the propellant component were cut off and drained along the bypass line into the measuring container. Thanks to this, the values of the stats of the residues of the propellant component were determined.

The prototype construction of the M_2 1:4 fuel tank was the lower part of the standard fuel tank, made of transparent organic glass, together with the lateral PMD and a pipeline, at the end of which a photometric continuity sensor was installed. The prototype construction of the fuel tank was integrated into a kinematic model which included: control and measurement system; pneumo-hydro system; video measurement system.

Before starting the experiment, the prototype construction of the fuel tank was filled with a model liquid (kerosene). The required value of the liquid flow rate, during the experiment, was provided by creating the required pressure value in the prototype construction of the fuel tank. During the experiment, thanks to the appropriate sensors, the following were recorded: pressure in the prototype construction of the fuel tank, fluid flow, continuity of the liquid flow at the outlet of the pipeline, pressure in the drain tank, video recording of the process of draining the model liquid from the prototype construction of the fuel tank into the drain tank.

The calculation of the residues of the propellant component was carried out by the computer station of the control and measurement system due to the data obtained (fixed) during the experiment.

Fig. 2 shows photos of the equipment of the hydrodynamic stand.

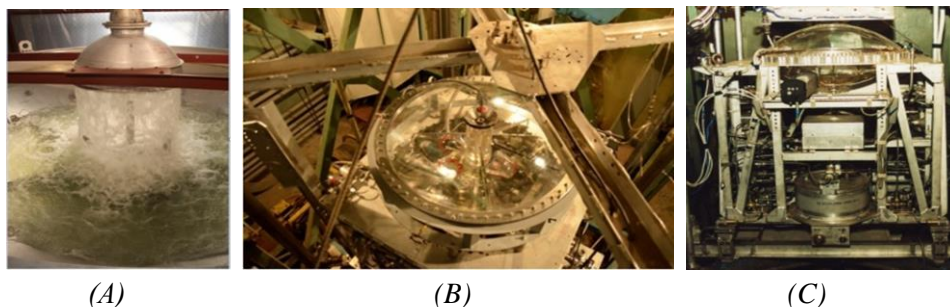


*Fig. 2. Photos of the equipment of the hydrodynamic stand.:
(A) process of filling the prototype construction M_1 1:1 with a model liquid (water);
(B) prototype construction of a fuel tank (top view) M_2 1:4; (C) general view of the kinematic model for hydrodynamic testing of a prototype construction of a fuel tank M_2 1: 4*

The results of experiments to determine the mass of static hydraulic residues of the propellant components in prototype construction of M_1 1:1 and M_2 1:4 scales for lateral PMD, depending on the Froude number (Fr), recalculated for natural flight conditions of the launch vehicle, are shown in Fig. 3.

1.2. Numerical modeling of hydrodynamic processes during tank emptying and determination of the residues of the propellant component for lateral PMD

With the development of computer technology and numerical methods for solving differential equations of fluid motion, it became possible to replace the almost universal use of empirical dependencies with a more accurate computational experiment which PMD design engineers began to use very actively [14, 15, 16, 17, 18].

So, by the 90s of the XXth century in the USA, “Lockheed Martin” and “PMD Technology” companies completely formed and repeatedly tested a scientific and engineering approach to the development of PMD, which made it possible to expand the model range, optimize design parameters, reduce design time, and the cost of the final products. This approach was based entirely on the computational fluid dynamics (CFD) method. Over time, it has become a universally recognized engineering tool.

The key projects that confirmed the possibility of using numerical methods in the development of PMD were the missions of the SDO and JWST telescopes; space experimental platform NFIRE; research satellite MESSENGER.

At the same time, during the MESSENGER mission in orbit of Mercury, the developers carried out numerous calculations in CFD to optimize the sequence of turning on the sustainer engine to extract the residues of the propellant component that “stuck” to the tank baffles. CFD forecasts were very accurate, which once again confirmed the economic and scientific feasibility of using numerical simulation methods in the rocket and space industry.

In Europe, in the absence of an accessible database of the results of ground-based experimental testing of various PMD designs, the process of introducing numerical methods in the development of PMD has been slower.

It was boosted by the work on the “Space Shuttle” project with the United States in the late 1980s. During its implementation, large-scale studies were carried out using the EMTE research platform, which made it possible to obtain a good initial database. In the future, the European developers of PMD, extending and expanding the database, in the implementation of various projects, carried out both experiments and calculations by numerical methods.

In Ukraine, the engineers of Yuzhnoye State Design Office have started using numerical methods in the design of PMD since 2012, after acquiring a license for the ANSYS software package. As in the case of European engineers, the replenishment of the experimental data base necessary for the verification of numerical calculations went along with the work on the “Cyclone-4” launch vehicle project. And if at the first stages of work the design parameters

of PMD were confirmed exclusively by the results of experiments on ground-based hydrodynamic stands and weightlessness stands, then at the final stages, the parallel use of numerical methods began. Numerical methods made it possible to reduce: the number of experimental designs that must be used, the required number of tests, the duration of the examinations, and, as the most important consequence, the overall material costs.

To solve the current problem, the simulation was carried out for a full-scale (natural) fuel tank and natural flight conditions of the “Cyclone-4” launch vehicle.

The process of solving the problem of numerical modelling of hydrodynamic processes when emptying the tank and determining the residues of the propellant component for lateral PMD in the ANSYS Fluent CFD software package consisted of the following steps: building a 3D model of the computational area of the fluid flow; constructing a computational grid; choosing the mathematical model of calculation; setting the properties of materials; setting initial and boundary conditions; setting solver parameters; calculating; visualization processing and analyzing calculation results.

The accuracy and reliability of the results of the numerical experiment depended on the correctness of the execution of each stage of the calculation.

During the numerical experiment, several simplifications and assumptions were made (mainly when constructing a 3D model), since it is practically impossible to consider all the factors that affect the behavior of the fluid under natural conditions of the launch vehicle flight.

Also, some deterioration in the accuracy of the numerical experiment was associated with the power of the available computer technology and the limitation of the time resource.

To carry out a numerical experiment, a 3D model of the computational domain of the fluid flow was built, i.e., the internal cavities of the full-scale (natural) tank bottom and the pipeline are modeled, not counting the wall thicknesses.

Based on the 3D model, a computational finite element mesh was created [19].

Later, in the ANSYS Fluent CFD module, after loading the computational grid, the numerical calculation was performed for natural conditions [20].

After the final settings in the Run Calculation section, the calculation was made and the results of the parameters of hydrodynamic processes during the emptying of the tank and the determination of the residues of the propellant component for the lateral PMD were obtained, which were displayed using the Results module.

Results of numerical modelling are shown in Fig. 5 and Table 2.

1.3. Verification of numerical simulation of hydrodynamic processes during tank emptying and determination of the residues of the propellant component for the lateral PMD based on the results of a physical experiment

The results of numerical simulation, as usual, are verified by the data of a physical experiment.

For a comparative analysis, the data of the physical experiment were plotted on the graph of the dependence of the mass of the propellant component residues on the Fr number

(see Fig. 3) along with numerical simulation data and data from preliminary calculations using empirical dependencies (see Table 1) for lateral PMD.

The values of the numbers Fr and the mass of the residues of the propellant component in Fig. 3 are given for a full-scale (natural) propellant tank (together with a pipeline) and full-scale flight conditions of the launch vehicle when the gas phase enters the inlet to the propulsion system.

At the same time, since the calculated value of the residues of the propellant component for the lateral PMD (see Table 1) was obtained for the propellant tank without the pipeline, at the time the gas phase entered the pipeline, its value at the time the gas phase entered the inlet to the propulsion system (M_L'') will be equal to:

$$(1) \quad M_L'' = M_{RC\ LPMD}^{total} + M_{pipeline}^{LPMD} - \tau' \cdot \dot{G}_{PS},$$

where:

$M_{RC\ LPMD}^{total}$ – is the total mass of the residues of the propellant component.

$M_{RC\ LPMD}^{total} = M_{RC}^{total}$, for lateral PMD (see Table 1);

$M_{pipeline}^{LPMD}$ – is the mass of the propellant component in the pipeline of the tank with the lateral PMD ($M_{pipeline}^{LPMD} = 10,67$ kg);

τ' – is the time during which the gas phase moves from the entrance to the pipeline to the entrance to the propulsion system. Theoretically, this time depends on the configuration of the pipeline, the distance that the gas phase overcomes from the entrance to the pipeline to the entrance to the propulsion system, and the speed of its movement. This time is $\sim 0,3$ s.

\dot{G}_{PS} – is the weight consumption of the propellant component for the propulsion system ($\dot{G}_{PS} = 38,57$ kg / s).

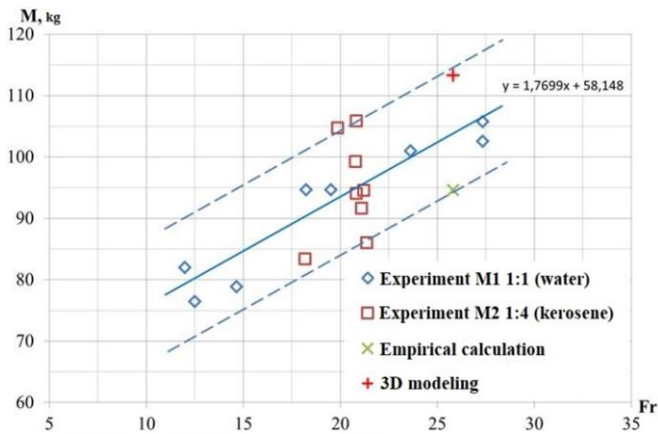
To more accurately take into account the mass of the propellant component, by which the total value of the residues of the propellant component will decrease during the movement of the gas phase from the inlet to the pipeline to the inlet to the propulsion system, we will replace the value of the multiplier ($\tau' \cdot \dot{G}_{PS}$) by the difference ($M_{TD} - M_{TC}$) in formula (1) (see Table 3). In this case, formula (1) will look like:

$$(2) \quad M_L'' = M_{RC\ LPMD}^{total} + M_{pipeline}^{LPMD} - M_L',$$

where:

$$(3) \quad M'_L = M_{TD} - M_{TC}.$$

For lateral PMD – $M'_L = 10,91 \text{ kg}$.



— linearly approximated mean value of experimental data;
 scatter limits of experimental data values

Fig. 3. Graph of the dependence of the mass of the residues of the propellant component, when the gas phase enters the inlet to the propulsion system on the number Fr

As we see from Fig. 3, the value of the residues of the propellant component for the lateral PMD obtained by numerical simulation is within the range of experimental data values. It has a deviation relative to the averaging line of the experimental data, equal to $\sim 9\%$ (average value of the residues of the propellant component approximated by the results of the experiment is 104 kg, at $Fr=25,81$) with a total deviation of the scatter of the values of the experimental data $\sim \pm 12\%$.

This testifies to the observance of hydrodynamic similarity in 3D modelling and confirms the correctness of the fulfilment of the set tasks of the numerical experiment.

The simplifications and assumptions adopted during the numerical experiment, which affect the behaviour of the fluid during the full-scale (natural) conditions of the launch vehicle flight, and the need to degrade the accuracy based on the power of the available computing equipment and the limitation of the time resource, did not significantly affect the accuracy of the results, because they are confirmed by physical experiment data.

This makes it possible to use the obtained mathematical model for numerical simulation of hydrodynamic processes during tank emptying and determination of the residues of the propellant component for siphon and annular PMD.

1.4. Numerical modeling of hydrodynamic processes during tank emptying and determination of the residues of the propellant component for siphon and annular PMD

Numerical simulation was performed for a full-scale (natural) fuel tank of the 1st stage and natural flight conditions of the "Cyclone-4" launch vehicle, with alternative PMD options: siphon and annular.

For numerical simulation, a 3D model of the computational area of the fluid flow was built, that is, internal cavities were modelled full-scale (natural) tank bottom and pipeline, without taking wall thicknesses into account – for siphon and annular PMD.

Based on the 3D model, a computational finite element mesh was created [19].

Later, in the ANSYS Fluent CFD module, after loading the computational grid, the settings were selected, and the initial and boundary conditions were set according to the methodology worked out for the lateral PMD (see section 1.2) [20].

After carrying out the calculations and obtaining the results of the parameters of hydrodynamic processes during emptying the tank and determining the residues of the propellant component for the siphon and annular PMD, they were visualized using the Results module.

Table 2 shows the values of the mass of the propellant component and the fluid continuity (at the end of the pipeline) in the propellant supply system of the propulsion system for 4-key moments (T_A , T_B , T_C , T_D) of emptying the propellant tank with a lateral, siphon and annular PMD.

Table 2. The value of the mass of the propellant component and the continuity of the liquid in the propellant supply system of the propulsion system for the lateral, siphon and annular PMD

Lateral PMD				
Parameter	T_A	T_B	T_C	T_D
Time, s	0,0213	38,5939	38,7271	39,0284
Continuity, %	100	100	100	98
Mass of the propellant component, kg	1547,64	129,09	124,19	113,28
Siphon PMD				
Parameter	T_A	T_B	T_C	T_D
Time, s	0,0445	40,7670	40,9919	41,2503
Continuity, %	100	100	100	99
Mass of the propellant component, kg	1542,03	46,24	36,44	26,96
Annular PMD				
Parameter	T_A	T_B	T_C	T_D
Time, s	0,0439	40,8234	40,9879	41,3169
Continuity, %	100	100	100	98
Mass of the propellant component, kg	1546,61	47,27	41,19	29,09

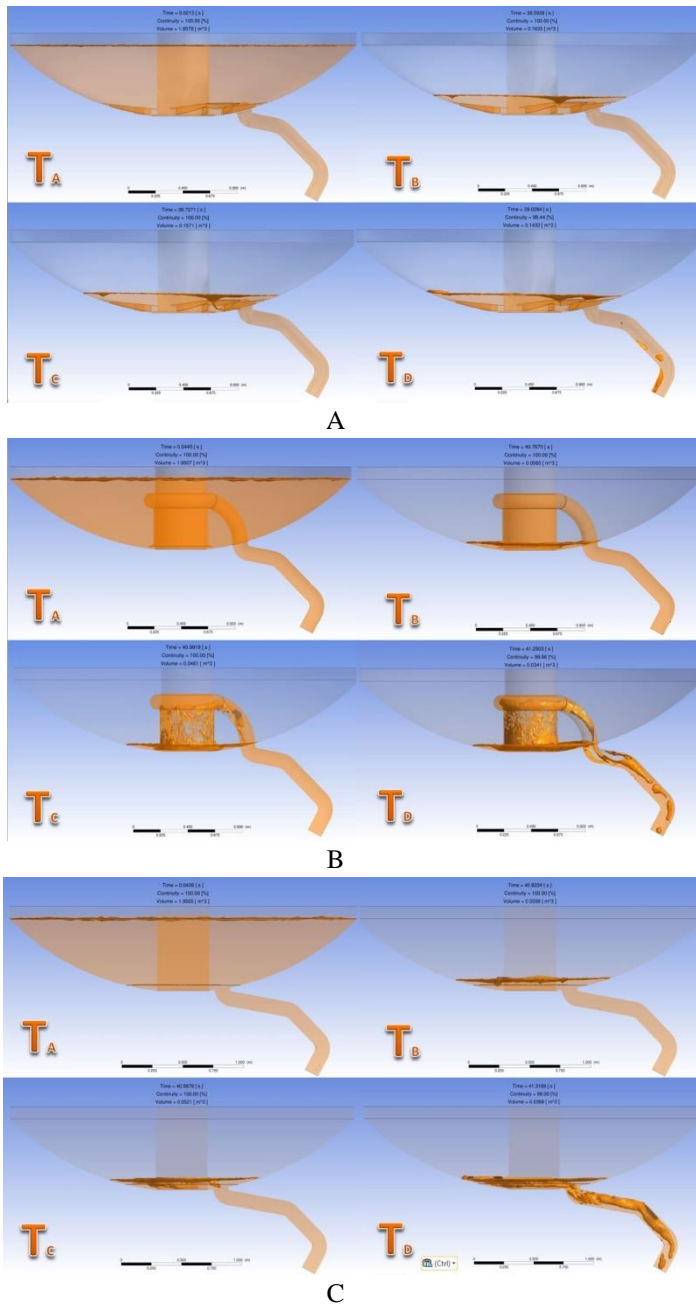


Fig. 4. Timing of the process of emptying the tank and determining the residues of the propellant component for 4-key moments the: (A) – lateral PMD; (B) – siphon PMD; (C) – annular PMD

Fig. 4 shows the timing of the process of emptying the tank and determining the residues of the propellant component for the lateral, siphon and annular PMD (respectively) for 4-key moments: T_A – the beginning of the emptying; T_B – immersion of the gas phase under the lateral/siphon/annular PMD; T_C – immersion of the gas phase to the entrance to the pipeline; T_D – immersion of the gas phase at the entrance to the propulsion system.

2. Analysis

Since the value of the hydraulic residues of the propellant components is determined for the power supply system of the propulsion system of the launch vehicle consisting of a fuel tank and a pipeline, then for a correct comparison and analysis of the results of analytical calculations, carried out without considering the pipeline, with the results of numerical simulation, in which the mathematical model of the calculation liquid flow area in the fuel tank and pipeline system – recalculations of the residues of the propellant components for the siphon and annular PMD should be carried out, which are shown in Table 1 according to the following formulas:

$$(4) \quad M_S'' = M_{RC\ SPMD}^{total} + M_{pipeline}^{SPMD} - M_S'$$

where:

$M_{RC\ SPMD}^{total}$ – is the total mass of the residues of the propellant component.

$M_{RC\ SPMD}^{total} = M_{RC}^{total}$, for siphon PMD (see Table 1)

$M_{pipeline}^{SPMD}$ – is the mass of the propellant component in the pipeline of the tank with the siphon PMD ($M_{pipeline}^{SPMD} = 10,75$ kg)

M_S' – is the mass of the propellant component, by which the total value of the residues of the propellant component will decrease during the time of gas phase immersion from the entrance to the pipeline to the entrance to the propulsion system for the siphon PMD.

For siphon PMD – $M_S' = 9,48$ kg .

$$5) \quad M_A'' = M_{RC\ APMD}^{total} + M_{pipeline}^{APMD} - M_A'$$

where:

$M_{RC\ APMD}^{total}$ – is the total mass of the residues of the propellant component.

$M_{RC\ APMD}^{total} = M_{RC}^{total}$, for annular PMD (see Table 1)

$M_{pipeline}^{APMD}$ – is the mass of the propellant component in the pipeline of the tank with the annular PMD ($M_{pipeline}^{APMD} = 12,09$ kg)

M'_A – is the mass of the propellant component, by which the total value of the residues of the propellant component will decrease during the time of gas phase immersion from the entrance to the pipeline to the entrance to the propulsion system for the annular PMD.

For siphon PMD – $M'_A = 12,10$ kg .

The results of the calculated values of the static hydraulics of the residues of the propellant component determined for the power system of the propulsion system of the launch vehicle according to the formulas (2), (4), (5) (M''), the results of numerical simulation (M''_{CFD}) for all three variants of the PMD, and their average deviation from the calculated values (σ) are given in Table 3.

Table 3. Significance of static hydraulic of the residues of the propellant components

No	Parameter	M'' , kg	M''_{CFD} , kg	σ , %	Change in payload mass $\Delta M''_{CFD}$, kg
1	Existing design of lateral plate PMD	94,56	113,28	20,8	0
2	Siphon PMD	32,87	26,96	18,0	+5,4
3	Annular PMD	47,48	29,09	38,7	+5,2

As we can see from Table 3, the results of numerical simulation have a significant deviation from the values of hydraulics of the residues of the propellant components calculated using the technique [12], based on empirical and semi-empirical dependencies, the coefficients of which were obtained from the results of experimental testing of the models, the design of which is most similar to the designed PMD. However, the data presented in section 1.3 indicate that the results of numerical simulation (for lateral PMD) have a deviation relative to the averaging line of experimental data equal to $\sim 9\%$ (the average approximated by the results of the experiment value of the residues of the propellant component is 104 kg, at $Fr = 25,81$) with a total deviation of the scatter of values experimental data $\sim \pm 12\%$.

This makes it possible to put forward a hypothesis that the developed method for numerical simulation of hydrodynamic processes during emptying the tank and determining the residues of the propellant components is valid, and the values of the residues of the propellant components for lateral, siphon and annular PMD obtained using it will be within the limits, no more $\sim \pm 15\%$ than the average approximated value of the physical experiment.

The deviation of the residues of the propellant components value according to the result of numerical simulation of the annular PMD is 38,7 % due to the fact that the analytical method [12], according to which the previous value of the residues of the propellant components was calculated, equal to 47,48 kg, does not take into account the fact that, when emptying the tank with the annular PMD, due to its design features, the flow of fluid in the chute under the perforated plate can occur according to the "piston" principle. This is possible

when the initial immersion of the gas phase under the plate occurs in its sector farthest from the pipeline, which can subsequently lead to the complete uniform emptying of the chute according to the “piston” principle. Partially, this effect is observed in the timing of the process of numerical simulation of emptying a tank with an annular PMD in Fig. 5 (T_B , T_C , T_D).

Thus, it can be concluded that of the residues of the propellant components’ values obtained by numerical simulation fully reproduce the physical picture of emptying the tank and of the residues of the propellant components formation and are more reliable than the values obtained by analytical calculations.

It follows from Table 3 that the siphon PMD provides the smallest mass of the residues of the propellant component, both according to analytical and numerical calculations.

Based on the obtained values of the residues of the propellant component in the fuel tank for the considered variants of PMD, according to the methodology and recommendations given in [21], the change in the energy characteristics of the “Cyclone-4” launch vehicle was determined. For this, the change in the mass of the payload that can be launched by the launch vehicle into a reference orbit relative to the existing lateral PMD was estimated.

Table 3 also shows the values of the change in the mass of the output payload in the case of the introduction of a siphon and annular PMD, relative to the lateral one, according to the results of numerical simulation.

Conclusions

The results of the computational-analytical and experimental work have shown that of residues of the propellant component is the smallest when using the siphon PMD.

The main advantages of which are:

- reducing the average approximated by the results of a physical experiment, the value of the static hydraulics of the residues of the propellant component in the power system of the propulsion system of the launch vehicle “Cyclone-4”, from 104 kg (for the existing lateral PMD), to 26,96 kg (the difference is $\Delta M = 77,04$ kg and is significant).

- ensuring a uniform decrease in the level of the fuel component in the tank;

- decreasing the dynamic component of the total balance, because of a decrease in H_{cr} due to the central selection of the fuel component;

- introducing a siphon PMD to power the steering propulsion system does not require refinement in the PMD fuel tank for the main propulsion system.

As a result, the introduction of a more advanced siphon PMD into the design of the fuel tank of the “Cyclone-4” launch vehicle instead of the lateral PMD will improve the energy characteristics of the launch vehicle by increasing the mass of the payload launched into the reference orbit by 5,4 kg.

As shown by the results of the work carried out, the use of numerical modeling methods (CFD methods) in the design work on development, optimization, and improvement, instead of the widespread use of empirical and semi-empirical dependencies, allows: getting more accurate results; reducing the number of prototype construction to be used; reducing the required number of tests; reducing the duration of experiments; reducing the total duration of computational and design and experimental work; reducing overall material and technical costs and, as a result, reducing the final cost of the development product, which will increase its competitiveness.

References

1. Baranov, D. A. Typical solutions in the design and construction of elements of launch vehicles. Textbook, Samara University Publishing House, 2020, 112 p. (in Russian).
2. Manning, R. E., I. Ballinger, M. Bhatia, et al. Design of the Europa Clipper Propellant Management Device. Propulsion and Energy Forum, 2019 AIAA, 19–22 August 2019 – Indianapolis, 2019, 19 p. DOI: <http://dx.doi.org/10.2514/6.2019-3858>.
3. Minai, O., O. Ivanov, I. Siedykh. Influence of long-term stay elements of capillary intake devices in liquid propellant components on their parameters. Aerospace Research in Bulgaria, 2020, 32, 175–192 p. DOI: <http://dx.doi.org/10.3897/arb.v32.e15>.
4. Minai, O., I. Siedykh, I. Kuzmich. Application of numerical simulation methods in experimental development of central-type the propellant management devices. Kharkiv, Aviatsiino-kosmichna tekhnika y tekhnolohiia, 2019, № 6(158), 33–41 p. DOI: <http://dx.doi.org/10.32620/akt.2019.6.05>.
5. Liu Jintao, Li Yong, Li Wen, et al. Experimental study on liquid distribution in a vane type propellant tank. Journal of Physics: Conference Series, 2019, Vol. 1314, 8 p. DOI: <http://dx.doi.org/10.1088/1742-6596/1314/1/012097>.
6. Lei Chen, Liu Jintao, Li Wen, et al. Numerical simulation and microgravity experiment of fluid flow in the vane type tank. IOP Conference Series: Materials Science and Engineering, 2019, Vol. 542, 8 p. DOI: <http://dx.doi.org/10.1088/1757-899X/542/1/012012>.
7. Chen Shangdong, Li Duan, Qi Kang. Study on propellant management device in plate surface tension tanks. Research paper: Acta Mechanica Sinica, 2021, 11 p. DOI: <http://dx.doi.org/10.1007/s10409-021-01121-y>.
8. Aamir Yusuf, P. K. Gopinathanb, K. Kamatchi, et al. Design & Development of Propellant Intake Device for Cryo Upper Stage LOX Tank. 71st International Astronautical Congress (IAC): The CyberSpace Edition, 12–14 October 2020, virtual, 12 p. Paper code: IAC-20,C4,2,2,x57098.
9. Belyaev, N. M. Calculation of pneumohydraulic systems of a rocket. Moskva, Mashinostroenie, 1983, 223 p. (in Russian)
10. Tokarev, V. E. Fluid outflow from a container with the formation of a funnel. Izvestiya vysshih uchebnyh zavedenij. Ser. Aviacionnaya tekhnika, 1967, № 3, pp. 92–94 (in Russian).
11. Kuzmich, I., O. Minai. Selecting the optimal design of the propellant management device in the fuel tank of the first stage of the "Cyklon-4" launch vehicle. Kharkiv, Aviatsiino-kosmichna tekhnika y tekhnolohiia, 2022, №1, 25–33 p. DOI: <http://dx.doi.org/10.32620/akt.2022.1.03>

12. Shevchenko, B. A. Estimated and experimental method for the development of means for collecting fuel components from tanks of aircraft with a liquid rocket engine, Dnepropetrovsk, KB «Juzhnoe» Publ., 1990, 209 (in Russian).
13. Mikishev, G. N. Experimental methods in spacecraft dynamics. Moskva, Mashinostroenie, 1978, 248 p. (in Russian).
14. Kuzmich, I. The influence of digitalization on the processes of design and experimental development in the rocket and space industry on the example of a capillary propellant management device. Materials of the XVI scientific lectures "Dnipro Orbit – 2021", Dnipro, October 28 – 30, 2021, 162–169 p.
15. Walter, T., B. Philipp, D. Jaekle, et al. The Evolutionary forces and the design and development of propellant management devices for space flight in europe and the united states. In conference: Space Propulsion, 2016, 25 p. SP2016_3124615
16. Walter, T., D. Jaekle. Review and history of ATK space systems surface tension PMD tanks. In conference: Space Propulsion, 2018, 24 p. SP2018_00023
17. Hartwig, J. W. Propellant Management Devices for Low-Gravity Fluid Management: Past, Present, and Future Applications. JOURNAL OF SPACECRAFT AND ROCKETS, 2017, Vol. 54, No. 4, July–August 2017. DOI: <http://dx.doi.org/10.2514/1.A33750>.
18. Hartwig, J. W. Liquid Acquisition Devices for Advanced In-Space Cryogenic Propulsion Systems. Elsevier Inc, 2016, 469 p.
19. Krivtsov, A. V. Studying the influence of mesh quality and turbulence models on the results of CFD calculation in ANSYS Fluent. Elektron. metod. ukazaniya k lab. rabotam, M-vo obrazovaniya i nauki RF, Samar. gos. aerokosm. un-t im. S. P. Koroleva (nac. issled. un-t). Samara, 2013, 47 p. (in Russian).
20. Ziganshin, A.M. Computational fluid dynamics. Setting and solving problems in the Fluent processor. Metodicheskoe posobie dlya uchebnoj i nauchnoj raboty studentov napravleniya 270800 – “Stroitelstvo” (kvalifikaciya «bakalavr» i «magistr») i aspirantov specialnosti 05.23.03. Izd-vo Kazansk. gos. arhitekt.-stroit. un-ta. Kazan, 2013, 79 p. (in Russian).
21. Bliznichenko, V. V., Y. O. Dzhur, R. D. Krasnikova. Design and construction of launch vehicles. Publishing House DNU, Dnepropetrovsk, 2007. 504 p.

ИЗБОР НА ОПТИМАЛЕН ДИЗАЙН НА СТРАНИЧЕН PMD С ИЗПОЛЗВАНЕ НА МЕТОДА CFD

О. Минай, И. Кузмич

Резюме

Остатъците от горивни компоненти в енергийната система на задвижващата система в края на експлоатацията на ракетата-носител влияят до голяма степен на нейните енергийни характеристики. Устройствата за управление на горивото (PMD), които са оборудвани с резервоари на съвременни ракетеносители, осигуряват непрекъснато подаване на компоненти на течно гориво

от резервоара към системата за задвижване, без да се нарушава непрекъснатостта на потока и минимизиране на остатъците от компонентите на горивото. В резервоара на ракета-носител наличието на тунелен тръбопровод затруднява, а в някои случаи и изключва възможността за вземане от полюса на резервоара. В този случай използването на страничен РМД позволява решаване на проблема с приема на гориво. Авторите извършиха търсене и обосновка на оптималната конструкция на РМД на примера на горивния резервоар на първата степен на ракетата-носител “Циклон-4”, който е оборудван с РМД под формата на профилна плоча. Разгледани са конструкциите на сифона и пръстеновидния РМД. Извършено е аналитично изчисление с помощта на емпирични зависимости, физичен експеримент и числена симулация на основните им параметри. Резултатът от експерименталната и изчислително-аналитичната работа беше определянето на най-оптималния вариант на РМД, който по няколко параметъра се оказва сифонен РМД. Въвеждането на по-усъвършенстван сифон РМД в конструкцията на горивния резервоар на ракетата-носител “Циклон-4” ще подобри енергийните характеристики на ракетата-носител чрез увеличаване на теглото на изходящия полезен товар с 5,4 kg.

AVIATION SAFETY AND IMPACT ON THE RELIABILITY OF DATA FROM DIFFERENT SOURCES OF PHYSICAL SIZES

Nikolay Zagorski

*Space Research and Technology Institute – Bulgarian Academy of Sciences
e-mail: nzagorski@space.bas.bg*

Keywords: *Flight safety, Reliability of data, Data backup*

Abstract

One of the most effective methods for increasing the flight safety of modern and promising aircraft is to increase the amount and reliability of information to on-board control systems. Basically, this refers to ensuring high reliability of data obtained from various sources of physical quantities. An analysis of the main types of information redundancy has been performed to achieve more efficient and fault-tolerant information structures in aircraft management systems.

Introduction

The efficiency of aircraft functional systems and aircraft safety depends to a large extent on the reliability of information on the ongoing process. This applies both to information on the processes taking place on board the aircraft and to the processes taking place in the environment and affecting the flight of the aircraft. All this diverse information is reported in different information sensors and enters the on-board computers of the aircraft. The information is then processed and used to control and manage the flight parameters.

The use of on-board computers to control complex and dynamic flight processes allows information to be processed simultaneously from many real-time information sources. At the same time, this allows the information to be distributed to different users (actuators). In performing these functions, on-board computers perform a series of extremely important operations:

- periodically asks the sensors for their condition and for the measured values of the controlled parameters;
- determine the true values of the measured values according to the readings of the sensors;
- recognizes or detects occurred events;
- produces control signals for regulation and control of complex systems and devices;

- develops feedback to ensure adaptive optimal management;
- performs statistical processing of the information and its storage for the predetermined period of time (for example, until the end of the flight).

Effective and high-quality process management in functional systems during the flight requires reliable information, which is usually difficult to learn due to the presence of interference or errors in information sources, unreliable sensors and more.

Study area

The physical nature of the operation of an information system with real signal sensors shows that it can be in one of three random and incompatible states [1, 2]: a – probability of true message (true state message); b – probability of reporting a “false state”; d – probability of “skipping” the condition (not to detect deviation from the normal parameters of the controlled condition).

Such a system with probability states is sufficiently complete and accurately described by a trinomial distribution [3, 4], which is an extended binomial distribution.

The probability that from the n -source of information k of them will miss messages, $(m-k)$ in number will report a „false“ message, and $(n-m)$ in number will be described by the following distribution [3,4]:

$$(1) \quad P_{(n-m, m-k, k)} = C_n^{n-m} a^{n-m} C_m^{m-k} b^{m-k} d^k,$$

where C_n^{n-m} is the number of combinations of n by $(n-m)$, as well as:

$$(2) \quad a + b + d = 1.$$

The probability characteristics a_n, b_n, d_n for n -number of parallel sources of information as follows [2–4]:

$$(3) \quad \begin{cases} a_{n,1} = 1 - (1 - a)^n; \\ b_{n,1} = (1 - a)^n - d^n; \\ d_{n,1} = d^n. \end{cases}$$

If a request signal is sent periodically (during a certain time interval) to the same source of information and the information received by it is stored and stored, then according to Bayes' Theorem [2–4], then at given probabilistic characteristics of the sources of information (as stated above): probability a for a reliable message; probability b for false message and probability d for not detecting the condition, then with a priori probability α , the a posteriori probabilities can be determined for: P_{1B} - for reliable message, P_{2B} - for not detecting the controlled state and P_{3B} - for message for “false state”, as follows:

$$(4) \quad \begin{cases} P_{1B} = \frac{\alpha a}{\alpha a + (1-\alpha)b}; \\ P_{2B} = \frac{\alpha a}{(1-\alpha)a + \alpha d}; \\ P_{3B} = \frac{(1-\alpha)b}{\alpha a + (1-\alpha)b}. \end{cases}$$

The concept of coefficient of precedence in the controlled state can be introduced and denoted by $\beta = \frac{1-\alpha}{\alpha}$, assuming that $b = d$, it is possible to introduce another coefficient - the quality of the source of information γ , which will take values $\gamma = \frac{b}{a} = \frac{d}{a}$, then the posteriori probabilities P_{1B}, P_{2B} и P_{3B} after k - number of repeated consecutive queries to the same source of information can be defined as:

$$(5) \quad \begin{cases} P_{1B}(k) = \frac{1}{1+\beta\gamma^k}; \\ P_{2B}(k) = \frac{\beta\gamma^k}{1+\beta\gamma^k}; \\ P_{3B}(k) = \frac{\gamma^k}{\beta+\gamma^k}. \end{cases}$$

To perform a comparative assessment of the effectiveness of sequential and parallel information redundancy, consisting in reducing the probabilities P_{2B} and P_{3B} depending on the number of consecutive queries- k to the same source of information and n -number of parallel sources of information. In such a case, coefficients may be introduced to take into account the impact of another request to reduce the likelihood of receiving a “false information” response to the condition or the likelihood of “missing” the condition (not to deviate from normal parameters controlled state) upon sequential reservation and, respectively, to be designated as N_{bA} and N_{dA} . In this order, similar coefficients can be introduced for parallel reductions, denoted as N_{bA} and N_{dA} . The values of the entered coefficients can be determined by the expressions determining the probability of answer for “false information” about the condition and for “skipping” the condition in the next $(k - 1)$ and k -query to the source of information, respectively, at $(n - 1)$ and n -th inclusion of the source of information [5]. As a result of such a number of operations and transformations the following expressions are obtained:

$$(6) \quad \begin{cases} N_{bB} = \frac{1+\beta\gamma^k}{\gamma(1+\beta\gamma^{k-1})}; \\ N_{bA} = \frac{(1-a)^{n-1}-d^{n-1}}{(1-a)^n-d^n}; \\ N_{dB} = \frac{\beta+\gamma^k}{(\beta+\gamma^{k-1})\gamma}; \\ N_{dA} = \frac{d^{n-1}}{d^n} = \frac{1}{d}. \end{cases}$$

With high quality of the information source, when the order of values of $\gamma \rightarrow 0$, and increasing the values of k -number of consecutive queries of one information source, and n -number of parallel connected information sources, the following can be entered coefficients $\tilde{N}x_{bB}, \tilde{N}x_{bA}, \tilde{N}x_{dA}, \tilde{N}x_{dB}$, which are determined by (6). At the same time, these coefficients are asymptotically reduced to the following simple dependences (7):

$$(7) \quad \begin{cases} \tilde{N}_{bB} = \lim_{k \rightarrow \infty} N_{bB} = \frac{1}{\gamma}; \\ \tilde{N}_{bA} = \lim_{k \rightarrow \infty} N_{bA} = \frac{1}{1-\alpha}; \\ \tilde{N}_{dB} = \lim_{k \rightarrow \infty} N_{dB} = \frac{1}{\gamma}; \\ \tilde{N}_{dA} = N_{bA} = \frac{1}{d}. \end{cases}$$

When performing the majority attribute, for example at $Q = 2$ (which shows how many sources of information signal “yes”), the coefficients N_{bA2} and N_{dA2} to reduce the probability P_3 for reporting “false” state and the probability P_2 for not detecting the controlled state of the parallel information system, which consists of the $(n - 1)$ source of information, with the inclusion of another additional source can be determined as follows:

$$(8) \quad \begin{cases} N_{bA2} = \frac{P_3(2,n-1)}{P_3(2,n)} = \frac{(1-a)^{(n-1)} - d^{(n-1)} - (n-1)bd^{(n-2)}}{(1-a)^n - d^n - nbd^{(n-1)}}; \\ N_{dA2} = \frac{P_2(2,n-1)}{P_2(2,n)} = \frac{d^{(n-1)} + (n-1)bd^{(n-2)} + (n-1)ad^{(n-2)}}{d^n + nbd^{(n-1)} + nad^{(n-1)}}. \end{cases}$$

Based on the expressions in (6), (7) and (8), coefficients $D_{bA}, D_{dA}, D_{bB}, D_{dB}$ can be entered to reduce the probabilities P_3 and P_2 , respectively, to provide information about the “false” state and not to detect of the controlled state at parallel and at consecutive reservation of the information for known, set values of k -number of consecutive inquiries and n -number of parallel connected information source. These coefficients are determined by the following expressions:

$$(9) \quad \begin{cases} D_{bA} = \prod_{i=1}^n \frac{(1-a)^{(i-1)} - d^{(i-1)}}{(1-a)^i - d^i}; \\ D_{dA} = \frac{1}{d^n}; \\ D_{bB} = \prod_{i=1}^k \frac{1 + \beta\gamma^i}{[1 + \beta\gamma^{(i-1)}]\gamma}; \\ D_{dB} = D_{dB} = \prod_{i=1}^k \frac{\beta + \gamma^i}{[\beta + \gamma^{(i-1)}]\gamma}. \end{cases}$$

From this follow several conclusions. First of all, consistent reservation makes it possible to significantly reduce the likelihood of reporting false information by incurring acceptable economic and technical costs. On the other hand, the

application of this method of reservation is limited by the time of “obsolescence” of information and correlations in case of accidental failures, in which the technical devices resume their work without the intervention of an operator or other technical device. The method of sequential information reservation is widely used in modern aircraft equipped with several on-board computers [6]. Consecutive information reservation is extremely effective in setting optimal criteria for confirming the authenticity of the message in cases where the m -number of possible (expected) messages received k in number and, assuming, for example, that k is equal to half of m , then the probability of submitting information about a “false” state and not detecting the controlled state will be equal. If the value of k is small enough, the probability of reporting “false” condition will be increased. If the value of k tends to the value of m , the probability of “skipping” the state will increase (not to deviate from the normal parameters of the controlled state).

Secondly, the parallel reservation of information significantly reduces the likelihood of “skipping” the condition (not to deviate from the normal parameters of the controlled state) and has little effect on reducing the likelihood of submitting information about “false” state. The application of the principle of majority logic allows reducing the likelihood of information with a “false” state, but at the same time requires an increase in the number of parallel channels, which in turn is associated with certain economic constraints.

Thirdly, the combined application of parallel and sequential redundancy allows to effectively reduce both the probability of information with a “false” state and the probability of “skipping” the state (not to deviate from the normal parameters of the controlled state) [7].

Using the approximate values of the coefficients $\tilde{N}x_{bB}$, $\tilde{N}x_{bA}$, $\tilde{N}x_{dB}$ and $\tilde{N}x_{dA}$, which are determined by (7) and (9), the following dependences can be written:

$$(10) \quad \begin{cases} \tilde{D}_{bA} = \frac{1}{(1-a)^n}; \\ \tilde{D}_{dA} = \frac{1}{a^n}; \\ \tilde{D}_{bB} = \frac{1}{\gamma^k}; \\ \tilde{D}_{dB} = \frac{1}{\gamma^k}. \end{cases}$$

Based on this expression, the value of k -number of consecutive queries to one source of information and n -number of parallel information channels can be determined, if the requirements of \tilde{D}_{bA} , \tilde{D}_{dA} , \tilde{D}_{bB} and \tilde{D}_{dB} to reduce the probability P_3 of submitting information about a “false” state and P_2 to “miss” the state, respectively, in parallel and sequential redundancy. The values of these probabilities can be determined as follows:

$$(11) \quad \begin{cases} n_{bA} > -\frac{\ln D_{bA}}{\ln(1-a)}; \\ K_{bB} > -\frac{\ln D_{dB}}{\ln \gamma}; \\ n_{dA} > -\frac{\ln D_{dA}}{\ln d}; \\ K_{dB} > -\frac{\ln D_{dB}}{\ln \chi}. \end{cases}$$

With the help of the above mathematical expressions, a number of practical problems can be solved. For example, consider controlling a fast-paced process. The speed of the process allows using no more than k number of consecutive queries to one source of information. In this case, the reduction of \tilde{D}_{bB} and \tilde{D}_{dB} , obtained by expressions (10), can provide unsatisfactory values, and it can be conditioned that these probabilities be reduced, respectively, not less than Y and Z times. Then the minimum number of parallel sources n can be determined to ensure that the requirements of Y and Z are met, according to the expressions [3, 7]:

$$(12) \quad \begin{cases} n_{bA} > -\frac{\ln Y - \ln D_{bB}}{\ln(1-a)}; \\ n_{dA} > -\frac{\ln Z - \ln D_{dB}}{\ln d}. \end{cases}$$

Naturally, the larger of the numbers n_{bA} and n_{dA} must be chosen to meet the requirements. Tables 1, 2, 3 and 4 present matrices that characterize the total reduction coefficients calculated by formulas (9). It should be noted that the number of columns corresponds to the number k of consecutive queries to the same source, and the number of rows determines the number n of parallel sources of information. In each cell of the matrix there is a reduction factor determined for the number of consecutive queries for the corresponding column number and for the number of parallel connected sources corresponding to the row number. For better clarity, the results obtained in the calculations are presented in decimal form.

Table 1. Factors to reduce the probability of submission of "false" state information determined from input data: $\alpha=0,9$; $\beta=1$; $b=d=0,05$

$\frac{k}{n}$	1	2	3	4	$\frac{k}{n}$	1	2	3	4
1	1	13,28	232,1	4139,3	1	-	1	2	3
2	12,39	105,73	1755	29274,3	2	-	2	3	4
3	57,42	906,1	15050	250885,4	3	1	2	3	5
4	609	8426,5	139965	2333208,2	4	2	3	5	6

Table 2. Coefficients for reducing the probability of “missing” a change in the observed condition, determined from baseline data: $\alpha=0,9$; $\beta=1$; $b=d=0,05$

$\frac{k}{n}$	1	2	3	4	$\frac{k}{n}$	1	2	3	4
1	1	13,28	232,1	4139,3	-	-	1	2	3
2	15	315,6	5242,2	87388	1	-	2	3	4
3	300	6312	1048442	1747721,5	2	1	3	5	6
4	6000	126240	2096846,4	34954429,5	3	2	5	6	7

Table 3. Coefficients for reducing the probability of reporting “false” status, determined from baseline data: $\alpha=0,9$; $\beta=9$; $b=d=0,05$

$\frac{k}{n}$	1	2	3	4	$\frac{k}{n}$	1	2	3	4
1	1	11,17	190,7	3007,4	-	-	1	2	3
2	6,7	74,8	1210,9	20149,3	-	-	1	3	4
3	57,42	641,4	10377,6	172682,4	1	1	2	4	5
4	609	5964,8	96510,1	1605928,7	2	2	3	4	6

Table 4. Coefficients for reducing the probability of “missing” a change in the observed condition, determined from baseline data $\alpha=0,9$; $\beta=9$; $b=d=0,05$

$\frac{k}{n}$	1	2	3	4	$\frac{k}{n}$	1	2	3	4
1	1	16,56	276,1	4601,8	-	-	1	2	3
2	15	331,2	5521,1	92036,8	1	-	2	3	4
3	300	6624	110422,1	1840736	2	1	3	5	6
4	6000	132480	2208441,6	36814721,5	3	2	5	6	7

From the results presented in Table 1, 2, 3 and 4, the following conclusions can be drawn:

1. The values of the a priori probabilities have a negligible influence on the increase of the reliability of the information by increasing the number of consecutive inquiries to the sensors of the system.

2. The combined parallel-sequential redundancy system simultaneously reduces the likelihood of “skipping” the state (not deviating from the normal parameters of the controlled state) and providing information about a “false” state. More effective in this case is the effect on reducing the likelihood of “missing” the condition.

3. The set coefficients for reducing the probability of “missing” the condition and the probability of submitting information about a “false” condition can be provided in two ways: either by increasing the number of consecutive queries with a given number of parallel sources, or by increasing the number of parallel sources at a given number of consecutive queries.

The probability of a complete group of events [2,8,9] in parallel-sequential reservation is determined as follows:

$$(13) \quad P_{1B}(1 - P_{1A}) + P_{1A}(1 - P_{1B}) + P_{1A}P_{1B} + (1 - P_{1A})(1 - P_{1B}) = 1,$$

where P_{1A} and P_{1B} are the probabilities of true message, respectively, only for parallel and only for sequential reservation of the information system. From formula (13) the probability P_{1C} can be determined in case of parallel-consecutive information reservation of the system:

$$(14) \quad P_{1C} = 1 - (1 - P_{1A})(1 - P_{1B}),$$

where

$$(15) \quad \begin{cases} P_{1A} = 1 - (1 - a)^n; \\ P_{1B} = \frac{1}{1 + \gamma^k}; \\ \gamma = \frac{1 - a}{a}. \end{cases}$$

Substituting (15) into (14) after a series of transformations, the following dependence can be obtained:

$$(16) \quad P_{1C} = 1 - (1 - a)^n \frac{(1 - a)^k}{a^k + (1 - a)^k}.$$

From the expression in (16) after some transformations we can get:

$$(17) \quad (1 - a)^n = \frac{(1 - P_{1C})[a^k + (1 - a)^k]}{(1 - a)^k}.$$

After logarithm of (17), the final expression can be determined to obtain the dependence $n(k)$ for the number of parallel sources of information from the number of consecutive queries k :

$$(18) \quad n(k) = \frac{\ln(1-P_{1C}) + \ln[a^k + (1-a)^k] - k \ln(1-a)}{\ln(1-a)}$$

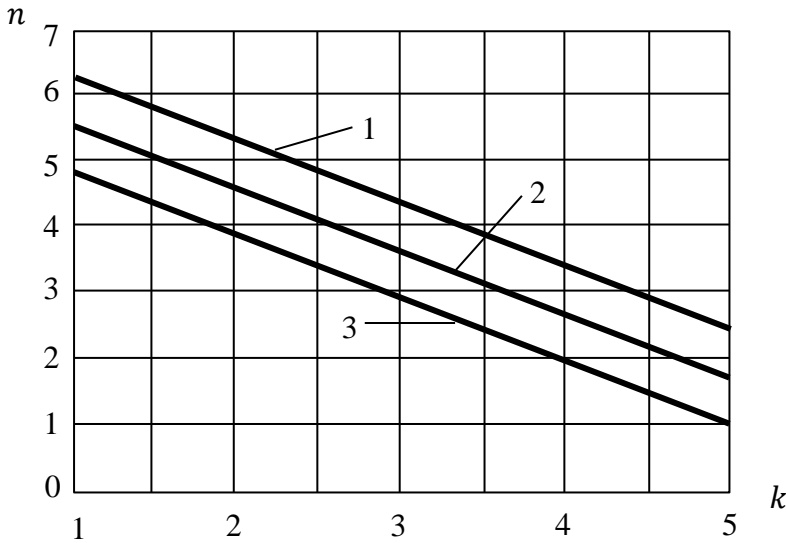


Fig. 1. Nomogram for the dependence $n(k)$ in case of parallel-consecutive reservation of information systems

Fig. 1 shows a nomogram based on the results of (18) with the following initial data: $k = 1, 2, 3, 4$ and 5 ; $a = 0,97$. The required probability P_{1C} for a true message in case of joint parallel-sequential reservation in the information system is presented in three variants: the first (1) $P_{1C} = 1 - 10^{-7}$, the second (2) $P_{1C} = 1 - 10^{-8}$ and the third (3) $P_{1C} = 1 - 10^{-9}$.

Thus, in accordance with the initial data of the nomogram, the required amount of n from parallel connected sources of information can be determined graphically at a given number k of consecutive incoming information (inquiries) from one source and, conversely, by a given number n the required number of consecutive queries can be determined from the parallel connected sources to ensure the required probability of P_{1C} in a system with parallel-sequential data reservation. To ensure the required probability P_{1C} by increasing the number of consecutive incoming data (inquiries), the number of parallel sources of information can be reduced. Similarly, as the number of n -parallel sources increases, the number k of consecutive queries can be reduced.

In the general case, the reliability of the information received from the individual sources of information, which determines the probabilities a, b and d , can be increased in two ways:

- by increasing the number n of information sources, increasing the probability P_{1n} of detecting and correctly recognizing the status of the controlled trait and, respectively, reducing the probabilities P_{3n} and P_{2n} of reporting false information and “miss” this state in a system of n -parallel sources of information;

- if k -number of inquiries are addressed to the same source of information in a certain time interval, it is obvious that the probability P_{1k} for the correct recognition of the state of the controlled feature after k -number of inquiries will also increase, and the probability P_{3n} for submitting information about the “false” state and P_{2k} about the probability of “missing” this state (not being detected), respectively, decrease.

It is also necessary to take into account the real limitations of the implementation of the two ways to increase the reliability of information. For the first of them, the increase in costs (by mass, financial, etc.) imposes certain restrictions related to increasing the amount of n sources of information. For the second method, the limitation is the time for “aging” (loss of relevance) of the information due to the extreme speed of the managed processes. The correlation between accidental short-term interruptions in work or self-correcting technical failures in the requested information source also has an impact. This should not exceed the time interval between two separate queries to the same information system sensor.

It can be argued that in the specific situation there are reservations for both n - in parallel reservation and k - in sequential reservation, which can significantly increase the reliability of information.

Conclusion

The method of parallel backup of information significantly reduces the likelihood of “missing” (not detecting) the observed condition and to a much lesser extent has the effect of reducing the likelihood of submitting information about a “false” condition. The application of the principles of majority logic allows reducing the likelihood of information with a “false” state of the information system, but to obtain this it is necessary to increase the number of parallel channels, which is associated with economic constraints.

The combined application of parallel and sequential redundancy allows to effectively reduce both the probability of a “false” state of the system and the probability of “missing” (not detecting) the observed state at minimal additional cost.

References

1. Marinov, Ass., G. Yordanov. Sensors for reporting flight parameters. Annual international scientific conference of the Faculty of Aviation. 2019. Collection of reports. ISBN 978-954-713-123-1, pp. 69–76 (in Bulgarian).
2. Iliev, R. Generalized model of decision making processes in the management’s systems with use of intuitionistic fuzzy sets. Proc. of the Ninth International Conference on

- Intuitionistic Fuzzy Sets - part 3, Vol. 11, Number 4, Sofia, Bulgaria, May 2005, pp. 146–150 (in Bulgarian).
3. Marinov, A. Numerical simulation of vortex sheets on an aircraft wing. Annual university scientific conference of Vasil Levski National University. 2010. Proceedings. Volume 5. ISSN 1314-1937. pp. 41–45 (in Bulgarian).
 4. Marinov, A. Convergence of wing aerodynamic force results by tetra and hexa meshes. Scientific conference “40 years since man stepped on the moon and 30 years since the flight of the first Bulgarian cosmonaut”. 2009. Proceedings. Vol. 1. ISBN 978-954-713-096-8. pp. 90–98 (in Bulgarian).
 5. Marinov, A. Experimental determination of the aerodynamic characteristics of an L-39 aircraft. Anniversary scientific session of the Faculty of Aviation. 2008, D. Mitropolia. Proceedings. ISBN 978-954-713-092-0. pp. 51–58 (in Bulgarian).
 6. Boyanov, P. Implementation of protection mechanisms of information resources in the local area networks, Annual of K. Preslavsky Univ. of Shumen, K. Preslavsky University Press, ISSN 1311-834X, Vol. IX E, 2019, pp. 115–121 (in Bulgarian).
 7. Marinov, A. Influence of the turbulence model on the aerodynamic performance of a NACA64A410 airfoil in numerical simulation. Annual university scientific conference of Vasil Levski National University. 2010. Proceedings. Volume 5. ISSN 1314-1937. pp. 46–54 (in Bulgarian).
 8. Genov, B. Need to apply non-destructive testing methods in the life cycle stages of defense products, 2012, International Conference “Days of Nondestructive Testing” 2012, Sozopol, 2011, ISSN 1310-3946, pp. 363–365 (in Bulgarian).
 9. Marinov, A. Comparison of oblique shock wave angle in analytical and numerical solution. Aerospace Research in Bulgaria, Vol. 31. 2019, pp. 137–142. DOI: <https://doi.org/10.3897/arb.v31.e12>.

АВИАЦИОННАТА БЕЗОПАСНОСТ И ВЛИЯНИЕ НА ДОСТОВЕРНОСТТА НА ДАННИТЕ ОТ РАЗЛИЧНИ ИЗТОЧНИЦИ НА ФИЗИЧНИ ВЕЛИЧИНИ

Н. Загорски

Резюме

Един от най-ефективните методи за повишаване на безопасността на полета на съвременните и перспективни въздухоплавателни средства е повишаване на количеството и достоверността на информацията към бордовите системи за управление. Основно това се отнася до осигуряването на висока надеждност на данните, получавани от различни източници на физични величини. Извършен е анализ на основните видове информационно резервиране за постигане на по-ефикасни и по-устойчиви на откази информационни структури в системите за управление на въздухоплавателни средства.

SPACE EXPERIMENT "OBSTANOVKA (1-STEP)", BLOCK DP - PM ON THE RUSSIAN SEGMENT OF THE INTERNATIONAL SPACE STATION

*Anna Bouzekova-Penkova¹, Stanislav Klimov², Valery Grushin²,
Olga Lapshinova², Denis Novikov², Dimitar Teodosiev¹*

¹*Space Research and Technology Institute – Bulgarian Academy of Sciences
e-mail: a_bouzekova@space.bas.bg*

²*Space Research Institute - Russian Academy of Sciences
e-mail: sklimov@iki.rssi.ru, vgrushin@iki.rssi.ru, olga.lapshinova@rsce.ru,
dnovikov@iki.rssi.ru*

Keywords: *Aluminium, Aluminium alloys, Glassy carbon, International space station (ISS), Fundamental and applied space research*

Abstract

In the presented work is described the methodology for conducting the technological experiment DP-PM, which is part of the space experiment "Obstanovka 1-step". The DP-PM block was installed on the Russian Segment of the International Space Station in the period from 04/19/2013 to 08/10/2015. The purpose of the experiment is to study the effect of outer space on the properties of graphite samples with a glassy carbon coating and samples of B95 (7075) aluminium alloy with a quantitative addition of ultradisperse diamond powder and tungsten after a long stay in near Earth orbit.

Introduction

The study of outer space leads to the creation of new materials or the improvement of existing ones for the construction of space vehicles. These materials must not only work, but also not lose their physical and mechanical properties during long stays in non-standard conditions of outer space (microgravity, intense radiation, a wide range of operating temperatures, micrometeor bombardment, vacuum, mechanical effects: acceleration, vibration, etc.). They must also combine high modulus of elasticity, heat resistance, wear resistance, density, and other properties useful for space engineering.

To obtain complete and real data on the consequences of a long stay of new materials used for space technology, it is necessary to conduct special technological experiments on board interplanetary stations, which ensure the possibility of returning samples of the studied materials back to Earth. For this

purpose, the DP-PM experiment was planned and implemented, which is part of the “Obstanovka 1-step” space experiment [1], within the framework of the "Long-term program for scientific and applied research and experiments on the Russian segment of the International Space Station (ISS)". This is an international project in the interests of fundamental space research and is of an exploratory nature, carried out with the help of a plasma-wave complex of scientific equipment.

Purpose of the experiment

The purpose of the experiment, associated with a device called the DP-PM block (Potential Sensor - Material Surfaces), is to study the influence of outer space on the properties of new materials after a long stay in near-Earth orbit.

The DP-PM block is a container (Fig. 1) made of aluminium alloy. It has a nickel coating on the back and experimental samples inside. On one side 8 pcs. rectangular graphite samples with a glassy carbon coating [2, 3] (Fig. 1a), and on the other side of the block there are 10 pcs. cylindrical tubes made of aluminium alloy B95 (7075) with a quantitative addition of ultradisperse diamond powder and tungsten (Fig. 1b). The experimental samples are the goal of our experiment, and the block is the place where the samples are fixed. They are attached to the container using a spring-loaded cotter pin in the holes on both sides for better and more convenient work with them when they are removed and installed by a cosmonaut outside the ISS, in zero gravity conditions.

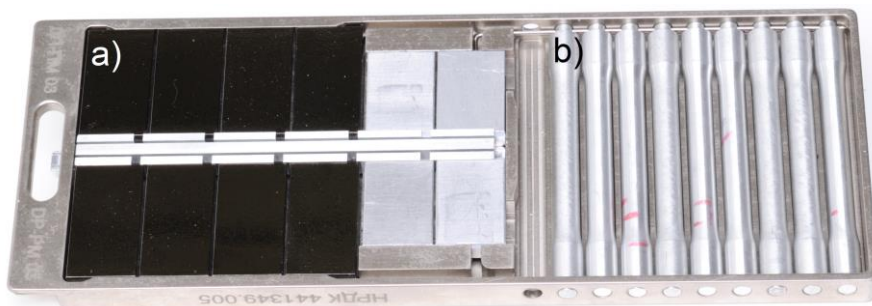


Fig. 1. Block DP-PM; a) graphite samples with a glassy carbon coating, b) samples of aluminium alloy 7075 (B95) with a quantitative addition of ultradisperse diamond powder and tungsten

The main stages in the development of the DP-FM block correspond to the specific stringent requirements for conducting experiments in space and include the preparation of a methodology for manufacturing and testing the device [4].

The first stage is associated with the construction (Fig. 2) and the manufacture of the DP-PM block, also called the Technological Sample (TS) for acceptance tests and design and finishing works.

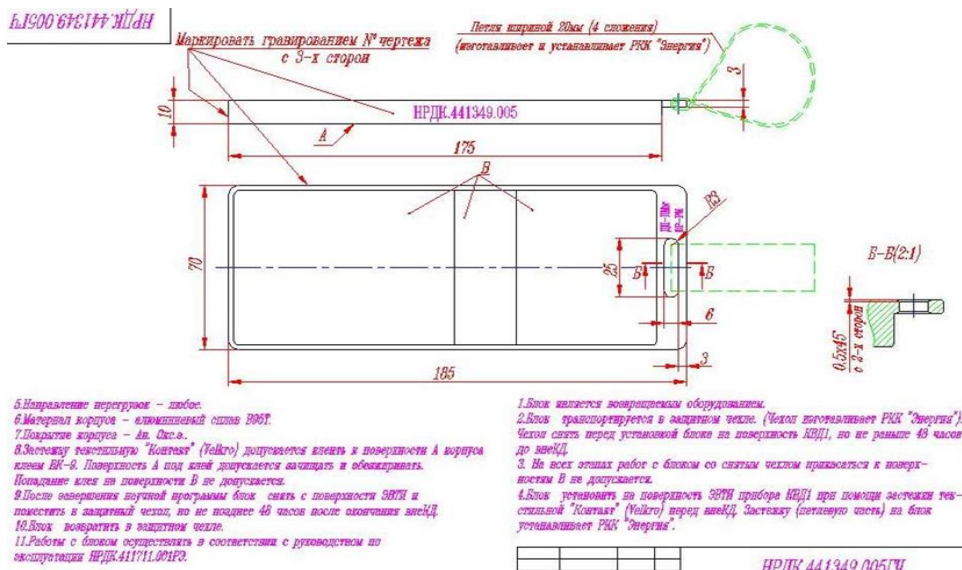


Fig. 2. Dimensional drawing of the DP-PM block

Certain requirements are imposed on the design of the DP-PM facility for solving experimental problems while simultaneously limiting the dimensions, connecting dimensions, weight, and appearance.

The developed DP-PM block meets the requirements of the program and methodology for conducting the DP-PM experiment, which is presented below:

1. Check the complete device package and documentation

The check is carried out in accordance with the current methodology, designations, markings, the presence of seals and factory numbering of the unit, as well as the availability of documentation required for testing.

2. Check the appearance, dimensions, connection dimensions and weight

2.1. Appearance check

The DP-PM block must be free of pores, dents, cracks, scratches on the protective coatings and other defects that affect the quality of the surface, compromising the subsequent studies of the quality of the samples. The marking must correspond to the dimensional drawings of the block. The device meets these requirements.

2.2. Check dimensions and connection dimensions

Checking the overall and connecting dimensions is carried out with measuring instruments having an accuracy of at least 0.1 mm.

Requirements for the dimensions of the DP-PM block are up to $200 \times 100 \times 20$ mm.

The manufactured block DP-PM has dimensions of $185 \times 70 \times 10$ mm.

2.3. Check the weight of the device

The mass of the product must not exceed 300 g, including the experimental samples contained in it, and must be checked on a balance with an accuracy of ± 50 g.

The mass of the Technological Model (TM) with experimental samples is 260 g, the mass of the Aircraft Model (AM, flying model) with experimental samples and loop grip is 268 g.

3. Vacuum tests

The DP-PM block is placed in a vacuum chamber. Its performance is checked in accordance with the procedure, then the pressure in the chamber is reduced to 10^{-4} and the unit is kept under these conditions in the chamber for 1 hour.

4. Test for high / low operating temperature

The tests are performed in a thermal chamber.

For the DP-PM installation the operating temperatures are from -50 °C to $+50$ °C.

The operability is checked in accordance with this methodology.

4.1. Check heat resistance at transport temperature

The DP-PM block is installed in a non-working state in a thermal chamber.

The chamber is heated to a temperature of $+50$ °C, the device is kept for three hours. The heating of the chamber is turned off and the temperature is set ($+20$ °C). The device is kept under these conditions for 2 hours and they begin to check the operability of the device using this methodology.

4.2. Check for cold resistance at transport temperature

The DP-PM block is installed in a non-working condition in a thermal chamber.

The chamber is cooled down to -50 °C, the device stays for 3 hours. The chamber heater is turned off, the temperature is reached ($+50$ °C) and the device is kept under these conditions for 1 hour.

5. Check for moisture resistance

The DP-PM block is placed in the humidity check chamber. After reaching the required test mode - temperature $+25\text{ }^{\circ}\text{C} \pm 10^{\circ}\text{C}$ and humidity $95 \pm 3\%$, the block stays in the chamber for 48 hours. The chamber turns off. Remove and temper under normal weather conditions for at least 3 hours.

6. Vibration resistance tests for sinusoidal accelerations at a frequency of 25 Hz

The DP-PM block is mounted on the plate of the vibrating stand by means of Velcro in the operating position. The vibrating stand is set at a frequency of 25 Hz, acceleration 2 g, and the block is vibrated for 30 minutes. At the end of the test, the block is removed from the hob, visually inspected for mechanical damage or background noise. After the test, no mechanical damage was observed, the integrity of the experimental samples, the surface contacts and the operability of the DP-PM block were established.

7. Impact test or linear load test

The DP-PM block must operate under conditions of external influencing factors that supplement and clarify the requirements for equipment according to OST 92-5100-2002.

The DP-PM block is fastened with Velcro to the platform of the impact stand. The test is carried out in accordance with the operating instructions on the bench, with a load of 40 g, pulse duration of 1–3 s, three impacts on each of the three mutually perpendicular axes of the block (18 strokes in total). The stand is turned off, the block is removed, an external inspection is carried out to identify mechanical damage and performance.

The DP-PM block does not need power supply and has no electronic elements. It is a mechanical structure, therefore all the requirements are mechanical and therefore, the block was subjected only to the necessary series of thermal and mechanical tests and subsequent incoming inspection in accordance with the technical requirements for the space experiment "Obstanovka 1-step" on the Russian segment of the International Space Station.

After the successful conducting of the tests of the Technological Model (TM) according to the approved methodology, two DP-PM blocks were manufactured. A Flight Model (LM), designed for full-time tests and one block DP-PM (GL - main model), intended for training a cosmonaut-operator in a hydro-laboratory pool. All samples are structurally identical.

The second stage of the project is connected with the development of a methodology, according to which the operator-cosmonaut trains in the hydro-laboratory pool. The goal is to make every action work and that each action is performed from the extraction of the block from the transport bag to its installation on the surface of the PWC1 (plasma wave complex), through the simulation of the

real environment in outer space. Both cosmonauts take part in each training session, each time wearing gloves that simulate the real conditions of mounting the block on the outside of the ISS in orbit.

The third stage is associated with the development of a methodology for delivering the DP-PM unit to the ISS, as well as installation on its outer side [5].

On April 12, 2013, the DP-PM unit was delivered by the Progress M418 transport spacecraft to the ISS. On April 19, 2013, it was taken out and installed by cosmonauts Pavel Vinogradov and Roman Romanenko on the outer side of the ISS, on the plasma-wave complex (PWC) through “Velcro” (Fig. 3).

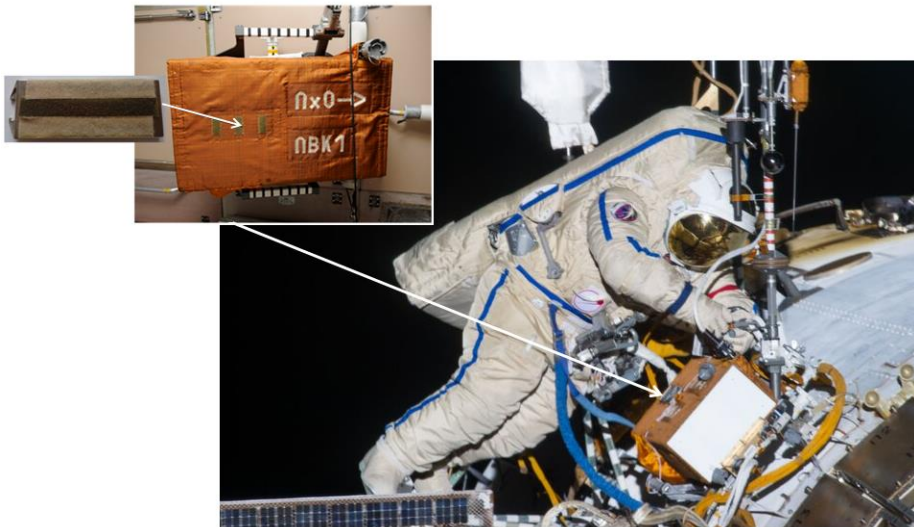


Fig. 3. Cosmonaut Pavel Vinogradov, Plasma Wave Complex (PWC) and DP-PM block installation

The fourth stage of the experiment "Obstanovka 1-step" includes the dismantling of the DP-PM unit in strict accordance with the special dismantling methodology [6–8] developed by SRTI-BAS, IKI-RAN and approved by RSC Energia.

After a stay of 2 years and 4 months, on August 10, 2015, the DP-PM block was dismantled from the surface of PWC1 without disrupting the operability of the plasma-wave complex (PWC1), which includes measuring equipment. The unit was dismantled and brought on board the ISS by cosmonauts Gennady Padalka and Mikhail Kornienko. All requirements are met to prevent mechanical damage to the surface of the samples and the integrity of the installation, as well as contamination when it is stored in the operator's bag.



Fig. 4. Hermetic container for storage of the DP-PM block

When storing the DP-PM unit on board the ISS, there are no special requirements for the composition of the atmosphere, humidity, and hermetic degree. The airtight container (Fig. 4) guarantees that the samples will not be damaged or contaminated during the storage of the facility on board the ISS, as well as during its delivery to Earth.

The methods for assembling and disassembling the DP-PM block are extremely accurate. Each action of the cosmonaut is described in detail, starting with opening the hatch and ending with its closing after the cosmonauts have completed their work in outer space. This includes an accurate timeline of the cosmonauts' activities. The entire process is monitored and controlled by the Mission Control Center in the Moscow Region.

The requirements for the delivery of the DP-PM block to Earth are identical to the requirements for the delivery of the DP-PM block on board the ISS. They are performed in accordance with the instructions of PKK "Energy" [8].

On September 12, 2015, the Soyuz TMA-16M transport spacecraft with a crew consisting of cosmonauts Gennady Padalka (Russia), Aiden Aimbetov (Republic of Kazakhstan) and astronaut Andreas Mogensen (Denmark) was launched from the International Space Station to Earth. On the same day, the lander vehicle landed in Kazakhstan (146 km southeast of the city of Zhezkazgan).

After the delivery of the DP-PM block from the ISS to Earth, in accordance with the requirements for ensuring the further safe operation of the samples, the block was first subjected to microbiological examination and autoclaving in accordance with the instructions (recommendations) of PKK Energia.

Results

The technological experiment DP-PM, which is part of the space experiment "Obstanovka 1-step", was successfully completed in the period 19.04.2013 - 10.08.2015 on the Russian Segment of the International Space

Station. The DP-PM block was launched (taken out) into outer orbit, was in space and returned to Earth intact, unharmed, and undamaged, both on itself and on the experimental samples.

Two separate methodologies have been developed based on modern methods for analysis and determining the influence of outer space on both materials: graphite samples with a glassy carbon coating and a newly created composite of B95 (7075) aluminium alloy with a quantitative addition of ultradisperse diamond powder and tungsten.

The methodology includes a precisely selected and complex set of spectroscopic, mechanical, and physical methods for characterizing the physicochemical, structural, and morphological changes that have occurred under the influence of space conditions.

The authors of the article express their gratitude to a number of organizations that have contributed to the implementation of the project and are practically co-authors of this article:

ИКИТ – БАН – П. Гецов, Р. Недков, **Г. Станев,** С. Нейчев ;

ИКИ РАН: В.С. Трошин . **Д. Мягких, А. М. Бородкин, Г. Е. Баранова, А. С. Григорьев;**

ПАО «РКК „Энергия” им. С.П. Королёва: **В. П. Коношенко, И. В. Чурило,**

В. Г. Осипов

НИИ Центр подготовки космонавтов им. Ю.А. Гагарина: **В. И. Васильев, П. Виноградов, Р. Романенко, Геннадий Падалка, Михаил Корниенко;**

Acknowledgements: This work is financially supported by the Bulgarian National Science Fund under Project KP-06-H27/2, 08.12.2018.

References

1. Klimov, S., V. A Grushin, K. Balajthy, [D. Bachvarov], S. M. Belyaev, J. Bergman, Cs. Ferencz, K. Georgieva M.P Gough, [A. B. Belikova], L.D. Belyakova, T. V. Grechko, V. P. Konoshenkov, V. E. Korepanov, B. Kirov, O. V. Lapshinova, J. Lichtenberger, A. Marusenkov, M. Morawski, J. Z. Nagy, [R. Nedkov], D.I. Novikov, V. G. Rodin, H. Rothkaehl, G. Stanev, S. Szalai, P. Szegedi Studying of Space weather electromagnetic parameters of ionosphere in “Obstanovka 1-Step” experiment on the Russian segment of the ISS, Space Engineering and Technologies, 2021, **1** (32), 20–41 p. (in Russian). DOI 10.33950/spacetech-2308-7625-2021-1-20-41

2. Teodosiev, D. K., I. D. Pechenykov, J. S. Georgiev, et al. Method for impregnation and coating of porous refractory materials with glassy-carbon, Bulgarian Certificate of Authenticity № 31847, МКП С 04 35/84, 1982; (in Bulgarian).
3. Stanev, G., M. Petrunova, D. Teodosiev, et al. Pimenov and S. Bilichenko, An Instrument for DC Electric Field and AC Electric and Magnetic Field Measurements Aboard "Intercosmos-Bulgaria-1300" Satellite, Adv. Space Res., 1982, 2 (7), 43–47; (in Bulgarian).
4. Program and methodology for acceptance and design and development tests of the DP device for measuring the potential of the ISS body, NRDК. 412131.000 PM; (in Russian).
5. Method of work on the installation of DP-PM, which is part of the plasma-wave complex (PWC), when implementing the SE "Obstanovka (1-step)", ID.PK 545-04- 12 / 04.2012; (in Russian).
6. Method of work for dismantling the DP-PM, which is part of the plasma-wave complex (PWC), during the implementation of the SE "Obstanovka (1-step)", ID.PK 545-04-08 / 11.2014; (in Russian).
7. Methodological requirements for the dismantling of the DP-PM block;(in Russian).
8. Methodological note on removing the DP-PM block from the board; (in Russian).

**КОСМИЧЕСКИ ЕКСПЕРИМЕНТ „ОБСТАНОВКА (1 - ЕТАП)",
БЛОК ДП – ПМ НА РУСКИЯ СЕГМЕНТ НА МЕЖДУНАРОДНАТА
КОСМИЧЕСКА СТАНЦИЯ**

*А. Бузекова–Пенкова, С. Климов, В. Грушин, О. Лапинова,
Д. Новиков, Д. Теодосиев*

Резюме

В настоящата работа е описана методиката на осъществяване на технологичен експеримент ДП-ПМ, който е част от космическия експеримент „Обстановка 1-етап”. Блок ДП-ПМ е бил монтиран на Руския сегмент на международната космическа станция в периода 19.04.2013–10.08.2015. Целта на експеримента е изследване на влиянието на открития космос върху качествата на графитни образци със стъкловъглеродно покритие и образци, изработени от алуминиева сплав В95 (7075) с количествена добавка на ултрадисперсен диамантен прах и Волфрам, след продължителен престой в околосемна орбита.

SEM AND EDX STUDY OF GLASSY CARBON COATINGS AFTER AN EXTENDED STAY ON THE INTERNATIONAL SPACE STATION (ISS)

**Boyko Tsyntsarski¹, Anna Bouzekova-Penkova², Urszula Szeluga³,
Georgi Georgiev¹, Petar Tzvetkov⁴, Dimitar Teodosiev²**

¹*Institute of Organic Chemistry with Centre of Phytochemistry – Bulgarian Academy
of Sciences*

²*Space Research and Technology Institute – Bulgarian Academy of Sciences*

³*Centre of Polymer and Carbon Materials – Polish Academy of Sciences*

⁴*Institute of General and Inorganic Chemistry – Bulgarian Academy of Sciences
e-mail: Boyko.Tsyntsarski@orgchm.bas.bg; a_bouzekova@space.bas.bg*

Keywords: *Glassy carbon, Cosmic ray and Gamma radiation, Scanning electron
microscopy (SEM), X-ray spectroscopy (EDX)*

Abstract

Graphite samples covered with glassy-carbon layers, have stayed for 2 years and 4 months under different conditions - terrestrial conditions and on the International Space Station. The influence of outer space on glassy carbon coatings was studied by scanning electron microscopy (SEM), energy dispersive X-ray spectroscopy (EDX), Raman and infrared spectroscopy. The results show presence of some defects and heteroatoms (traces of O, F, Na, Cl) after staying in space, probably due to radiation and other effects. SEM data provide valuable information about the existence of undamaged glassy carbon layer with thickness of 20 μm . There are no structural changes in the layers of glassy carbon after stay in space. Data show that these materials can be successfully applied for electrical field measurements in ionosphere.

Introduction

Glassy carbon belongs to the family of carbons, which have the ability to form a variety of carbon allotropes (sp, sp², sp³) [1–4], resulting in complex and versatile microstructure of glassy carbon. Glassy carbon is a black non-transparent material, which have found application as antireflective coatings. Modern physico-chemical methods, like XRD and Raman spectroscopy, help to characterize glassy carbon structures [1–4]. The carbonization of thermosetting resins (poly-aryl acetylene, furfuryl alcohol, phenolic resins) in atmosphere leads to formation of low-ordered, non-graphitizing carbon-based material, denoted ‘glassy carbon’ (GC, known also as vitreous carbon or glass-like carbon). Glassy carbon is a stiff, fragile material, and it exhibits a surface fracture, similar to that presented by the glass (conchoidal fracture), which explains the term “glassy”. Unlike graphite, glassy

carbon is a hard and isotropic material. Besides, glassy carbon low impermeability towards molecules of gases and liquids, excellent chemical and thermal stability, very good thermal and electrical conductivity. Glassy carbon is applied in many fields – electrochemical devices and sensors, energy storage, wastewater decontamination, tools for precision molding, ablative shields. Due to its good biocompatibility, glassy carbon may be also used in medical applications μm heart valves, implants, tissue regeneration [4–7].

In connection with the development of the technique for measuring constant and alternating electric fields in space plasma, various materials are developed and used for the preparation of satellite probes. The increased requirements for these materials are determined mainly by the requirement to increase the accuracy and sensitivity of the measurements. The accuracy of measuring constant and alternating electric fields by the double probe method strongly depends on the variations of photoelectron work function at the surface of each probe in inhomogenous ionosphere-magnetosphere [8–9].

The technology used for the production of spherical probes for measuring electric fields on boards of the satellites IC-Bulgaria 1300, IC-24 Active, IC-25 APEX, INTERBOL-2, the sub-satellites Magion-2, Magion-3, Magion-4, Magion-5 and ISS, for the period from 1981 till now, is invented in Bulgarian Academy of Sciences [8–14], whereas spherical probes with glassy carbon coatings were tested in laboratory conditions, simulating those in outer space (sudden temperature changes, shock and vibration loads, etc.), and then implemented in scientific equipment on the boards of the above mentioned satellites.

To verify and confirm the results of earth laboratory tests, and also to study the effects of the influence of outer space on the physico-chemical and structural properties of glass-carbon coatings, the technological experiment DP-PM was planned and conducted within the international project "Obstanovka 1-stage", aboard the Russian module of the ISS. For this purpose, graphite samples (30×15×8 mm) were prepared, covered with glassy carbon, and placed in the DP-PM block, which is a container made of aluminum alloy with total dimensions of 185×70×10 mm.

This work is dealing with glassy carbon preparation and its physico-chemical properties, before and after stay in space. The research presented is a continuation of our previous investigations on the same topic [15]. New samples are studied, whereas the analysis and the interpretation of the obtained results are expanded. The aim is to improve the knowledge on the resistance of glassy carbon coatings, deposited on graphite samples, which have stayed in outer space for a long time. The changes in the integrity and structure of the glassy carbon coating are further investigated. The obtained results allow to assess its applicability for the purpose of studying phenomena in the conditions of outer space.

Experimental

Materials

The investigations were performed with two graphite samples covered with glassy carbon. The first sample is called “reference” sample, and it stayed on the earth, and the second sample, called “space” sample, was located on the outer surface of International Space Station (ISS) in the open space. The “space” sample is subjected to radiation (cosmic radiation), which could vary in nature and quantity, according to ISS orbit, ISS coordinates, geophysical and heliophysical conditions. The sample was subjected to temperature changes in wide temperature interval, from down to -120°C up to $+150^{\circ}\text{C}$, every 2 h, for a period of 2 years and 4 months.

Methods of characterization

In the present work, an assessment of the changes in “space” samples (cut to investigate the inner morphology), as a result of the cosmic conditions, and comparison with the “reference” samples have been made, by using different methods.

The morphological study was performed using scanning electronic microscope FEI Quanta 250 FEG, with high vacuum and beam deceleration, using an accelerating voltage of 10.0–15.0 kV. FEI Quanta 250 FEG is a large stage environmental SEM with BF/DF STEM detector (Fig. 1).

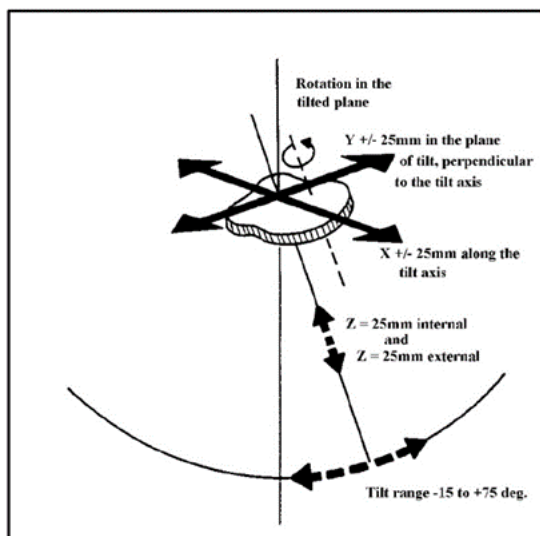


Fig. 1. Scheme of SEM experiment

The equipment has low and extended vacuum mode up to 1000 Pa (ESEM), temperature control range -25° to $+55^{\circ}$, and EDX chemical analysis

including elemental and phase mapping. It is possible to perform X-ray mapping of low-Z elements at low voltages. X-Ray Microanalysis (EDX or EDX or sometimes referred to also as EDS analysis) is a technique used for identifying the elemental composition of the specimen, or an area of interest thereof. It works as an integrated feature of a scanning electron microscope (SEM) and cannot operate on its own without the latter. Raman experiments ($4000\text{--}400\text{ cm}^{-1}$) are performed using Bruker Senterra II Raman Apparatus, with 1 cm^{-1} spectral resolution, and 514.5 nm laser.

Attenuated Total Reflection Fourier-Transformed Infrared Spectroscopy (ATR-FTIR) ensures solid (transparent or non-transparent) and liquid samples to be studied directly. ATR-FTIR spectra are collected using infrared spectrophotometer Bruker Tensor 27, at wavenumber $4000\text{--}600\text{ cm}^{-1}$, resolution 0.5 cm^{-1} , with MIRacle-Diamond/ZnSe Crystal Plate ATR accessory - Pike technology.

Results and discussion

SEM and EDX analysis

The structure of glassy carbon was explored using scanning electron microscopy (SEM). Morphology of glassy carbon obtained by SEM is shown in Fig. 2 and Fig. 3. Electronic microscope images of the samples, oriented to different directions, are performed. Samples are oriented with the upper side up (electronic beam is running down the sample, which is on the bottom of the chamber), back side up, and lateral side up.

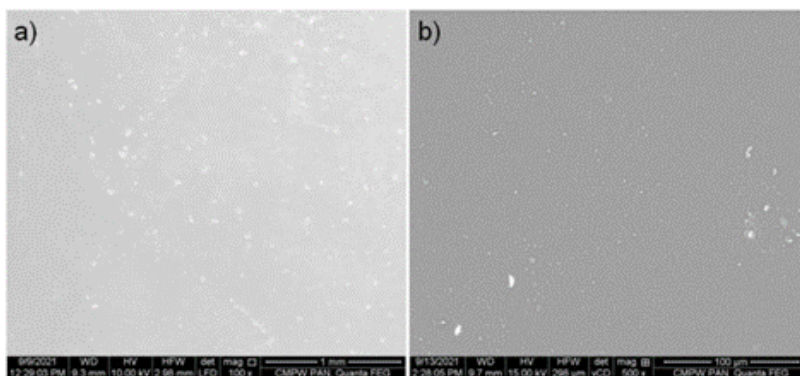


Fig. 2. SEM images of the “reference” sample at different magnification – 1 mm (a) and $100\text{ }\mu\text{m}$ (b)

In Fig. 3a there are shown some traces on glassy carbon surface, which follow the morphology of graphite support. This is an indication of small disturbances in the glassy carbon coating, that occurred during the stay of the

material in outer space. However, traces are negligible ($< 1 \mu\text{m}$), and they do not noticeable affect the overall coating electrical characteristics of the sample.

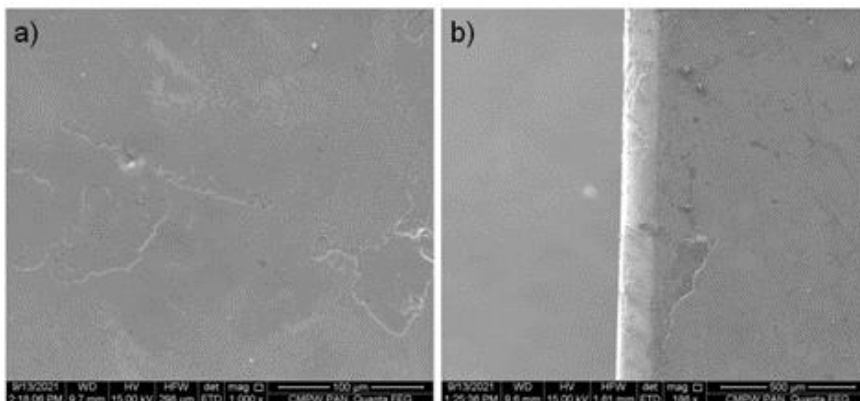


Fig. 3. SEM images of the “space” sample. Image of a) back side and b) lateral side (cut cross-section) under 45°

To observe the glassy carbon layer and graphite layer, the sample holder is rotated to 45° and on the SEM image lateral side (cut cross-section) under 45° stage rotation is seen in Fig. 3b. The image in Fig. 3b confirms the presence of glassy carbon (thin light layer) and graphite (right part of the image). The light layer under angle of 45° is around $25 \mu\text{m}$ wide.

SEM data provide valuable information about the existence of undamaged glassy carbon layer with thickness of $20 \mu\text{m}$.

EDX study (Fig. 4) shows the elemental analysis on the glassy carbon surface. The main element is carbon (more than 90 wt. %). The results show presence of some defects and heteroatoms (traces of O, F, Na, Cl) after staying in space, probably due to radiation and other effects (space contamination, contact with other devices, transportation, synthesis technology of glassy carbon layers).

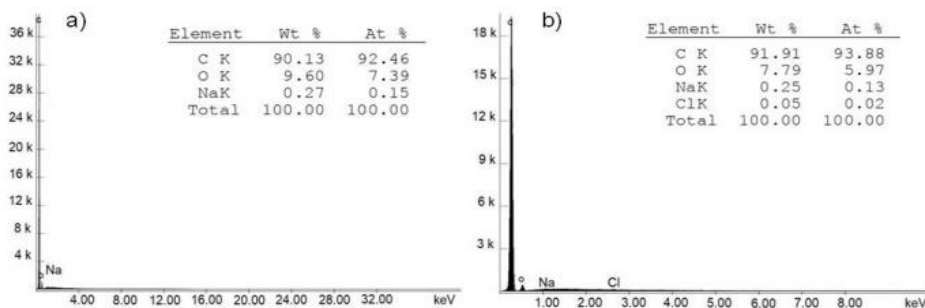


Fig. 4. EDX results for the a) “reference” sample and b) “space” sample

Raman analysis

Raman study was carried out with all the samples (in 2–3 points for every sample), and the Raman spectra are shown in Fig. 5 and Fig. 6.

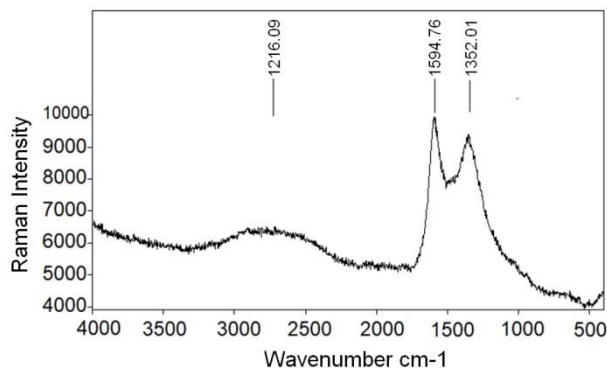


Fig. 5. Raman spectrum of the “reference” sample [15]

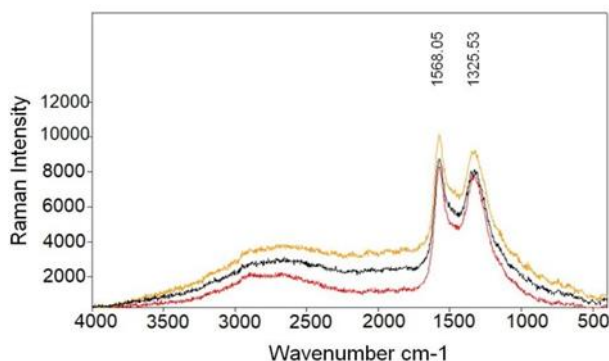


Fig. 6. Raman spectrum of the “space” sample (measured in three different points)

Fig. 5 and Fig. 6 show Raman spectra of “reference” and “space” samples, respectively. Two main Raman bands are detected for both samples – D band (D for defect, representing the disordered structures) around 1350 cm^{-1} and G band located around 1580 cm^{-1} . G-band (G for graphite) arises from the stretching of the C–C bond in graphitic materials and is characteristic for all sp^2 carbon systems.

The presence of D- and G- Raman bands with equal intensity are characteristic for existence of glassy carbon layer.

FTIR analysis

Attenuated Total Reflection Fourier-Transformed Infrared Spectroscopy (ATR-FTIR) Spectra of the samples (back) are shown on Fig. 7.

There are almost no surface groups detected on the reference sample.

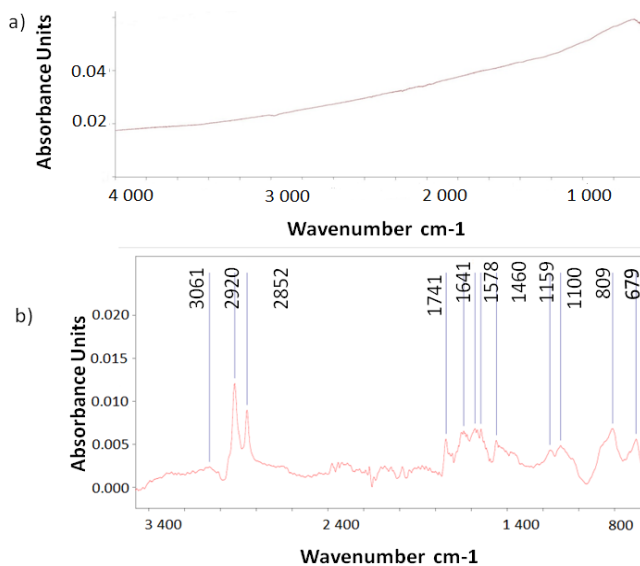


Fig. 7. ATR-FTIR spectra of a) “reference” and b) “space” samples

In the IR spectra of space sample there are bands at 3000–2800 cm^{-1} , associated to aliphatic C-H stretching vibrations at 3000–2800 cm^{-1} , as well as C-H deformation vibrations in the region 1450–1350 cm^{-1} , due to aliphatic structures. The band at 1740 cm^{-1} is assigned to stretching vibrations of C=O. The bands at 1700–1500 cm^{-1} could be due to aromatic ring stretching vibrations or C=C bonds in aromatic structures. The bands detected in the region of 1200–1000 cm^{-1} are assigned to C–O in ethers or ring structures.

Data obtained from IR spectroscopy show, that on the surface of the space sample different surface groups are detected – aliphatic and aromatic C–H groups, carbonyl groups C=O, hydroxyl groups O-H, C=C structures, etc. Most probably formation of surface groups and surface species on the space sample is due to oxidation of the exposed parts of the graphite pad as a result of violations of the glassy carbon coating that occurred during the stay in open space.

Conclusions

Our results show that glassy carbon coatings, due to their hardness and chemical inertness, can stay years in outer space in order to collect accurate data on the plasma parameters. No substantial change was detected in the structure of the glassy carbon layers due to stay in space. The glassy carbon coatings deposited onto graphite substrate can be successfully used for electrical field ionosphere measurements.

The results show presence of some defects and heteroatoms (traces of O, F, Na, Cl) after staying in space, probably due to radiation and other effects.

Acknowledgements: This work is financially supported by the Bulgarian National Science Fund under Project KP-06-H27/2, 08.12.2018.

References

1. Kharissova, O. V., B. I. Kharisov, C. M. Oliva Gonzalez, Carbon-carbon allotropic hybrids and composites: synthesis, properties, and applications, *Ind. Eng. Chem. Res.*, 2019, 58, 3921-3948. <https://doi.org/10.1021/acs.iecr.8b05857>
2. Uskokovic, V. Disordering the disorder as the route to a higher order: incoherent crystallization of calcium phosphate through amorphous precursors, *Cryst. Growth Des.*, 2019, 19(8), 4340-4357.
3. Inagaki, M., *New carbons: control of structure and functions*, Elsevier, 2000, 1-13.
4. L. de Souza Vieira. A review on the use of glassy carbon in advanced technological Applications, *Carbon*, 2022, 186, 282-302. <https://doi.org/10.1016/j.carbon.2021.10.022>
5. Field, J., M. Swain. The indentation characterisation of the mechanical properties of various carbon materials: glassy carbon, coke and pyrolytic graphite, *Carbon* 1996, 34, 1357-1366. [https://doi.org/10.1016/S0008-6223\(96\)000711](https://doi.org/10.1016/S0008-6223(96)000711).
6. Gaefke, C., E. Botelho, N. Ferreira, M. Rezende. Effect of Furfuryl alcohol addition on the cure of furfuryl alcohol resin used in the glassy carbon manufacture, *J. Appl. Polym. Sci.* 2007, 106, 2274-2281. <https://doi.org/10.1002/app.26938>
7. Pesin, L., Review: structure and properties of glass-like carbon, *J. Mater. Sci.*, 2002, 37, 1-28. <https://doi.org/10.1023/A:1013100920130>.
8. Teodosiev, D., N. Isaev. Physicochemical Properties of Probes for Measuring Electric Fields in the Near-Earth Plasma, *Chem. Phys. Reports*, 2001, 19(6), 1165 et al. 1175.
9. Teodosiev, D. K., I. D. Pechenykov, J. S. Georgiev, P. A. Petrov, R. P. Dobrev et al, Method for impregnation and coating of porous refractory materials with glass-carbon, Bulgarian Certificate of Authenticity № 31847, MKII C 04 35/84, 1982 (in Bulgarian).
10. Stanev, G., M. Petrunova, D. Teodosiev, I. Kutiev et al. An Instrument for DC Electric Field and AC Electric and Magnetic Field Measurements Aboard "Intercosmos-Bulgaria-1300" Satellite, *Adv. Space Res.*, 1982, 2(7), 43-47. [https://doi.org/10.1016/0273-1177\(82\)90146-6](https://doi.org/10.1016/0273-1177(82)90146-6)
11. Teodosiev, D., G. Stanev, G. Galev, S. Neichev, P. Pushchaev. Spherical probes for measurements of electric fields on the INTERBALL-2 satellite in the IESP-2M instrument, *Cosmic Research*, 2000, 38(6), 574-578. <https://doi.org/10.1023/A:1026690701594>
12. Triska, P., J. Vojta, A. Czapek, D. Teodosiev, G. Galev, I. Shibaev. Measurements of electromagnetic ULF fields onboard the Magion-4 satellite: The ULF experiment, *Aerospace Research in Bulgaria*, 2003, 17, 47-53. https://www.researchgate.net/publication/252423766_Measurements_of_electromagnetic_ULF_field_onboard_the_Magion-4_satellite_the_ULF_experiment

13. Teodosiev, D., P. Nenovski, P. Hristov, R. Koleva, J. Vojta et al, ULF wave measurements aboard the Magion-4 subsatellite: narrow-band wave events observed in the magnetopause regions, *Planetary and Space Science*, 2005, 53 (1–3), 317–326. <https://www.doi.org/10.1016/j.pss.2004.09.058>
14. Bouzekova-Penkova, A., R. Nedkov, G. Stanev, S. Klimov et al. Technological Experiment "Environment" on board the International Space Station, *Journal of BAS* 5/2017, ISSN 0007-3989, 2017, 22–26 (in Bulgarian).
15. Teodosiev, D., A. Bouzekova-Penkova, K. Grigorov, R. Nedkov, P. Tzvetkov, B. Tsyntsarski, A. Kosateva, S. Klimov et al. Structural and mechanical properties of glass-carbon coatings after an extended stay on the International Space Station (ISS), *Comptes Rendus de L'Academie Bulgare des Sciences*, 2021, 74(2), 197–206. <https://www.doi.org/10.7546/CRABS.2021.02.05>

SEM И EDX ИЗСЛЕДВАНЕ НА СЪТКЛОВЪГЛЕРОДНИ ПОКРИТИЯ СЛЕД ПРОДЪЛЖИТЕЛЕН ПРЕСТОЙ НА МЕЖДУНАРОДНАТА КОСМИЧЕСКА СТАНЦИЯ (МКС)

*Б. Цинцарски, А. Бузекова-Пенкова, У. Шелуга, Г. Георгиев,
П. Цветков, Д. Теодосиев*

Резюме

Образци от графит, покрити със стъкловъглеродни слоеве, са престояли 2 години и 4 месеца при различни условия – земни условия и на Международната космическа станция. Влиянието на космическото пространство върху стъкловъглеродните покрития е изследвано чрез сканираща електронна микроскопия (SEM), енергийно дисперсионна рентгенова спектроскопия (EDX), раманова и инфрачервена спектроскопия. Резултатите показват наличие на някои дефекти и хетероатоми (следи от O, F, Na, Cl) след престой в Космоса, вероятно поради радиация и други ефекти. SEM данните предоставят ценна информация за съществуването на ненарушен стъкловъглероден слой с дебелина 20 μm . Няма структурни промени в слоевете стъкловъглерод след престой в Космоса. Данните показват, че тези материали могат успешно да се прилагат за измерване на електрическо поле в йоносферата.

OPPORTUNITIES TO OPTIMIZE THE MANAGEMENT OF AEROSPACE PROJECTS

Nadia Marinova

*New Bulgarian University
e-mail: nmarinova@nbu.bg*

Keywords: *Aerospace projects, Global satellite systems, Optimizing, Single dynamic model of the Earth*

Abstract

The creation and effective functioning of global satellite systems will allow to create an information base for solving problems related to the regeneration and rational use of natural resources, the creation of a single dynamic model of the Earth, including geological, climatic, biosphere, ecological and social factors.

Great attention should also be paid to the problem of increasing the safety of human life in the conditions of the rapid development of intercontinental transport links.

Introduction

The well-being of a society directly depends on the ability to provide funds for the development of the most science-intensive and technically advanced industries, which in the future will play the role of the "locomotive" of the economy. An example of this can be the automotive industry in the USA or the electronics industry in Japan.

It became obvious that the new era in the development of humanity is in outer space and is connected with the absorption of the energy of the Sun, the Cosmos and its inexhaustible resources.

Without space, space technology and space research, humanity has no future, no opportunity to solve the key problems of its development. They can include energy provision, informatics and food provision and the problems of preserving the living environment.

The main trends in space activity in the 21st century will be related to increasing the saturation of the information space, which will raise the information security of the countries and their population to a qualitatively new level, directly related to their intellectual potential. The problems of access to information, the services of global information networks, data banks and knowledge bases - all this

is unthinkable without promising information technologies, including space methods and means of communication.

Another important aspect of society's life is the problem of the state of the environment. The anthropogenic impact on it reached levels at the end of the 20th century, exceeding which, without taking adequate measures for its protection, can lead humanity to disasters and environmental catastrophes. All forms of impact on the environment become critical - pollution, entry of harmful substances into the air and water environment, degradation of the soil and the ozone sphere, the greenhouse effect.

A key problem in this sense is the creation of systems for monitoring environmental parameters, the state of hazardous productions and predicting the occurrence of dangerous phenomena. This problem is solved globally with the help of space tools for remote sensing of the Earth and atmosphere.

Such priority research and applied tasks as:

- the study of planetary processes, including the dynamics of the atmosphere and the ozone layer, the radiation balance of the planet and the evolution of climate, the biochemical and hydrological cycles of the planet, the global processes in the mesosphere and the world ocean;

- research and control of regional and local mineral deposits, reporting and control of natural resources and sources of environmental pollution;

- study of solar-terrestrial connections and their impact on the biosphere, human activity and human health;

- researching the causes, discovering the prerequisites and controlling the consequences of natural destructive processes (typhoons, earthquakes, floods and other environmental catastrophes).

Remote methods of Earth research are part of the world community's efforts to preserve and restore ecosystems, solve global problems of energy and food security. In this regard, the task of effective international integration has no alternative. The "Mission for Planet Earth" program is also in this spirit.

The creation and effective functioning of global satellite systems will allow to create an information base for solving problems related to the regeneration and rational use of natural resources, the creation of a single dynamic model of the Earth, including geological, climatic, biosphere, ecological and social factors.

Great attention should also be paid to the problem of increasing the safety of human life in the conditions of the rapid development of intercontinental transport links.

Many factors suggest the creation of a global navigation system with high accuracy, allowing users to receive information about their own position on Earth or in space around Earth at any time. In combination with space vehicles, these systems as a close prospect can provide effective guidance of the movement of all types of transport, taking into account the high safety requirements. As a more distant perspective, they can become an integral part of personal monitoring

systems, including health monitoring. The COSPAS/SARSAT system has already helped to save more thousands, and the prospective personal monitoring system could be several times more effective.

Of great interest are the possibilities of using the conditions of orbital flight (weightlessness, vacuum) to create substances and materials with properties unattainable on Earth. To date, thousands of experiments have been carried out on spacecraft to study problems in castings, crystallization in weightlessness, obtaining compositions from substances immiscible in terrestrial conditions, and also obtaining ultrapure biologically active substances, drugs and other biological preparations.

One of the key issues for the exploitation of space will be the provision in the future of opportunities for life with productive human activity in the conditions of orbital flight and on planets of the Solar System, which will become the basis for the exploitation of interplanetary space.

Orbital stations, transport, and cargo ships, means of extra-orbital activity, robotic means, etc., are imposed as the main place for solving the mentioned problems. A large volume of research and experiments in space medicine and biology, research of Earth's natural resources, space technologies, astrophysics, development of new types of scientific apparatus and methods for solving research tasks in space and from space is carried out on board the orbital stations. All this, in turn, is used in the creation of the specialized automatic systems for the International Space Station.

The creation and operation of longer-life space facilities is a long-term trend in the strategy of the major space powers – the USA, Russia, China, etc.

One of the main tasks that will be solved at the ISS is remote research of the Earth and environmental monitoring, which also includes the development of new methods and means of remote research and environmental monitoring.

Such projects are valued in the billions of dollars to achieve several goals:

- promoting commercialization in space research,
- expanding international ties by including international partners
- continuous development of space science and technology.

Space stations are being built as science laboratories in low Earth orbit, offering a variety of conditions (eg, power, low-gravity environment, manpower and laboratory space) that can be used by NASA, RKA (Russia), ESA (Europe) and other countries with space exploration ambitions. The station is a very complex, multidimensional R&D project for which good management is an essential necessity.

Several possible options and their implementation for the operation, pricing and evolution of the space station and the range of benefits to be obtained by users have been developed. Although it is sometimes difficult to accept, prices affect behavior and sample usage, which in turn affects the bottom line of any project intended to operate over a long period of time. Modern economic analyzes

arm us with an apparatus for examining these applications and evaluating their impact on desired ends.

An economic theory that offers the most predictions is the "theory of mechanisms" or the "theory of implementation."

The basic framework of this organizational design theory is based on two key hypotheses:

First, the information that is needed to achieve organizational goals is initially scattered and difficult to discover through simple observation;

Second, individuals disclose this information and comply with instructions and requirements only if it is in their best interest to do so.

The designer of the institutional rules that determine who does what and says it to whom and who performs what actions may do nothing about the initial distribution of information or the motivations of the various actors in the organization. The designer can only optimize the subject of organizational goals to informational and incentive constraints. But within these constraints there can be a wide range of options, some of which will be much more desirable than others.

According to the model of this theory, first a description of the space station environment (those features of the design that are not really under the designer's control) is presented, then some of the objectives to be achieved are briefly given, and finally some options for competitive pricing.

The space station is a multiple product that is highly uncertain (unstable), and that is a public enterprise, i.e. has a wide range of users from the public and private sectors. Like any product, it includes technology and costs, consumption and benefits, pricing objectives. What determines their content:

First - from the technology and costs. Each space station (SC) is a complex public facility. The basic intensive initial capital investment produces a real-life facility that provides a flow of resources all the time, requiring correspondingly low and possibly relatively constant per-unit operating costs. But the differences between the CS and the standard facility are important. At KS, the technology is not well described and understood. The uncertainty exists because this technology has never before operated in space on this scale. Second, the resources to be produced are also required as inputs: power must not only be provided to the users of the CS, but it is also a necessary input for life support and command systems. Because there is significant uncertainty about how much of these resources will be needed for internal use, there is exaggerated uncertainty about the net values available to users. These costs for internal needs should be known after the CS is fully operational, but for any contractual agreements made in advance this is a significant uncertainty. Likewise, because this technology is new, there is great uncertainty regarding the cost of construction and operation. For this reason, it is a large and complex project for which it is difficult to find comparable (comparable) efforts. Standard public utility or regulated facility models where

there is a satisfactory degree of certainty about technology, costs and requirements are simply not applicable as models for CS.

Second - consumption and benefits. There is already an incredible variety of CS users, but the main five categories relate to: commercial users, science and technology missions of NASA and Russia, other US government users (mainly the Department of Defense), international partners (Canada, the European Space Agency, China, and Japan), and all others. Although each of these classes of consumers presents different problems and limitations in terms of pricing policies, they have one thing in common. The benefits and demand are largely unknown to them and to the CS designers and operators. Economists have absolutely no way of using modern economic analysis to determine demand (and therefore, perhaps, to determine value added to consumers) as can be done in designing pricing policy for public electric facilities. Also, one cannot simply ask potential CS users to state exactly how much of each resource they wish to consume and then plan for the approximate aggregate response. Even if they are certain of their benefits, they have little incentive to reveal all their information. If charging does not depend on their responses, then they have an incentive to exaggerate their needs; if billing depends on their responses, then they have an incentive to claim only meager benefits of use. There is no independent market for the data that NASA and Russia can use to verify the validity of the data. Some data is available through the shuttle missions, which, except for the satellite launches, tend to be short-lived research projects launched virtually free of charge. There seems to be a very tenuous connection between these projects and the long-term ones as we imagine the Space Station. A rule of thumb in pricing or other organizational choices is that information about the correct demand or utility should not be assumed to be available.

Third - pricing goals. To provide reasonable analyzes of alternative pricing policies for CS, one should first analyze the objectives. What does it mean for someone to try to end (deal with) pricing policy? Any economist should expect the desired results to be twofold: first, recovery of some or all of the costs of design, development, and operation; second, effective use of the CS once it is in place.

According to Pareto efficiency, given some individual vector or desired outcomes, the total life cycle cost of the station and all its payloads must be minimized to achieve those outcomes. This is a broader view than just minimizing station costs but is more relevant in a broader economic perspective. Minimizing the station's costs in a way that imposes a significant burden on user costs to build and operate its own payloads would not only be inefficient (Pareto), but could also prove politically risky for NASA, Russia, and other actors.

Three other objectives may be at least as important as the first two: first, the presentation (promotion) of the commercialization of space; second, science

and technology and third, international relations. They are important because they relate to the three main user groups: private industry, NASA's technology and science missions, Russia and other partners, and potential international partners. It is known that projects with a larger organization and with larger total costs and with smaller operating costs are usually not able to satisfy all five objectives at the same time. For example, an ineffective approach to achieving objectives 3 through 5 is to make the station's resources available for free to these users. This obviously goes directly against the goal of cost recovery. Also less obvious is the controversy about effective use. There will be too few users using too many resources. Therefore, although a small number of potential users will benefit from the policy of "free (free) access", a greater benefit can be obtained from a more effective pricing policy. The last three objectives will gain more if the CS is used and operates in as efficient a way as possible and that these objectives can also be thwarted if the pricing policy is ineffective. Efficiency means "more accurate hits" ie. more resources acquired per monetary resource invested, which means the ability to supply more payload of any type.

Can the conflicting goals of reimbursement be resolved in a reasonable way?

For traditional projects with high costs of organization, low marginal (side) costs and a satisfactory degree of certainty, economists propose pricing by maximizing benefits depending on the costs incurred. This policy requires either direct knowledge of demand functions (to calculate the added value (asset balance) for consumers directly) or a tatonemic process with little distortion. No option is available to CS if demand and benefit uncertainty preclude the former, while cost uncertainty (combined with the discovery principle) precludes the latter.

A simple proposal that would meet the cost-recovery goal with little detriment to efficiency would be to charge a single price per payload equal to the cost of the shuttle flight plus a percentage to cover the remaining costs of staying in The Space Station. This is a reasonable policy under only two assumptions:

- first, that the designers, builders, operators and users of the Space Station are one team; agree with the objectives of the Space Station and, although perhaps asymmetrically informed, be prepared to provide all information in their possession upon request;

- second, that none of the users change their decisions as a result of the price they are charged (prices are set only based on costs, not resources).

Conclusion

It is easy to predict what would happen if the "project plus percentage" formula were established. Payloads will be designed to conserve their mass and dimensions, but not their power and personnel, two of the station's resources that are designed to be in a constant state of increased demand. Since station time is not

included in billing calculations, time-consuming missions that require the recruitment of more mission-appropriate specialists will be preferred by users over short missions even when the latter use only a few station resources. Designers try to build the best possible station for the lowest possible upfront (initial) cost. Although they recognize the need to minimize current discounted (discounted) construction and operating costs, the limited congressional budget they are given does not encourage compromise over time. Designers are incentivized to minimize construction costs and hope that operating costs will not be too high. Robotics is ignored - staff will do it. Food preservation methods will be downplayed; shuttle trips will be increased. This will not be done on purpose, it will simply be a reasonable response to the constraints and coercion imposed by the builders. High operating costs mean more expensive, or possibly less, resources once the station is operational. This form of pricing policy clearly leads to inefficiencies and fails to accomplish most of the objectives of the Space Station.

At the stations, almost all easily observable events that can be used for corresponding contracts are composed of the actions of one of the participants and some exogenous (external) event. This is very difficult to separate to the satisfaction of all parties without extensive monitoring and auditing (financial due diligence). Therefore, this type of contingent (conditional) contract is unlikely to lead to effective CS operations. The standard solution to this moral hazard problem is the use of principal-agent (intermediary) contracts.

If moral hazard exists, but it is possible to organize the project so that the uncertainty is either exogenous or under the control of only one of the parties (the agent/intermediary/), and if this agent (intermediary) is less willing to take risk than the others (the principal/principals/), then the effective contract consists in giving the agent (intermediary) full control over the project, thereby giving the agent (intermediary) all the rights to the uncertain benefits and responsibility for the uncertain costs, and paying the others one fixed charge (possibly negative, possibly similarly) that is not contingent (conditional) on any of them. One example: NASA could agree to deliver a fixed vector of resources to each user for some fixed payment (to be negotiated). If NASA is risk neutral, this is the most efficient contract; if any other contract is awarded, there are trade-off terms for it in which both NASA and the user are not very interested.

For large contracts (which include, for example, 1/3 of the designed power to be delivered), NASA is not risk neutral. An efficient contract then involves the agent (intermediary) ceding some of the risk to the principal in return for better trading conditions or for a reduced fixed fee. In profitable operations, this can be done through a revenue-sharing arrangement (for example, the principal receives 20% of the net profit in response to an investment of USD 1,000), but there is no market for most of the results obtained in the CS and therefore in such a contract it must be stipulated under what conditions the resources are to be supplied. A user projecting a large demand for resources over an extended period of time may wish

to receive 20% of the station's realized net resources in return for the payment of some fixed sums in advance. This type of user could conceivably be a private venture capitalist who buys to resell or a large non-US government user such as one of the international partners. This type of contract again admits the risky moral problem, but the consumer assumes this risk in response to some discounts (concessions) in the price.

There are at least three other difficulties with principal-agent (intermediary) contracts. NASA cannot maintain its savings due to Congressional funding (its budget is set by Congress); this blunts her incentives as an agent. Over time, the evolution of CS can be managed to compete with new users and new information; a brokerage contract does not necessarily provide the situationally correct incentives with intensive learning by doing. Finally, many aspects of CS use depend on input provided by both users and CS managers. If it is not possible to organize it in such a way as to isolate the effects of each party, then it is necessary to arrange some form of partnership.

In conclusion, when an output is produced as a result of inputs provided by both parties, and when these inputs cannot be easily observed or separated from external exogenous events, then principal-agent (intermediary) type contracts are inappropriate.

References

1. Crouch, Tom D. *The Bishop's boys: a life of Wilbur and Orville Wright*. New York, W. W. Norton, c1989. 606 p.
2. Winter, Frank H., and F. Robert van der Linden. *100 years of flight: a chronology of aerospace history, 1903-2003*. Reston, VA, American Institute of Aeronautics and Astronautics, c2003. 524 p.
3. Hansen, Ole Steen. *The story of flight*. New York, Crabtree Pub., 2003. 190 p.
4. Taylor, Michael John Haddrick. *The Times aviators: a history in photographs*. New York, HarperCollins, c2005. 192 p.
5. Turner, John Frayn. *Heroic flights*. Barnsley, South Yorkshire, Eng., Leo Cooper, 2003. 279 p.

ВЪЗМОЖНОСТИ ЗА ОПТИМИЗИРАНЕ НА УПРАВЛЕНИЕТО НА АЕРОКОСМИЧЕСКИ ПРОЕКТИ

Н. Маринова

Резюме

Създаването и ефективното функциониране на глобалните спътникови системи ще позволи да се създаде информационна база за решаване на проблемите, свързани с регенерацията и рационалното използване на природните ресурси, създаването на единен динамичен модел на Земята, включващ геоложките, климатичните, биосферните, екологичните и социалните фактори.

Голямо внимание следва да се отдели и на проблема за повишаване на безопасността на човешкия живот в условията на бурното развитие на междуконтиненталните транспортни връзки.

REVIEW OF THE APPLICATIONS OF SATELLITE REMOTE SENSING IN ORGANIC FARMING (PART I)

Milen Chaney, Lachezar Filchev

*Space Research and Technology Institute – Bulgarian Academy of Sciences,
e-mail: mchaney@space.bas.bg, lachezarhf@space.bas.bg*

Keywords: *Remote Sensing, Satellite data, Precision farming, Organic farming*

Abstract

Organic farming is a much more sustainable farming system than conventional farming. It is part of humanity's efforts to preserve biodiversity and provides healthy and safe food to humans. Remote sensing methods are widely used in agriculture. Their use will help the transition from conventional to organic farming. They can help farmers choose the most suitable place to build an organic farm. Remote sensing methods are a very powerful tool for weed control in organic farming. They can be used to determine the level of stress that crops experience. They provide a good opportunity to forecast yields on organic farms. Remote sensing methods can optimize fertilization on organic farms. They can be used to distinguish between organic and conventional agriculture, as well as to monitor biodiversity in agricultural areas. Remote sensing methods can help organic farmers make timely and adequate decisions in managing their farms.

Introduction

A major way to achieve sustainable agriculture is through the integration of remote sensing (RS) technologies. The use of RS technologies is mandatory today to achieve highly productive and sustainable agriculture [1]. The use of aerospace methods can improve the transition from conventional to organic farming. According to [2] RS technologies at various scales often prove to be an appropriate tool for crop monitoring. The potential of these technologies in relation to organic farming has not been fully explored [3]. Remote sensing monitoring in organic farming should generate information at different levels to be used for resource planning and contribute to sustainable agricultural production [4]. The use of remote sensing methods, GPS technology and hyperspectral image analysis is helping farmers to switch to agro-environmental and organic farming, which is a turning point in agriculture [5]. According to [6], the implementation of RS technologies in agriculture and especially their use in organic farming allows not only to obtain

significant cost savings of up to 25 %, an increase in productivity by 1.7 to 2.3 and yield, but also effective environmental protection. Research and technological advances in remote sensing have significantly improved our ability to detect and quantify physical and biological loads that affect crop productivity [2, 7]. Precision farming technologies that are based on RS technologies can address some of the problems in organic farming related to water and soil management, plant protection and mechanization [8].

Remote sensing methods are widely used for agricultural applications, they are the basis of precision agriculture and it cannot exist without them [9–11]. Remote sensing methods offer new perspectives and methodological approaches for precision agriculture [12–19]. Historically, the Earth's artificial satellites have dominated this area. Drones can carry spectral sensors, and also allow real-time estimates of crop yields, pests and diseases, and more [11]. Other researchers, such as [10, 20–24] also emphasize the great potential of unmanned aerial vehicles (UAVs) in the field of agriculture. Another very important application of remote sensing methods in agriculture is the ability to track the development of crops in their various phenophases [10, 25]. A number of studies aim to identify crops, assess areas, and identify diseases and pests and more [26]. Differences between vegetation and soil reflective characteristics in the near infrared region have been shown to be successful in separating plants from soils. Biochemical measurements can be performed using the field spectroscopy method. These methods use the reflection spectrum of the measured object. Thus, physiological information is obtained in each pixel. This method is very suitable for use by researchers in organic farming to better understand the biochemical components of biological fields without the need for destructive analysis [11, 19, 27]. Reflected solar radiation in specific visible, near and medium infrared ranges of the electromagnetic spectrum has proved useful in detecting nutrient deficiencies, diseases, pests, and weeds. High-resolution multispectral satellite images can be used to develop monitoring products and to support agricultural solutions. Multispectral vegetation indices derived from crop reflections over relatively wide ranges can be used to monitor plant growth in relation to measured or predicted climate variables. Any deviation from the expected seasonal pattern signals a potential problem and requires further research by farmers [7, 19, 26, 28–30]. Remote sensing allows monitoring phenology of the crops [31]. Precision farming technology based on RS and GIS technologies provides good opportunities for effective crop management [32]. This technology should be used to optimize resources (natural and socio-economic), thus serving to increase the profitability and sustainability of agriculture and support the development of organic farming [8, 33].

The objective of the paper is to attempt to review the use of satellite RS in organic farming in specific problem areas. This study is a continuation of an overview published in Bulgarian by the authors [19].

Materials and methods

This study provides an overview and a comprehensive analysis of articles, reports and materials published on the Internet in the following scientific database Scopus, Research Gate, and Google Scholar. A combination of keywords with logical queries was used when searching the scientific and specialized database for the period from the beginning of space remote sensing from the late 1980s to 2021. The main keywords that we used are: "organic farming" AND "remote sensing", "organic farming" AND "satellite data".

Results and discussion

The analysis of the reviewed literature indexed in CrossRef and parsed by the Scite platform (<https://scite.ai>), revealed that most cited top 25 publications are published by Elsevier, followed by AAAS, Wiley, and MDPI, see Fig. 1.

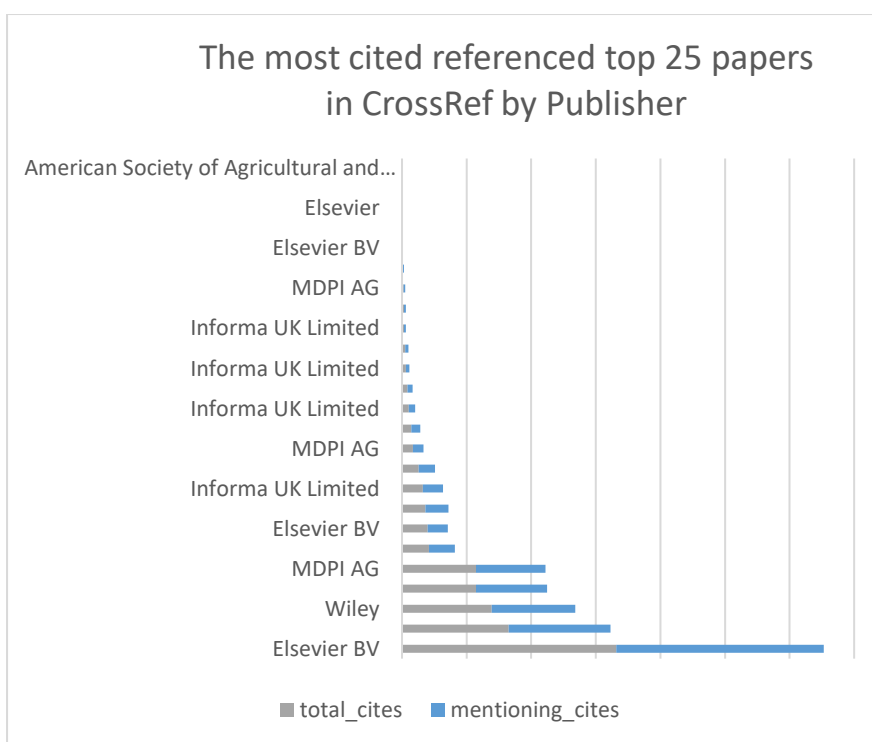


Fig. 1. Top 25 publications referenced in CrossRef by publisher

Interestingly, the most cited of the works is published almost 10 years ago, i.e. in 2013, see Fig. 2. This paper is followed by citations of a paper from 2010 and 2011. It is evidence that the interest in organic farming applications of remote

sensing sprout in the last 12 years. Although, the first referenced works in this list are from 1986. The top 3 most cited papers are those of [9] with 972 citations [33] with 641 citations, and [66] with 325 citations.

The most cited referenced top 25 papers in CrossRef by Year

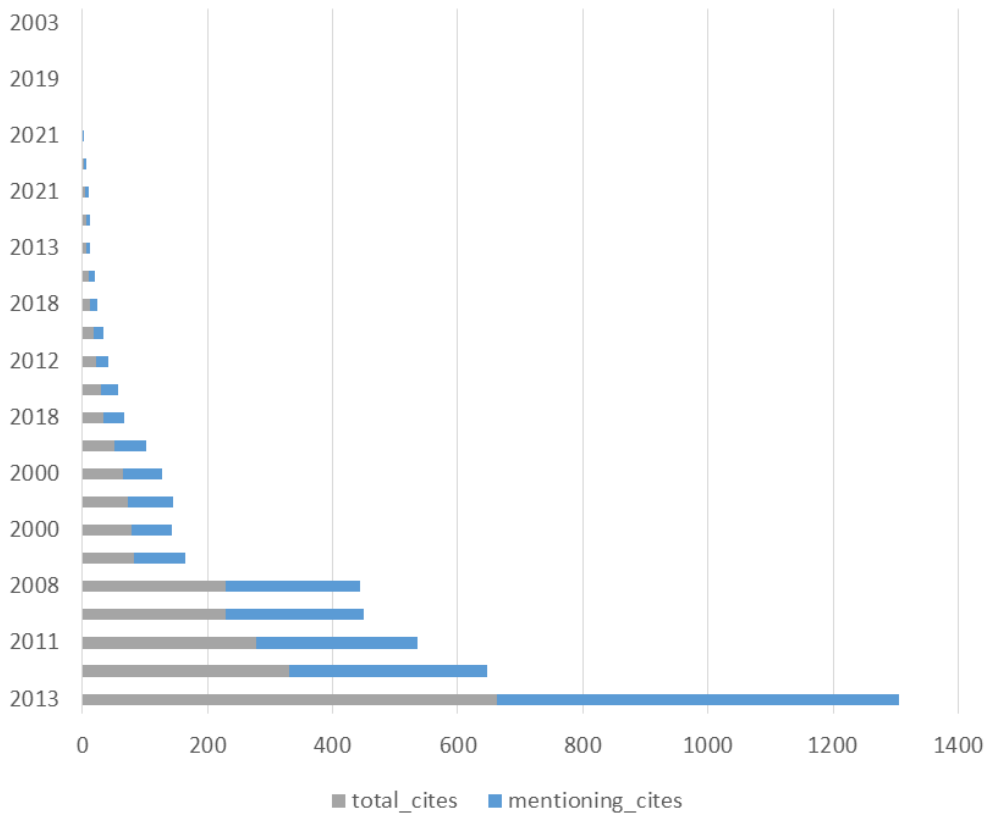


Fig. 2. Top 25 cited papers in CrossRef by number of citations

systems (GIS) can help the process of identifying the most suitable terrain for the purpose [34, 35]. With the help of RS and GIS, suitable terrains are identified, for which different criteria are selected, such as soil types, terrain slope, slope aspect, categorization of agricultural land, etc., with the help of which to create a suitability map [35, 36]. The criteria must be in line with regional natural conditions, local legislation in the field of organic farming, as well as the requirements of the crops to be harvested.

A procedure has been developed to assess the suitability of the land for organic wheat cultivation [37]. It combines seventeen eligibility criteria, which are divided into five main categories, which include climatic parameters, soil characteristics and qualities, soil chemistry, soil fertility and organic matter content, and flood and erosion hazards using GIS, multiple criteria analysis, and square root method. Uddin et al. (2018) [38] use remote sensing methods in combination with GIS and global positioning systems (GPS) to identify vulnerable to floods and low-carbon objects. They believe that this will help manage the soil and crops in organic farming.

In the second part of this publication, the following applications of remote sensing in organic farming will be considered:

- *Satellite remote sensing monitoring of weeds*
- *Remote sensing of crops' stress and the need for irrigation*
- *Forecasting of yields using remote sensing methods*
- *Remote sensing monitoring of plant nutrition*
- *Biodiversity monitoring with remote sensing*

Acknowledgements

Milen Chaney, PhD student is supported through his PhD subsidy. Milen Chaney and Lachezar Filchev have conceptualized the research overview. Milen Chaney have collected the literature and drafted the manuscript. Lachezar Filchev revised and edited it.

Conflicts of Interest

The authors reported no potential conflicts of interest.

References

1. Martos, V., Ahmad, A., Cartujo, P., & Ordoñez, J. (2021) Ensuring agricultural sustainability through remote sensing in the era of agriculture 5.0. *Appl. Sci.*, 11(13), 5911.
2. Gitelson, A. Remote sensing estimation of crop biophysical characteristics at various scales. In: *Hyperspectral Remote Sensing of Vegetation*, Thenkabail, P. S., Lyon, J. G., & Huete, A., Eds.; CRC Press. USA, 2012. ISBN 978- 1-4398-4537-0.

3. Diacono, M., De Benedetto, D., Castrignanò, A., Rubino, P., Vitti, C., Abdelrahman, H.M., Sollitto, D., Coccozza, C., & Ventrella, D., (2013). A combined approach of geostatistics and geographical clustering for delineating homogeneous zones in a durum wheat field in organic farming, *NJAS – Wageningen Journal of Life Sciences*, Vol. 64–65, 47–57, ISSN 1573-5214, DOI:10.1016/j.njas.2013.03.001
4. Syiem, M. D. (2003). Impact of agricultural literature on organic farming in northeastern region. *Indian Journal of Hill Farming (India)*. *Indian Journal of Hill Farming*, 16 (1 & 2), 101–103.
5. Niggli, U., Wang-Müller, Q., Willer, H., & Fuchs, J. (2021). Innovation in agroecological and organic farming systems. *中国生态农业学报 (中英文)*, 29(3), 1. DOI:10.13930/j.cnki.cjea.200469
6. Moisseenko, O. V., Bobkov, S. I., Kozlova, M. F., Jabassova, Z. G., & Kukhar, V. S. (2022). Integration of logistic principles into resource-saving technologies, precision and organic farming. In: *IOP Conference Series: Earth and Environmental Science* (Vol. 949, No. 1, p. 012104). IOP Publishing. DOI:10.1088/1755-1315/949/1/012104
7. Hatfield, P. L. and Pinter. P. (1993). Remote sensing for crop protection. *Crop Protection*. 12(6): 403–413. DOI:10.1016/0261-2194(93)90001-y.
8. Ferreira, S., Sánchez, J.M., & Gonçalves, J. M., (2021). Can Organic Farming development be driven by Remote Sensing technology?, In: *Proceedings of the 1st International Electronic Conference on Agronomy*, 3–17 May 2021, MDPI: Basel, Switzerland, DOI:10.3390/IECAG2021-10014
9. Mulla, D. J. (2013). Twenty five years of remote sensing in precision agriculture: Key advances and remaining knowledge gaps. *Biosystems Engineering*, 114(4), 358–371. DOI:10.1016/j.biosystemseng.2012.08.009.
10. Bendig, J., Bolten A., & Bareth, G. (2013). UAV-based Imaging for Multi-Temporal, very high Resolution Crop Surface Models to monitor Crop Growth Variability. *Photogrammetrie – Fernerkundung – Geoinformation*. (6): 551–562. DOI:10.1127/1432-8364/2013/0200.
11. Jung, A., Hegedus, B., Drexler, D., & Vohland, M. Rapid treatment monitoring by field spectroscopy. In: *Proceedings of the 4th ISOFAR Scientific Conference 'Building Organic Bridges'*, Organic World Congress 2014, 13-15 Oct., Istanbul, Turkey.
12. Baranyai, L. and F. Firtha. (1997). Comparison of grain color and shape by image analysis, <http://physics2.kee.hu/default.php?id=6> (in Hungarian).
13. Lang, Z., Kriston-Vizi, J., and Molnar, S. (2000). Precision Farming in Fruit Production. MTA. AMB Conference. Godollo, Hungary. (in Hungarian).
14. Felföldi, J., Fekete, A., Gyori, E., & Szepes, A. (2001). Variety identification by computer vision. *Acta Horticulturae*. 562: 341–345.
15. Tamas, J. (2001). Precision Agriculture, Mezogazdasági Szaktudás Kiado, Budapest. (in Hungarian).
16. Nemeth, T., Harnos, Zs., & Nemenyi, M. (2004). Precision farming, *Biotechnológiai és Agrárgazdasági Fejlesztések*. 67–76 (in Hungarian).
17. Fekete, A., Foldesi, I., Kovacs, L., Kokai, M., & Heger, L. (2004). Automatic control systems for precision farming. In: *Proc. of NKFP*, Bábolna (in Hungarian).

18. Jung, A., Kardevan, P., & Tokei, L. (2006). Hyperspectral Technology in Vegetation Analysis. *Progress in Agricultural Engineering Sciences*. 2(1): 93–115. DOI:10.1556/Progress.2.2006.1.5.
19. Chanev, M., Filchev, L., & Ivanova, D. (2020). Opportunities for Remote Sensing Applications in Organic Cultivation of Cereals—a Review. *Journal of the Bulgarian Geographical Society*, Volume, 43, 31–36.
20. Grenzdörffer, G. J., Engel, A., & Teichert, B. (2008). The photogrammetric potential of lowcost UAVs in forestry and agriculture. *Int. Archives of the Photogrammetry. Rem. Sens. and Spat. Inform. Sci.*, XXXVII(B1): 1207–1214.
21. Hunt, E. R., Hively, W. D., Fujikawa, S. J., Linden, D. S., Daughtry, C. S. T., & McCarty G. W. (2010). Acquisition of NIR-green-blue digital photographs from unmanned aircraft for crop monitoring, *Remote Sensing*. 2: 290–305.
22. Lelong, C., Burger P., Jubelin, G., Roux, B., Labbé, S., & Baret, F. (2008). Assessment of Unmanned Aerial Vehicles Imagery for Quantitative Monitoring of Wheat Crop in Small Plots. *Sensors*. 8(5). DOI:10.3390/s8053557.
23. Jeleu, G. (2018). Types of drones. In: *Proceedings of the Scientific Conference "Space, Ecology, Security"- SES 2018*, 236–252. SRTI-BAS, ISSN 2603-3313.
24. Roslim MHM, Juraimi, A.S., Che'Ya N.N., Sulaiman, N., Manaf, M.N.H.A., Ramli, Z., & Motmainna, M. (2021). Using Remote Sensing and an Unmanned Aerial System for Weed Management in Agricultural Crops: A Review. *Agronomy*. 2021; 11(9):1809. DOI:10.3390/agronomy11091809
25. Hoffmeister, D., Bolten, A., Curdt, C., Waldhoff, G., & Bareth, G. (2010). High resolution Crop Surface Models (CSM) and Crop Volume Models (CVM) on field level by terrestrial laserscanning. In: *SPIE Proceedings*. 7840.
26. Usha, K. and B. Singh. (2013). Potential applications of remote sensing in horticulture - A review. *Scientia Horticulturae*. 153: 71–83. doi:10.1016/j.scienta.2013.01.008
27. Akhtman, Y., Golubeva E., Tutubalina, O., & Zimin, M. (2017). Application of hyperspectral images and ground data for precision farming. *Geog., envir., sust.* 10(4): 117–128. DOI:10.24057/2071-9388-2017-10-4-117-128
28. Johnson, L. F., Roczen, D. E., Youkhana, S. K., Nemani, R. R., & Bosch, D. F. (2003). Mapping vineyard leaf area with multispectral satellite imagery. *Comput. Electron. Agric.* 38: 33–44.
29. Ray, S., Dutta, S., & Kundu, N. (2006). A GIS and remote sensing based approach to develop cold storage infrastructure for horticultural crops: a case study for potato crop in Bardhaman district, West Bengal. <http://www.GISdevelopment.net>
30. Panda, S. and Hoogenboom, G. J. P. (2009). Distinguishing blueberry bushes from mixed vegetation land-use using high resolution satellite imagery and geospatial techniques. *Computers and Electronics in Agriculture*. 67(1–2): 51–59.
31. De Beurs, K., Ioffe, G., & Nefedova, T. (2012). Agricultural change in the Russian grain belt: a case study of Samara oblast. *Geography, environment, sustainability*. 5(2): 95–110. DOI:10.24057/2071-9388-2012-5-2-95-110
32. Naumov, A., Pereira de Oliveira, R., Bardy Prado, R., & Turetta, P. A. (2012). Balanced fertilization for sustainable development of agriculture in the savannas of South America: towards a geographical approach. *Geography, environment, sustainability*. 5(4): 84–95. DOI:10.24057/2071-9388-2012-5-4-84-95

33. Gebbers, R., & Adamchuk, V. I. (2010). Precision Agriculture and Food Security. *Science*, 327(5967), 828–831. DOI:10.1126/science.1183899
34. Kamkar, B., Dorri, M.A., & Teixeira da Silva, J.A., (2014). Assessment of land suitability and the possibility and performance of a canola (*Brassica napus* L.) – soybean (*Glycine max* L.) rotation in four basins of Golestan province, Iran. *Egypt. J. Remot. Sens. Space Sci.*, 17 (1), 95–104. DOI:10.1016/j.ejrs.2013.12.001.
35. Mishra, A. K., Deep, S., & Choudhary, A. (2015). Identification of suitable sites for organic farming using AHP & GIS. *Egyptian Journal of Remote Sensing and Space Science*, 18(2), 181–193. DOI:10.1016/j.ejrs.2015.06.005
36. Xu, Y., Sun, J., Zhang, J., Xu, Y., Zhang, M., & Liao, X., (2012). Combining AHP with GIS in synthetic evaluation of environmental suitability for living in China's 35 major cities. *Int. J. Geogr. Inf. Sci.*, 26 (9), 1603–1623.
37. Karimi, F., Sultana, S., Shirzadi B. A., & Royall, D. (2018). Land Suitability Evaluation for Organic Agriculture of Wheat Using GIS and Multicriterial Analysis. *Papers in Applied Geography*, 1–17.
38. Uddin, Md. J., Mohiuddin, A.S.M., & Hossain Shaikh Tanveer (2018). Identification of vulnerable sites for the adoption of organic farming using geo-spatial technologies in Bangladesh. In: Proceedings of 3rd Organic Asia Congress, pp. 1–4.

ПРИЛОЖЕНИЕ НА СПЪТНИЦИ В БИОЛОГИЧНОТО ЗЕМЕДЕЛИЕ (ЧАСТ I)

М. Чанев, Л. Филчев

Резюме

Биологичното земеделие е много по-устойчива земеделска система от конвенционалното земеделие. То е част от усилията на човечеството да запази биоразнообразието и да осигури здравословна и безопасна храна за хората. Методите за дистанционно наблюдение се използват широко в селското стопанство. Използването им ще подпомогне прехода от конвенционално към биологично земеделие. Те могат да помогнат на земеделските производители да изберат най-подходящото място за изграждане на биоферма. Методите за дистанционно наблюдение са много мощен инструмент за борба с плевелите в биологичното земеделие. Те могат да се използват за определяне на нивото на стрес, което изпитват културите. Те дават добра възможност за прогнозиране на добивите в биологичните стопанства. Методите за дистанционно наблюдение могат да оптимизират торенето в органичните стопанства. Те могат да се използват за разграничаване на органичното от конвенционалното земеделие, както и за наблюдение на биоразнообразието в земеделските райони. Методите за дистанционно наблюдение могат да помогнат на биологичните земеделски производители да вземат навременни и адекватни решения при управлението на стопанствата си.

POST-FIRE RECOVERY MONITORING USING REMOTE SENSING: A REVIEW

Nataliya Stankova

*Space Research and Technology Institute – Bulgarian Academy of Sciences
e-mail: natalia_hs@space.bas.bg*

Keywords: *Remote sensing, Post-fire, Forest recovery, Vegetation indices, Tasseled cap transformation*

Abstract

Wildfires are a common disturbance factor, while climate change is thought to be one of the main causes of the fires. The detection of disturbance and post-fire recovery monitoring are vital for ecological research. This article aims to provide a review of current research of post-fire recovery monitoring based on remotely sensed data. While a close relationship between vegetation indices (VIs) and physiological parameters of vegetation has been established, VIs have become the main tool for assessing and monitoring vegetation status. Research on the effects and recovery from fires has been conducted by a number of authors, with VIs being used mainly in the methodologies. Tasseled Cap Transformation (TCT) method is also used to assess the state of the ecosystem before and after a fire. When viewed in series, Disturbance Index (DI) images provide an immediate way to recognize the pixels of the forests affected by the fire, different from those characteristics of the normal state of forests. The incorporation of various remote sensing data with field data is able to support the monitoring of post-fire effects and forest recovery.

Introduction

Monitoring the recovery processes of burned forests is a bit more complicated task than identifying them, mainly due to the smaller scale of the recovery areas compared to the total area, and due to the fact that the change in the signature may be barely noticeable, especially in the initial recovery stages. Fire creates heterogeneity on the landscape, which impacts the dynamics of the forest regrowth process. Recovery in areas partially affected by fire can be difficult to detect.

In the last few years, when the consequences of the forest fires in some regions of Bulgaria reached enormous dimensions, more detailed studies began [1–5].

Ecological framework

The ecological consequences of forest fire are multifaceted – deforestation and soil erosion, change in water flow, disruption of the heat and water balance of ecosystems, destruction of unique habitats of rare, protected, and endemic species, biological diversity limitation, deterioration of sanitary conditions of forests, disrupting the CO₂ cycle in nature.

The damage in terms of biodiversity loss and soil erosion is practically irreversible. The main fuel for wildfires consists basically of vegetation, while large fires can leave an entire area without vegetation cover, which can lead to significant climatic, ecological, and hydrological risks. In addition, after a fire, plant communities can be replaced by new different types of communities, which is due to invasive species, as a result of the variety of secondary effects that occur. When the vegetation cover is burned, almost all environmental conditions change. Forest fires destroy vegetation, animals, and microorganisms, which are necessary for the normal function of the cycle in living nature. It also destroys the soil humus, thus disrupting homeostasis, i.e. the sustainability of ecosystems.

After a fire, the amount of light on the soil increases. That is why the first species that settle on the burnt areas are the light-loving ones. The lack of plant cover increases the direct penetration of precipitation into the soil and disturbs the water balance. Waterlogging of the soil and the appearance of erosion processes are possible. A forest fire primarily burns the undergrowth and also destroys the seed stock. The fire burns the forest floor, which leads to destruction of the numerous micro- and macro-organisms, inhabiting the surface layer of the soil [4].

In the areas that are prone to forest fires, where fires are a constant phenomenon, many tree species (pyrophytes) have adapted to the effects of fire and successfully survive. Their seeds have a hard and strong shell that protects them from fire and preserves their ability to germinate. As a rule, pyrophytes are fast-growing species and begin to bear fruit early. Some tree species contain in their leaves a little burning substances and a greater water content, which is also an adaptation to reduce the destructive effect of fire and its limitation.

Unlike pyrophytes, coniferous species contain a lot of resinous substances, which contributes to their rapid burning and the damage from fires is significantly greater. Beech (*Fagus*), fir (*Abies*), spruce (*Picea*), Balcan pine (*Pinus Peuce*), birch (*Betula alba*), and aspen (*Populus tremula*) tree species have thin bark that burns easily and is quickly damaged by fire. In contrast, oaks (*Quercus*), black pines (*Pinus nigra*), larches (*Larix*) have thick bark, which makes them resistant to ground fires. Important for the resistance of tree species against fires is the presence of dormant buds, especially when they are on the root system. Aspens, hornbeams, beeches, lindens, etc. have the ability to give many root shoots [4, 5].

Forest fires lead to soil degradation, which is expressed in the reduction of its nutrient supply (burning of organic matter, reduction of nitrogen content,

change in the content and ratio between the total and exchangeable forms of nutritional elements) and development of erosion. It has been established that about three years after a fire, the limitation of degradation processes begins, expressed mainly in the levels of soil indicators to those before the fire.

In cases where, as a result of a fire, there is a real supply of nutrients in exchangeable forms, it is possible for them to be adsorbed by the plants, and after decomposition of the leaf mass – to fall into the soil again. The temporary accumulation of nutrients facilitates rapid vegetation recovery. If the frequency of fires is high, as observed in some areas, the food supply of the ecosystems is not fully restored. The long-term post-fire effect for our geographical latitudes and climatic conditions is expressed in a gradual reduction of soil nutrient reserves, a slowing down of the rate of vegetation recovery, an intensification of erosion processes, which in turn lead to irreversible desertification processes.

The consequences of forest fires continue for decades, and in our climatic conditions they almost always lead to negative consequences in terms of the productivity of ecosystems, including tree stands. In addition to damaging ecosystems, wildfires create conditions that favor the occurrence of new fires. This is due to a violation of the integrity of the forest, which on one hand leads to a disturbance of the microclimate and a decrease in moisture, and on the other – allows the appearance of grasses, lianas, and bushes, thus increasing the amount of light, easily flammable combustible materials.

The assessments obtained by remote sensing methods for the heterogeneity and spatial distribution of burned areas were also used to identify priority areas for fuel reduction and post-fire recovery. Post-fire recovery of forests depends on adequate seed dispersal and favorable microclimate conditions, which in turn are related to the location and type of landscapes (height, slope, and aspect). Large areas with high burn severity may have fewer surviving trees to provide seeds. Unburned or areas with low burn severity within high burn severity areas can provide sources of seed to increase the rate of forest recovery. After a fire, the environment can change significantly within a year and some aspects may be predictable, while others may depend on local weather conditions.

Passive and active sensors

In terms of the remote sensing of post-fire effects, we can divide the available sensor systems into passive and active. The most commonly used type of active sensor being used to evaluate fire-related information is light detection and ranging (Lidar) systems. These provide information on the elevation (and thus relative height) of a surface by measuring the time taken for a pulse of laser light to journey between a sensor and a surface. Lidar systems are predominately aerial-based and have been widely used to characterize individual-tree and stand-level canopy structure. Spaceborne SAR data also provides an alternative approach for

monitoring the regrowth of post-fire forests, since backscatter is also sensitive to forest structural parameters. The majority of remote sensing systems that have been used to infer post-fire characteristics have been passive sensors measuring the reflection or emission of electromagnetic radiation from surfaces. Multispectral airborne and satellite sensors use radiometers that are sensitive to narrow bandwidths (bands) of the electromagnetic spectrum.

VIs

Research on the effects and recovery from fires has been conducted by a number of authors, with VIs being used mainly in the methodologies. VIs are usually dimensionless quantities obtained by satellite data in different spectral ranges, mainly used to show the amount of green vegetation available. Due to this fact, VIs have become the main tool for assessing and monitoring vegetation status. A close relationship between VI and physiological parameters of vegetation (LAI, biomass, photosynthetic activity, productivity, etc.) has been proven. Although LAI is the major morphological parameter of vegetation cover associated with satellite VIs, its measurement and assessment are very complex. For this reason, VIs are appropriate indicators for monitoring and assessment of vegetation condition.

Although one of the first, Normalized Difference Vegetation Index (NDVI) [6] is one of the most commonly used VIs for assessing green vegetation biomass as well as for remote assessment of recovery processes of vegetation after fire. A study by Chèret and Denux [7] found that changes in NDVI values correlated with the De Marton Drought Index. The spectral reflective characteristics of vegetation in the visible and near infrared range, in contrast to those of the soil, explain the use of NDVI to distinguish vegetation cover. In addition, NDVI partially normalizes the influence of external factors in the reflection of vegetation, i.e. errors associated with changes in illumination or atmospheric scattering.

As the processes of vegetation and drought are not very dynamic, the data with average spatial resolution are more suitable for detailed studies of small areas. What is specific is that the VIs based on optical data are particularly sensitive to the presence of any clouds. To be correctly determined, it must be ensured that the cloud cover is zero over the studied area. When using low-resolution satellite data, there is a risk of cloud cover for some parts occupying an area of less than one pixel of the image. In this case, NDVI index is artificially lowered. To avoid this, indices are used that are formed by channels with a longer wavelength (EVI, NDWI or NDII).

Normalized Difference Water Index ($NDWI_{1.24\mu m}$) [8] uses a wavelength in the mid-infrared range, less affected by atmospheric absorption. $NDWI_{1.64\mu m}$ shows less saturation than $NDWI_{1.24\mu m}$.

Normalized Difference Infrared Index (NDII) is used analogously to NDWI when lacks data in the SWIR range [9].

Normalized Multi-band Drought Index (NMDI) is used simultaneously to study the dryness of the soil layer and the moisture content in the leaf mass of plants [10]. This improved drought index is able to calculate the water content of both soil and vegetation and is therefore expected to offer more accurate estimates of the degree of drought and the impact of fire [10].

Normalized Difference Dust Index (NDDI) is used to study the effect of soil and leaf drought on the vegetation process of plants, as well as the effect of fires on vegetation [11].

Enhanced Vegetation Index (EVI) [12] is used similarly to NDVI for the study of vegetation, as the lower the value, the less the vegetation and the leaf mass of plants. The decrease of the index over the years signals deforestation of a given area [9]. Unlike NDVI, this index is less sensitive to the presence of scattered clouds or small dust particles in the atmosphere, which reduce the radiation reflected by the object reaching the sensor.

Moisture Stress Index (MSI) is used to determine the stress in vegetation, measured by changes in moisture content [13].

Soil-Adjusted Vegetation Index (SAVI) uses an L-factor to correct the different reflectivity of soils [14]. SAVI is more closely related to LAI than to NDVI.

An alternative approach to soil line correction is the Perpendicular Vegetation Index (PVI) [15]. PVI is interpreted geometrically as the perpendicular distance of a measured point from the soil line. The perpendicular distance of the R/NIR measurement from the soil line is not linearly related to LAI.

The fire impacts are assessed significantly more frequently by the Normalized Burn Ratio (NBR) index [16], which using the near and middle infrared channel is designed to be maximally sensitive to overall changes in spectral reflectance characteristics caused by fire. Differenced Normalized Burn Ratio (dNBR) is the result of differences in NBR index before and after fire. NBR and dNBR are key indicators of burn severity and can be used to determine post-fire effects, fire size, and burn severity classifications. NBR is also used for the degree of post-fire recovery. The dNDVI and dNBR indices are distinguished by higher map accuracies and regression relationships in forested areas, compared with results for studies conducted in environments with lower gross primary productivity.

The Mid-infrared Bispectral Index (MIRBI) was created to assess the burnt vegetation in the savanna [17]. Although MIRBI was developed only to assess burned vegetation, NBR and dNBR have been widely used to assess post-fire landscape effects in the USA, as well as in South African savannas. In addition to measuring burned vegetation, NBR is used to measure the extent of ecological change after a fire.

Terrestrial data on post-fire effects include assessment of soil color change; soil infiltration and hydrophobicity; the change in plant char and ash cover; tree scars and organic fuel consumption.

In an attempt to integrate these different measurements, Key and Benson [18] developed the terrestrial Composite Burn Index (CBI). CBI is based on a visual assessment of the amount of burned vegetation, the degree of soil charring and the degree of vegetation regeneration. The CBI was established for the purpose of ground validation of the NBR spectral index. After the effects of the fire on 30 m x 30 m test plots in five separate horizontal layers (from soil to tree crowns) were assessed separately and then combined into one total "burn severity" value for the plot. The CBI method is quite fast but very subjective.

The presence of areas with similar environments, behavior and post-fire impacts has led to the use of the term "severity classes" within both the ecological literature and remote sensing. And yet there are significant variations in the so-called "low", "moderate" and "high" degree of classification depending on the region and types of vegetation. In forested areas, remotely sensed "burn severity" maps often show a strong correlation with fire effects on the upper canopy and exhibit low correlation with terrestrial and soil variables where vegetation obscures the ground.

The use of temporal series and transformations are widespread. Remote sensing with time series data offers considerable potential in the trajectory of post-fire forest dynamics, beyond monitoring forest succession and current structural attributes of forests after fires. Many studies have addressed this issue by using moderate-to-low resolution time series NDVI, SAVI, EVI, albedo, NDVI-based Net Primary Productivity (NPP), fraction of absorbed photosynthetically active radiation (fAPAR) and, recently, the vegetation optical depth (VOD) parameter from the Advanced Microwave Scanning Radiometer for Earth Observing System (EOS) (AMSR-E) sensor as surrogates representing the recovery of vegetation after fire disturbances.

TCT

The model for orthogonalization of satellite images proposed by Kauth and Thomas [19] is a very effective method for interpretation, classification and analysis of phenomena and processes related to the dynamics of the main components of the earth's surface – soil, vegetation, and water. This type of transformation is called Tasseled Cap Transformation (TCT) [19]. The method used for linear spectral transformation in multidimensional space to reduce the correlation between its individual elements using three components – soil, vegetation and humidity – is also used to assess the state of the ecosystem before and after a fire. TCT is related to the change of the coordinate axes in the spectral space from the original ones in three uncorrelated directions, preserving their orthogonality – Brightness (TCB), Greenness (TCG) and Wetness (TCW).

The TCB index is the sum of all channels corresponding to the direction of the main change in soil reflection. The TCG index represents the contrast between the infrared and the visible channel, orthogonal to the TCB. The TCW index refers to plant and soil moisture, orthogonal to the TCB and TCG. Different sensors use different transformation matrices, fixed only for them.

Healey et al. [20] calculated Disturbance Index (DI), which is a linear combination of the three Tasseled Cap indices. The calculation of DI is based on the observation that burned forests are usually characterized by higher values of the TCB and lower values of the TCG and TCW compared to unaffected forest areas [20]. However, as there are variations that exist in the acquisition date between images, the detection index adopted should be relatively insensitive to the Bidirectional Reflectance Distribution Function variability and phenology. Thus, spectral normalization of the TCB, TCG, and TCW indices should be performed which use within-image statistics to normalize radiometric change. Therefore, the areas affected by the fire have high positive nTCB values and low negative nTCG and nTCW values (where the prefix “n” stands for “normalized”). They show high DI values. Conversely, unaffected areas should present low DI values [20]. DI quantifies how close the pixel is to an area in the scene, characterized by the highest TCB and the lowest TCG and TCW indices. When viewed in series, DI images provide an immediate way to recognize the pixels of the forests affected by the fire, different from those characteristics of the normal state of forests.

Conclusion

Aerospace remote sensing methods are a high-tech tool for reliable and large-scale monitoring of recovery processes in forest ecosystems after a fire. The study of the consequences of forest fires is determined by their large-scale and long-lasting effects on the ecological situation of huge territories. For operational, reliable, and large-scale research, remote aerospace methods and technologies are vital. Incorporation of various remote sensing data with field data is able to support the monitoring of post-fire effects and forest recovery.

References

1. Димитров, П., А. Гиков, Идентификация и оценка на следи от пожари в Рила планина чрез използване на спектрални индекси по данни от Landsat. Сборник доклади от Петата научна конференция с международно участие SENS' 2009, Ноември 2009, София, България, ИКИ-БАН, 142–149, ISSN 1313-3888 <http://www.space.bas.bg/SENS2009/6-R.pdf>.
2. Nedkov, R., E. Velizarova, D. Avetisyan, and N. Georgiev, Assessment of forest vegetation state through remote sensing in response to fire impact. Proc. SPIE 11524, Eighth International Conference on Remote Sensing and Geoinformation of the Environment (RSCy2020), 115240Q (26 August 2020); <https://doi.org/10.1117/12.2570808>.

3. Spassova, T., R. Nedkov. A differentiated approach to monitoring natural objects based on aerospace data from different spectral ranges, interdisciplinary doctoral forum 2016, p. 40.
4. Андреев, В., В. Александров, Е. Бъчварова. Актуални рискови явления в атмосферата, 2010. София, Деметра.
5. Мардиросян, Г. Природни бедствия и екологични катастрофи – изучаване, превенция, защита, Акад. Издателство „Проф. Марин Дринов“, София, 2009, ISBN 978-954-322-350-3.
6. Rouse, J., R. Haas, J. Schell, and D. Deering, Monitoring Vegetation Systems in the Great Plains with ERTS. Proceedings of Third Earth Resources Technology Satellite-1 Symposium, Greenbelt, MD, USA, 1973, 309–317.
7. Chèret, V., and J. Denux, Mapping wildfire danger at regional scale with an index model integrating coarse spatial resolution remote sensing data. Journal of geophysical research. 2007, 112, 1–11.
8. Gao, B., NDWI – A normalized difference water index for remote sensing of vegetation liquid water from space. Remote Sensing of Environment, 1996, 58, 257 – 266.
9. Cheng, Y., S. Ustin, D. Riaño, and V. Vanderbilt, Water content estimation from hyperspectral images and MODIS indexes in Southeastern Arizona. Remote Sensing of Environment, 2008, 112, 363–374.
10. Wang, L., and J. Qu, NMDI: a normalized multi-band drought index for monitoring soil and vegetation moisture with satellite remote sensing. Geophysical Research Letters, 2007, 34, L20405. doi:10.1029/2007GL031021.
11. Qu, J., X. Hao, M. Kafatos, and L. Wang, Asian Dust Storm Monitoring Combining Terra and Aqua MODIS SRB Measurements. IEEE Geoscience and Remote Sensing Letters, October 2006, 3, 4.
12. Huete, A., K. Didan, T. Miura, *et. al.*, Overview of the radiometric and biophysical performance of the MODIS vegetation indices. Remote Sensing of Environment, 2002, 83, 195–213.
13. Jensen, J., Remote Sensing of the Environment An Earth Resource Perspective Second Edition Pearson Prentice Hal, 2007. ISBN-10: 0-13-188950-8.
14. Huete, A., A soil adjusted vegetation index (SAVI). Remote sensing of environment, 1988, 25, 295–309.
15. Richardson, A., and C. Wiegand, Distinguishing vegetation from soil background. Photogrammetric Engineering and Remote Sensing, 1977, 43, 1541 – 1552.
16. Key, C., and N. Benson, The Normalized Burn Ratio (NBR): A Landsat TM Radiometric Index of Burn Severity. 1999. URL = <http://www.nrmc.usgs.gov/research/ndbr.htm> visited April 2007.
17. Trigg, S., and Flasse, An evaluation of different bi-spectral spaces for discriminating burned shrub-savanna. International Journal of Remote Sensing, 2001, 22, 13, 2641–2647.
18. Key, C., and N. Benson N., Landscape assessment: Ground measure of severity, the Composite Burn Index; and remote sensing of severity, the normalized burn ratio. In ‘FIREMON: Fire Effects Monitoring and Inventory System.’ (Eds DC Lutes, RE Keane, JF Caratti, CH Key, NC Benson, LJ Gangi), USDA Forest Service, Rocky Mountain Research Station General Technical Report, RMRS-GTR-XXX. (Ogden, UT), 2005. XX pp.

19. Kauth, R., and G. Thomas, The Tasseled Cap – a graphic description of the spectral – temporal development of agricultural crops as seen by Landsat. Proceedings second ann. symp. machine processing of remotely sensed data. West Lafayette’ Purdue University Lab. App. Remote Sensing, 1976.
20. Healey, S., W. Cohen, Z. Yang, and O. Krankina, Comparison of Tasseled Cap-based Landsat data structures for use in forest disturbance detection. Remote Sensing of Environment, 2005, 97, 301–310. doi: <http://dx.doi.org/10.1016/j.rse.2005.05.009>.

МОНИТОРИНГ НА ВЪЗСТАНОВИТЕЛНИТЕ ПРОЦЕСИ СЛЕД ПОЖАР С ИЗПОЛЗВАНЕ НА ДИСТАНЦИОННИ МЕТОДИ: ПРЕГЛЕД

Н. Станкова

Резюме

Откриването на засегнати територии и мониторингът на възстановителните процеси след пожар са жизненоважни за екологичните изследвания. Тази статия има за цел да направи основен преглед на текущите изследвания на мониторинга за възстановителните процеси след пожар въз основа на данни от дистанционно наблюдение. Тъй като е установена тясна връзка между вегетационните индекси (ВИ) и физиологичните параметри на растителността, ВИ се превръщат в основен инструмент за оценка и мониторинг на състоянието на растителността. Изследвания върху ефектите и възстановяването от пожари са проведени от редица автори, като в методологиите им се използват главно ВИ. Методът Tasseled cap трансформация (ТСТ) също се използва за оценка на състоянието на екосистемата преди и след пожар. Разглеждани последователно, ДІ изображенията осигуряват начин за разпознаване на пикселите на горите, засегнати от пожара, различаващи се от тези, характерни за нормалното състояние на горите. Обединяването на различни данни от дистанционно наблюдение с полеви данни е в състояние да подпомогне мониторинга на последствията след пожар, както и последващото възстановяване на горите.

REMOTE SENSING TECHNOLOGY IN ENGINEERING GEODESY



After nearly nine years of work, G. Milev and I. Milev completed the series of 5 books on Applied Geodesy - Part 1 Engineering Geodesy (2022). In its essence, this work summarizes the modern problems of construction, architecture, the organization of the territory and the role and place of Engineering Geodesy. Thus, for the first time, these activities and characteristics of surveying are jointly considered from an interdisciplinary perspective. Engineering geodesy exists as an inseparable element of this complex activity, in which various specialties and, especially, geospatial technologies have an indisputable role.

The books reflect the views of the authors, their long-term research, teaching experience and participation in research and construction of engineering objects with original spatial-constructive solutions. The exposition is in accordance with the current regulatory framework and the possibilities offered by modern digital devices, tools, systems and technologies.

The series offers a number of original solutions: 1. A new concept is introduced in the literature - System/s of monographs; 2. Three groups of matter are distinguished; 3. An original, consistent multi-level (triple) four-level numbering of the content (up to 3 levels), figures, tables, quotations is developed and offered for use; 4. A large number of specific examples from the practice of the objects under consideration are given; 5. The principles, exposition and general joint presentation of construction, architecture, land use, engineering geodesy applied here are prerequisites and fit into BIM, which is the desired perspective.

The bibliographic description of the books is as follows:

Milev, G., I. Milev. Applied Geodesy. Part 1, Engineering Surveying:

Book 1. Basics, Systems and Technologies in Engineering Surveying. Sofia, USLMB. Avangard Publ. House. 2017. 498 p.;

Book 2. Design and Implementation of Physical and General Plans. Sofia, USLMB. Avangard Publ. House. 2017. 330 p.;

Books 3. Construction of Linear Objects, Buildings, Structures and Installation of Technological Equipment. Plans of Built Complex Objects. {Books 3(3.1), 2019. 524 p.; 3(3.2), 2022, 530 p.; 3(3.3), 2022, 466 p.}.

Corr. Member Peter I. Y. Velinov

**IN MEMORY OF LEV DORMAN
(01.05.1929–27.07.2022)**

The world-famous Russian and Israeli space scientist Lev Isaakovich Dorman left this earth at the age of 94. His life was spent in Russia, Israel (since 1992) and the USA (Princeton University). In fact, he was a citizen of all mankind. It stood far above ordinary human understanding, above politics, above the storms and struggles of this world. His motto was: science and only science, and that in its purest and truest form. He remained a tireless and active scientist until the end.

In the 1950s, Lev Dorman laid the foundations for the study of cosmic ray variations of atmospheric, magnetospheric and extraterrestrial origin. The main discoveries he made in the early years of his scientific activity can be summarized with the following significant discoveries:

- separation of the two types of plasma flows from the Sun. The first type of flows have relatively weak frozen magnetic fields with an intensity roughly constant during the solar cycle. Flows of the second type have about an order of magnitude higher magnetic fields and their intensity is approximately proportional to the level of solar activity, cause strong magnetic storms on Earth and Forbush- decrease with the intensity of cosmic rays. Later, the first type of flows were identified with the solar wind, and the second with coronal mass ejections and interplanetary shock waves (1955–1957);

- the diffusion nature of the spread of solar cosmic rays in interplanetary space (1957);

- the resonant scattering of cosmic ray particles during propagation in the cosmic plasma (1959);

- the acceleration of the drift of cosmic rays by shock waves (1959);

- determining the size of the heliosphere from about 100 a.u. (1967) by CR variations, many years before direct space measurements.

Lev Dorman has published over 1,500 original scientific articles and 32 fundamental monographs. He visited Bulgaria several times, making an outstanding contribution to the development of space physics in our country.

Lev Dorman, sparing no effort and time, created the necessary organization and scientific potential for cosmic ray research in Russia and Israel. Thanks to his efforts, the results of these studies received wide international recognition and fame. He trained many of his students who are successfully working in many countries around the world.

We will forever cherish the wonderful memory of this bright man and outstanding scientist-cosmonaut.

Corr. Member Peter I. Y. Velinov